10-17-2019

Characterization of Laser-Cladded AISI 420 Martensitic Stainless Steel for Additive Manufacturing Applications

Mohammad Khurshed-Ul Alam
University of Windsor

Characterization of Laser-Cladded AISI 420 Martensitic Stainless Steel for Additive Manufacturing Applications

By

Mohammad Khurshed-Ul Alam

A Dissertation

Submitted to the Faculty of Graduate Studies

through the Department of Mechanical, Automotive and Materials Engineering

in Partial Fulfillment of the Requirements for

the Degree of Doctor of Philosophy

at the University of Windsor

Windsor, Ontario, Canada

2019

Characterization of Laser-Cladded AISI 420 Martensitic Stainless Steel for Additive Manufacturing Applications

By

Mohammad Khurshed-Ul Alam

APPROVED BY:

_____

A. Gerlich, External Examiner
University of Waterloo

_____

M. Wang
Department of Mechanical, Automotive and Materials Engineering

_____

R. Bowers
Department of Mechanical, Automotive and Materials Engineering

_____

H. Hu
Department of Mechanical, Automotive and Materials Engineering

_____

A. Edrisy, Co-Advisor
Department of Mechanical, Automotive and Materials Engineering

_____

R.J. Urbanic, Co-Advisor
Department of Mechanical, Automotive and Materials Engineering

October 2, 2019

DECLARATION OF CO-AUTHORSHIP/PREVIOUS PUBLICATIONS

I. Co-Authorship

I hereby declare that this dissertation incorporates the outcome of research performed under the supervision of Dr. Afsaneh Edrisy and Dr. R. Jill Urbanic as well as collaboration with Dr. Navid Nazemi, Dr. Mehdi Mehdi, and James Pineault. The collaboration is covered in some portions of Chapter 2-6 of this dissertation. Contributions by the collaborators were primarily through the provision of some preliminary simulation and EBSD work.

I am aware of the University of Windsor Senate Policy on Authorship and I certify that I have properly acknowledged the contribution of other researchers to my dissertation and have obtained written permission from each of the co-authors to include the above material(s) in my thesis.

I certify that, with the above qualification, this dissertation, and the research to which it refers, is the product of my own work.

II. Previous Publication

This dissertation includes materials from the original peer reviewed journal articles that have already been published or submitted to the peer reviewed journals.

Dissertation Chapter	**Publication title and citation information**	**Publication status**
Chapter 2	M.K. Alam, R.J. Urbanic, N. Nazemi, A. Edrisy, Predictive modeling and the effect of process parameters on the hardness and bead characteristics for laser-cladded stainless steel, Int. J. Adv. Manuf. Technol. (2017). doi:10.1007/s00170-017-0898-5	published
Chapter 3	M.K. Alam, A. Edrisy, J. Urbanic, J. Pineault, Microhardness and Stress Analysis of Laser - Cladded AISI 420 Martensitic Stainless Steel, J. Mater. Eng. Perform. 26 (2017) 1076–1084. doi:10.1007/s11665-017-2541-x	published

Chapter 4	M.K. Alam, A. Edrisy, R.J. Urbanic, Microstructural Analysis of the Laser-Cladded AISI 420 Stainless Steel, Metall. Mater. Trans. A. Online (2019). doi:https://doi.org/10.1007/s11661-019-05156-6.	published
Chapter 5	M.K. Alam, M. Mehdi, R.J. Urbanic, A. Edrisy, Electron Backscatter Diffraction (EBSD) Analysis of Laser-Cladded AISI 420 Martensitic Stainless steel, Journal of Materials Characterization. (Ref. MATERIALSCHAR_2019_1647)	Under review
Chapter 6	M.K. Alam, M. Mehdi, R.J. Urbanic, A. Edrisy Mechanical Behavior of Additive Manufactured AISI 420 Martensitic Stainless Steel. Journal of Materials Science and Engineering A. (Ref. MSEA-D-19-04444)	Under review

I certify that I have obtained a written permission from the copyright owners to include the above published materials in my dissertation. I also certify that the above material describes work completed during my registration as a graduate student at the University of Windsor.

III. General

I declare that, to the best of my knowledge, my dissertation does not infringe upon anyone's copyright nor violate any proprietary rights and that any ideas, techniques, quotations, or any other materials from the work of other people, published or otherwise, are fully acknowledged in accordance with the standard referencing practices. Furthermore, to the extent that I have included copyrighted material that surpasses the bounds of fair dealing within the meaning of the Canada Copyright Act, I certify that I have obtained a written permission from the copyright owner(s) to include such material(s) in my thesis.

I declare that this is a true copy of my dissertation, including any final revisions, as approved by my advisory committee and the Graduate Studies office and that this dissertation has not been submitted for a higher degree to any other University or Institution.

ABSTRACT

Laser cladding is an additive manufacturing (AM) process that uses lasers to melt and deposit metallic powders in layer by layer to coat a substrate or to build three dimensional object. However, the AM industry encounters problems in handling residual stresses in the cladded parts or coating that lead to high hardness and distortion. Also, anisotropic properties developed in the laser-cladded AM parts are a challenge to use them as a functional component. This study aims to understand those problems with the laser-cladding AM process using AISI 420 martensitic stainless steel (MSS) powder in a coaxial direct powder deposition method. Primarily, this study focuses on the effect of process parameters, microstructural evolution, and associated residual stress development in the single bead of laser-cladded 420 MSS. Subsequently, the study was expanded to analyze the mechanical behavior of additive manufactured 3D samples using systematic approaches with X-ray diffraction, scanning and transmission electron microscopy (SEM/TEM), electron backscattered diffraction (EBSD) and MTS mechanical testing frame.

This study revealed that laser speed has the most significant effect on the microhardness, while the powder feed rate has the most significant effect on the bead geometry. A detailed TEM study discovered various morphologies of martensitic phases that explained the reason behind the development of residual stress throughout the three zones, such as bead zone (BZ), dilution zone (DZ), and heat affected zone (HAZ) in a single bead clad. A high profile tensile residual stress (310–486 MPa) was observed in the upper BZ, while compressive stress (420–1000 MPa) was seen in the rest of the BZ and the DZ. This laser-cladded stainless steel

showed a ~16% increase in yield strength (YS ~ 521 MPa), ~ 63% increase in tensile strength (TS ~ 1774 MPa), and a ~ 22% increase in ductility in terms of percentage of area reduction when compared with a similar 420 commercial grade MSS (YS - 483 MPa, TS - 1087 MPa), in the rolling direction with pre-hardened condition.

The study showed that a post-cladding heat treatment at 565 °C for an hour reduced the tensile residual stress substantially in a single bead clad. A similar heat treatment also improved the fracture mode of 3D AM sample from brittle to ductile fracture and changed the anisotropic properties of the as-cladded sample in the transverse direction. This indicated that for design purposes, a simple post-cladding heat treatment (at 565 °C for an hour) is very important to minimize the anisotropy in the mechanical properties of as-cladded transverse sample. Also, it showed that a parts building technique with 30° angle to the base improved the ultimate tensile strength and partially eliminated the directionality issue. These findings could be important information for the designers with respect to "design for AM strategies." It is expected that the above findings will be useful for the laser-based additive manufacturing application of AISI 420 martensitic stainless steel in designing functional components. However, the ratio of the yield strength vs. tensile strength of as-cladded AM sample needs to be improved to use this AM alloy in potential automotive applications.

DEDICATION

I want to dedicate this thesis to the Almighty Allah, who has created me with an intelligent fashion and who has given me the ability and strength to carry out this research and writing of this dissertation.

"Indeed, my prayer, my service of sacrifice, my life, and my death are all for Allah alone, the Lord of the worlds."

ACKNOWLEDGEMENTS

Prophet Muhammad, peace and blessings be upon him, said, "He who does not thank people is not thankful to Allah." In this regard, I would like to take the opportunity to express my heartiest thanks and gratitude to both of my supervisors Dr. Ruth Jill Urbanic and Dr. Afsaneh Edrisy, for their time, intellectual guidance, and research direction in carrying out my Ph.D. research and this dissertation. I am honoured and privileged to have both of them who have given me a wonderful opportunity to expand my skills in both industrial and metallurgical engineering.

I would also like to thank to my advisory committee members Dr. Randy Bowers, Dr. Henry Hu, and Dr. Michael Wang, for their guidance and inputs. Special thanks to Dr. Adrian Gerlich, the external examiner of my dissertation from the University of Waterloo, for his valuable comments that enriched my thesis.

My sincere thanks go to Dr. Reza Riahi, Dr. Derek Northwood, Dr. Al Conle, and Dr. Jerry Sokolowski for their continuous inspiration in carrying out my research. Contributions of our industrial partner in using their materials, equipment's and facilities are highly appreciated with sincere thanks and acknowledgement.

I would like to acknowledge with sincere gratitude of receiving Ontario Graduate Scholarship (OGS) for three years and "Student Opportunity Grant (SOG)" from the Government of Ontario, entrance scholarship from the University of Windsor, and research funding from my supervisors through the Ontario Center of Excellence Collaborative Research program, Natural Sciences and Engineering

Research Council of Canada through the Discovery Grant, and MITACs, throughout my PhD studies.

I sincerely acknowledge prior works of Dr. Syed, complementary works of Dr. Navid, and Dr. Mehdi related to my research. Collaborative work with Dr. Mehdi in the EBSD analysis has enhanced my research and enriched this thesis. Special thanks go to my colleagues Mehdi, Hamed, Liza, Olufisayo, Ryan, Peter, Khaled, Angela, and Sharon, for their valuable help in my daily activities.

Finally, I would like to express my deepest gratitude to my family members including my beloved parents (late), my brothers, and my sisters for their true love and support throughout my life; as well as to my dear wife Kashfia Nehrin and my beloved son Ahmad Tashfeen, for their absolute love and understanding during the tough time of my life. It would have been impossible to complete this Ph.D. research and writing this dissertation without their unlimited support and encouragement. Moreover, I am indebted to my wife, who sacrificed her own Ph.D. offer from the University of Ryerson in 2014 for my Ph.D. study. My words will not be enough to express my gratitude towards her for this unprecedented favor.

Above all, my words cannot encompass my sincere gratitude towards the almighty Allah for His continuous mercy and blessings upon me to overcome any hardship and struggles that I faced during this journey of Ph.D. study as well as my lifelong journey on this earth. *"All thanks and gratitude are due for Allah, the creator and the sustainer of the worlds, who is the most merciful and the most beneficent."*

TABLE OF CONTENTS

LIST OF TABLES

LIST OF FIGURES

LIST OF APPENDICES

LIST OF NOMENCLATURE

AM	*Additive Manufacturing/Additive Manufactured*
DED	*Directed Energy Deposition*
PBF	*Powder Bed Fusion*
LC	*Laser Cladding*
2D	*2 Dimensional*
3D	*3 Dimensional*
ANOVA	*Analysis of Variance*
CCD	*Central Composite Design*
RSM	*Response Surface Methodology*
2FI	*2 Factor Interaction*
FR	*Powder Feed Rate*
LP	*Laser Power*
FL	*Focal Length of Lens*
LS	*Laser Speed*
CTD	*Contact Tip to Workpiece Distance*
HV	*Hardness (Vickers Microhardness)*
SS	*Sum of Squares*
MS	*Mean Squares*
DF	*Degree of Freedom*
SGT	*Shielding Gas Type*
LPS	*Laser Pulse Shape*

PFA	*Powder Feed Angle*
PFP	*Powder Feed Position*
FP	*Focal Position of a laser beam*
SD	*Spot Diameter*
SOD	*Stand-Off Distance*
W/H	*Bead Width to Height Ratio*
D/W	*Depth of Penetration to Bead Width Ratio*
AISI	*American iron and steel institute*
LC	*Laser-cladding*
CAD	*Computer aided design*
BZ (C)	*Center of bead zone*
DZ (C)	*Center of dilution zone*
DZ (I)	*Dilution zone with interface*
IZ	*Interface zone*
HAZ	*Heat affected zone*
MSS	*Martensitic stainless steel*
SS	*Stainless steel*
GOS	*Grain orientation spread*
IPF	*Inverse pole figure*
IQ	*Grain average image quality*
EBSD	*Electron backscatter diffraction*
RS	*Residual stress*
OIM	*Orientation imaging microscopy*

LOM	*Light optical microscopy*
OM	*Optical microscopy*
SEM	*Scanning electron microscopy*
TEM	*Transmission electron microscopy*
PAG	*Prior austenite grain*
PAGB	*Prior-austenitic grain boundary*
bcc	*Body centered cubic*
YS	*Yield strength*
UTS	*Ultimate tensile strength*
TE	*Total elongation*
CFD	*Computational fluid dynamics*
FEA	*Finite element analysis*

CHAPTER 1 Introduction

Background

The demand for developing innovative new manufacturing processes and their uses for industrial applications is continuous. Laser-based additive manufacturing (AM) is such a potential process that has been an industrial curiosity for the past 20 years. AM process can combine many sub-processes to produce a single part in one step with improved mechanical properties. For example, conventional manufacturing process welds 20 parts to produce a fuel nozzle (Fig.1.1), while AM produces this single piece (made of ceramics matrix composite) in one step that is 25% lighter, five times more durable, and reduces fuel burn by 15% [1]. Additive equipment can now use metallic powders such as stainless steel to "print" a range of functional components.

Figure 1. 1 3D printed fuel Nozzle tip for LEAP engine [1]

Stainless steels (SS) are widely used in the automotive, tool and die, aerospace, medical device, and pipeline industries because of their relatively low density, high strength, and excellent corrosion resistance. This group of steel can be ferritic, austenitic, martensitic, or combination of all phases depending on the chemical composition and major

alloying elements (e.g., Cr, Ni). Among all SS alloys, AISI 420 Martensitic stainless steel (MSS) has the highest hardness, and its properties can be improved by heat treatment [2]. It has a growing demand in the automotive, medical, and aerospace industries due to its moderate corrosion resistance, high hardness, and good tensile properties [2]. At a pre-hardened and tempered condition, the alloy has a tensile strength in the range of 700 - 930 MPa depending on the process parameters setting [3]. This SS can be processed by conventional manufacturing processes such as casting, metal forming, powder metallurgy, and welding [4].

MSS shows better mechanical properties when processed by using a novel additive manufacturing (AM) technique called laser cladding (LC) or direct energy deposition (DED) [5]–[9] due to the high cooling rates and extremely fine microstructure. The direct energy deposition (DED) process is one of the AM processes that utilizes laser power to melt the metallic powders (or wire) to coat part of the substrate or to fabricate a near-net shape in a layer by layer manner directly from a 3D CAD/CAM model [10]. This process is an extension of the laser cladding process, which is also used to modify or improve the surface properties of industrially used components. This process provides engineers the ability to tailor the mechanical properties of materials to suit a range of different applications [11]. This process is also known by many different names such as direct metal deposition (DMD) or laser powder deposition (LPD), laser engineered net shaping (LENS), direct laser deposition (DLD), and direct laser fabrication (DLF) [12], [13]. In this research, the term “laser cladding” will be used for the processing of AISI 420 MSS.

Additive Manufacturing

Additive manufacturing (AM) is a recently developed process of adding material to create a 3-dimensional (3D) physical part. Since the concept of AM is based on adding layers, it is also known as "layer-based technology." Initially, "Additive Manufacturing" was known as "Rapid Prototyping" or "Generative Manufacturing" when the concept entered into the market in 1987. However, AM has become a third window of the entire manufacturing technology along with the well-established "Subtractive Manufacturing," such as milling or turning, and the "Formative Manufacturing," such as casting or forging [14]. AM is very wide in terms of using metallic or non-metallic powder or wire feedstock, powder bed or powder flow, melting or sintering, and overall processing techniques. As per the American Society for Testing and Materials (ASTM) "ASTM F42 – Additive Manufacturing", there are seven categories of Additive Manufacturing processes, as shown in Fig. 1.2 [13].

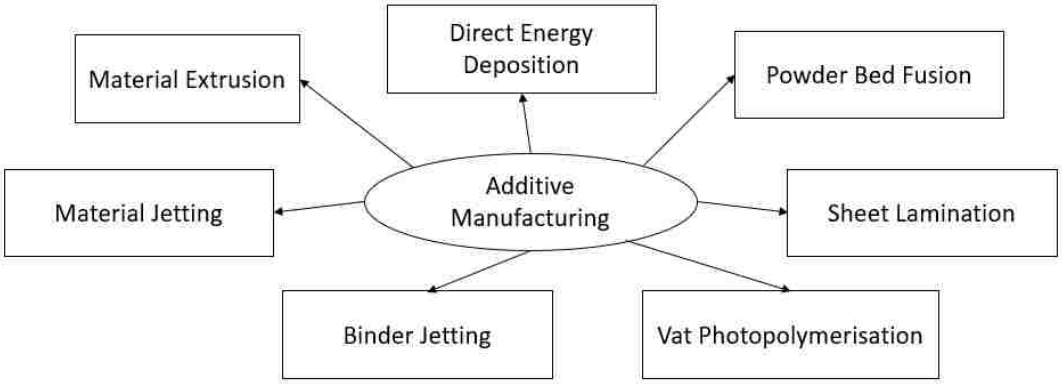

Figure 1. 2 ASTM Categories for Additive Manufacturing (AM) techniques

1.2.1 The Principle of Layer-Based AM Technology

The principle of layer-based technology is to create a 3-dimensional physical object called “part” from many layers of equal thickness. It is characterized by a process chain illustrated in Fig. 1.3 [14]. The process starts with a 3D CAD design. Then the 3D data set is first sliced into layers, using special software in a computer system. Consequently, a set of contoured virtual slices with an even thickness is obtained. The data set that consists of the contour data (x-y), the layer thickness (dz), and the layer number (or z-coordinate) of each layer is submitted to a machine that executes two elementary process steps per layer in order to create the part [14].

The creation of the physical layer can be done using a range of materials, such as plastics, metals, or ceramics, supplied as powders, fluids, solids, foils, or sheets. Different physical effects are used, such as photo-polymerization, selective fusing, melting, or sintering, cutting, particle bonding, or extrusion [14]. The contouring of each layer requires an energy source (e.g., laser, electron beam) that generates the chosen physical effect and a handling device that controls the x-y coordinates [14].

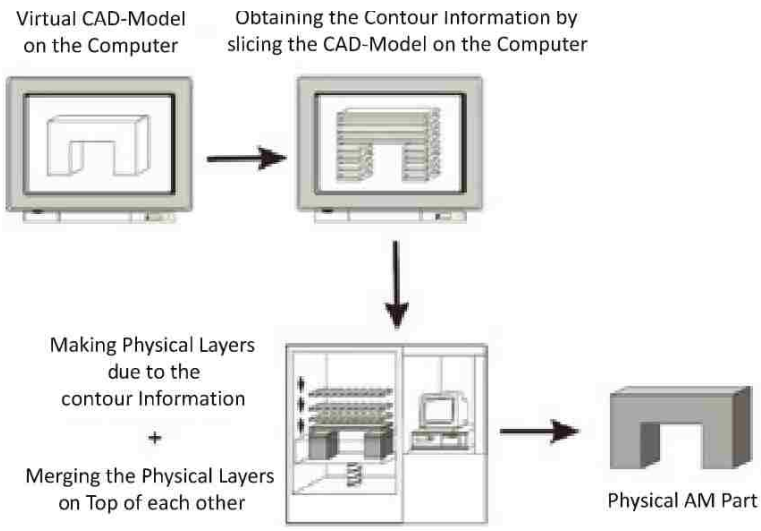

Figure 1. 3 Additive manufacturing (AM) process chain [14]

1.2.2 Laser-based AM Processes for Metallic Components

As per the ASTM standard, the AM processes for metallic components fall into two main categories, such as Powder Bed Fusion (PBF) and Directed Energy Deposition (DED). The primary heat sources for these AM processes are a laser (L), electron beam (EB), plasma arc (PA), and gas metal arc (GMA). Fig. 1.4 illustrates those two main AM processes based on the laser heat sources. These processes have been developed based on the AM principle mentioned earlier to fabricate complex net-shaped functional metallic components that are difficult to produce by the conventional casting methods. As required by the automotive, biomedical, and aerospace industries, those functional components can be made from any metallic alloy powder (as shown in Table 1.1) using these AM processes [13]. A comparison of the DED and PBF based AM process is shown in Table 1.2. The right AM process can be selected based on the desired product quality, materials, sizes, and complexity as well as cost of the AM equipment.

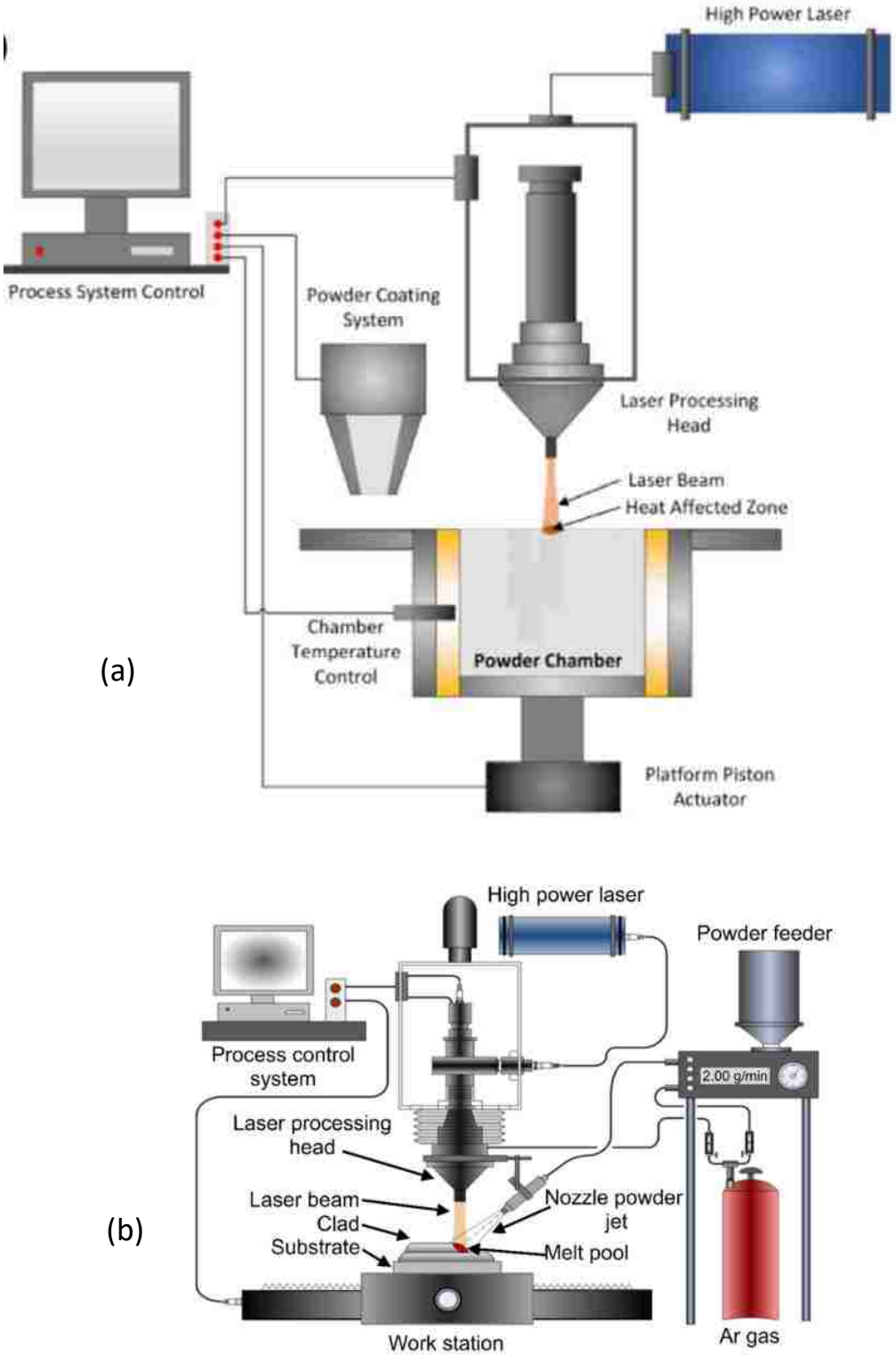

Figure 1. 4 Schematic diagram of (a) PBF (b) (d) DED [15]

Table 1. 1 Usages of alloy powder with AM applications [16]

	Alloys				
Applications	Aluminum	Stainless steel	Titanium	Cobalt chrome	Nickel superalloys
Aerospace	x	x	x	x	x
Medical		x	x	x	
Energy, oil, and gas		x			
Automotive	x	x	x		
Marine		x	x	x	x
Corrosion resistance		x	x	x	x
High temperature		x	x	x	x
Tools and molds		x			

Table 1. 2 Comparison between the DED and PBF [16]

Process	**DED**			**PBF**
Feedstock	**Powder**	**Wire**	**Plasma/arc**	**Powder**
Heat source	**Laser**	**E-beam**	**electric arc**	**Laser/EB**
Power (w)	100-3000	500-2000	1000-3000	50-1000
Speed (mm/s)	5-20	1-10	5-15	10-1000
Feed rate (g/s)	0.1-1.0	0.1-2.0	0.2-2.8	-
Build size (cm)	20x15x7.5	20x15x7.5	50x30x10	50x28x32
Production time	high	medium	low	high
Dimensional accuracy (mm)	0.5-1.0	1-1.5	0.5-1.2	0.5-1.3
surface roughness (μm)	4-10	8-15	very rough	7-20
Post-processing	machining is seldom required	machining is required	machining is essential	machining is seldom required

Apart from the above classification, based on the metallurgical bonding and solidification mechanisms, those AM process are further classified as complete melting and partial melting process, which are then sub-divided into laser sintering (LS), laser melting (LM) and laser cladding (LC) process as shown in Fig. 1.5. Laser Sintering is a process of

forming a solid object from powder materials by using laser heat and atomic diffusion mechanism without melting it to the point of liquefaction. In the sintering process, the materials never reach to a liquid phase as compared to melting, where a phase transition from a solid state to a liquid state occurs. Both the laser sintering and melting process are based on the powder bed system before laser scanning, whereas the laser cladding is based on the coaxial blown powder feeding system with synchronous laser scanning [13]. Laser cladding is the generic name of laser metal deposition (LMD) or direct energy deposition (DED). The Laser cladding (LC) process will be reviewed in section 1.7.

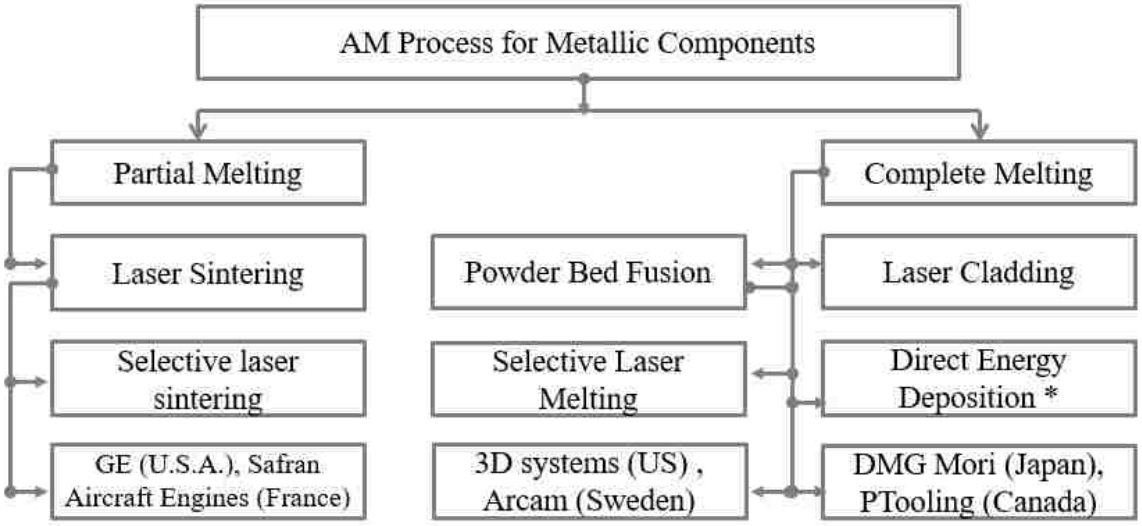

* It is also known as Laser engineered net shaping (LENS), Direct metal deposition, Direct laser deposition and Direct laser fabrication

Figure 1. 5 Laser based AM process for metallic components (based on the metallurgical bonding and solidification mechanisms), modified after [13]

Research Motivation and Problem Statements

The laser cladding AM technology is a solution for cladding/coating or building layer-based 3-dimensional physical objects directly from 3D-CAD/CAM program. One of the important features of the AM process is that it starts from point(s), continues to line(s), and layer(s), and then ends with the completed 3D part [17]. However, being a novel process, there is a lack of detailed research on the proper characterization of laser-cladded coating or component fabrication.

Based on the ongoing demand for the laser-based additive manufacturing solutions, collaborative research was established between the University of Windsor and Whitfield Welding Inc using AISI 420 martensitic stainless-steel powder with the laser cladding process for experimental studies. Initial laser cladding experiments for single bead deposition scenarios was designed by other researchers [18], [19] using the Central Composite Design (CCD) matrix, and Response Surface Methods (RSM). CCD is one kind of response surface design or methodology (RSM), which is an advanced Design of Experiment (DOE) technique that helps to understand non-linear behaviors and optimize experiment's responses. Their research was limited to mainly process development and collecting bead geometry data for various process configurations as well as designing predictive models and analyzed them using artificial neural networks and analysis of variance (ANOVA).

The AM industry also encounters challenges in handling residual stresses developed during the laser cladding process. Moreover, anisotropic properties developed in the laser-cladded AM parts is a challenge for load bearing applications. It is important

to know how the process parameters affect the metallurgical characteristics of the bead geometry. A detailed analysis of the microstructure and mechanical properties would help to understand the functional behavior of the laser cladded parts. However, no metallurgical analysis or materials characterization has been done to address those issues. Those gaps are addressed in this research using a systematic approach.

Research Objectives, Hypothesis, and Approaches

Considering the above stated problems, this research aims to achieve the following objectives:

1. To investigate the effect of process parameters on the bead geometry and microhardness variations in a single bead laser-cladded AISI 420 MSS as well as to develop a predictive model of bead geometry and microhardness at various process parameters.

2. To examine the microhardness and residual stress profile in a single bead laser-cladded AISI 420 MSS and provide a solution to minimize their effect.

3. To analyze the microstructural evolution and martensitic phase transformation in a single bead cladding of AISI 420 MSS in order to correlate them with the residual stress developed in the cladded parts.

4. To investigate the mechanical behavior of laser-cladded and additive manufactured (AM) sample of AISI 420 MSS at different orientation and compare them against the pre-hardened commercial grade of AISI 420 martensitic stainless steel.

The following hypotheses and approaches were adopted to achieve the above-mentioned objectives:

1. It was hypothesized that three main process parameters such as laser power, scanning speed, and powder feed rate had a statistically significant effect on the bead geometry and microhardness. Multiple regression was done using statistical software “Minitab” and “Design Expert” to develop a predictive model and to analyze the effect of process parameters on the microhardness and bead geometry.

2. It was hypothesized that the residual stress developed due to unknown microstructural evolutions during the laser cladding process creates distortion in the crystal lattice structure. To address the residual stress issue, the X-Ray diffraction method was used in collaboration with Proto Manufacturing using their XRD desktop machine. The residual stresses developed in a single bead were analyzed, and a suitable heat-treatment process with a short holding period were proposed to minimize the residual stress.

3. It was hypothesized that metastable phases evolved during the rapid non-equilibrium solidification for the laser-cladded AIS 420 MSS. To address this issue, microstructural behavior was analyzed using the light optical microscopy (LOM), Scanning Electron Microscopy (SEM), Transmission Electron Microscopy (TEM), and Electron Backscatter Diffraction (EBSD) techniques. Thus, the associated metallurgical phases and their effect on the microhardness, residual stress, and mechanical properties were correlated.

4. It was hypothesized that the building direction of laser cladding created anisotropic mechanical properties in the laser-cladded AM samples. To address the

mechanical properties, a miniature type specimen was developed for tensile testing to evaluate the yield strength, ultimate tensile strength, and ductility in terms of percentage of area reduction. An MTS mechanical testing frame was used to evaluate those properties in the as-cladded and heat-treated conditions of AISI 420 MSS.

Limitations and Scope of this Research

This research work is an extended part and continuation of earlier works, as mentioned in section 1.3. The laser cladding was conducted at the facility of the industrial partner using a robotic arm equipped with a nozzle assembly, which provides the laser spot size of 4.3 mm only. The AISI 420 MSS powder was chosen as cladding materials for all single bead and layer-based multiple beads experiments. One of the reasons to choose this stainless-steel powder was due to its extensive use by the industrial partner for the surface treatment for die and molds, and repair of pipeline surfaces. Moreover, this alloy was readily available with the industrial partner as well as being less expensive compared to the other types of stainless steel and carbide powders.

The scope of this research is mainly focused on the characterization of microstructural and mechanical properties of single bead samples and additive manufactured (AM) samples. It is to be noted that heat transfer and temperature monitoring or controlling during the cladding process are important but not considered in this research. Similarly, the effect of external factors such as ambient temperature, powder shielding gas, and varying laser spot size are also beyond the scope of this work. This research used some of the simulation data regarding temperature distribution, microhardness, and residual stress distribution in a single bead, which were made based on experimental results

produced in this research. The research methodology is displayed in Fig. 1.6. This flowchart illustrates different steps that were followed to achieve the research objectives.

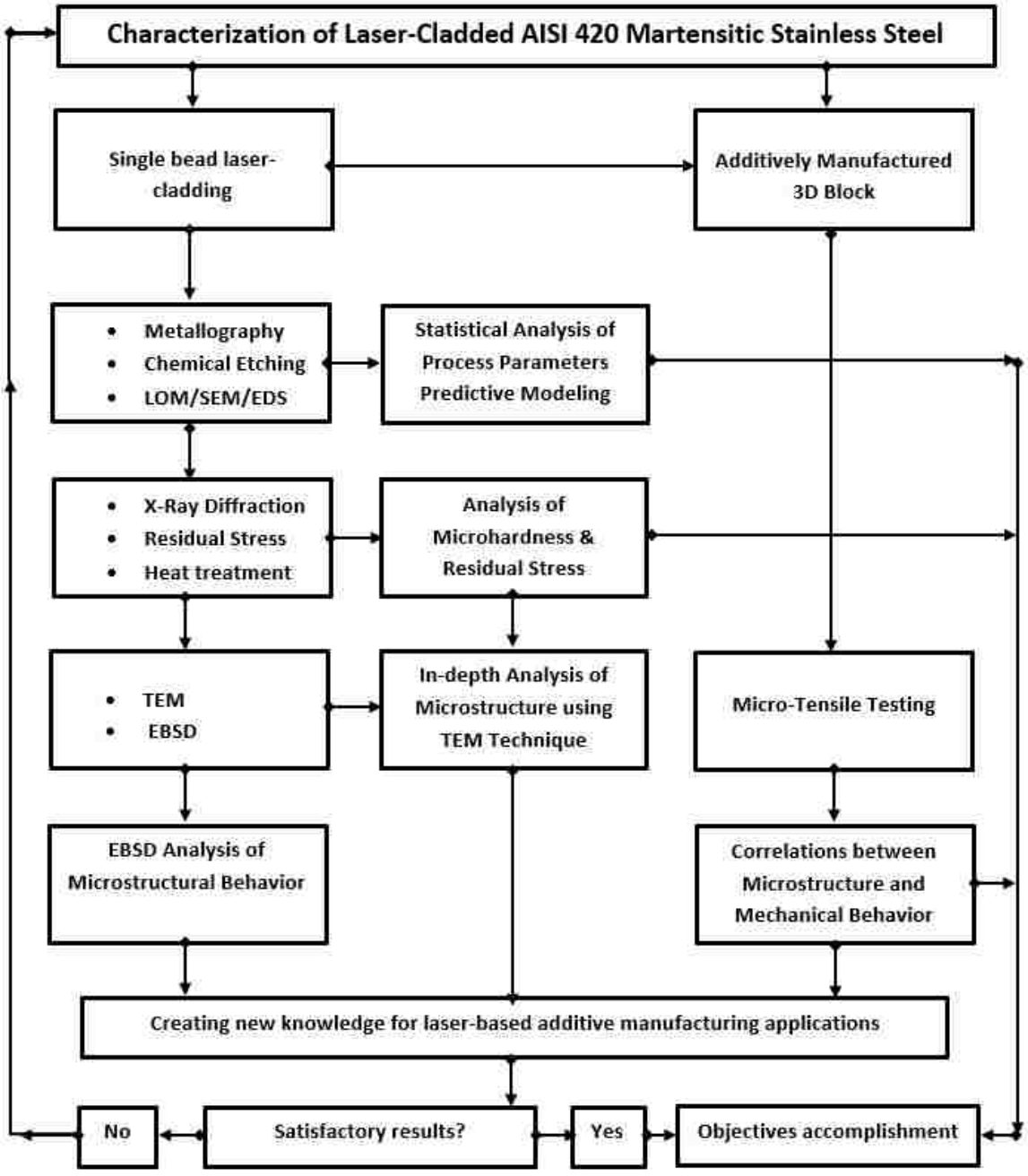

Figure 1. 6 The research methodology flowchart illustrating different steps that were followed to achieve the research objectives. [3D – three dimensional, LOM – light optical microscopy, SEM – Scanning electron microscopy, TEM – Transmission electron microscopy, EBSD – Electron Back-Scattered Diffraction, EDS – Energy Dispersive Spectroscopy]

Dissertation Organization and Chapter Outline

The thesis consists of seven chapters, and the organization of the thesis is presented in Figure 1.7. Chapter one presents a summary on additive manufacturing processes, research motivation and problem statements, research objectives, hypotheses, and approaches, as well as the limitations and scope of this research in sections 1.1 - 1.5. Section 1.6 of this chapter describes the organization of this dissertation. Section 1.7 provides a brief literature review on the laser cladding process, stainless steels, and the characterization of laser-cladded materials.

Chapter two evaluates statistical significance of the process parameters used for the entire design of experiments (DOE) of the single bead laser cladding. The study was published in the International Journal of Advanced Manufacturing Technology (IJAMT) [9]. It describes the experimental set-up and the processing parameters of laser cladding of AISI 420 martensitic stainless steel on an AISI 1018 substrate. This chapter explores the effect of those process parameters on the bead geometry and microhardness profile for single-track laser-cladded specimens. In this chapter, robust predictive models for hardness and bead geometry such as bead aspect ratio, and wetting angle with the substrate were determined using multiple regression analysis for steady state regions in the bead center.

Chapter three focuses on the hardness and residual stress profile in the selected samples of single bead laser cladding of AISI 420 martensitic stainless steel produced with different process parameters (e.g., laser power, laser speed, and powder feed rate). The study was published in the Journal of Materials Engineering and Performance (JMEP) [7]. X-ray diffraction technique was used to calculate the residual stress and microstructural

phases in the single bead clads. The microstructures, residual stresses, and microhardness profiles were correlated in this chapter for a better understanding of the laser-cladding process.

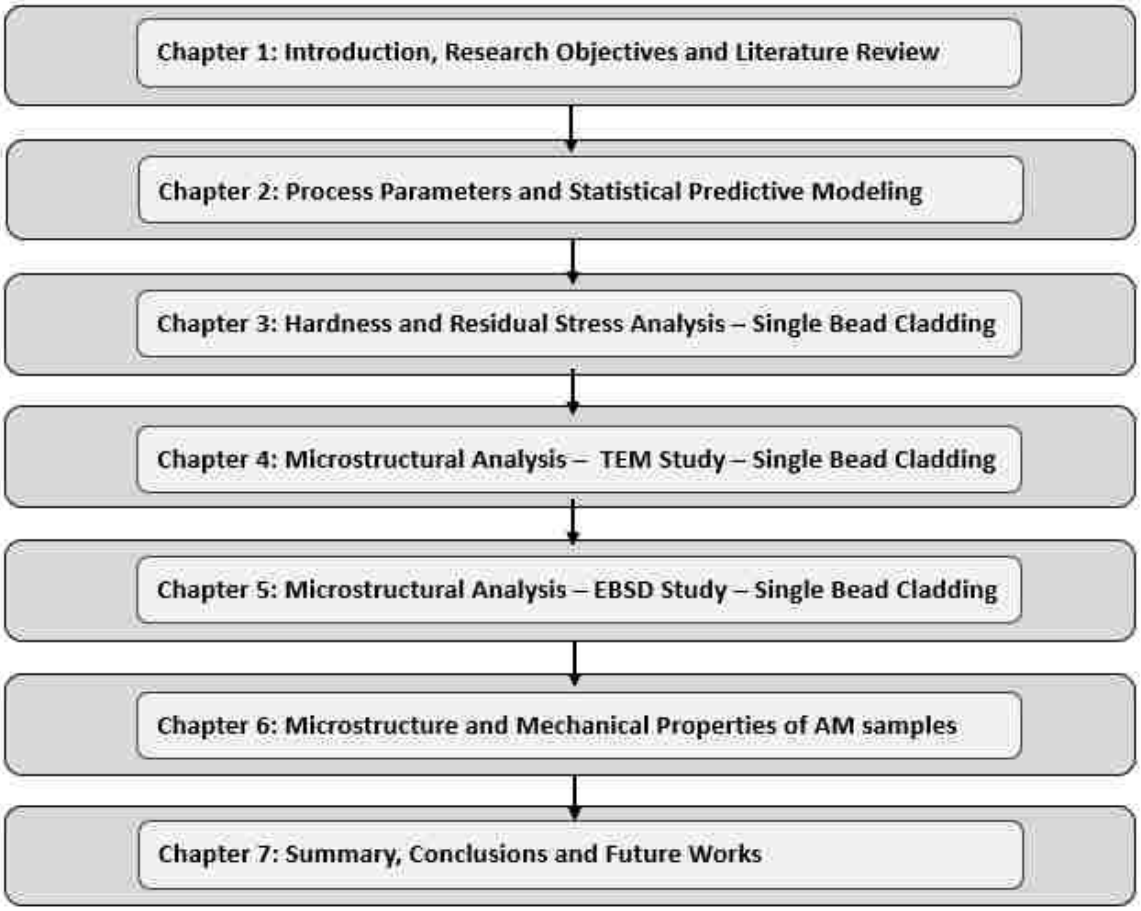

Figure 1. 7 Thesis organization

Chapter four provides detailed microstructural analysis and phase transformation for the laser-cladded AISI 420 martensitic stainless steel. The study was published in the Metallurgical and Materials Transaction A (MMTA) [6]. The analytical microstructural analysis of the laser-cladded sample was examined using Optical Microscopy (OM), Scanning Electron Microscopy (SEM), and Transmission Electron Microscopy (TEM) equipped with Energy-Dispersive Spectroscopy (EDS). Three regions (the bead zone,

dilution zone, and an interface zone) were investigated. The TEM study revealed various morphologies of martensitic phase in each region. The martensitic transformation with various morphologies provided crucial information about the development of residual stress throughout the three zones.

Chapter five describes the microstructural characterization of the laser-cladded AISI 420 martensitic stainless steel using the Electron Backscatter Diffraction (EBSD) technique. The study was submitted to the Journal of Materials Characterization and accepted for review [20]. This chapter analyses the substructure of martensite in the selected zones, such as the bead zone (BZ), the dilution zone (DZ), and the interface with the heat affected zone (HAZ)] of the bead. The EBSD Inverse Pole Figure (IPF), as well as the Grain Orientation Spread (GOS) and grain average Image Quality (IQ) techniques, were used to quantify the grain misorientation and residual strain/stress in those selected zones. The IQ value was compared and correlated with the experimental values of residual stresses (RS) measured by XRD methods to understand residual strain distribution in those zones.

Chapter six explores the mechanical behavior of laser-cladded and additive manufactured AISI 420 martensitic stainless steel deposited in different directions and orientations. The study is submitted to the journal of Materials Science and Engineering A (MSEA). This chapter studies the mechanical properties and relates them to different microstructural features in both longitudinal and transverse directions. It was shown that a post-cladding heat treatment at 565 °C for an hour improves the anisotropic properties of the laser-cladded 420 stainless steel substantially. This chapter further explores the parts building technique at angular powder deposition (with 30° angle to the base) that improved

the ultimate tensile strength and partially eliminated the directionality issue. The study also compared the mechanical properties of as-cladded AM samples with the commercial grade AISI 420 MSS for comparison.

Chapter seven provides a summary of the research findings and conclusions. Some recommendations for future study are also proposed at the end of the chapter.

Literature Survey

This literature survey introduces the process and materials used in this research. This section provides a brief summary of laser cladding process, stainless steel, and some highlights from the literature review in the characterization of the laser-cladded materials.

1.7.1 Laser Cladding

Laser Cladding (LC) is a method of depositing material by which a powdered or wire feedstock material is melted and consolidated by use of a laser to coat part of a substrate or fabricate a near-net shape part [21], [22]. LC involves the melting of an additive material and the melting of a thin layer of the substrate [23]. The dilution between the additive material and the substrate allows forming a strong metallurgical bonding. For a good quality clad bead, the percentage dilution should be maintained between 2%- 5%. However, earlier studies done by Aggarwal [18] and Syed [19] revealed that dilution varied between 3%-46% based on the process parameter settings. Mechanical properties of a cladding diffusion layers are dictated mainly by bead geometry, heat affected zone (HAZ) area, strengthening mechanisms, and heat input during laser cladding [24],[25]. Cladded

parts, as well as the base metal in the vicinity of deposited cladded layer, undergoes a considerable change metallurgically and mechanically due to thermal cycle during solidification [11]. Specifically, plastic deformation and microstructural changes between the cladding dilution, HAZ, and their surrounding areas can result from non-uniform thermal expansion and contraction due to highly localized transient heat and nonlinear temperature fields in the heating and cooling processes.

1.7.1.1 How does it work as a 3D AM solution?

Laser Cladding is fundamentally a type of coating technology that utilizes a focused or a defocused high-power laser beam to melt the thin surface layer of a substrate and the added materials locally while forming a new layer of material simultaneously with desired properties after solidification [26]. Exposure to large areas is possible through layer by layer coating or overlapping individual tracks. The melting of the substrate is controlled through a complete metallurgical bond at the interface, keeping a minimum dilution from the substrate is minimal and allowing the newly formed layer to retain the original composition and properties of the cladded materials.

The most common method of laser cladding is one-step process. In the 1-step process, the coating material is in the form of powder or wire. Out of these two forms, powder is most extensively used due to higher efficiency and availability of a wider range of different cladding materials in powder. During 1-step laser cladding, the coating material is continuously fed into a melt pool created by the laser. The coating material is melted or preheated, and a thin part of the base material is melted. As the laser focus moves along

the base material, the melt pool will also move, leaving a solidified weld bead consisting of the coating material [38].

There are two types of powder blown laser cladding techniques, off-axis, and coaxial powder feeding. In the off-axis powder feeding, the laser source and the feeder are separated, and the powder is blown into the melt pool from a different angle compared to the laser. Good catchment efficiency can be accomplished with off-axis powder feeding when using a larger angle between the feeding nozzle and the laser beam. This will expose the powder to a larger cross-section area of the melt pool, and the powder will hit the melt pool uphill. However, coaxial powder feeding system is most popular where blown powder and laser beam coincide in the same focal point. In order to protect the powder stream and the cladding from the surrounding atmosphere, inert shielding gas can be blown in together with the powder stream. Coaxial powder feeding is shown schematically in Fig. 1.8.

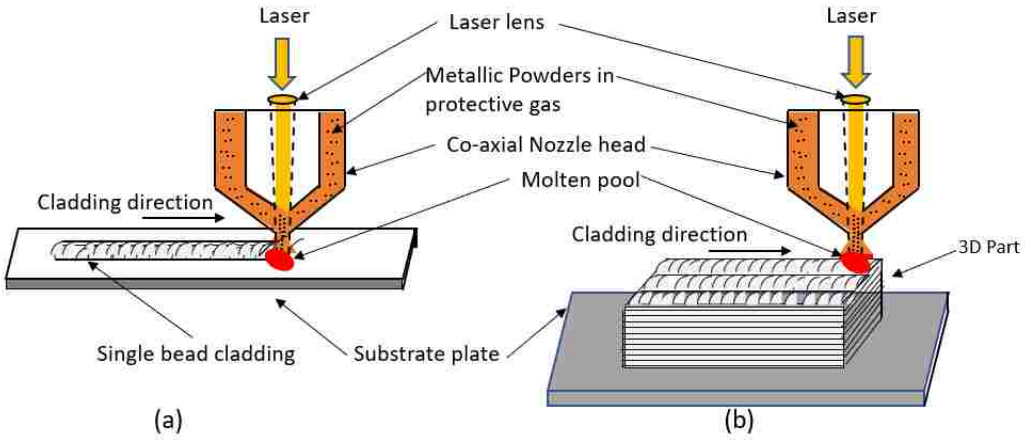

Figure 1. 8 Schematic diagram of laser cladding process (coaxial powder feeding)

1.7.1.2 Advantages and Applications of Laser Cladding

Laser cladding offers a unique prospect for non-equilibrium production of materials which possess novel microstructures due to the intrinsic rapid solidification and high concentration of key elements on the surface [27]. It can generate a very high cooling rate up to 10^6 K/s due to its controlled heat input, small and thin layer melt pool, and heat conduction to the bulk substrate [21]. The microstructure of the deposited layer is typically very fine, resulting in superior metallurgical properties. Coatings having such microstructures (metastable phases or extended solid solutions) generally cannot be developed by conventional casting methods. Excellent properties can be attained, such as improved wear resistance, corrosion resistance, fatigue, and high temperature resistance, by optimizing the cladding parameters and selecting suitable powder materials. It is generally observed that grain refinement, martensitic transformation, extended solid solution, and particulate reinforcement are the main reasons for those excellent properties [26].

Though today's most significant application for laser cladding is for repair, applications, and improvement of surface properties of high value components such as molds, tools, or turbine and engine parts [28], laser cladding has a high potential to be used for revolutionary industrial applications of AM in the medicine, dentistry, aviation, automotive industries, and consumer products. In the field of wear and corrosion protection, laser cladding also has potential applications for unique components such as oil drilling machine parts, engine parts of big diesel engines, and steel pipelines.

1.7.1.3 Laser Cladding Process Parameters and Materials' Selection

Since laser cladding is a melting process, the resulting microstructure is always a cast structure compared to conventional casting. The formation of different phase morphologies and their composition depends on some parameters. Those parameters can be divided into process and material parameters. Process parameters include actual process parameters, which are variable, fixed laser parameters dictated by the choice of laser and optics, and parameters related to the feeding of coating material. Among the process parameters, the laser power (LP), laser scanning speed (LS), and powder feed rate (FR) are the three principal parameters since they have the largest effect on the process results [29],[30]. However, the mechanical and metallurgical properties of laser cladded parts also depend on the chemical composition, microstructural evolutions, and phase transformation occurs during fast solidification. The microstructural evolutions are dependent on the laser cladding process parameters, which are chosen based on cladding materials and base materials, and available laser characteristics [29].

Many process parameters and process variables introduce complexity in the mechanical and metallurgical characteristics of materials. Laser cladding is such a process for additive manufacturing that combines strengthening mechanisms to improve wear resistance, corrosion resistance, fatigue, and high temperature resistance, by optimizing the cladding parameters and selecting suitable powder materials. Different grades of stainless steel, tool steel, titanium-based alloy, nickel-based alloy, tungsten carbide, and cobalt based alloys are prominent choice for metallic AM processes. However, this research concentrates on the iron based AISI 420 Martensitic stainless steel.

1.7.2 Stainless Steels

Stainless steels are important engineering materials with increased demand in various industrial applications because of their combination of good corrosion resistance and mechanical properties. This special type of steel is basically a high alloy steel containing a minimum of 10.5 wt% chromium in order to be stainless or have corrosion resistance. This level of chromium allows the formation of a passive chromium oxide that prevent corrosion of the underlying surface of the metal at ambient non-corrosive conditions[31]. Based on the application of this alloy, the percentage of chromium can be varied up to 30 wt% Cr to get high resistance to oxidation at high temperature such as 1000 °C [31]. Because of the corrosion and high temperature oxidation resistance, the use of stainless steels is intensely demonstrated by the numerous applications from the kitchen utensils, home furniture, and building construction to the very sophisticated dental instruments, parts for space vehicles, boilers in chemical industries, power generation and cooling channels in nuclear reactor [32].

There are five standard classes of stainless steels based on their chemical composition, percentage of chromium, and ability to resist of corrosion. They are listed below:

- Martensitic Stainless Steel (MSS)
- Ferritic Stainless Steel (FSS)
- Austenitic Stainless Steel (ASS)
- Duplex (austenite and ferrite) Stainless Steel (DSS)
- Precipitation Hardenable Stainless Steel (PHSS)

1.7.2.1 Martensitic Stainless Steel (MSS)

Martensitic stainless steels are the base stainless steel and the most marginally corrosion resistant of all. These stainless steels are based on the Fr-Cr-C ternary system, and they undergo an allotropic transformation from austenite to martensite under most thermomechanical processing conditions. It contains relatively low chromium (12-14 wt%) and a high carbon content compared to other stainless steels, and hence they are generally selected for applications where a combination of high strength and low corrosion resistance are required under ambient conditions [31].

1.7.2.2 Ferritic Stainless Steel (FSS)

The ferritic stainless steels are mainly iron and chromium (Fe-Cr) based alloys containing about 12 to 30 wt% Cr with a body centered cubic (bcc) structure as pure iron. The predominant metallurgical phase present in this alloy is ferrite. Compared to austenitic stainless steels, they have poor weldability, susceptibility to embrittlement at 475°C, and notch sensitivity [31]. The FSS resist corrosion in normal and non-aggressive atmospheres, and they are generally used in industrial applications where the conventional carbon steels would rust. However, their applications mainly depend on the percentage of alloying elements and the service condition, hence they can be used in automotive exhaust systems, chemical plants, pulp, and paper mills [32].

1.7.2.3 Austenitic Stainless Steel (ASS)

The austenitic stainless steels usually contain nickel in addition to iron and chromium, which stabilizes the face-centered cubic (fcc) austenite structure at room temperature. They are mostly non-magnetic [31]. The nickel can be replaced to some extent

by other austenite stabilizing elements such as manganese. The austenitic stainless steels have higher corrosion resistance compared to the ferritic and the martensitic stainless steels, and highly alloyed austenitic steels can resist corrosion in aggressive and reducing atmospheres and are thus commonly used in the chemical industry. Other common applications are kitchen appliances, e.g., kitchen sinks, and in these applications, the austenitic steels are desired because of their combination of good formability and corrosion resistance[32].

1.7.2.4 Duplex Stainless Steel (DSS)

The duplex stainless steels consist of both austenite and ferrite, with approximately 50wt% of each phase. They combine some of the favorable properties of the two phases to produce a steel with superior yield strength and stress corrosion cracking resistance compared to pure austenitic grades. These properties make the duplex stainless steels attractive for load-bearing applications in corrosive atmospheres, e.g., in the off-shore industry [31].

1.7.2.5 Precipitation Hardenable Stainless Steel (PHSS)

The precipitation hardenable (PH) grades stainless steels are formed by precipitation hardening during an aging heat treatment. They are further sub-grouped according to the phase or matrix in which the precipitates are formed, such as austenitic, semi-austenitic, or martensitic [31]. The strength of the martensitic structure can be increased by precipitation hardening to obtain ultra-high strength steel. The precipitation hardened alloys are mostly used in specialized high technology industries due to the high price involved with this alloy.

1.7.2.6 Why AISI 420 Martensitic Stainless Steel?

AISI 420 is widely used in the oil and gas industry because of its toughness and strength. Mechanical properties of this martensitic stainless steel can be tailored by heat treatment. It provides excellent wear resistance and high surface hardness as a laser-cladded coating for die and tool repair. By using this stainless steel, drive shafts and drive couplers can also be repaired. The repair saved 50% of the cost of the new component and improved the wear life [5]. This MSS is also one of the potential alloys for additive manufacturing application. It is reported that up to 35% or greater weight reduction is possible with this MSS relative to the baseline designs with enhanced fuel economy and maintenance cost [34]. This MSS has a high potential to be used as advanced high strength stainless steel for structural components and assemblies in automotive applications that require high strength, toughness, and corrosion resistance. For example, automotive sub frames, door beams, B-pillars, seat rails, tow hooks, and fuel rail assemblies [34].

1.7.3 Characterization of the Laser-Cladded Materials

This review will explore the recent research on the characterization of laser cladded materials. Many researchers [18], [21], [26], [29], [30], [35]–[58] worked on the characterization of laser cladded materials. However, only the iron-based alloys are discussed here. It is anticipated that some of the literature are repeated in the chapters 2-6 because of the nature of this manuscript-based dissertation (as published earlier).

1.7.3.1 Microstructural Characteristics in AM Alloys

Microstructure has a tremendous effect on mechanical properties of any metallic materials. The microstructure is a direct result of materials' inherent chemistry, manufacturing process, associated process parameters, and post-processing heat treatment [71]. Traditionally, stainless steels have been developed in conjunction with a specific manufacturing process, such as casting, powder metallurgy, forging, welding, or forming. Laser-based AM is relatively a new process that offers distinct advantages, as mentioned earlier, for rapid design and implementation [71]. This AM technology is currently being considered by many industries, such as GE, for their aerospace application. Many existing aerospace alloys are capable of being processed through various AM technologies as a functional component, as noted earlier. It is expected that the current research in laser cladding (LC) will lead to the development of unique microstructures that will have a significant influence on the chosen martensitic stainless steel's mechanical properties.

In both laser-based powder bed fusion (PBF) and direct energy deposition (DED) or LC processes, the AM parts gone through various thermal cycles, such as: (i) rapid heating due to the absorption of laser energy, (ii) fast solidification of the melted region in the absence of heat source, (iii) substantial temperature gradients, (iv) accumulated heat and (v) re-heating/re-cooling due to the laser energy in the adjacent layers/tracks. The frequent re-melting and re-solidifying progressions are continued when the subsequent layers are exposed to heat [15]. The influence of the thermal cycles associated with many process variables create heterogeneity in the microstructural evolutions. However, the microstructural characteristics of AM parts is still poorly understood.

Generally, the microstructure in AM is developed based on the above-mentioned thermal history and three main grain morphologies are observed in the stainless steel processed by AM methods, such as (i) columnar, (ii) equiaxed, and (iii) combination of both columnar and equiaxed grains [15]. These three types of grains are commonly observed in three different regions, namely, (i) interface zone, (ii) bead zone, and (iii) dilution or inter-diffusion zone. The prediction of microstructure is governed by solidification parameters such as temperature gradient G and grain growth rate R, as well as their combined forms of GR and G/R. The ratio G/R determines the mode of solidification while the product GR governs the scale of the solidification microstructure [72]. The effect of G/R and GR on the solidification microstructure are illustrated in Fig. 4.11 (chapter 4). The solidification microstructures can also be planar, cellular, columnar dendritic, or equiaxed dendritic with decreasing G/R values. The dimensions of all the four solidification microstructures decrease with increasing cooling rate GR. In a relatively high G/R value, the predominant solidification microstructure would be columnar dendrites, and smaller G/R value gives rise to equiaxed grains. In the powder bed method, the heat is mostly transmitted through the previously deposited layers and develops the highest temperature gradient in that direction, which ultimately influences the formation of directional columnar dendrites [15].

The solidification, phase transformation, and microstructural development in AM processed steels are completely different compared to the conventional cast steels [15]. During the layer-based AM process, the bottom layer is heated for a long time, which may cause special thermal effects, and the accumulated heat may lead to tempering or spheroidizing annealing at a slow cooling rate. Conversely, the top upper layers solidify

very quickly and have no time to grow coarsely due to rapid cooling rate [15]. Besides, complex microstructures can be developed due to continuous re-melting process that promotes heat flow in directions in the same melt pool, which eventually creates different grain growth orientations [73]. It was suggested that the higher heat dissipation occurred through the build direction compared to the other directions, and solidification in that direction leads to anisotropy in the grain morphology as well as in the mechanical properties [15]. Also, in both laser-based AM process, cooling rates tend to be high because of the smaller laser spot size. This led to smaller heat affected zones and finer microstructures compared to conventionally cast samples [73]. Song et al. [74] reported to have better mechanical property in AM processed iron-based samples due to the presence of smaller grains and higher dislocation density, associated with rapid solidification. Sun et al. [75] observed primary austenite (fcc γ) and small amount of retained ferrite (bcc δ) without any martensite in AM processed austenitic SS 316 L. The high temperature ferrite phase was not transformed to a low-temperature austenite phase during the fast cooling stage involved in AM processed SS 316 L [15].

Krakhmalev et al. [76] studied the in situ heat treatment in selective laser melted AISI 420 martensitic stainless steels. They observed differences in microstructure and hardness in the upper layers in comparison to the rest of the sample. Top upper layers showed a hardness of 750HV with 21±12 vol.% austenite phase compared to the bulk of the sample. The bulk consisted of thermally decomposed martensite and high amounts of austenite (57±8 vol.%) with a hardness in the range of 500–550HV. Their results indicated that the occurrence of thermal cycling during the additive manufacturing process resulted in partitioning and austenite reversion in the inner regions of the sample [76].

Chen et al. [21] investigated the laser consolidated AISI 420 stainless steel (SS420) and found that directionally solidified fine dendritic microstructure with duplex austenite (A) and martensite (M) phases along with considerable amount of retained austenite. They also observed large amount of dispersed carbides (M_7C_3, $M_{23}C_6$), which might cause the depression of martensite transformation temperature M_s.

Gururaj et al. [53] studied the effect of laser cladding of AISI H13 tool steel powders on a hardened and tempered AISI H13 tool steel substrate and post-cladding tempering (550 C) for 2 hours on the microstructure and mechanical properties (hardness, tensile strength, and wear resistance) of the clad zone. They found martensite laths (undissolved or precipitated), fine alloy carbides, and retained austenite in the clad zone, as shown in Fig. 1.10. They observed an improvement in microhardness value up to 600 to 650 VHN in the as-clad surface compared to 480 VHN measured on hardened and tempered AISI H13 tool steel substrate.

Sun et al. [45] found a fine martensitic phase appeared within the fine austenite dendrites due to rapid cooling rates in the laser deposited AISI 4340 clad layer on the same steel substrate. The HAZ contained coarse austenite and an acicular martensitic/bainitic structure. They found that the hardness of the clad was 30-40% higher than the base material. The high hardness in the clad was associated with martensite formation during rapid cooling of the melt pool. It was revealed to them that after Post Heat Treatment (PHT), both the clad and HAZ hardness decreased by 40% to 400Hv (Fig. 1.11).

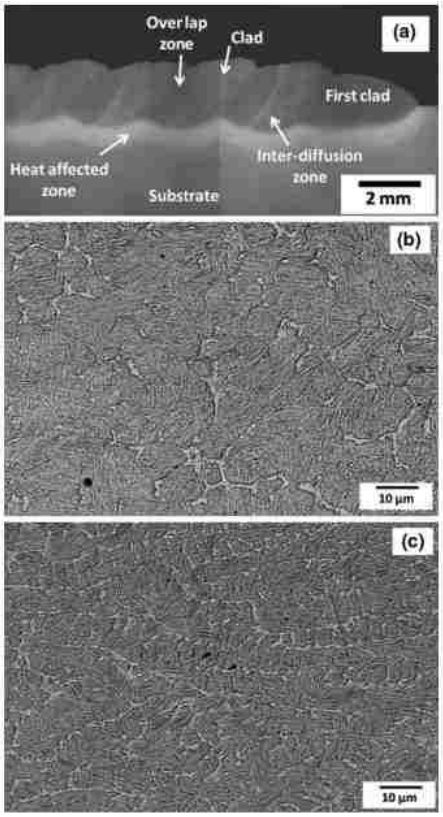

Figure 1. 9 SEM images of the cross-section of multi-track laser clad AISI H13 tool steel processed with a laser energy density of 133 J/mm2 and powder density of 13.3 g/mm^2 showing the (a) low-magnification view of the clad zone and the high-magnification views of (b) clad zone and (c) overlapped zone, respectively.

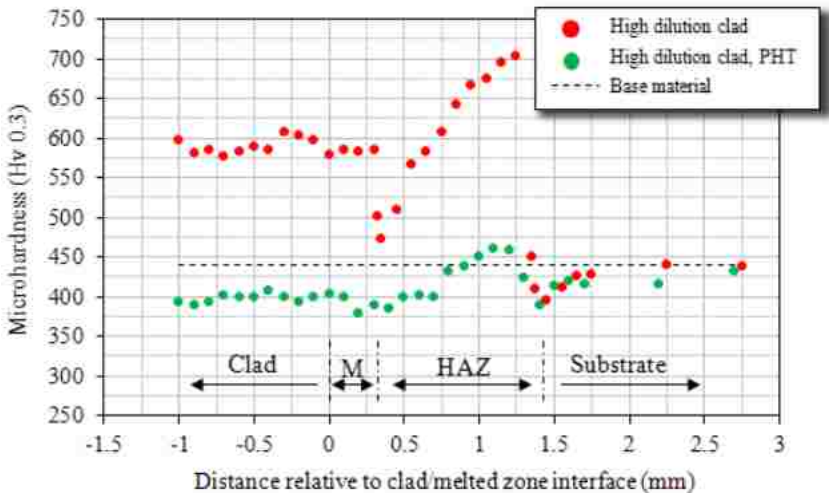

Figure 1. 10 Vertical microhardness profile, measured relative from the clad/melted zone interface showing the effect of PHT [45]

Fenech et al. [46] investigated a post deposition heat treatment of co-deposited Cr_3C_2 and AISI 410 stainless steel using coaxial laser deposition technique. They found that increasing carbon percentage in the mixture, post-deposition heat treatment for full re-austenizing, and tempering are essential to reduce the effects of layer re-tempering and solute trapping, which they assumed might affect the material mechanical properties negatively.

In another investigation, Zhang et al. [77] examined laser cladded $FeCoNiCrCuTiMoAlSiB_{0.5}$ high-entropy alloy (HEA), as shown in Fig. 1.11. The lath-like martensitic phase with a high density of dislocations has been observed. The nucleation of the martensite phase is co-triggered by laser rapid solidification and interstitial boron solute. The strengthening by martensite and interstitial solutes may enhance both hardness (11.6 GPa) and toughness 50.9 $MPam^{1/2}$.

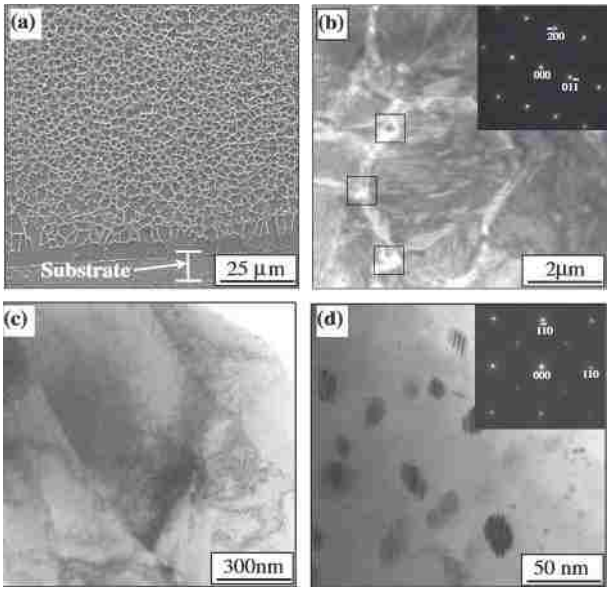

Figure 1. 11 The microstructure of $B_{0.5}$-HEA: (a) cross-sectional microstructure; (b) lath-like martensite with SAED pattern after solidification; (c) the magnified martensite containing many dislocations; (d) the precipitated ordered B2 nanocrystals with SAED pattern after annealing at 900°C [77]

Hemmati et al. [67] examined the effects of the laser cladding velocity on the phase constitutions, hardness, and wear rate of laser deposited AISI 431 martensitic stainless steel coatings and explained the controlling mechanisms. Their microstructural investigation through Scanning Electron Microscopy (SEM) and Orientation Imaging Microscopy (OIM) revealed that martensite lathes are stopped by the dendrite boundaries in various locations, as shown in Fig. 1.13.

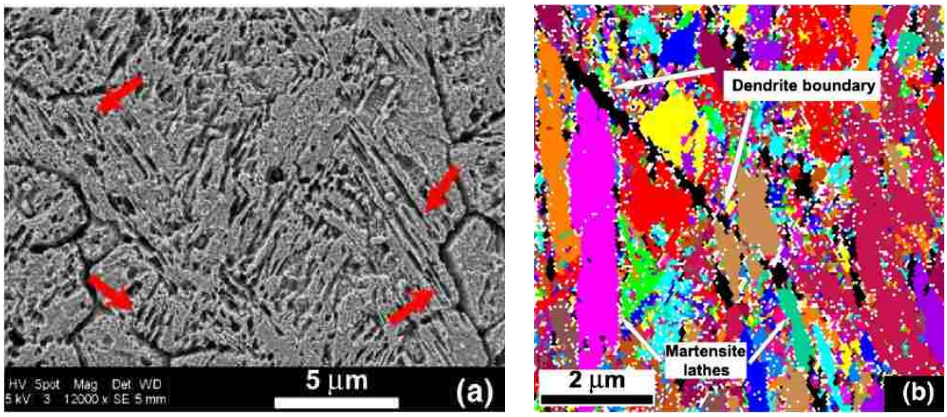

Figure 1. 12 (a) SEM micrograph and (b) OIM grain map showing how martensite lathes are halted at dendrite boundaries. Arrows show martensite lathes in (a) and dendrite boundaries in (b).[67]

Wu [27] investigated the clad coating alloy, a powder mixture of Fe, Cr, W, Ni, and C with a weight ratio of 10:5:1:1:1 and found that the coating microstructure consisted of the primary phase as γ-austenite of the f.c.c. structure with interdendritic lamellar eutectic shown in Fig. 1.14(a)-(d). The corresponding *Selected Area Diffraction Pattern (SADP*) in Fig. 1.14(d) indicates that the eutectic is composed of γ-austenite and the M_7C_3 carbide. Thus, the clad coating revealed to have the hypoeutectic microstructure, i.e., $\gamma + (\gamma + M_7C_3)$, where γ-Austenite is a non-equilibrium phase with an extended solid solution of alloying elements. They also observed a high density of dislocations, stacking faults, and twins, in both the primary and the eutectic γ-austenite, as shown in Fig. 1.14(e). TEM observation

and X-ray diffraction confirmed to them that no martensite exists in the as-coated microstructure.

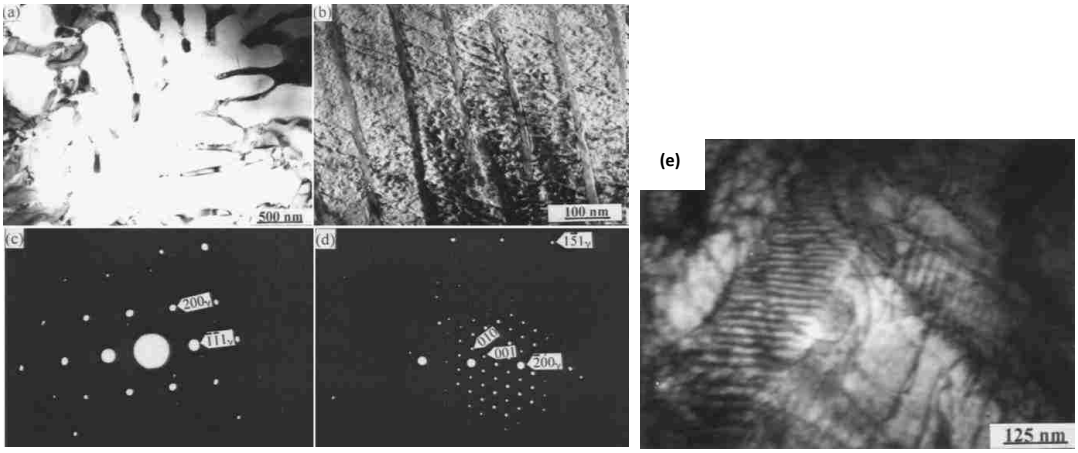

Figure 1. 13 TEM bright-field images showing the hypoeutectic microstructure of the laser-clad coating: (a) primary dendritic γ-austenite; (b) interdendritic lamellar eutectic consisting of γ-austenite and M_7C_3 carbide; (c), (d) SADPs of γ-austenite in (a) and of (γ+M_7C_3) in (b) respectively (laser parameters: 16 mm s^{-1} beam scanning speed, 3 mm beam diameter, 2 kW laser power, and 0.3 g s−1 feed rate) [27].

1.7.3.2 Mechanical Properties

Many researchers [4], [5], [53], [76], [78], [79] reported the mechanical behavior of Titanium and iron-based alloys processed with laser cladding or similar laser-based additive manufacturing processes. Chen et al. [21] observed low yield strength and tensile strength in the laser consolidated AISI 420 stainless steel (SS420) compared to their wrought counterparts of commercial grade. However, they found higher mechanical properties in the heat-treated sample of the same at 1008 °C for 0.5 hr with tempering at 316 °C for 2hr. Their findings are summarised in Table 1.4.

Table 1. 3 The Mechanical properties of LC SS420 steel [21]

Specimen condition	**Hardness**	**$\sigma_{0.2}$ (MPa)**	**σ_{UTS} (MPa)**
LC SS420 As-consolidated	536 HV (52 HRC)	833	1602
LC SS420 Austenized at 1008°C for 0.5 hr and tempered at 316 °C for 2hr	525 HV (51 HRC)	1550	1888
LC SS420 Austenized at 1008 °C for 0.5 hr and tempered at 600 °C for 2hr	376 HV (38 HRC)	977	1184
Wrought SS420 bar tempered at 204 °C	52 HRC	1480	1720

Khodabakhshi et al. [4] studied two types of stainless steel (austenitic S316-L and martensitic S410-L) processed with powder-feed laser additive manufacturing (LAM). They compared their uniaxial tensile testing results with the commercial counter parts of those SS at different testing mode with different strain rates (0.001, 0.01, 0.1, and 1.0 sec−1, respectively). They observed lower mechanical properties in the LAM austenitic stainless steel [YS (281-304) MPa, UTS (433-463) MPa] compared to their commercial counter parts [YS 304-365 MPa, UTS (617-641) MPa] at all testing modes. Interestingly, they observed higher mechanical properties in the LAM martensitic SS [YS (375-391) MPa, UTS (537-672) MPa] compared to the commercial grade [YS (156-278) MPa, UTS (238-387) MPa]. However, their results showed lower ductility in both the LAM stainless steels compared to the commercial grades.

Ravi et al. [5] investigated SC420 stainless steel processed with the Direct Laser Fabrication (DLF). They reported that the DLF process can produce three-dimensional (3D) near net-shape metallic parts with varying thickness along the vertical direction with a higher yield strength (1000 MPa) and tensile strength (1400 MPa) but with low

elongation (5%). They did not observe any influence of deposition direction on the yield and tensile strength. However, they observed a brittle fracture surface in both directions with very low ductility. They applied high isostatic pressure (HIP) at a high temperature (1000 °C) that reduced the residual stresses and improved the tensile properties.

Kurzynowski et al. [79] reported the influences of laser power input, scanning speed, and building strategies on the tensile properties of 316 L stainless steel processed by selective laser melting (SLM). They observed a double increment in the yield strength with a much smaller improvement in the ultimate tensile strength in comparison to a similar alloy processed with conventional methods.

Deev et al. [78] studied anisotropic mechanical properties of 316 SS deposited by laser melting. They found a strong dependence of the parameters related to the powder melting and the build direction on the mechanical properties. Other researchers [15], [16], [78], [80]–[85] reported the anisotropic mechanical properties in the AM-processed materials and compared their results to their cast and wrought material counterparts. The trend for the observed anisotropy is mainly related to the tensile strength and ductility, while most of the reported yield strength did not show anisotropy. They have excelled the minimum values of yield strength for their cast and wrought counterparts [85]. For example, no significant anisotropy was observed in yield strength of EBM-built and DED-built Ti-6Al-4V. However, in the case of SLM- built Ti-6Al-4V, higher anisotropy was observed in the yield strength between the different build orientations [85].

One important feature regarding the tensile properties of DED built AM steels is the building orientation of the parts that affects the resultant tensile properties of the

component [15]. It is believed that this anisotropic behavior is due to the occurrence of inter-diffusion layers in the transverse direction, which provides a simple path for shear bands. Various cooling rates in these deposition directions might affect microstructure and mechanical properties [15]. It is also suggested that the anisotropic property is most likely due to the epitaxial growth of columnar grains from each inter-diffusion zone observed in the microstructure of AM parts [85].

1.7.3.3 Development of Residual Stress

Development of residual stresses (RS) in the laser deposited coating or AM part is a common issue. The residual stresses can lead to the part distortion and loss of geometric tolerances [16]. The main factors responsible for the origin of AM residual stresses include (1) the spatial temperature gradient due to localized heating and cooling by the traveling heat source, (2) thermal expansion and contraction of material due to such heating and cooling, and (3) strain compatibility (uneven distribution of inelastic strains), force equilibrium and stress- strain constitutive behavior especially with respect to cyclic plastic flow. Finally, the large volume expansion due to martensitic transformation upon cooling was found to influence the residual stresses and distortion [16].

Farahmand and Kovacevic [52] examined single and multi-track laser cladding of AISI H13 tool steel by a high-power direct diode laser (HPDDL). They found that the value of the residual stress in multi-track cladding is relatively lower than in the case of single-track cladding due to the stress relief caused by post-heating during the cladding of the adjacent tracks. Their study revealed that the higher residual stress concentrated in the clad zone instead of the surrounding zone.

Gururaj et al. [53] reported significant magnitudes of residual compressive stress on the surface (670 ± 15 MPa) as compared to that on the hardened and tempered AISI H13 tool steel (280 ± 30 MPa). In another study, Nie et al. [86] reported maximum residual stress in the interface between the deposited layer and substrate due to complicated thermal cycles during the LHW process with H13 steel deposition.

Others [87]–[89] used 3D sequential thermal and elastic plastic analysis by SYSWELD, ABAQUS, and ANSYS to model the RS in the laser-based AM. Wang et al. [87] reported dominant compressive stress at the interior and tensile stress towards the edge in LENS-deposited AISI 410 stainless steel plates. They observed that the laser travel velocity has no significant effect on the z-component residual stress in the range of their study. They indicated that higher laser powers can increase the magnitude of the z-component residual stress.

Summary and Conclusions

As a novel AM process, laser- cladding AM technology has promising future to produce commercially viable functional components in many industrial sectors, including aerospace, medical, dental, oil and gas and automotive industries. Laser cladding is also utilized in metallic coating and surface repairing for the next generation industrial applications such as die and mold repair. Many researchers investigated on the microstructural evolutions, heat treatment, and mechanical properties of the laser-cladded Iron, Nickle, and titanium-based alloys as shown in the literature review matrix in Table 1.3. From the iron-based alloys, austenitic stainless steel and H13 tool steel were mostly studied. However, research findings were not consistent for the similar materials and found

to be varied based on AM process settings. Fundamental and scientific information are still being developed for the AM technology.

Moreover, AISI 420 martensitic stainless steel was not given much attention despite having its uses in many domains with laser cladding AM process. Considering the growing demand of AISI 420 MSS for high strength steel parts in automotive application, it is necessary to expand further research in characterizing the microstructural and mechanical properties of this martensitic stainless steel built with the laser cladding AM technology at different direction and orientations. It is also important to compare these materials properties with the similar alloy processed with traditional manufacturing methods. Since AISI 420 martensitic stainless steel is an important alloy currently being used in the surface repairing of die and tools industry, and has a high potentiality to be manufactured through laser cladding process as a high strength stainless steel for automotive application, this research focused on the in-depth study of microstructure and mechanical properties of this alloy in order to fill-up the gap found in the literature.

Table 1. 4 Literature Review Matrix

Major Articles Reviewed	Key words for Ranking													
	Laser based AM	Laser Welding	Austenitic stainless steel	Martensitic stainless steel	AISI 420 MSS	H13/ Tool steel	Titanium based alloy	Nickle based alloy	Process Parameter	Micro-structures	Micro-hardness	Tensile Testing	Residual stress	Heat treatment
Khodabakhshi et al. 2019 [4]	1	0	1	1	0	0	0	0	0	0	1	0	0	0
Ravi et al. 2013 [5]	1	0	0	1	1	0	0	0	1	01	1	0	0	0
Chen et al. 2008 [21]	1	0	0	1	1	0	0	0	1	0	1	0	0	0
Huang et. al. 2011 [30]	1	0	0	0	0	0	1	1	1	1	0	0	0	0
Adak et al. 2005 [36]	1	0	0	0	0	0	1	1	1	0	0	0	0	0
Chen et al. 2011 [42]	1	0	0	0	0	0	1	0	1	0	0	1	0	0
Yu et al. 2012 [44]	1	0	0	0	0	1	0	0	0	0	1	0	0	0
Sun et al. 2012 [45]	1	0	0	0	0	1	0	0	0	0	1	0	1	0
Baghjari et al. 2013 [50]	0	1	0	1	1	0	0	0	1	1	1	0	0	1
Köse & Kaçar 2014 [63]	0	1	0	1	1	0	0	0	1	1	1	0	1	1
Wang et al. 2008 [87]	1	0	0	1	0	0	0	0	0	0	0	1	0	0
Hemmati et al. 2011 [67]	1	0	0	1	0	0	0	0	1	1	0	1	0	0
Telasang et al. 2015, [53]	1	0	0	0	0	1	0	0	0	1	1	1	1	1
Farahmand et al. 2014 [52]	1	0	0	0	0	1	0	0	0	0	0	0	1	0
Cottam 2014 [65]	1	0	0	0	0	1	0	0	1	1	0	0	1	0
Sun et al. 2016 [75]	1	0	1	0	0	0	0	0	0	1	0	0	0	0
Krakhmalev et al. 2015 [76]	1	0	0	1	1	0	0	0	0	1	1	0	0	0
Khan et al. 2010 [66]	0	1	0	1	0	0	0	0	0	1	1	0	1	0
Niu & Chang 2000 [56]	1	0	0	0	0	1	0	0	0	1	0	0	0	0
Deev et al.2016 [78]	1	0	1	0	0	0	0	0	0	1	1	0	0	0
Xiaolei Wu 1999 [27]	1	0	0	0	0	1	0	0	0	0	1	0	0	0
Kurzynowski et al. 2018 [79]	1	0	1	0	0	0	0	0	1	1	1	1	0	0
Ghose et al. 2019 [88]	1	0	0	0	0	1	0	0	0	0	0	0	1	0
Carroll et al. 2013 [83]	1	0	0	0	0	0	1	0	0	0	0	1	0	0
Deng D. 2018 [80]	1	0	0	0	0	0	0	1	0	1	1	1	0	0
	22	3	4	8	5	8	4	3	10	13	13	7	7	4

Ranking: Key words available: 1, not available: 0

References

[1] G. A. Blog, “New manufacturing milestone: 30,000 additive fuel nozzles,” *GE Additive*, 2018. [Online]. Available: https://www.ge.com/additive/blog/new-manufacturing-milestone-30000-additive-fuel-nozzles. [Accessed: 20-Jul-2019].

[2] A. N. Isfahany, H. Saghafian, and G. Borhani, “The effect of heat treatment on mechanical properties and corrosion behavior of AISI420 martensitic stainless steel,” *J. Alloys Compd.*, vol. 509, no. 9, pp. 3931–3936, 2011.

[3] J. Brnic, G. Turkalj, M. Canadija, D. Lanc, and S. Krscanski, “Martensitic stainless steel AISI 420 - Mechanical properties, creep and fracture toughness,” *Mech. Time-Dependent Mater.*, vol. 15, no. 4, pp. 341–352, 2011.

[4] F. Khodabakhshi, M. H. Farshidianfar, A. P. Gerlich, M. Nosko, V. Trembo, and A. Khajepour, “Materials Science & Engineering A Microstructure , strain-rate sensitivity , work hardening , and fracture behavior of laser additive manufactured austenitic and martensitic stainless steel structures,” vol. 756, no. April, pp. 545–561, 2019.

[5] G. A. Ravi, X. J. Hao, N. Wain, X. Wu, and M. M. Attallah, “Direct laser fabrication of three dimensional components using SC420 stainless steel,” *Mater. Des.*, vol. 47, pp. 731–736, 2013.

[6] M. K. Alam, A. Edrisy, and R. J. Urbanic, “Microstructural Analysis of the Laser-Cladded AISI 420 Martensitic Stainless Steel,” *Metall. Mater. Trans. A*, vol. 50, no. 5, pp. 2495–2506, 2019.

[7] M. K. Alam, A. Edrisy, J. Urbanic, and J. Pineault, “Microhardness and Stress Analysis of Laser - Cladded AISI 420 Martensitic Stainless Steel,” *J. Mater. Eng. Perform.*, vol. 26, no. 3, pp. 1076–1084, 2017.

[8] M. K. Alam, J. Urbanic, S. M. Saqib, and A. Edrisy, “Effect of Process Parameters On The Microstructural Evolutions of Laser Cladded 420 Martensitic Stainless Steel,” in *Materials Science and Technology Conference Proceedings (MS&T15), October 4-8*, 2015, pp. 35–54.

[9] M. K. Alam, R. J. Urbanic, N. Nazemi, and A. Edrisy, “Predictive modeling and the effect of process parameters on the hardness and bead characteristics for laser-cladded stainless steel,” *Int. J. Adv. Manuf. Technol.*, 2017.

[10] R. M. Mahamood and E. T. Akinlabi, “Laser Additive Manufacturing,” *3D Print.*, pp. 154–171.

[11] C. S. Toyserkani, E., Khajepour, A., *Laser Cladding*. New York: CRC Press, 2005.

[12] K. V. Wong and A. Hernandez, “A Review of Additive Manufacturing,” *ISRN Mech. Eng.*, vol. 2012, pp. 1–10, 2012.

[13] D. D. Gu, W. Meiners, K. Wissenbach, and R. Poprawe, “Laser additive manufacturing of metallic components: materials, processes and mechanisms,” *Int. Mater. Rev.*, vol. 57, no. 3, pp. 133–164, 2012.

[14] A. Gebhardt, *Understanding Additive Manufacturing*. Munich: Hanser Publishers, 2011.

[15] H. Fayazfar *et al.*, “A critical review of powder-based additive manufacturing of ferrous alloys: Process parameters, microstructure and mechanical properties,” *Mater. Des.*, vol. 144, pp. 98–128, 2018.

[16] T. DebRoy *et al.*, “Additive manufacturing of metallic components – Process, structure and properties,” *Prog. Mater. Sci.*, vol. 92, pp. 112–224, 2018.

[17] P. Han, “Additive Design and Manufacturing of Jet Engine Parts,” *Engineering*, vol. 3, no. 5, pp. 648–652, 2017.

[18] K. Aggarwal, “Investigation of Laser Clad Bead Geometry to Process Parameter Settings for Effective Parameter Selection, Simulation, and Optimization -MASc Thesis,” University of Windsor, 2014.

[19] S. M. Saqib, “Experimental Investigation of Laser Cladding Bead Morphology and Process Parameter Relationship for Additive Manufacturing Process Characterization - PhD Dissertation,” University of Windsor, 2016.

[20] Alam, M. K., Mehdi, M., Urbanic, R.J., and A. Edrisy, “Electron Backscatter Diffraction (EBSD) Analysis of Laser-Cladded AISI 420 Martensitic Stainless Steel,” *Meterials Charact.*, no. MATERIALSCHAR_2019_1647, 2019.

[21] J. Chen, L. Xue, and S. Wang, “Microstructure Characterization of Laser-Consolidated AISI 420 Stainless Steel,” in *Materials Science and Technology (MS&T) 2008*, 2008, no. Lc, pp. 1388–1396.

[22] H. Tim, “From looms to thermal spray to laser cladding,” *The Fabricators &*

Manufacturer's Association Intl., Jun-2014.

[23] K. Weisheit, A., Gasser, A., Backes, G., Jambor, T., Pirch, N. and Wissenbach, "Laser-Assisted Fabrication of Materials," in *Laser-Assisted Fabrication of Materials*, vol. 161, J. D. Majumdar and I. Manna, Eds. Berlin, Heidelberg: Springer- Verlag Berlin Heidelberg, 2013, pp. 221–240.

[24] H. Om and S. Pandey, "Effect of heat input on dilution and heat affected zone," *Sadhana - Indian Acad. Sci.*, vol. 38, Part 6, no. December, pp. 1369–1391, 2013.

[25] J.F. Lancaster, *Metallurgy of Welding*, Sixth Edit. Abington, Cambridge: Abington Publishing, 1999.

[26] M. Zhong and W. Liu, "Laser surface cladding: the state of the art and challenges," *Proc. Inst. Mech. Eng. Part C J. Mech. Eng. Sci.*, vol. 224, no. 5, pp. 1041–1060, Jan. 2010.

[27] X. Wu, "Rapidly solidified nonequilibrium microstructure and phase transformation of laser-synthesized iron-based alloy coating," *Surf. Coatings Technol.*, vol. 115, pp. 153–162, 1999.

[28] T. Torims, "The Application of Laser Cladding to Mechanical Component Repair, Renovation and Regeneration," in *DAAAM International Scientific Book*, B. K. & Z. Tekic, Ed. Vienna, Austria: DAAAM International, 2013, pp. 587–608.

[29] J. Tuominen, "Engineering Coatings by Laser Cladding – The Study of Wear and Corrosion Properties, Ph.D Dessertation," Tampere University of Technology,

2009.

[30] F. X. Huang, Z. H. Jiang, X. M. Liu, J. S. Lian, and L. Chen, “Effects of Process Parameters on Microstructure and Hardness of Layers by Laser Cladding,” *ISIJ Int.*, vol. 51, no. 3, pp. 441–447, 2011.

[31] J. Lippold and D. Kotecki, “Welding Metallurgy and Weldability of Stainless Steels,” *Wiley-Interscience*. John Wiley & Sons, New Jersey, pp. 56–86, 2005.

[32] K. Saeidi, *Stainless steels fabricated by laser melting, Doctoral Thesis, 2016*. Department of Materials and Environmental Chemistry, Arrhenius Laboratory, Stockholm University, 2016.

[33] M. V. Boniardi and A. Casaroli, *Stainless Steels*. Milan Italy: Gruppo Lucefin S.P.A, 2014.

[34] D. S. Codd, “Automotive Mass Reduction with Martensitic Stainless Steel,” *SAE Tech. Pap.*, 2011.

[35] H. Gedda, “Laser Cladding : An Experimental and Theoretical Investigation - Doctoral Thesis,” Lulea University of Technology, 2004.

[36] B. Adak, P. Nash, D. Chen, and A. Swiglo, “Microstructural characterization of laser cladding of Cu-30Ni,” *J. Mater. Sci.*, vol. 40, pp. 2051–2054, 2005.

[37] R. Jendrzejewski, G. Śliwiński, M. Krawczuk, and W. Ostachowicz, “Temperature and stress during laser cladding of double-layer coatings,” *Surf. Coatings Technol.*, vol. 201, no. 6, pp. 3328–3334, Dec. 2006.

[38] D. Lepski and E. Beyer, “Modeling the Influence of Process Parameters and Additional Heat Sources on Residual Stresses in Laser Cladding,” *J. Therm. Spray Technol.*, vol. 16, no. September, pp. 355–373, 2007.

[39] D. Lepski and F. Bruckner, “Laser cladding,” in *The Theory of Laser Materials Processing*, Online., vol. 119, J. Dowden, Ed. Springer Netherlands, 2009, pp. 235–279.

[40] A. Emamian, S. F. Corbin, and A. Khajepour, “Effect of laser cladding process parameters on clad quality and in-situ formed microstructure of Fe–TiC composite coatings,” *Surf. Coatings Technol.*, vol. 205, no. 7, pp. 2007–2015, Dec. 2010.

[41] Q. Wu and W. Li, “The Microstructure and Wear Properties of Laser-Clad WC-Cr3C2 Cermet Coating on Steel Substrate,” *Mater. Trans.*, vol. 52, no. 3, pp. 560–563, 2011.

[42] J. Chen, S. H. Wang, and L. Xue, “On the development of microstructures and residual stresses during laser cladding and post-heat treatments,” *J. Mater. Sci.*, vol. 47, no. 2, pp. 779–792, 2012.

[43] S. Marimuthu *et al.*, “Finite element modelling of substrate thermal distortion in direct laser additive manufacture of an aero-engine component,” *Proc. Inst. Mech. Eng. Part C J. Mech. Eng. Sci.*, vol. 227, no. 9, pp. 1987–1999, Dec. 2012.

[44] J. Yu, M. Rombouts, G. Maes, and F. Motmans, “Material Properties of Ti6Al4V Parts Produced by Laser Metal Deposition,” *Phys. Procedia*, vol. 39, pp. 416–424, 2012.

[45] S. Da Sun, Q. Liu, M. Brandt, M. Janardhana, and G. Clark, “Microstructure and Mechanical Properties of Laser Cladding Repair of AISI 4340 Steel,” in *28th International Congress of the Aeronautical Sciences (ICAS)*, 2012, no. i, pp. 1–9.

[46] M. Fenech, B. Mallia, M. Grech, and J. C. Betts, “Post-deposition heat treatment of co-deposited Cr3C2 and AISI 410 stainless steel using the coaxial laser deposition technique,” *J. Mater. Sci.*, vol. 48, no. 5, pp. 2224–2235, 2013.

[47] M. Hao and Y. Sun, “A FEM model for simulating temperature field in coaxial laser cladding of TI6AL4V alloy using an inverse modeling approach,” *Int. J. Heat Mass Transf.*, vol. 64, pp. 352–360, Sep. 2013.

[48] A. Piasecki, A, Bartkowski, D., Mlynarczak, “Laser Claddiing of Stellite 6 on Low Carbon Steel for Repairing Components in Automotive Applications Using Disk Laser,” *Arch. Mech. Technolgy Autom.*, vol. 33, no. 2, pp. 2–11, 2013.

[49] H. Kong, R. M. Mahamood, E. T. Akinlabi, M. Shukla, and S. Pityana, “Laser Metal Deposition of Ti6Al4V : A Study on the Effect of Laser Power on Microstructure and Microhardness,” in *Proceedings of the International MultiConference of Engineers and Computer Scientists 2013 Vol II, IMECS*, 2013, vol. II, pp. 6–11.

[50] S. H. Baghjari and S. A. A. Akbari Mousavi, “Effects of pulsed Nd:YAG laser welding parameters and subsequent post-weld heat treatment on microstructure and hardness of AISI 420 stainless steel,” *Mater. Des.*, vol. 43, pp. 1–9, 2013.

[51] V. G. Niziev, M. D. Khomenko, R. V Grishaev, S. Pityana, and C. V Rooyen, “Numerical Study to Represent Non-Isothermal Melt-Crystallization Kinetics at

Laser-Powder Cladding," *Model. Numer. Simul. Mater. Sci.*, vol. 3, no. April, pp. 61–69, 2013.

[52] P. Farahmand and R. Kovacevic, "An experimental–numerical investigation of heat distribution and stress field in single- and multi-track laser cladding by a high-power direct diode laser," *Opt. Laser Technol.*, vol. 63, pp. 154–168, Nov. 2014.

[53] G. Telasang, J. Dutta Majumdar, N. Wasekar, G. Padmanabham, and I. Manna, "Microstructure and Mechanical Properties of Laser Clad and Post-cladding Tempered AISI H13 Tool Steel," *Metall. Mater. Trans. A*, vol. 46, no. 5, pp. 2309–2321, 2015.

[54] Q. Ming, L. C. Lim, and Z. D. Chen, "Laser cladding of nickel-based hardfacing alloys," *Surf. Coatings Technol.*, vol. 106, pp. 174–182, 1998.

[55] A. Guo, W., Kar, "Microstructural analysis and performance evalution in laser cladding of stainless steel on the plain carbon steel," in *Elevated Temperature Coatings: Science and Technology lll*, 1999, pp. 231–241.

[56] H. J. Niu and I. T. H. Chang, "Microstructural evolution during laser cladding of M2 high-speed steel," *Metall. Mater. Trans. A*, vol. 31, no. 10, pp. 2615–2625, 2000.

[57] J. T. M. Pei., Y.T., De Hosson, "Producing Functionally Graded Coatings by Laser-Powder Cladding," *JOM-e J. Miner. Met. Mater. Soc.*, vol. 52, no. 1, 2000.

[58] P. Wu, C. Z. Zhou, and X. N. Tang, "Microstructural characterization and wear behavior of laser cladded nickel-based and tungsten carbide composite coatings,"

Surf. Coatings Technol., vol. 166, pp. 84–88, 2003.

[59] W. E. Frazier, "Metal additive manufacturing: A review," *J. Mater. Eng. Perform.*, vol. 23, no. 6, pp. 1917–1928, 2014.

[60] N. Shamsaei, A. Yadollahi, L. Bian, and S. M. Thompson, "An overview of Direct Laser Deposition for additive manufacturing; Part II: Mechanical behavior, process parameter optimization and control," *Addit. Manuf.*, vol. 8, pp. 12–35, 2015.

[61] A. Rajasekhar, "Influence of Microstructure on Mechanical Properties of Martensitic Stainless Steel Welds," *IOSR J. Mech. Civ. Eng.*, vol. 12, no. 2, pp. 2320–334, 2015.

[62] D. Thibault, P. Bocher, and M. Thomas, "Residual stress and microstructure in welds of 13%Cr–4%Ni martensitic stainless steel," *J. Mater. Process. Technol.*, vol. 209, no. 4, pp. 2195–2202, 2009.

[63] C. Köse and R. Kaçar, "The effect of preheat & post weld heat treatment on the laser weldability of AISI 420 martensitic stainless steel," *Mater. Des.*, vol. 64, pp. 221–226, 2014.

[64] Y. C. Lin and S. C. Chen, "Effect of residual stress on thermal fatigue in a type 420 martensitic stainless steel weldment," *J. Mater. Process. Technol.*, vol. 138, no. 1–3, pp. 22–27, 2003.

[65] R. Cottam, J. Wang, and V. Luzin, "Characterization of microstructure and residual stress in a 3D H13 tool steel component produced by additive manufacturing," *J.*

Mater. Res., vol. 29, no. 17, pp. 1978–1986, 2014.

[66] M. M. A. Khan, L. Romoli, M. Fiaschi, F. Sarri, and G. Dini, "Experimental investigation on laser beam welding of martensitic stainless steels in a constrained overlap joint configuration," *J. Mater. Process. Technol.*, vol. 210, no. 10, pp. 1340–1353, 2010.

[67] I. Hemmati, V. Ocelík, and J. T. M. De Hosson, "The effect of cladding speed on phase constitution and properties of AISI 431 stainless steel laser deposited coatings," *Surf. Coatings Technol.*, vol. 205, no. 21–22, pp. 5235–5239, 2011.

[68] J.-Y. Chen, K. Conlon, L. Xue, and R. Rogge, "Experimental study of residual stresses in laser clad AISI P20 tool steel on pre-hardened wrought P20 substrate," *Mater. Sci. Eng. A*, vol. 527, no. 27–28, pp. 7265–7273, 2010.

[69] L. E. Murr *et al.*, "Metal Fabrication by Additive Manufacturing Using Laser and Electron Beam Melting Technologies," *J. Mater. Sci. Technol.*, vol. 28, no. 1, pp. 1–14, 2012.

[70] L. E. Murr, "Metallurgy of Additive Manufacturing: Examples from Electron Beam Melting," *Addit. Manuf.*, vol. 5, pp. 40–53, 2014.

[71] L. Yang *et al.*, "Additive Manufacturing of Metals: The Technology, Materials, Design and Production," pp. 45–61, 2017.

[72] S. Kou, *Welding Metallurgy, Second Edition*, Second Edi. New Jersey: A John Wiley & Sons, Inc., 2003.

[73] K. Zhang, S. Wang, W. Liu, and X. Shang, “Characterization of stainless steel parts by Laser Metal Deposition Shaping,” *J. Mater.*, vol. 55, pp. 104–119, 2014.

[74] B. Song, S. Dong, S. Deng, H. Liao, and C. Coddet, “Optics & Laser Technology Microstructure and tensile properties of iron parts fabricated by selective laser melting,” *Opt. Laser Technol.*, vol. 56, pp. 451–460, 2014.

[75] Z. Sun, X. Tan, S. Tor, and W. Y. Yeong, “Selective laser melting of stainless steel 316L with low porosity and high build rates,” *JMADE*, vol. 104, pp. 197–204, 2016.

[76] P. Krakhmalev, I. Yadroitsava, G. Fredriksson, and I. Yadroitsev, “In situ heat treatment in selective laser melted martensitic AISI 420 stainless steels,” *Mater. Des.*, vol. 87, pp. 380–385, 2015.

[77] H. Zhang, Y. He, and Y. Pan, “Enhanced hardness and fracture toughness of the laser-solidified FeCoNiCrCuTiMoAlSiB0.5 high-entropy alloy by martensite strengthening,” *Scr. Mater.*, vol. 69, no. 4, pp. 342–345, 2013.

[78] A. A. Deev, P. A. Kuznetcov, and S. N. Petrov, “Anisotropy of mechanical properties and its correlation with the structure of the stainless steel 316L produced by the SLM method,” *Phys. Procedia*, vol. 83, pp. 789–796, 2016.

[79] T. Kurzynowski, K. Gruber, W. Stopyra, B. Kuźnicka, and E. Chlebus, “Correlation between process parameters, microstructure and properties of 316 L stainless steel processed by selective laser melting,” *Mater. Sci. Eng. A*, vol. 718, no. January, pp. 64–73, 2018.

[80] D. Deng, *Additively Manufactured Inconel 718 : Microstructures and Mechanical Properties*, no. 1798. 2018.

[81] A. A. Popovich, V. S. Sufiiarov, E. V. Borisov, I. A. Polozov, D. V. Masaylo, and A. V. Grigoriev, "Anisotropy of mechanical properties of products manufactured using selective laser melting of powdered materials," *Russ. J. Non-Ferrous Met.*, vol. 58, no. 4, pp. 389–395, 2017.

[82] J. J. Lewandowski and M. Seifi, "Metal Additive Manufacturing: A Review of Mechanical Properties," *Annu. Rev. Mater. Res.*, vol. 46, no. 1, pp. 151–186, 2016.

[83] B. E. Carroll, T. A. Palmer, and A. M. Beese, "Anisotropic tensile behavior of Ti-6Al-4V components fabricated with directed energy deposition additive manufacturing," *Acta Mater.*, vol. 87, pp. 309–320, 2015.

[84] L. Hitzler, J. Hirsch, B. Heine, M. Merkel, W. Hall, and A. Öchsner, "On the anisotropic mechanical properties of selective laser-melted stainless steel," *Materials (Basel).*, vol. 10, no. 10, 2017.

[85] Y. Kok *et al.*, "Anisotropy and heterogeneity of microstructure and mechanical properties in metal additive manufacturing: A critical review," *Mater. Des.*, vol. 139, pp. 565–586, 2018.

[86] Z. Nie *et al.*, "Journal of Materials Processing Technology Experimental study and modeling of H13 steel deposition using laser hot-wire additive manufacturing," *J. Mater. Process. Tech.*, vol. 235, pp. 171–186, 2016.

[87] L. Wang, S. D. Felicelli, and P. Pratt, “Residual stresses in LENS-deposited AISI 410 stainless steel plates,” vol. 496, pp. 234–241, 2008.

[88] S. Ghosh and J. Choi, “Modeling and Experimental Verification of Transient / Residual Stresses and Microstructure Formation in Multi-Layer Laser Aided DMD Process,” vol. 128, no. July 2006, 2019.

[89] E. Foroozmehr and R. Kovacevic, “Effect of path planning on the laser powder deposition process : thermal and structural evaluation,” pp. 659–669, 2010.

CHAPTER 2 Predictive Modeling and the Effect of Process Parameters on the Hardness and Bead Characteristics of Laser - Cladded Stainless Steel

Introduction

Laser cladding (LC) is one of the potential additive manufacturing (AM) processes for fabricating a metallic near-net shape 3D part, layer by layer directly from the CAD file. Its usage is also growing as a protective coating solution to repair the worn surfaces of engine parts and tools by depositing a high-quality coating. A laser is used as a heat source to melt the depositing metallic powder (or wire) and the outer part of the substrate [1]. A high power diode laser beam used in this process can be tailored to a variety of industrial applications with a small to big spot size (less than 1 mm to 7.2 mm) with localized and minimal heat input [2]. The superior mechanical properties of laser cladded parts and the homogenous metallurgical bond with a low dilution and heat affected zone (HAZ) in the substrate makes LC technology an attractive process for both cladding and AM.

The mechanical and physical properties of laser cladded parts are partially dependent on the process parameters associated with the LC process, and they are largely unknown. Understanding these relationships is essential in developing robust process solutions which are minimally affected by the external sources of variability [3].

As summarized in Table 2.1, the main process parameters explored by researchers include (but are not limited to): the laser power (LP), the powder feed rate (FR), the laser scanning speed (LS), the lens focal length (FL), and the distance between the contact tip to the workpiece (CTD). Additional input parameters, such as the powder grain sizes, surface normal to torch angle, etc. are described in Urbanic et al. [4]. Several experimental design

methodologies [2,5–16] are proposed by researchers to examine the statistical relationships between the process parameters and their impact on the bead geometries and mechanical properties. Those researchers have reported the use of design of experiments and process parameters optimization using full factorial design, Taguchi design, and the Response Surface Method (RSM) with a central composite design.

Table 2. 1 Summary of literature review

Author Reference	Materials/ Process	DOE strategy	Expt. Factors	Output Variable
Farahmand et al. [2]	H13/LC	RSM/CCD	LP, FR, LS	Bead geometry, hardness
Sun et al. [5]	Ti6Al4V/LC	RSM/CCD	LP, FR, LS	Bead geometry
Onwubolu et al. [9]	Diamalloy'02/LC	RSM	LP, FR, LS	clad angle
Liu et al. [10]	Fe-based alloy (CrMoNiCFe) /LC	RSM/CCD	LP, FR, CGFR, SOD	Powder catchment efficiency, clad geometry
Lee[17]	Co alloy powder/LC	Taguchi	SGT, LPS, FR, LS, PFA, PFP, FP	deposition efficiency
Graf et al. [18]	René 80 (Ni)/LC	Full Factorial	LP, SD, LS, FR	Bead geometry
Urbanic et al. [6], [8], [12]	420 St. steel/LC	RSM/CCD	FR, LP, FL, LS, CTD	Bead geometry
Mondal et al.[13]	NiCrMo Alloy/LC	Taguchi	FR, LP, LS	Bead Geometry

LC - Laser Cladding; **DOE** - Design of Experiments; **RSM** - Response Surface Methodology; **CCD** - Central Composite Design; **CTD** - Contact Tip to Workpiece Distance; **CGFR** - Carrier Gas Flow Rate; **FR** - Powder Feed Rate; **FL** - Focal Length of the Lens; **FP** - Focal Position of a laser beam; **LP** - Laser Power; **LS** - Laser Speed; **LPS** - Laser Pulse Shape; **PFA** - Powder Feed Angle; **PFP** - Powder Feed Position; **SD** - Spot Diameter; **SGT** - Shielding Gas Type; **SOD** - Stand Off Distance

Farahmand and Kovacevic [2] used a Central Composite Design (CCD) with the Response Surface Methodology (RSM) for the multi-objective optimization for cladding with AISI H13 using the process parameters LP, FR, and LS on the clad-bead geometry and clad microhardness. They found that the FR and LS had a significant effect on the clad height, the heat affected zone (HAZ) depth, and the clad microhardness.

Sun et al. [5] employed the CCD and RSM to build a mathematical model. They examined the influence of the LP, LS, and FR on the cladding-bead geometry of Ti6Al4V cladding on a TC4 substrate, but they did not assess hardness. They used the ANOVA method to establish relationships between the process parameters and the output responses. Their analysis indicated that the FR had a significant effect on the width and height of cladding coating, while LS had the most significant effect on the penetration depth.

Liu and Kovacevic [10] investigated the effects of the main processing parameters such as the LP, FR, the carrier-gas flow rate, and the stand-off distance on the output results of powder catchment efficiency and the clad geometry. They also used the RSM with a CCD to find out the statistical relationships and optimal processing parameters. They found that the carrier- gas flow rate had the most significant effect on the powder catchment efficiency. The FR, carrier-gas flow rate and interaction of the carrier gas and stand-off distance were the most significant factors affecting the clad height while the LP was the most effective factor affecting the clad width.

Lee [17] used the Taguchi Method to maximize the deposition efficiency in the cladding of Co alloy powder. He found that the powder feed position had the most significant effect on the deposition efficiency. Graf et al. [18] used a full factorial design

to determine the effect of process parameters on the bead geometry of laser metal deposition of a Nickel-based superalloy René 80. Saqib et al. [6], Urbanic et al. [8], and Aggarwal et al. [12] performed similar analyses using RSM and CCD along with an artificial neural network to establish statistical model and relationship between bead geometry (width, height, penetration and dilution) and the main process parameters for laser-cladded AISI 420 stainless steel. The present study used all five process parameters, including the FL and CTD, which are shown in Fig. 2.1.

Most of the researchers have focused on the bead geometry when developing predictive models. However, two important characteristics of bead geometry, namely the aspect ratio of the bead (width-to-height ratio and depth of penetration to bead width ratio) and the bead wetting angle, have not been investigated. Also, there is a lack of research on the statistical relationships between the process parameters and the bead microhardness. The clad geometry functional characteristics must be considered in tandem with the bead geometry for effective process planning solutions. The current authors investigated [19] predictive modeling approaches for microhardness by using a simple multiple regression for a narrow set of parameters and experimental settings by perturbing one factor at a time around a central set point. However, the model was not expandable for a wide range of process parameter settings. For process planning, quadratic models need to be developed for the large set of variables involved in the laser cladding process.

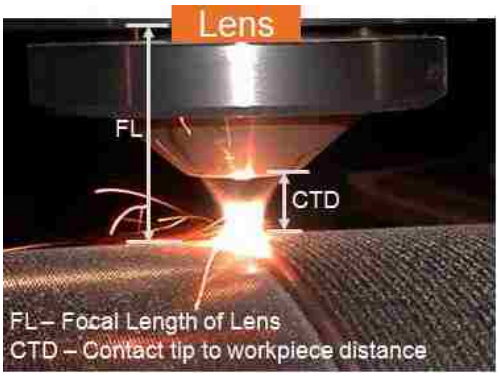

Figure 2. 1 Laser cladding

The present research targets laser-cladded AISI 420 stainless steel for single track beads. The application of 420 stainless steel is increasing as one of the potential alloys for laser cladding additive fabrication. Unlike other stainless steels, the properties of this stainless steel can be changed by heat treatment [20]. Hence, these steels are generally used for a wide range of applications such as steam generators, pressure vessels, mixer blades, cutting tools, and medical applications. Moreover, it provides excellent wear resistance and high surface hardness required for the die and tool repair when coated by laser cladding [21].

In this paper, the Response Surface Method (RSM) is applied using the Central Composite Design (CCD) to establish the experimental conditions. *F*-statistics from the analysis of variance (ANOVA), perturbation, surface mapping, and contour plotting methods are employed to investigate the statistical correlations among the process parameters, bead geometry, and the bead microhardness. Quantitative and qualitative analyses are performed to illustrate the non-linear influence of the laser cladding process. The long-term goal of this research is to develop process planning strategies for the additive manufacturing process to fabricate a component with the desired geometry and physical

characteristics. This research will help to predict the bead aspect ratio as the width can be easily measured (i.e., with a camera control system), while functional characteristics such as hardness can easily be correlated to the strength of laser-cladded AISI 420 stainless steel [22,23].

Research Methodology

The methodology for the experimentation strategy, data collection, and simulations is presented in this section. The process flow for the overall research plan is illustrated in Fig. 2.2, showing the various experimentation, simulation, and analysis aspects. This paper focuses on the statistical analyses' elements, which are presented in section 2.3.

2.2.1 Design of Experiments (DOE)

The statistical software Design-Expert Version 10 was employed to configure the experiments using the response surface methodology with a CCD. It is hypothesized that the CCD approach can provide the necessary information related to the process parameters and their interactions on the response variables (e.g., microhardness, bead geometry) over a wide range of process settings.

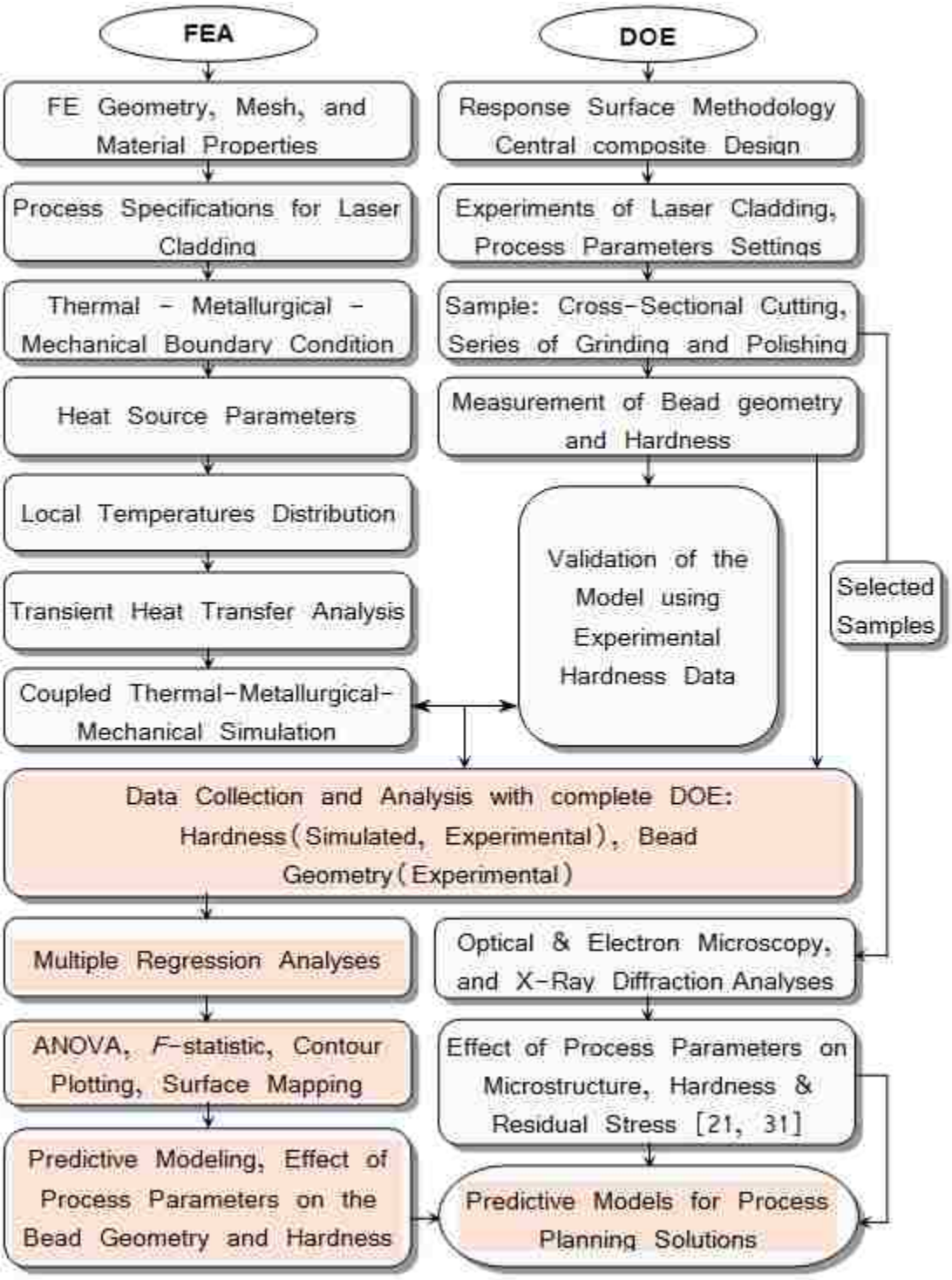

Figure 2. 2 Procedure of the experimentation, simulation, validation, and research outputs.

This design approach is also readily expandable, if necessary. A five-factor, five-level design matrix was established at a half fraction and an alpha value of 2, with 3 replicates of the factorial and the axial points, and 18 replicated central points. The CCD approach provides 96 experimental runs (18 central points and 78 non-central points) in contrast to a full factorial Design of Experiments (DOE) approach, which would require 5^5 experiments [24]. The experimental configuration and codes are shown in Table 2.2.

Table 2. 2 Process parameters and coding.

Factors	Units	Notations	Coding and values of Factors				
			-2	-1	0	1	2
Powder Feed Rate (FR)	gm/min	FR	10	15	20	25	30
Laser Power (LP)	kW	LP	1	2	2.5	3	4
Focal Length of Lens (FL)	mm	FL	380	390	400	410	420
Laser Speed (LS)	mm/s	LS	5	7.5	10	12.5	15
Contact Tip to Workpiece Distance (CTD)	mm	CTD	21	22	23	24	25

2.2.2 Laser Cladding Experiments

The experiments were performed at an industrial facility using a 4 kW fiber diode laser coupled to an articulated robotic arm on a 6.4 mm flat bar of medium carbon steel substrate. The powder density of the stainless steel was 4.37 gm/cm^3 with a 53-180 µm grain size [21]. The chemical composition of the alloy powder is shown in Table 2.3.

A high-power laser beam was focused on the substrate materials to generate a molten pool while the AISI 420 stainless steel metal powder was injected simultaneously into the focal area of the laser through coaxial nozzles with flowing argon gas. The argon gas serves as a shield to protect the molten pool from oxidation. A series of the single beads were cladded on the substrate with different processing parameters (Table 2.2) [21].

Table 2. 3 Chemical composition of the cladding powder (420 stainless steel).

Chemical Elements	Percentage of composition (%)
Carbon	0.23
Manganese	1.2
Chromium	12.6
Silicon	0.5
Iron	Balance
Cobalt	0.02

2.2.3 Light Optical Microscopy and Measurement of Bead Geometry

The metallographic work such as grinding and polishing of the cross-sectional samples was done manually as per the Struers application notes for the stainless steel materials [25]. The microscopy observations were made using a Leica Q5501W light microscope. The bead width, height, and depth of penetration were measured using Image-Pro Plus software as per the bead geometry shown in Fig. 2.3a. The bead width to height ratio, the penetration depth to the bead width ratio, and the bead wetting angle are calculated based on the measured bead geometry.

2.2.4 Measurement of Bead Microhardness

A Buehler microhardness tester was used to measure the bead microhardness (Vickers) using a load of 200 g and a loading time of 12 s. The measurements were

performed at the center of the bead at a 100 µm interval from the top of the bead through the dilution and heat affected zones (HAZ), and part of the substrate materials. Two measurements were performed at a 250 µm distance from each side of the first indentation set (Fig. 2.3a) [21]. The average hardness values were measured from these three measurements. This generated 5 – 8 values per bead. This set of averaged hardness values from the center line is used to generate a baseline set for the finite element analysis (FEA) simulation models. This experimental microhardness data is collected from a selected set of experiments. The balance of the data is generated from simulation results, as the FEA model results correlate well to the collected hardness data.

2.2.5 Simulation of Bead Microhardness

The LC simulation was performed with the finite element (FE) software, SYSWELD. This simulation solution considers the variable thermal and mechanical properties of the cladded and substrate materials along with the metallurgical reactions. The nodal temperatures and phase transformations are calculated in a coupled thermal-metallurgical-mechanical analysis. The thermo-physical properties depend on the temperature and the metallurgical proportions of each phase. Information on the heat source, boundary conditions, the governing thermal equations, the mesh, and convergent studies for the simulation, and the model goodness of fit for single and overlapping beads are provided in the current authors' earlier study, Navid et al. [26–28]. Similar analytical model of laser cladding by power injection are also found in the study of Toyserkani et al. [29] and Fu et al. [30].

Experimental hardness data from a wide variety of bead shapes are used to validate the model. Fig. 2.3b depicts the simulated hardness variation data from the top of the bead

to the HAZ in the substrate. The simulation hardness data and the experimental data are found to have a good agreement (Fig. 2.3c); consequently, simulation data is used along with the average measured hardness values.

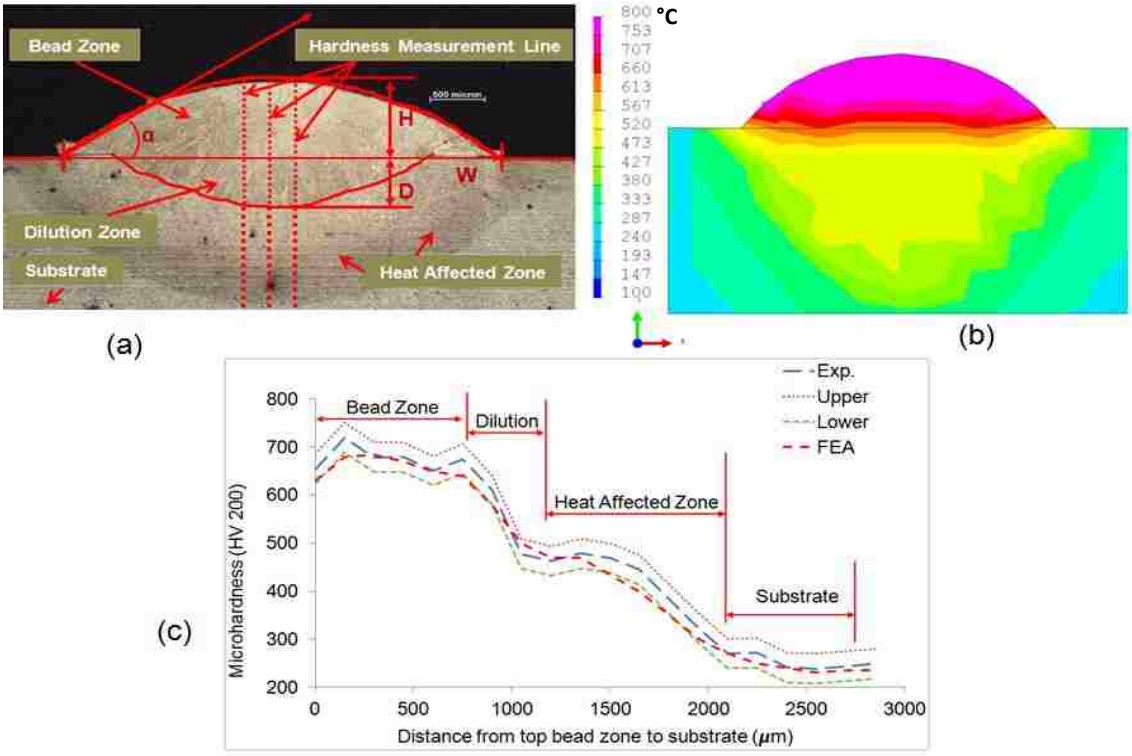

Figure 2. 3 a) A cross-sectional bead sample showing the bead geometry (W- Width, H- Height, D- Depth of penetration, α – Wetting Angle), dilution zone (diffusion between clad and substrate), heat affected zone, substrate, and the hardness measurement lines. (b) FEA model for a single bead laser cladded sample. (c) Comparison of hardness profile of experimental results with the simulated result for a single bead sample.

2.2.6 Predictive Modeling

The experimental and simulation data are utilized to develop statistical based predictive models. The analysis of variance (ANOVA) technique was utilized for finding the statistically significant process parameters and their interactions. To develop the relationship between various processing parameters and the corresponding response

variables, a second-order regression model was used to fit the experimental data as described in Eq. (1):

$$y = \beta_0 + \sum_{j=1}^{k} \beta_j x_j + \sum_{i,j=1}^{k} \beta_{ij} x_i x_j + \sum_{j=1}^{k} \beta_{jj} {x_j}^2 + \epsilon \ldots\ldots\ldots\ldots\ldots\ldots\ldots\ldots\ldots (1)$$

Where, y is the predicted response value for this quadratic model with β_0 as the y-intercept and β_j, β_{ij}, and β_{jj} are the regression coefficient of linear, interaction, and quadratic terms, x_j is the processing parameter, k is the number of factors, and ε is the associated error.

When considering the effects of five process parameters associated with the LC process, Eq. (1) can be re- written as:

$$\begin{aligned} y = \beta_0 + \beta_1 * \mathrm{FR} + \beta_2 * \mathrm{LP} + \beta_3 * \mathrm{FL} + \beta_4 * \mathrm{LS} + \beta_5 * CTD + \beta_{12} * \mathrm{FR} * \mathrm{LP} \\ + \beta_{13} * \mathrm{FR} * \mathrm{FL} + \beta_{14} * \mathrm{FR} * \mathrm{LS} + \beta_{15} * \mathrm{FR} * \mathrm{CTD} + \beta_{23} * \mathrm{LP} \\ * \mathrm{FL} + \beta_{24} * \mathrm{LP} * \mathrm{LS} + \beta_{25} * \mathrm{LP} * \mathrm{CTD} + \beta_{34} * \mathrm{FL} * \mathrm{LS} + \beta_{35} \\ * \mathrm{FL} * \mathrm{CTD} + \beta_{45} * \mathrm{LS} * \mathrm{CTD} + \beta_{11} * (\mathrm{FR})^2 + \beta_{22} * (\mathrm{LP})^2 \\ + \beta_{33} * (\mathrm{FL})^2 + \beta_{44} * (\mathrm{LS})^2 + \beta_{55} (\mathrm{CTD})^2 \ldots\ldots\ldots\ldots\ldots\ldots\ldots (2) \end{aligned}$$

Where, FR = Power feed rate; LP = Laser power; FL = Focal length of lens; LS = Laser speed; CTD = Contact tip to workpiece distance.

The multiple regression results were utilized to predict the optimal settings and to create a final model equation for the respective responses as per equation 2.

Results and Discussions

2.3.1 Multiples Regression Analysis

The Analysis of Variance (ANOVA) method was used to trace the significant process parameters and their interactions effect on the predicted responses. The key results for the ANOVA outcomes are presented in Table 2.4. The overall regression model for bead W/H ratio, bead D/W ratio, bead angle, and bead microhardness are found to be significant with an *F*-value of 43.36, 41.17, 32.13, and 65.98 respectively with a P-value of 0.0001. There is only a 0.01% chance that such a large *F*-value could occur due to noise. Usually, values of "Prob > F" being less than 0.05 indicate that the model terms are significant at a 95% confidence level [31].

Table 2. 4 Analysis of Variance (ANOVA) Results for Multiple Responses

Model	Sum of Squares (SS)		Degree of Freedom (df)		Mean Square (MS)		F- Value	p-value	R-Squared value	Adj. R-Sqd. value	Pred. R- Sqd. value
Responses	Regression	Residuals	Regression	Residuals	Regression	Residuals		Prob > F			
Bead W/H Ratio	215.8	17.2	20	69	10.79	0.25	43	0.0001	**0.93**	**0.90**	**0.88**
Bead D/W Ratio	0.22	0.02	20	69	0.01	$2.6x10^{4}$	41	0.0001	**0.92**	**0.90**	**0.87**
Bead Wetting Angle	2515	270.02	20	69	125.8	3.91	32	0.0001	**0.90**	**0.87**	**0.85**
Bead Micro-hardness	$3.6x10^{5}$	18824	20	69	18000	272.8	66	0.0001	**0.95**	**0.94**	**0.92**

The R-Squared values for all the models are between 0.90 and 0.95 (Table 2.4). This means approximately 90-95% of the variability of the response values are accounted for with equation (2). However, to understand how close these data are fitted to the

regression line or how well the quadratic model fits those set of observations, two additional types of R-squared values are calculated: the Adjusted R-squared (between 0.87 - 0.94) and Predicted R-squared values (between 0.85 - 0.91). Both sets of values are in reasonable agreement with each other as the differences between each set of adjusted and predicted R-squared values is less than 0.2 [31]. It is to be noted that the adjusted R-squared provides an unbiased estimate of the population R-squared.

Table 2.5 summarizes the most significant factors in the predictive models. Fig. 2.4 illustrates the significance of the process parameters (linear term) on the predictive responses as per their rank based on the *F*-statistics.

Table 2. 5 Most Significant Factors on the Bead Geometry and Bead Microhardness

Most Significant Factors on the Bead Geometry and Bead Microhardness (Based on ANOVA, *F* - Statistics)												
Ranking # parameters	Bead Geometry									Bead Microhardness		
	W/H Ratio			D/W Ratio			Wetting Angle					
	Linear	Interaction	Quadratic	Linear	Interaction	Quadratic	Linear	Interaction	Quadratic	Linear	Interaction	Quadratic
1	**FR**	**FR***LS	**FR**^2	**FR**	**FR***LS	**FR**^2	**FR**	**FR***LP	**FR**^2	***LS***	FR****LS***	CTD^2
2	**LS**	FL*CTD	CTD^2	**LS**	FL*CTD	CTD^2	**LS**	FL*CTD	CTD^2	FL	LP*FL	LS^2
3	CTD	LS*CTD	LS^2	CTD	LS*CTD	LS^2	LP	LS*CTD	LP^2	FR	LP*CTD	LP^2
4	LP	FR*LP	LP^2	LP	FR*LP	LP^2	CTD	LP*LS	LS^2	LP	FL*CTD	FL^2
5	-	FL*LS	FL^2	-	FL*LS	FL^2	-	-	FL^2	CTD	FL*LS	FR^2

FR - Powder Feed Rate; **LP** - Laser Power; **LS** - Laser Speed; **CTD** - Contact Tip to Workpiece Distance; **FL** - Focal Length of Lens; **W/H** - Width to Height Ratio; **D/W** - Depth of Penetration to Width Ratio.

It is revealed that the FR is the most significant process parameter for the bead aspect ratio and wetting angle, while LS is most significant for the bead microhardness. Similar observations were reported by Farahmand et *al.* [2] and Sun et *al*. [5]. Though the

FL is the most insignificant process parameter for the bead geometric characteristics, it has a significant effect on the bead microhardness. Most interestingly, the LP is found to be less significant despite being a prime input for melting the alloy powder and substrate. It is believed that the melt pool saturation temperature could be attained at a much lower range of power (1000-2500 W). Therefore, more than 2500 kW of LP is a waste and does not have any significant effect [19]. More details on the individual effect of those process parameters and their interactions are discussed in section 3.2.1.

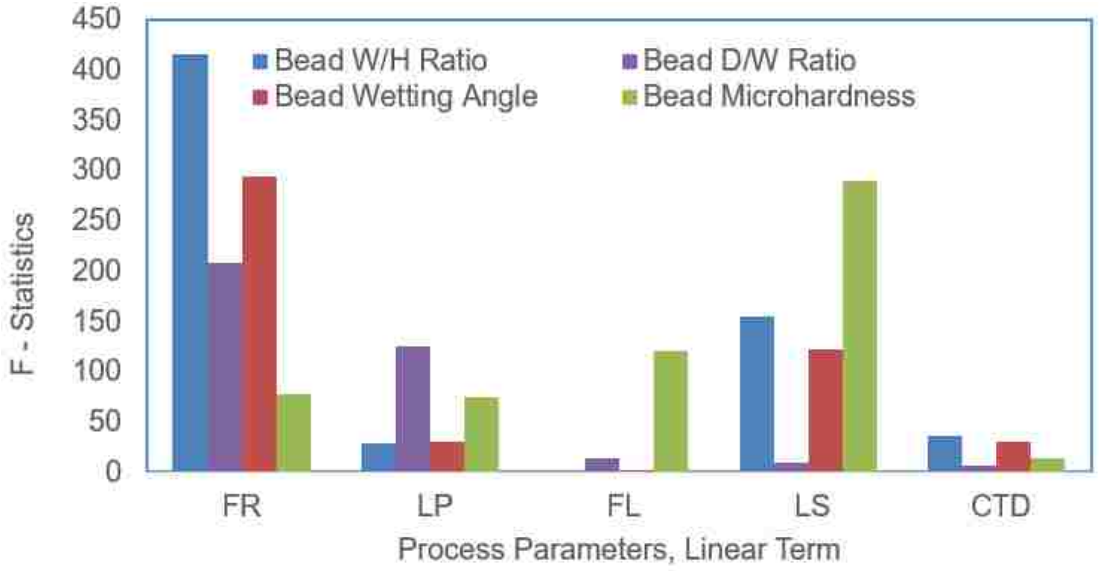

Figure 2. 4 Significance of process parameters on the predicted Bead geometry and bead microhardness.

2.3.2 Development of Predictive Models

Based on the coefficient estimates of RSM multiple regression shown in Table 2.6, the final regression equation for the predictive models of the bead W/H ratio, D/W ratio, bead wetting angle, and bead microhardness are expressed in the equation 3, 4, 5, and 6. These regression coefficients represent the expected change in response variables per unit change in factors when all remaining factors are held constant. The coefficients for each of

the factors indicate the amount of change one could expect in the response output given a one-unit change in the value of that factor at a constant value for all other factors in the model. For example, if FR is considered as a factor, then an increase of 18.51 in the microhardness value for every one-unit increase in FR is expected, keeping all other factors in the model equation 6 constant.

Table 2. 6 Estimated coefficients for complete quadratic models

Coefficients estimate	Response outputs			
	Bead W/H Ratio	Bead D/W Ratio	Bead Wetting Angle	Bead Microhardness
Intercept	4.08	0.0870	26.3	615.53
β_1	-1.2	-0.0280	4	17.14
β_2	0.38	0.0420	-1.5	20.19
β_3	-0.075	-0.0019	0.15	25.61
β_4	0.73	-0.0210	-2.62	33.14
β_5	0.35	-0.0023	-1.26	7.08
β_{12}	0.15	-0.0016	-1.04	8.58
β_{13}	-0.083	0.0025	0.12	13.25
β_{14}	-0.5	0.0086	0.51	-16.67
β_{15}	0.033	-0.0029	-0.45	5.46
β_{23}	-0.094	-0.0050	0.43	-15.83
β_{24}	-0.1	-0.0014	0.87	-0.83
β_{25}	0.13	-0.0070	-0.45	15.46
β_{34}	0.15	-0.0014	-0.51	14.08
β_{35}	-0.22	-0.0035	0.94	-15.21
β_{45}	-0.15	0.0062	0.89	-11.46
β_{11}	0.53	0.0030	-1.27	8.13
β_{22}	0.28	0.0061	-1.2	-19.11
β_{33}	0.19	-0.0037	-0.69	19.01
β_{44}	0.23	0.0039	-0.75	17.8
β_{55}	0.28	0.0044	-1.25	31.76

$$Bead\ \frac{W}{H}\ Ratio = 4.08 - 1.2 * FR + 0.38 * LP - 0.075 * FL + 0.73 * LS + 0.35 * CTD + 0.15 * FR * LP - 0.083 * FR * FL - 0.5 * FR * LS + 0.033 * FR * CTD - 0.094 * LP * FL - 0.1 * LP * LS + 0.13 * LP * CTD + 0.15 * FL * LS - 0.22 * FL * CTD - 0.15 * LS * CTD + 0.53 * (\mathrm{FR})^2 + 0.28 * (\mathrm{LP})^2 + 0.19 * (\mathrm{FL})^2 + 0.23 * (\mathrm{LS})^2 + 0.28 * (\mathrm{CTD})^2 \quad \text{.....(3)}$$

$$Bead\ \frac{D}{W}\ Ratio = 0.087 - 0.028 * FR + 0.042 * LP - 1.9 \times 10^{-3} * FL - 0.021 * LS - 2.35 \times 10^{-3} * CTD - 1.59 \times 10^{-3} * FR * LP + 2.55 \times 10^{-3} * FR * FL + 8.61 \times 10^{-3} * FR * LS - 2.89 \times 10^{-3} * FR * CTD - 5.04 \times 10^{-3} * LP * FL - 1.38 \times 10^{-3} * LP * LS - 7.0 \times 10^{-3} * LP * CTD - 1.44 \times 10^{-3} * FL * LS - 3.46 \times 10^{-3} * FL * CTD + 6.23 \times 10^{-3} * LS * CTD + 3.02 \times 10^{-3} * (\mathrm{FR})^2 + 6.1 \times 10^{-3} * (\mathrm{LP})^2 - 3.74 \times 10^{-3} * (\mathrm{FL})^2 + 3.89 \times 10^{-3} * (\mathrm{LS})^2 + 4.37 \times 10^{-3} * (\mathrm{CTD})^2 \quad \text{.....(4)}$$

$$Bead\ Wetting\ Angle = 26.3 + 4.0 * FR - 1.5 * LP + 0.15 * FL - 2.62 * LS - 1.26 * CTD - 1.04 * FR * LP + 0.12 * FR * FL + 0.51 * FR * LS - 0.45 * FR * CTD + 0.43 * LP * FL + 0.87 * LP * LS - 0.45 * LP * CTD - 0.51 * FL * LS + 0.94 * FL * CTD + 0.89 * LS * CTD - 1.27 * (\mathrm{FR})^2 - 1.2 * (\mathrm{LP})^2 - 0.69 * (\mathrm{FL})^2 - 0.75 * (\mathrm{LS})^2 - 1.25 * (\mathrm{CTD})^2 \quad \text{.....(5)}$$

$$Microhardness = 620.36 + 18.51 * FR + 2.88 * LP + 23.85 * FL + 31.76 * LS + 8.46 * CTD + 10.65 * FR * LP + 11.19 * FR * FL - 18.73 * FR * LS + 7.52 * FR * CTD - 17.90 * LP * FL - 2.90 * LP * LS + 17.52 * LP * CTD + 16.15 * FL * LS - 17.27 * FL * CTD - 13.52 * LS * CTD + 3.31 * (\mathrm{FR})^2 + 4.10 * (\mathrm{LP})^2 + 14.77 * (\mathrm{FL})^2 + 12.97 * (\mathrm{LS})^2 + 26.93 * (\mathrm{CTD})^2 \quad \text{.....(6)}$$

2.3.3 Validation of the Developed Models

Fig. 2.5 shows the residuals vs. predicted values of the multiple regression for all models. There is no strong curvature or clusters or unequal variation observed in the

distribution of data that may indicate problems with the regression models. Data points fall randomly on both sides of the zero line. No outlier residuals are observed outside of the two red lines. This indicates that there is no problem with the residuals and predicted responses. Since the number of data points were large, and the residuals are normally distributed, the significant relationship between the process parameters and the output responses indicated by the p-value is accurate.

Based on the Equations 3-6, the predicted value of the bead W/H ratio, D/W ratio, bead wetting angle, and bead microhardness are calculated for the coded value of the process parameters and depicted in Fig. 2.6. These graphs illustrate that the models are well fitted with the experimental and regression results. For instance, 100% of the predicted microhardness values are found within a 0±4% error, where, 80% response is within a 0±2% error. Similarly, 83% of the predicted response of bead aspect ratio is found to be within a ±10% error.

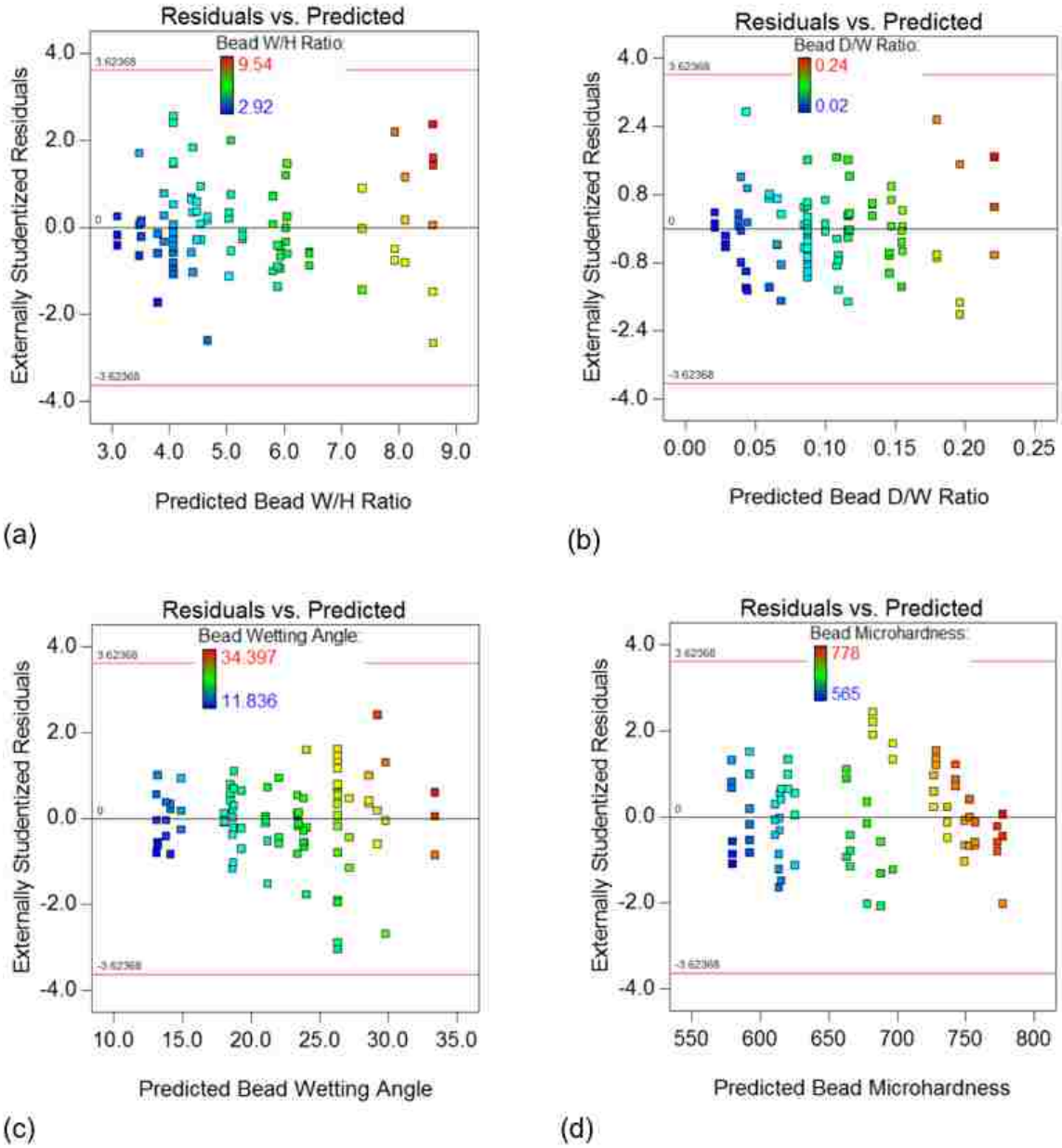

Figure 2. 5 Residual vs. predicted value of data points.

2.3.4 Relative Effects of the Process Parameters on the Predictive Responses

The determination of the relative effects of the process variables is an important aspect of multiple regression analysis. The relative importance and the relative effects of the main process parameters (factors) and their interactions are ranked based on their

respective *F*-statistics (Table 2.5). Since *F*-statistics measures the variations of the sum of squares, more variations come from the more sensitive or more significant factors [32]. However, *F*-statistics cannot illustrate the effect of individual process parameters and their interaction on the response outputs. Therefore, perturbation plots are created to explain the relative effect of the individual process parameters, while 2D contour plots and 3D surface plots are created to explain the interactions of those process parameters on the response outputs.

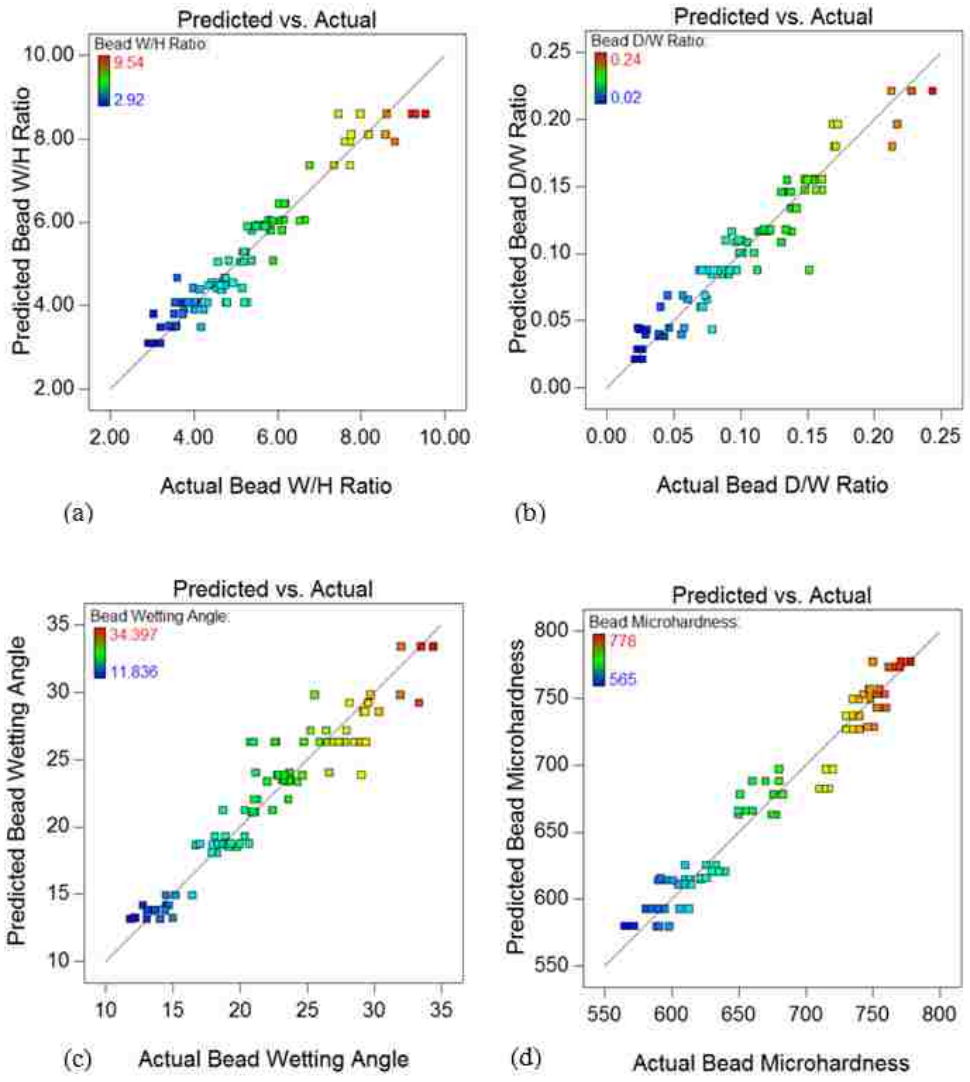

Figure 2. 6 Actual value vs. predicted value of bead characteristics and bead microhardness.

2.3.5 Individual Effect Analyses

Fig. 2.4 illustrates the relative importance and significance level of the individual process parameters on the respective predictive responses. However, their detailed effects are illustrated by the perturbation plots shown in Fig. 2.7. These plots also compare the significant effects of all the factors at a particular point in the design space for their respective models. The predicted responses are plotted against the coded factors by changing only one factor over its range while holding all the other factors constant. The reference point is set to the experimental configuration midpoint.

In Fig. 2.7, the curves AA (FR), BB (LP), DD (LS), and EE (CTD) have large curvatures, which indicates that the related process parameters are very sensitive to the respective response in their respective model. The curve CC (FL) shows a relatively flat line in Fig. 2.7 a, b, c indicating that the FL is truly insensitive to its respective responses. The curve EE also shows a flat line in Fig. 2.7b indicating its (factor CTD) insensitivity to the D/W ratio.

Fig. 2.7a and 2.7b show that the FR curve AA has the highest negative effect on the bead W/H and D/W ratios compared to any other factors. However, the FR has the highest positive effect on the bead wetting angle, as shown in Fig. 2.7c, which is logical. The AA curve in Fig. 2.7d shows that FR has a mild positive effect on the bead microhardness.

Fig. 2.7b shows that the LP curve BB has the highest positive effect on the D/W ratio, which is realistic as more laser power will increase the penetration depth. The LP (curve BB) also shows the mild effect on the bead W/H ratio (Fig. 2.7a) and a mildly

negative effect on the bead wetting angle (Fig. 2.7c). Curve BB has a shallow convex shape for the bead microhardness in Fig. 2.7d, so its influence is situation dependent.

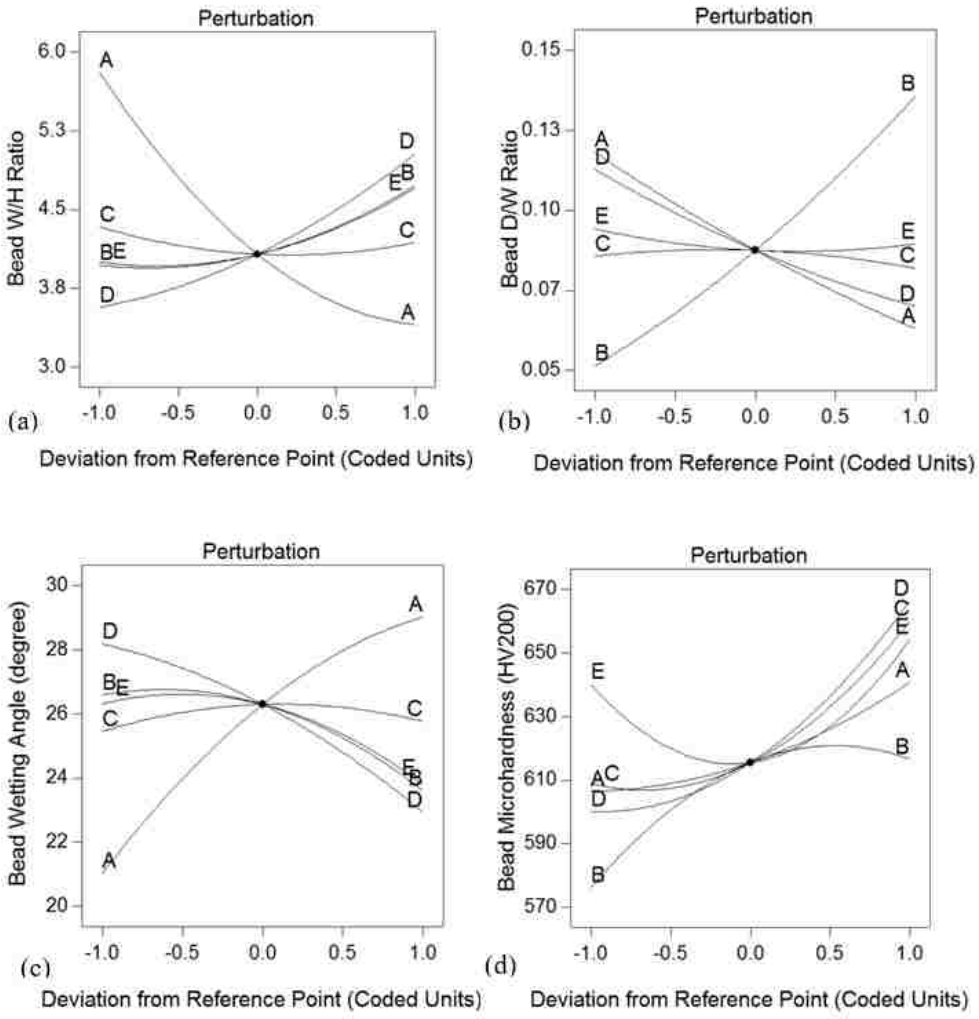

Figure 2. 7 Perturbation plots showing the effect of all processing parameters on the predicted responses. (Curves AA, BB, CC, DD, and EE represent FR, LP, FL, LS, and CTD respectively)

The curve DD in Fig. 2.7d shows that the LS has a very positive effect on the bead microhardness. Interestingly, this finding is strongly supported by the earlier study done by the current authors [21],[33] using different analysis techniques. It was found that at a higher laser speed, a higher residual stress generated due to higher cooling rate during solidification of the laser-cladded sample. Consequently, a very fine martensitic matrix

along with eutectic delta ferrite and carbide phases (e.g., $Cr_{23}C_6$) contributed to the higher hardness in the bead zone [33].

The curve DD in Fig. 2.7a shows that the LS has a positive effect on the bead W/H ratio. However, it has a negative effect on the D/W ratio (Fig. 2.7b) and the bead wetting angle (Fig. 2.7c). On the other hand, it is observed that the FL curve CC does not show any significant effect on the bead geometry (W/H ratio, D/W ratio, and bead wetting angle), but there is a concave curve for the bead microhardness (Fig. 2.7d). Similar to the LP, this parameter's influence is situation dependent.

The curve EE shows that CTD has a positive effect on the bead W/H ratio (Fig. 2.7a) while a negative effect on the bead wetting angle (Fig. 2.7c). However, it does not show a significant effect on the D/W ratio despite showing both positive and negative effects on the bead microhardness. The trends observed in all those curves are elaborated in section 3.2.3

2.3.6 Two-factors Interaction Effect Analyses

Selected two-factor interaction effects are depicted in the 2D contour plots and 3D surface mapping plots in Figs. 2.8-2.17. The plots are non-linear and asymmetric and include saddle surfaces. There is a strong interaction effect of FR and LS on the bead W/H ratio (Fig. 2.8) and a moderate interaction effect of FL and CTD on the same response output (Fig. 2.9). Both figures illustrate an asymmetric concave response surface. The FR influence on the D/W ratio depends on the LS (Fig. 2.10). Both the magnitude and direction are in variety, as can be seen by the surface twist. The influence of the LP has also impacted the CTD values. The smaller the CTD value (a shorter distance) and the higher the power, the greater the D/W ratio, which is realistic. The interaction effects of the FR and LP; and

FL and CTD on the bead wetting angle generates convex surfaces (Fig. 2.12, Fig. 2.13). Noticeable asymmetry can be observed with the FR and LP relationships.

The two-factor relationships for the microhardness are more complex. In Fig. 2.14, at the minimum FR and LS values, the lowest hardness results. Changing either or both increases the hardness. A saddle surface is generated when evaluating the LP and FL, and the LP and CTD (Figs. 2.15 – 2. 16). Fig. 2.15 shows that bead microhardness increases at a higher FL with a medium LP setting and decreases at the interaction of both at their lower values, while Fig. 2.16 shows that microhardness increases at both extremely high and extremely low value of LP and CTD compared to the average central value. These surfaces clearly illustrate the difficulty in developing predictive models that can capture the process variation effects. For the FL and CTD interaction, a concave surface, with limited asymmetry, is generated. The contours of the predicted response are almost concentric circles. The predicted bead microhardness is found unchanged in an increasing manner as the interaction of the FL and CTD is rotated about the center (0,0). This rotatability is a rational basis for the selection of a response surface design [3].

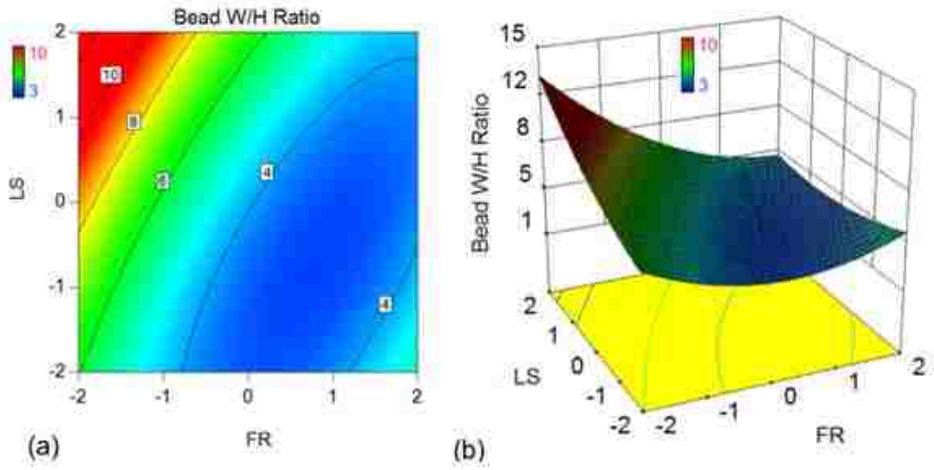

Figure 2. 8 (a) 2D contour plot and (b) 3D response surface plot show the interaction effect of powder flow rate (FR) and laser speed (LS) on the bead width to height ratio.

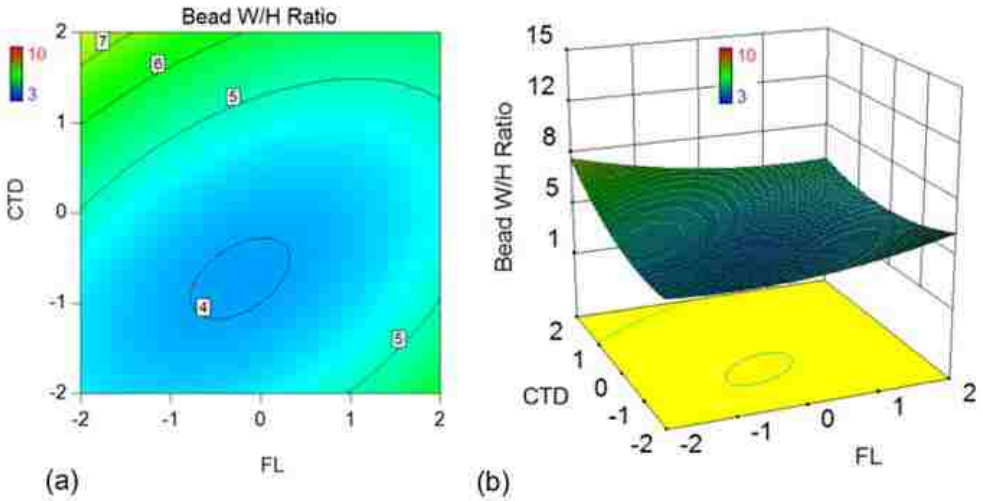

Figure 2. 9 (a) 2D contour plot and (b) 3D response surface plot show the interaction effect of focal length of the lens (FL) and contact tip to workpiece distance (CTD) on the bead width to height ratio.

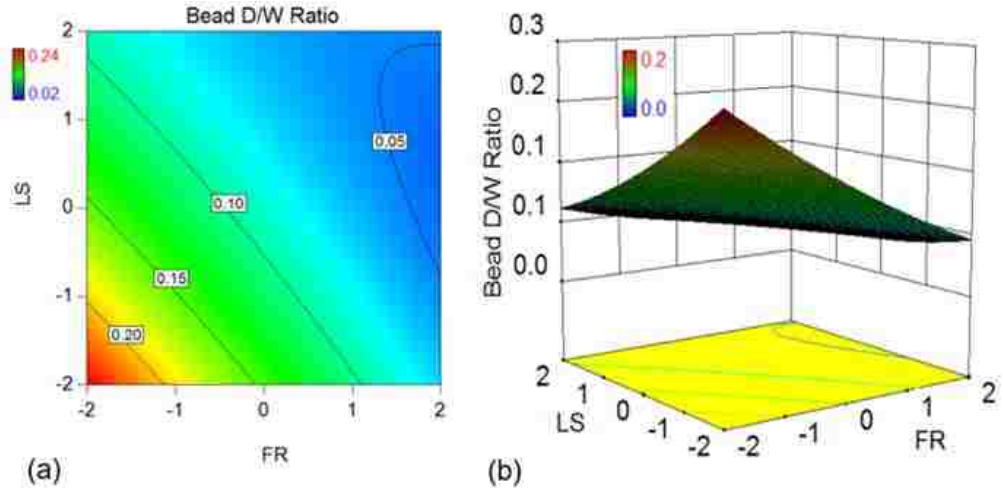

Figure 2. 10 (a) 2D contour plot and (b) 3D response surface plot show the interaction effect of powder flow rate (FR) and laser speed (LS) on the depth of penetration to bead width ratio.

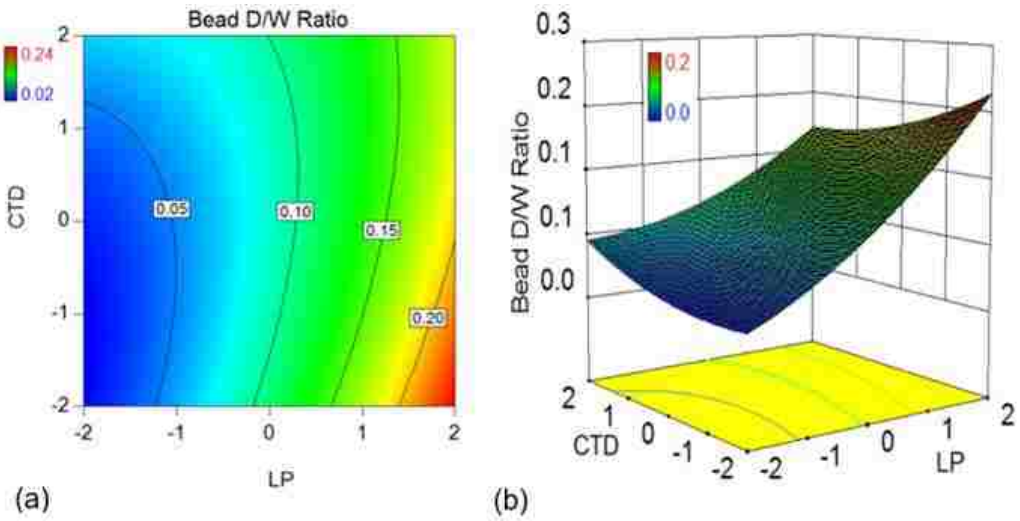

Figure 2. 11 (a) 2D contour plot and (b) 3D response surface plot show the interaction effect of laser power (LP) and contact tip to work distance (CTD) on the depth of penetration to bead width ratio.

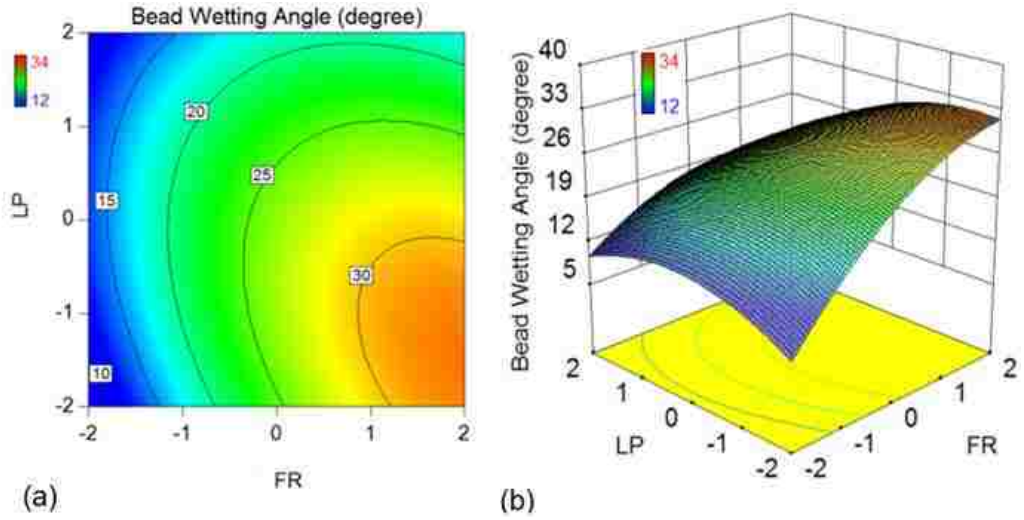

Figure 2. 12 (a) 2D contour plot and (b) 3D response surface plot show the interaction effect of powder flow rate (FR) and laser power (LP) on the bead wetting angle.

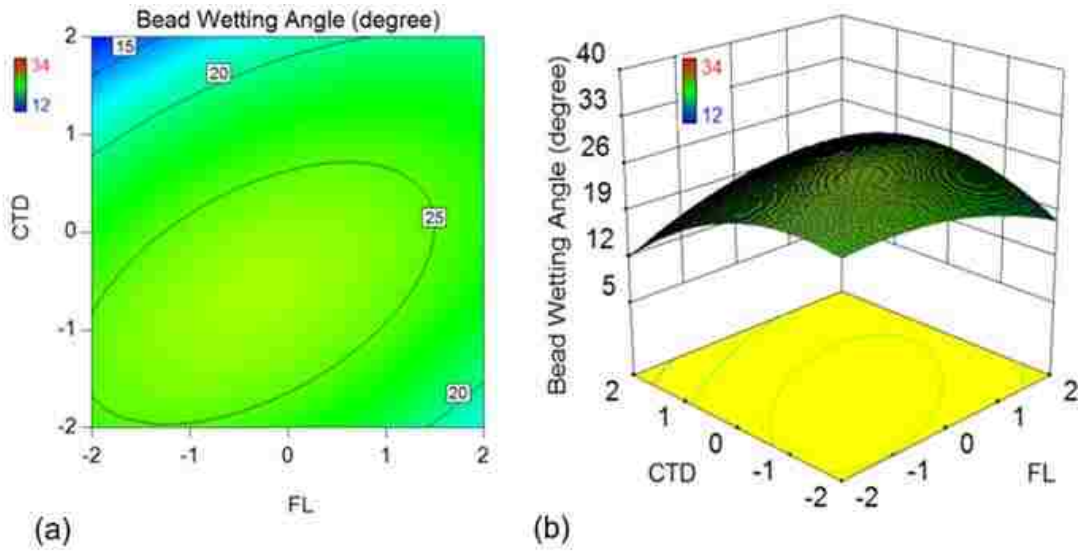

Figure 2. 13 (a) 2D contour plot and (b) 3D response surface plot show the interaction effect of focal length of the lens (FL) and contact tip to work distance (CTD) on the bead wetting angle.

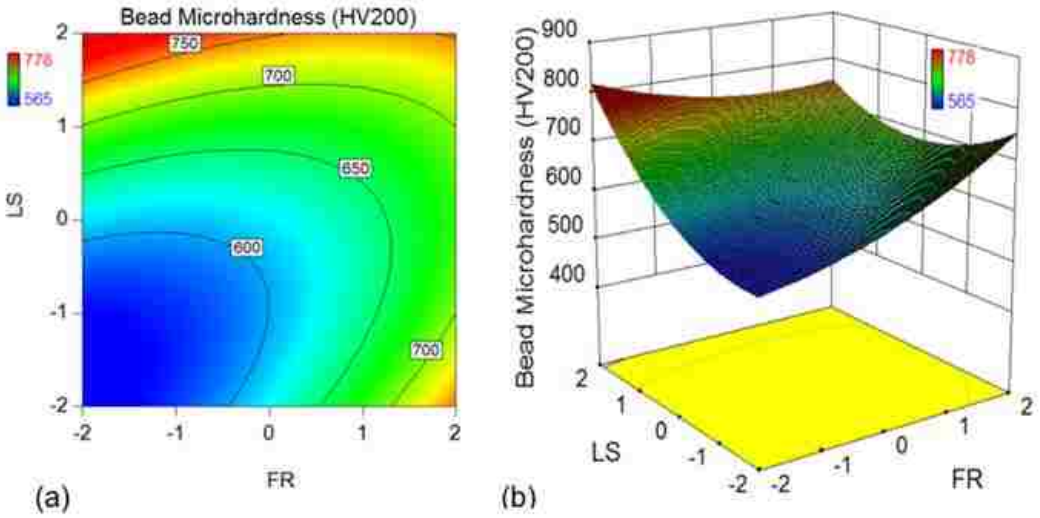

Figure 2. 14 (a) 2D contour plot and (b) 3D response surface plot show the interaction effect of powder flow rate (FR) and laser speed (LS) on the bead microhardness.

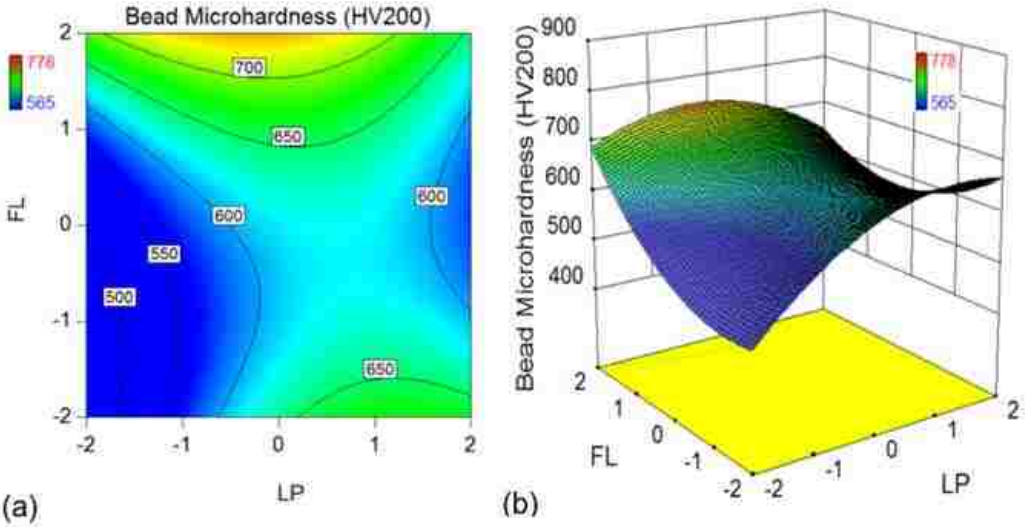

Figure 2. 15 (a) 2D contour plot and (b) 3D response surface plot show the interaction effect of laser powder (LP) and focal length of the lens (FL) on the bead microhardness.

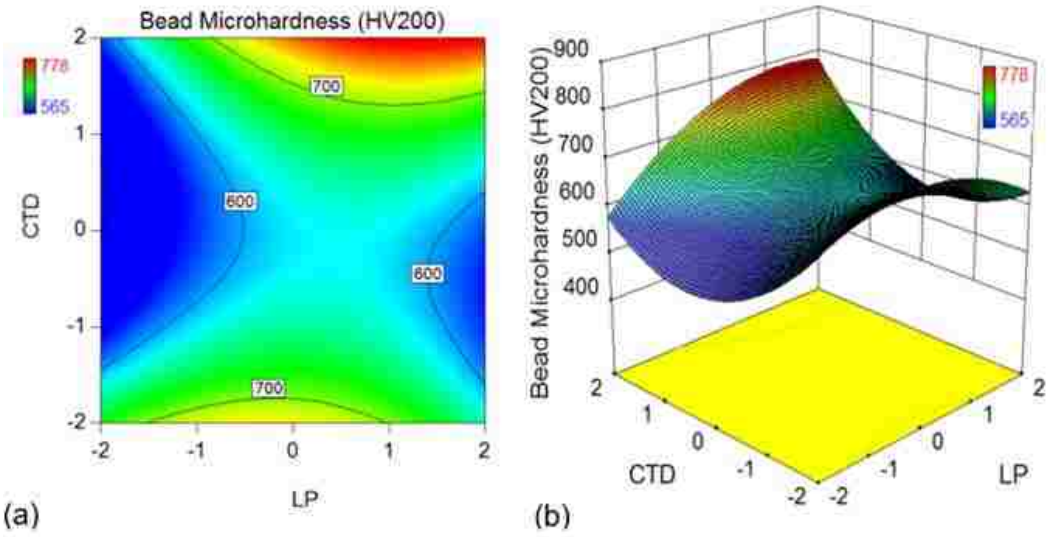

Figure 2. 16 (a) 2D contour plot and (b) 3D response surface plot show the interaction effect of laser powder (LP) and contact tip to work distance (CTD) on the bead microhardness.

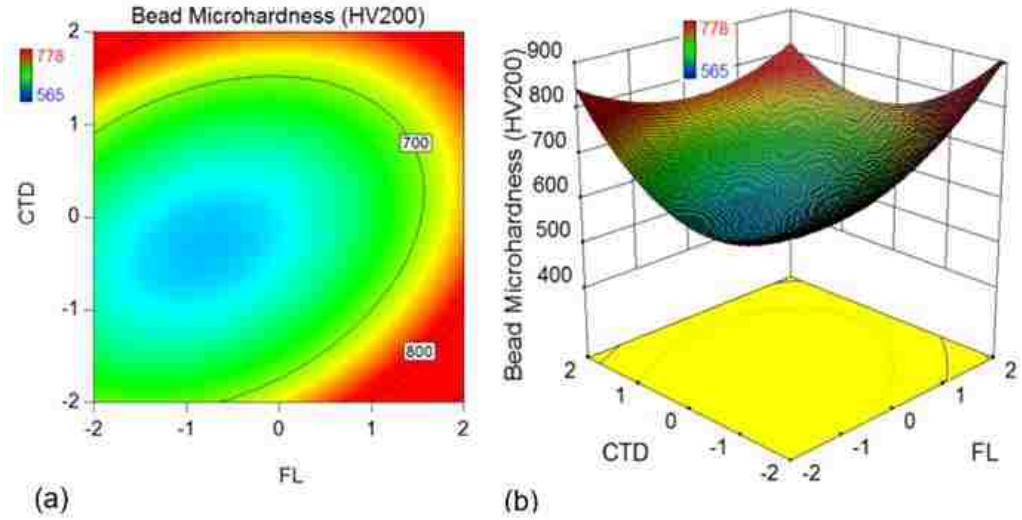

Figure 2. 17 (a) 2D contour plot and (b) 3D response surface plot show the interaction effect of focal length of lens (FL) and contact tip to workpiece distance (CTD) on the bead microhardness.

2.3.7 Quadratic Effect Analyses

The perturbation plots, as well as the contour and surface plots, are used to portray the actual quadratic effect by adding significance level of curvature on the individual curve and 2FI surfaces.

As can be seen in Fig. 2.7d, the curve EE (relating to factor CTD) has the highest curvature compare to all other factors on the respective responses showing the highest quadratic effect of CTD on the bead microhardness. On the other hand, the curve CC (relating to factor FL) is found to be relatively flat in Figs. 2.7 a, b, and c, which indicates that the FL has the least quadratic effect on the D/W ratio (Fig. 2.7b), W/H ratio (Fig. 2.7a) and bead wetting angle (Fig. 2.7c). Interestingly, all factors show a concave relationship with the bead W/H ratio (Fig. 2.7a), a convex relationship with the bead wetting angle (Fig. 2.7c), a combination of concave & convex relationship with the bead microhardness (Fig. 2.7d), and a combination of concave, convex and almost flat (least quadratic effect) relationship with the D/W ratio (Fig. 2.7b). These trends are summarized in Table 2.7.

Table 2. 7 Quadratic Effect of Process Parameters on the Bead Characteristics

Process Parameter	Related Curve (Fig. 2.7)	Quadratic/ Curvature (Type, magnitude and slope) Effect of Process Parameters on the Bead Characteristics			
		W/H Ratio	D/W Ratio	Wetting Angle	Microhardness
FR	**AA**	C, Steep, -ve	Flat, Steep, -ve	VX, Steep, +ve	C, Shallow, +ve
LP	**BB**	C, Shallow, +ve	Flat, Steep, +ve	VX, Shallow, -ve	VX, Steep, +ve
FL	**CC**	C, Shallow, ±ve	VX, Shallow, ±ve	VX, Shallow, ±ve	C, Steep, +ve
LS	**DD**	C, Shallow, +ve	Flat, Steep, -ve	VX, Shallow, -ve	C, Steep, +ve
CTD	**EE**	C, Shallow, +ve	C, Shallow, ±ve	VX, Shallow, -ve	C, Steep, ±ve

C - Concave, **VX** - Convex, **+ve** - Positive, **-ve** – negative, **±ve** - positive/negative

Similarly, when those quadratic effects are applied on the 2D contour plots and 3D surface plots, they may create a minimum, maximum, or a saddle point response surface. However, sometimes, there are variations from the pure minimum, maximum, or saddle point response surfaces. In those cases, quadratic effect indicates a rising ridge or a falling ridge systems [34]. Figs. 2.8, 2.9, and 2.17 illustrate a response surface with a minimum, Fig. 2.13 shows a maximum and Figs. 2.15 - 2.16 illustrate surfaces with a saddle point. On the other hand, Figs. 2.10, 2.11, 2.12, and 2.14 deviate from the pure minimum or maximum surface, thus created a falling ridge (Fig. 2.10) and rising ridge systems (Figs. 2.11-2.12, 2.14). These plot shapes are summarized in Table 2.8.

In all cases, the factors with high quadratic effect facilitate to locate the optimum predicted response or a stationary point with reasonable precision by characterizing the shape of the surface [3].

Table 2. 8 Quadratic Effect of Two Factor Interactions on the Bead Characteristics

Two Factor interactions	Quadratic/ Curvature (Type, magnitude) Effect of Two Factor Interactions on the Bead Characteristics			
	W/H Ratio	D/W Ratio	Wetting Angle	Microhardness
FR*LS	Concave, Minimum (Fig. 2.8)	Concave, Falling Ridge (Fig. 2.10)	--	Concave, Rising Ridge (Fig. 2.14)
FL*CTD	Concave, Minimum (Fig. 2.9)	-	Convex, Maximum (Fig. 2.13)	Concave, Minimum (Fig. 2.17)
LP*CTD	-	Concave, Rising Ridge (Fig. 2.11)	-	Twist, Saddle (Fig. 2.16)
FR*LP	-	-	Convex, Rising Ridge (Fig. 2.12)	-
LP*FL	-	-	-	Twist, Saddle (Fig. 2.15)

2.3.8 Process Planning Challenges

The complex, highly coupled characteristics associated with laser cladding have been highlighted in these predictive modeling analyses. The parameters that have a great influence on hardness have a lesser influence on the bead geometry, but all process parameters and several interactions are statistically significant. For example, if a process planner desired a 4 ±0.1 mm bead width, with a minimum 0.7 mm bead height (features readily measurable for real-time feedback control), there is a wide array of process settings that can generate the required geometry. There are five inputs (four inputs are controllable, and one input is a setup parameter – the focal length) and three geometric output requirements. A sample of experimental settings that provide a geometric solution is shown in Table 2.9. It can be seen that there is a wide range of settings for each parameter.

Table 2.9 Experimental Settings and Measured Bead Geometry for a 4±0.1 mm Bead Width

FR	LP	FL	LS	CTD	Width (mm)	Height (mm)	Depth (mm)	W/H Ratio	D/W Ratio
25	3	390	12.5	22	3.9	0.9	0.4	4.33	0.10
25	2	410	7.5	24	3.9	0.9	0.3	4.33	0.08
20	2.5	400	15	23	4.0	0.7	0.2	5.71	0.05
15	2	410	7.5	22	4.0	0.8	0.5	5.00	0.13
20	2.5	400	10	25	4.0	0.8	0.4	5.00	0.10
20	2.5	400	10	23	4.1	1.1	0.3	3.73	0.07
Average					4.0	0.8	0.3	4.68	0.09

FR - Powder Feed Rate; **LP** - Laser Power; **LS** - Laser Speed; **CTD** - Contact Tip to Workpiece Distance; **FL** - Focal Length of Lens; **W/H** - Width to Height Ratio; **D/W** - Depth of Penetration to Width Ratio.

However, from equation 6, the predicted bead hardness indicates that the hardness can vary between 616 – 757 HV200. This is a wide range of hardness values, and as there is an empirical relationship between hardness and ultimate tensile strength [22,23,35], there will be an impact on the mechanical properties of the clad. Establishing a threshold range for the desired hardness as well as the bead aspect ratios, can provide constraints assist in selecting optimal settings that will result in desired geometry and functional characteristics.

Summary and Conclusions

Selecting process settings to fabricate a laser clad bead, which has the desired geometry and mechanical properties, is a challenge. Consequently, a structured experimental approach was taken to investigate relationships and develop predictive models. To minimize experiments, a response surface methodology (RSM) study, using a central composite design (CCD), for predicting bead geometry and bead microhardness characteristics for laser cladded AISI 420 stainless-steel single-track beads has revealed important relationships among the process parameters and the response outputs. Predictive models for the bead geometry (W/H ratio, D/W ratio, bead wetting angle), and the bead microhardness are developed using the RSM regression analysis. The statistical significance of the individual process parameters, their two-factor interactions, and quadratic effects on the predicted response output are analyzed using the *F*-statistics, perturbation plots, 2D contour plots, and 3D surface plots. While *F*-statistics can identify the relative importance of the factors over the others on the predictive response, it cannot quantify the effects whether happened in a positive or negative way. That limitation of *F*-statistics can overcome by using perturbation plots. Perturbation plots can identify and quantify both the positive and negative effects of the linear factors on the respective

predictive responses. However, a perturbation plot cannot show the interaction effect of the process parameters. 2D contour plots and 3D surface plots are employed to interpret the two-factor interaction effect keeping the other factors constant at reference level (coded 0) where the quadratic effects are reflected, indicating the trends of curvature in the response values. Based on the performed RSM multiple regression and ANOVA results, the following conclusions can be drawn:

1. The RSM analysis with a CCD approach is found to be a very efficient methodology to develop a robust prediction model using multiple process parameters for the bead aspect ratios, wetting angle, and the bead microhardness.

2. The ANOVA results for the R-squared values, the predicted R-Squared, and the adjusted R-square values show that the regression models are significantly fitted with the data for a wide range of process settings. Therefore, a general model with a database of coefficients can be used to select process parameters and/or predict results for the bead geometry characteristics and hardness with confidence.

3. The FR and LS are found to be the most significant process parameters on the bead geometry characteristics and the bead microhardness, respectively. Consequently, selecting process parameters to generate a bead geometry only may lead to undesirable hardness results.

4. The interaction of the FR and LS has the most significant effect on the bead aspect ratios and bead microhardness, while the interaction of the FR and LP has the most significant effect on the bead wetting angle. The interaction of the FR and FL has the most insignificant effect on the predicted bead geometry. However, this

interaction factor is still significant for the bead microhardness. The interaction of the LP and LS had the most insignificant effect on the predicted bead microhardness though this factor is still significant for the bead aspect ratio. Therefore, a very intriguing and complex relationship is observed within the process parameters and their interactions on the predicted bead geometry and bead microhardness. This analysis illustrates the difficulty in generating optimal solutions.

5. The CTD has the highest quadratic effect on the bead microhardness, followed by LS. The FR has the highest quadratic effect on the bead geometry despite having the least effect on the bead microhardness. The FL has the least quadratic effect on the responses except for the bead microhardness. The quadratic effects of those process parameters add significant curvature on the contour plots as well as identify a minimum, maximum, or a saddle point and ridge (rising ridge or a falling ridge) systems on the response surfaces of their respective 2D contour plots and 3D surface plots; therefore, simplified and linearized models cannot effectively predict solutions unless the range of process settings is narrow.

6. The 83% of the predicted response of the bead aspect ratios are found to be within ±10% error. However, 100% of the predicted responses for the bead microhardness are found to be within the ±4% error against the actual microhardness. Hence, these

predictive model structures are found to be representative for a wide range of settings for laser cladding of AISI 420 stainless steel.

7. Due to the observed non-linear results, more experimental data needs to be collected to expand the models for overlapping and stacked beads for the laser cladding process.

This research will be expanded upon using the experimental approaches described in this work, to consider evaluating the hardness and geometric characteristics for overlapping, and multi-layer deposition scenarios. Also, the influence of the process parameters on the resultant residual stresses will be analyzed. This research will provide a foundation for optimization models for process planners to develop an optimal fabrication strategy.

References

[1] F. Lepski, D., Bruckner, Laser cladding, in: J. Dowden (Ed.), Theory Laser Mater. Process., Online, Springer Netherlands, 2009: pp. 235–279. doi:10.2351/1.521888.

[2] P. Farahmand, R. Kovacevic, Parametric Study and Multi-Criteria Optimization in Laser Cladding by a High Power Direct Diode Laser, Lasers Manuf. Mater. Process. (2014) 1–20. doi:10.1007/s40516-014-0001-0.

[3] D.C. Montgomery, Design and Analysis of Experiments, 2012. doi:10.1198/tech.2006.s372.

[4] R.J. Urbanic, R.W. Hedrick, C.G. Burford, A process planning framework and virtual representation for bead-based additive manufacturing processes, Int. J. Adv. Manuf. Technol. 90 (2017) 361–376. doi:10.1007/s00170-016-9392-8.

[5] Y. Sun, M. Hao, Statistical analysis and optimization of process parameters in Ti6Al4V laser cladding using Nd:YAG laser, Opt. Lasers Eng. 50 (2012) 985–995. doi:10.1016/j.optlaseng.2012.01.018.

[6] S. Saqib, R.J. Urbanic, K. Aggarwal, Analysis of laser cladding bead morphology for developing additive manufacturing travel paths, Procedia CIRP. 17 (2014) 824–829. doi:10.1016/j.procir.2014.01.098.

[7] K.Y. Benyounis, A.G. Olabi, Optimization of different welding processes using statistical and numerical approaches - A reference guide, Adv. Eng. Softw. 39 (2008) 483–496. doi:10.1016/j.advengsoft.2007.03.012.

[8] R.J. Urbanic, S.M. Saqib, K. Aggarwal, Using Predictive Modeling and Classification Methods for Single and Overlapping Bead Laser Cladding to Understand Bead Geometry to Process Parameter Relationships, J. Manuf. Sci. Eng. 138 (2016) 051012. doi:10.1115/1.4032117.

[9] G.C. Onwubolu, J.P. Davim, C. Oliveira, A. Cardoso, Prediction of clad angle in laser cladding by powder using response surface methodology and scatter search, Opt. Laser Technol. 39 (2007) 1130–1134. doi:10.1016/j.optlastec.2006.09.008.

[10] S. Liu, R. Kovacevic, Statistical analysis and optimization of processing parameters in high-power direct diode laser cladding, Int. J. Adv. Manuf. Technol. 74 (2014)

867–878. doi:10.1007/s00170-014-6041-y.

[11] K. Aggarwal, Investigation of Laser Clad Bead Geometry to Process Parameter Settings for Effective Parameter Selection, Simulation, and Optimization -MASc Thesis, University of Windsor, 2014.

[12] and L.A. Kush Aggarwal, Ruth Urbanic, A Methodology for Investigating and Modelling Laser Clad Bead Geometry and Process Parameter Relationships, SAE Int. 7 (2014) 269–279.

[13] S. Mondal, C.P. Paul, L.M. Kukreja, A. Bandyopadhyay, P.K. Pal, Application of Taguchi-based gray relational analysis for evaluating the optimal laser cladding parameters for AISI1040 steel plane surface, Int. J. Adv. Manuf. Technol. 66 (2012) 91–96. doi:10.1007/s00170-012-4308-8.

[14] I.F. Ituarte, E. Coatanea, M. Salmi, J. Tuomi, J. Partanen, Additive Manufacturing in Production: A Study Case Applying Technical Requirements, Phys. Procedia. 78 (2015) 357–366. doi:10.1016/j.phpro.2015.11.050.

[15] J. Dutta Majumdar, I. Manna, Laser material processing, Int. Mater. Rev. 56 (2011) 341–388. doi:10.1179/1743280411Y.0000000003.

[16] Z. Zhu, V.G. Dhokia, a. Nassehi, S.T. Newman, A review of hybrid manufacturing processes – state of the art and future perspectives, Int. J. Comput. Integr. Manuf. 26 (2013) 596–615. doi:10.1080/0951192X.2012.749530.

[17] H.K. Lee, Effects of the cladding parameters on the deposition efficiency in pulsed

Nd:YAG laser cladding, J. Mater. Process. Technol. 202 (2008) 321–327. doi:10.1016/j.jmatprotec.2007.09.024.

[18] B. Graf, S. Ammer, A. Gumenyuk, M. Rethmeier, Design of experiments for laser metal deposition in maintenance, repair and overhaul applications, Procedia CIRP. 11 (2013) 245–248. doi:10.1016/j.procir.2013.07.031.

[19] M.K. Alam, N. Nazemi, R.J. Urbanic, S. Saqib, A. Edrisy, Investigating Process Parameters and Microhardness Predictive Modeling Approaches for Single Bead 420 Stainless Steel Laser Cladding, SAE Int. (2017) 1–10. doi:10.4271/2017-01-0283.Copyright.

[20] S.H. Baghjari, S. A. A. Akbari Mousavi, Effects of pulsed Nd:YAG laser welding parameters and subsequent post-weld heat treatment on microstructure and hardness of AISI 420 stainless steel, Mater. Des. 43 (2013) 1–9. doi:10.1016/j.matdes.2012.06.027.

[21] M.K. Alam, J. Urbanic, S.M. Saqib, A. Edrisy, Effect of Process Parameters On The Microstructural Evolutions of Laser Cladded 420 Martensitic Stainless Steel, in: Mater. Sci. Technol. Conf. Proc. (MS&T15), Oct. 4-8, Columbus, Ohio, USA, 2015: pp. 35–54.

[22] P. Zhang, S.X. Li, Z.F. Zhang, General relationship between strength and hardness, Mater. Sci. Eng. A. 529 (2011) 62–73. doi:10.1016/j.msea.2011.08.061.

[23] J. Datsko, L. Hartwig, B. Mcclory, On the Tensile Strength and Hardness Relation for Metals, J. Mater. Eng. Perform. 10 (2001) 718–722.

doi:10.1361/105994901770344601.

[24] S.M. Saqib, Experimental Investigation of Laser Cladding Bead Morphology and Process Parameter Relationship for Additive Manufacturing Process Characterization - PhD Dissertation, University of Windsor, 2016.

[25] E. Weidmann, Struers Application Notes - Metallographic Preparation of Stainless Steel, (2005). doi:01.05 / 62140005.

[26] N. Nazemi, J. Urbanic, M.K. Alam, Hardness and residual stress modeling of powder injection laser cladding of P420 coating on AISI 1018 substrate, Int. J. Adv. Manuf. Technol. (2017).

[27] N. Nazemi, J. Urbanic, A Finite Element Analysis for Thermal Analysis of Laser Cladding of Mild Steel with P420 Steel Powder, in: Proc. ASME 2016 Int. Mech. Eng. Congr. Expo. IMECE2016 - Novemb. 11-17, 2016, Phoenix, Arizona, USA, n.d.: pp. 1–10.

[28] N. Nazemi, M.K. Alam, R.J. Urbanic, S. Saqib, A. Edrisy, A Hardness Study on Laser Cladded Surfaces for a Selected Bead Overlap Conditions, SAE Int. (2017). doi:10.4271/2017-01-0285.Copyright.

[29] E. Toyserkani, A. Khajepour, S. Corbin, 3-D finite element modeling of laser cladding by powder injection: Effects of laser pulse shaping on the process, Opt. Lasers Eng. 41 (2004) 849–867. doi:10.1016/S0143-8166(03)00063-0.

[30] Y. Fu, A. Loredo, B. Martin, A.B. Vannes, A theoretical model for laser and powder

particles interaction during laser cladding, J. Mater. Process. Technol. 128 (2002) 106–112. doi:10.1016/S0924-0136(02)00433-8.

[31] A.W. Anderson, MJ, Whitcomb, PJ, Kraber, SL, Handbook for Experimenters, Stat-Ease, Inc, Minneapolis, MN, 2016. http://www.statease.com/pubs/handbk_for_exp_sv.pdf.

[32] Jon A. Epps, Compatibility of a Test for Moisture-induced Damage with Superpave Volumetric Mix Design - NCHRP Report 444, National Cooperative Highway Research Program, National Academy Press, Washington D. C 2000, 2000.

[33] M.K. Alam, A. Edrisy, J. Urbanic, J. Pineault, Microhardness and Stress Analysis of Laser-Cladded AISI 420 Martensitic Stainless Steel, J. Mater. Eng. Perform. Springer o (2017). doi:DOI 10.1007/s11665-017-2541-x.

[34] NIST/SEMATECH e-Handbook of Engineering Statistics, http://www.itl.nist.gov/div898/handbook/pri/section3/pri336.htm, access date 09.02.2017, 2013.

[35] M. Gasko, G. Rosenberg, Correlation Between Hardness and Tensile Properties in Ultra-High Strength Dual Phase Steels–Short Communication, Mater. Eng. …. 18 (2011) 155–159. http://fstroj.uniza.sk/journal-mi/PDF/2011/27-2011.pdf.

CHAPTER 3 Microhardness and Stress Analysis of Laser-Cladded AISI 420 Martensitic Stainless Steel

Introduction

Martensitic stainless steel grade 420 powder is considered to be one of the potential alloys for creating additive manufacturing functional components [1]. This alloy is also used for coating and surface repair applications in the tool and die industry because of its high resistance to wear, corrosion, and degradation [1]. Unlike other stainless steels, martensitic stainless steels are heat treatable, and properties can be tailored for specific applications such as steam generators, mixer blades, cutting tools, and medical application [2].

The use of laser cladding as an additive manufacturing process has been growing as it has many unique advantages over conventional cladding done through welding or metal deposition in terms of low dilution, less heat affected zone (HAZ), less distortion to the substrate, and overall quality of the deposited materials [1-2]. Laser cladding provides a localized and relatively low heat input to produce a clad with perfect diffusion bonding to the substrate [3]. Hence, it reduces undesired major deterioration of the desired mechanical properties of the substrate as well as the bead layers. However, despite having a relatively low heat input, a significant amount of internal residual stresses and minor distortions are developed due to the rapid cooling and the high temperature gradient between the cladded bead and the substrate materials during the melting and solidification of the cladding materials along with part of the base materials [3]. Moreover, a moving laser beam creates thermal cycling during melting and re-solidification of the cladded powders, which leads to the development of internal thermal stresses in the laser cladded

bead as well as in the heat affected zone (HAZ) [4]. The development of residual stresses is mainly influenced by the thermal effects and the temperature-dependent physical and mechanical responses of the material employed in laser cladding. In the laser-cladded martensitic stainless steel of grade 420, the generation of residual stress is quite complex. Both tensile and compressive stresses could exist in the cladded materials. The presence of compressive stresses at the surface of the clad parts could improve its service life, while the existence of tensile stresses could result in its premature failure through micro-cracks. These residual stresses could be minimized by controlling the heat input through the laser process parameters during cladding or by post cladding heat treatment (PCHT) [3]. PCHT could reduce the residual stress and thermal mismatch; it could also improve ductility and toughness by transforming martensite to ferrite and fine carbides particles [5]

Several researchers [1]–[3], [6]–[11] investigated the microstructure and mechanical properties of "as cladded" and post-cladding heat treated ferrous and non-ferrous alloys, e.g., AISI 420 stainless steel, AISI P20 tool steel, AISI H13 tool steel, AISI 4340, nickel-based IN-625 super-alloy, cobalt-based hardfacing Stellite 6 alloy, and high-vanadium CPM 10V tool steel. Chen et al. [12] observed the dendritic columnar structure with a large amount of martensite and a small amount of retained austenite in the as cladded AISI P20 tool steel. They also reported biaxial compressive stresses in the clad zone and biaxial tensile stresses in the heat affected zone (HAZ) of the substrate materials, which was significantly reduced after post cladding stress relieving treatment [12].

Gururaj et al. [10] studied the microstructure and mechanical properties, e.g., hardness, tensile strength, and wear resistance of the clad zone for AISI H13 tool steel powders on hardened and tempered AISI H13 tool steel substrate using the laser cladding

and post-cladding tempering. They reported martensite laths, and undissolved or precipitated fine carbides, and retained austenite in the clad zone. They also reported compressive residual stress (670 ± 15 MPa) in the laser cladded surface, which was reduced to 580±30 MPa after tempering at 550°C for 2 hours. They also observed an increase in the microhardness values up to 650 VHN in the as-clad surface compared to 480 VHN measured on the hardened and tempered AISI H13 tool steel substrate. They found that post cladding tempering reduced the hardness value to 550 VHN, which was still significantly higher than that of conventionally hardened and tempered H13 substrate.

Farahmand and Kovacevic [13] examined single and multi-track laser cladding of AISI H13 tool steel generated by a high-power direct diode laser (HPDDL). They found that the value of the residual stress in the multi-track cladding was relatively lower than that of the single-track cladding, this was attributed to the relief of the stress by post-heating during cladding of adjacent tracks. Their study revealed that the higher residual stress concentration was located in the clad zone instead of the surrounding substrate, including the heat affected zone.

As discussed earlier, the development of residual stress in welding and laser cladding is a common challenge resulted due to variable process parameters and the difference between the thermal expansion coefficients between the cladded powdered alloy and the dissimilar substrate materials [14]. Since the residual stress distribution, especially the tensile stresses, significantly influence the structural integrity of laser cladding bead geometry, it becomes an utmost focus in this research to identify the residual stress profile in the as cladded and post cladding heat-treated samples.

Here microhardness variations and residual stresses were measured across the laser cladded and post cladding heat-treated samples of 420 martensitic stainless steel. The results were correlated, which would help with the development of processing parameters.

Materials and Methods

The powder density of 420 martensitic stainless steel was 4.37 g/cm^3, and the powder size was within a mesh size of 53-180 µm. The chemical composition of the powder was in the range of 0.20-0.25 wt% C, 12.6-13.5 wt% Cr, 1.0-1.4 wt% Mn, 0.4-0.6 wt% Si, and Fe. A 10 mm flat bar of AISI 1018 steel was used as a substrate material.

Laser cladding experiments were carried out at the industrial partner facility. A 4 kW fibre laser coupled with a 6-axis robotic arm shown in Figure 1 was used to make the samples where the laser beam (spot size 4.3 mm) focused on the preheated substrate carbon steel to generate a molten pool with 420 martensitic stainless steel powder injected simultaneously into the focal area of laser through the coaxial nozzles. Argon gas provided a shield to protect the molten pool from oxidation. A single bead was deposited by the robot movement onto the substrate. A series of the single beads were cladded on the substrate with different processing parameters, as listed in Table 3.1. These process settings generated distinct bead shapes, as discussed in earlier papers [1], [15]. Based on the characteristic bead geometry two samples A and B were selected for detailed characterizations.

The post cladding heat treatment was done at 565°C ± 5°C for 1 hour to release a substantial amount of residual stress while increasing the toughness and ductility of the material [5],[16], [17]. The samples were inserted into the pre-heated furnace, kept for one hour, and then air cooled.

Table 3. 1 Process Parameters

Sample	Power (kW)	Laser Speed mm/s	Laser Energy J/mm^3	Powder Feed Rate(g/min)	Focal Length of Lens (mm)	Contact Tip to Work Dist. (mm)
A	2	7.5	18.37	15	390	24
B	2.5	10	17.22	20	400	21

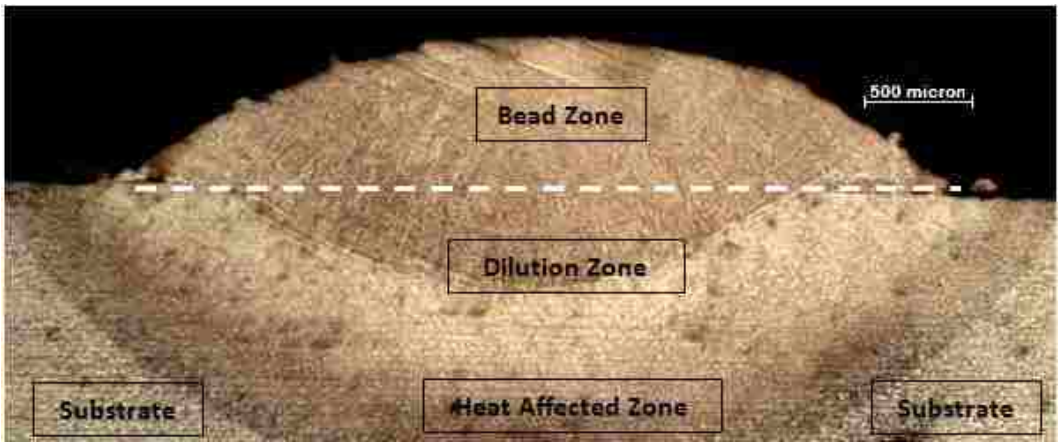

Figure 3. 1 LOM cross - sectional microstructure of 420 martensitic stainless-steel laser cladded at powder feed rate: 15 g/min; laser power: 2 kW; laser speed: 7.5 mm/s (Sample A, with etched with Ralph reagent).

The grinding and polishing operations of cross-sectional samples were done manually as per Struers application notes for stainless steel materials [18]. The microscopy observations were made using a Leica Q5501W light microscope in combination with the FEI Quanta 200 FEG scanning electron microscope (SEM) equipped with energy dispersion spectroscopy (EDS).

A Buehler microhardness tester was used to measure the Vickers microhardness using a load of 200 g and a loading time 12 s. The measurements were performed on cross-sectional sample starting at the center of the bead at 50 µm below the surface with 150 µm interval through to the dilution, HAZ, and the substrate materials. Two more measurements

were performed at a 250 µm distance from each side of the first indentation set. The values reported are the average of these three measurements.

X-Ray Diffraction **(**XRD)[†] analysis was performed with the target Cu ($K_{\alpha 1,2}$ 1.541 Å) and target power 30 kV, 20 mA. The phase analysis was done using the database of National Institute for Materials Science (NIMS) AtomWork [19]. The residual stress (RS) measurement was done according to ASTM E 915 [20] using the Proto X-ray diffraction system (Lab 002/LXRD 06024). The experimental setups are summarized in Table 3.2. The measurements were done on the surface at the center of the bead and perpendicular to the bead line in addition to six subsurface points at an incremental depth of 300 microns approximately.

Table 3. 2 Experimental Setup Parameters for Residual Stress Measurement

Target: Cr ($K_{\alpha avg}$ 2.29100 Angstroms) Target Power: 30.00 kv, 25.00 mA Gain Material: Titanium - Beta Gain Power: 23.00 kv, 25.00 mA Filters: None Material: 420 Stainless Steel X-Ray Elastic Constant: 1762154.75 MPa Crystallographic Plane: {211} Bragg Angle (2θ): 155.1° Aperture: 1.0 mm round	Oscillation(s): Beta 4.00° Collection Time: 1 second x 10 exposures Total Collection Time: 4 minutes Peak Fit: Gaussian 85% Two Peak Model: No LPA Correction On: Yes Gain Correction: P/G Background Subtraction: Linear Peak Shift Method: Absolute Peak Psi Zero Assignment: Curve Fit Linear
Powder Correction: No Auto remove Bad Points: No Psi Tilts: 22	Instrument: Lab 002/LXRD 06024 Software Version: 2.0 Build 87 Goniometer Configuration: Psi
Tilts: (0, ±25.00, ±20.50, ±15.65, ±12.45, ±3.33)	

Results and Discussions

The cross-sectional optical image of the laser cladded 420 martensitic stainless-steel single bead in Figure 3.1 reveals three distinct zones, namely bead zone, dilution zone, and heat affected zone. As a high energy laser beam was used in the cladding experiments, these three zones had undergone through varying cooling rates with a rapid non-equilibrium solidification. This mode of highly non-equilibrium solidification is commonly observed in the conventional welding and laser cladding process [2], [6], [21]–[29]

Figure 3.2 shows the hardness - depth profiles for sample A and B. Sample A showed an average microhardness of 594 $HV_{0.2}$ in the bead zone while a sharp decrease to 422 $HV_{0.2}$ was observed in the dilution zone. Interestingly, the hardness reduced exponentially in the HAZ area from 422 to 260 $HV_{0.2}$, with a further decrease to 233 $HV_{0.2}$ in the substrate regions. On the other hand, sample B showed significantly higher hardness values of 743 $HV_{0.2}$ in the bead zone while keeping an almost similar trend of changes in the dilution and HAZ. Sample B also showed less fluctuations in addition to the higher hardness than sample A, due to a higher level of laser power and laser speed, but lower energy density, as summarized in Table 3.1.

XRD analysis were performed to explain the hardness values and investigate formation of non-equilibrium phases during cladding. Figure 3.3 shows the XRD results and confirmed the presence of non-equilibrium phases such as martensite, delta ferrite, retained austenite (γ-Fe), and metastable metallic carbides phases such as $Cr_{23}C_6$, Cr_7C_3, Fe_7C_3 and (Cr. Fe)C for sample A and B. Metallurgical phases are tabulated in Table 3.3 with their respective crystallographic planes, diffraction angles and space group/number [19].

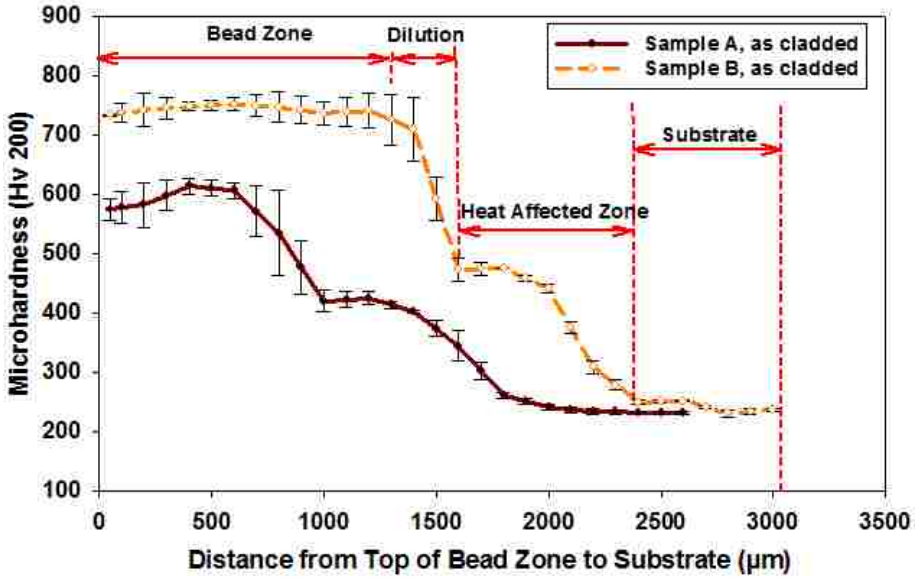

Figure 3. 2 Microhardness profile throughout the bead zone, dilution zone, heat effected zone, and substrate materials in the as cladded sample A and B.

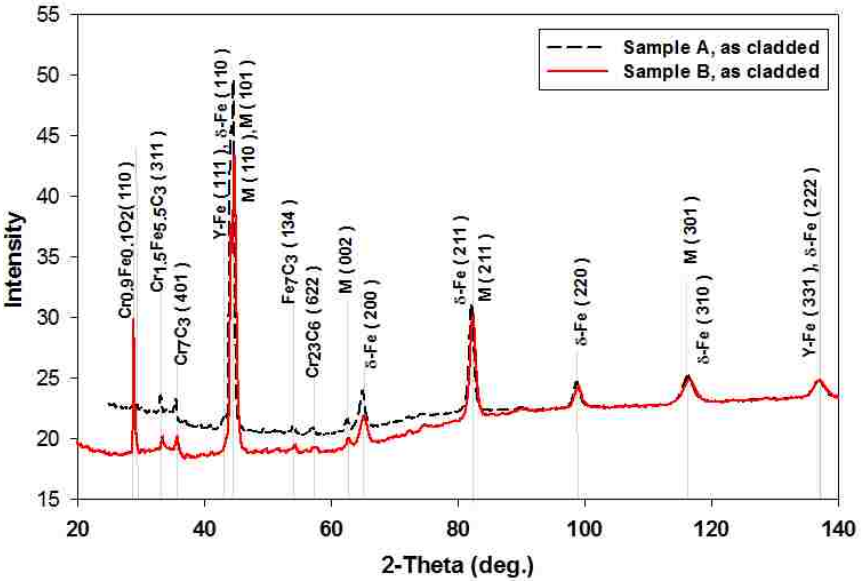

Figure 3. 3 XRD analysis of sample A and B. Sample A laser cladded at powder feed rate: 15 g/min; laser power: 2 kW; laser speed: 7.5 mm/s and Sample B laser cladded at powder feed rate: 20 g/min; laser power: 2.5 kW; laser speed: 10 mm/s.

Table 3. 3 XRD Results of Metallurgical Phases for as Cladded and Post cladding Heat Treated (PCHT) Sample A and Sample B

Metallurgical phases	**Crystallographic Planes**		**Diffraction Angle (2θ degree)**	**Space Group**/No.
	As cladded	PCHT		
Delta ferrite (bcc)	{110}, {200}, {211}, {220}, {222}, {310}	{110}, {200}, {211}, {220}, {222}, {310}	44.73, 65.13, 82.38, 98.91, 116.48, 137.06	**Im^{-}3m** /229
Martensite (bct)	{101}, {110}, {002}, {211}, {301}	{101}, {110}, {002}, {211}, {301}	44.25, 44.73, 62.61, 82.38, 116.48	**I4/mmm**/139
ε-martensite (hcp)		{100}, {102}	42.64, 64.99	**P63/mmc**/194
Austenite	{331}	{111), {331}	136.65, 43.14, 136.82	**Fm-3m**/225
$Cr_{1.5}Fe_{5.5}C_3$	{131}	{311}, {410}, {201}	33.44, 33.23, 34.77, 40.93	**Pnma**/62
Cr_7C_3	{401}	{401}	35.81	**P6$_3$mc**/186
Fe_7C_3	{134}	{134}	54.34	**Pnma**/62
$Cr_{23}C_6$	{622}	{622}	57.11	**Fm-3m**/225
Fe_3C		{221}	49.44	**Pnma**/62
MnS_2		{200},{002}, {231}	29.40, 49.53, 56.32	**Pa-3**/205
MnS		{400}	72.13	**Fm-3m**/225

The related microstructural features of the laser cladded 420 martensitic stainless steel are shown in Figs. 3.4a and 3.4b. In both cases, a martensitic matrix with a second phase in the interdentridic regions were revealed. The microstructure in the bead zone of laser cladding depends on the solidification behavior of the melt pool [21], which is typically controlled by the laser power, scanning speed, and powder feed rate parameters. The melt pool experienced rapid non-equilibrium solidification with high cooling rate, which led austenite to transform into a martensitic matrix. The microstructure in sample B (Fig. 3.4b) shows a higher percentage (6.06%) of a second phase compared to 2.65% in sample A (Fig. 3.4a), which is expected to be responsible for the higher hardness in sample B. The metastable metallic carbides as revealed by XRD might contribute for increasing

the hardness. However, carbide phaes were not revealed in microstructures etched by the Ralph reagents.

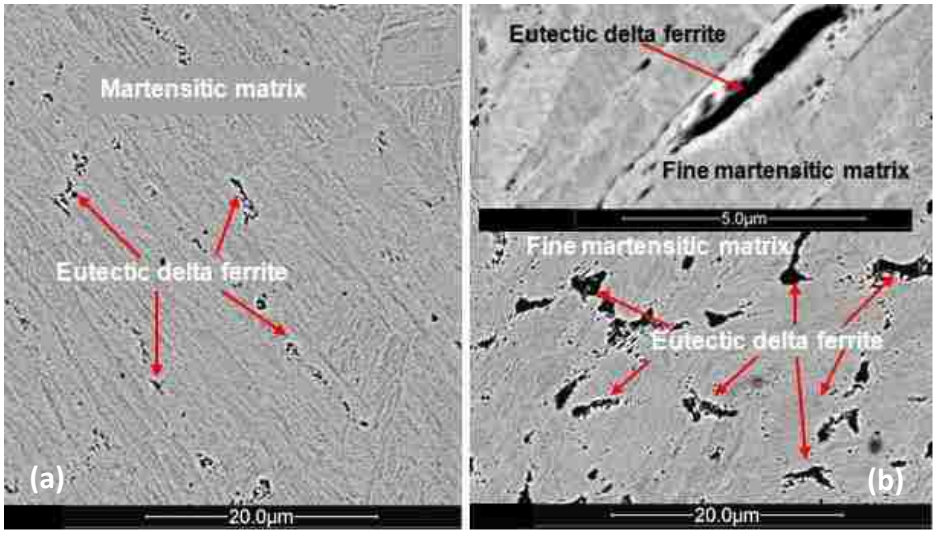

Figure 3. 4 SEM cross-sectional microstructure (BSE) of 420 martensitic stainless steel as cladded (a) Sample A, (b) Sample B, Bead zone: eutectic delta ferrite as dark second phase in a martensitic matrix (etched with Ralph reagent).

The second phases observed in Figures 3.4a and 3.4b were expected to be a non-equilibrium phase commonly observed in martensitic stainless steel processed with rapid solidification processes like welding and laser cladding. Most of the researchers identified this non-equilibrium phase as "delta ferrite" [30]–[32], while some researchers defined it as "eutectic ferrite" or "eutectic delta ferrite" (δ_e Fe) [33], [23]. This phase reported to be formed at the end of solidification as residual phase and does not transform to austenite upon further cooling.

The residual stresses in the as cladded samples A and B are presented in Figure 3.5. The figure shows that a 310 MPa tensile stress was developed on the surface of the bead zone of sample A, which is as high as the yield strength of an annealed 420 martensitic steel. However, the tensile stress then gradually faded within 300 micron depth in the subsurface of bead zone before turning to a compressive stress. The rest of the bead zone

and dilution zone is observed to contain a varying compressive stress. The maximum compressive stress is 420 MPa, which occurs at a depth of 1200 micron from the surface. This is an inflection point.

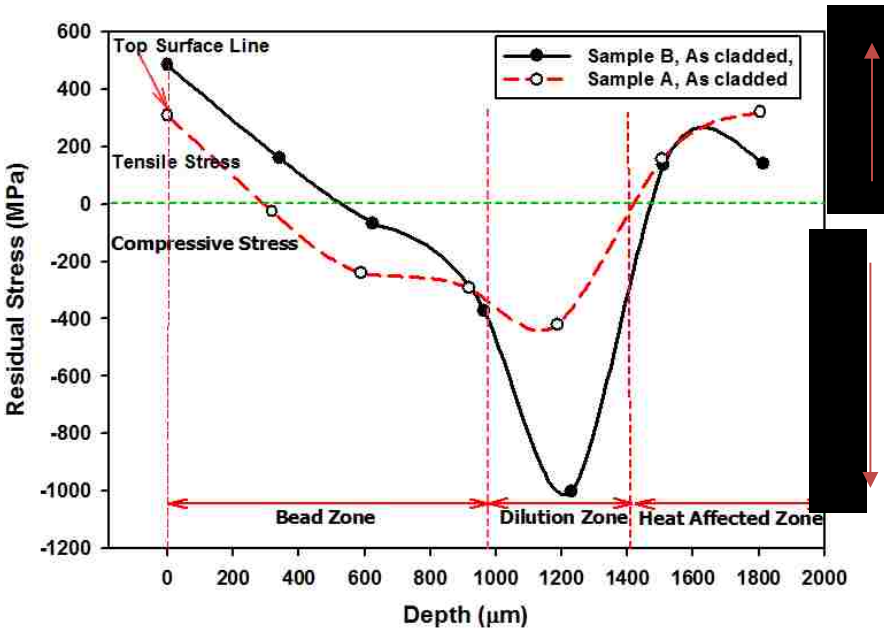

Figure 3. 5 Residual stress profile of as cladded (a) sample A (b) Sample B “positive (+) stress" indicate the tensile residual stress and the "negative (-) stress" designated as compressive residual stress.

The compressive stresses dramatically shift to tensile stresses at a depth of 1500 micron and up to 321 MPa tensile stresses are developed in the HAZ. Similarly, in sample B, a high tensile stress of 486 MPa was developed on the surface of the bead. It then gradually decreased to 162 MPa at a depth of 340 microns and almost 0 MPa within a 600 micron depth. Below this point, compressive stresses exist, that gradually increase to 371 MPa through the rest of the bead zone. Surprisingly, a sharp increase of the compressive stress from 371 MPa to a high value of 1002 MPa was observed in the first half of the dilution zone at a depth of 1200 micron from the surface. This is an inflection point. From here, the compressive stresses are reduced and changed to a tensile stress of 142 MPa at a depth of 1500 micron from the surface. This tensile stress exists in the bottom part of the

dilution to the major area of the HAZ. For sample B, the high laser power and high laser speed did not allow much time to release the heat from the bead zone. It experienced a high cooling rate that generated the high residual stresses. Unlike sample B, sample A experienced less residual stress.

These high residual stresses are also believed to be generated due to microstructural evolutions during the rapid non-equilibrium solidifications and solid state phase transformation in the laser cladding [12]. The top and bottom of the bead zone, as well as the HAZ, experienced different cooling rates along with differential volumetric changes of crystal structures during the laser cladding. Since rapid solidification occurred from delta ferrite to austenite, and then austenite to martensite, small fractions of delta ferrite believed to be segregated while the bulk amount transformed to austenite. It is also likely that a small amount of austenite was retained during the transformation of austenite to martensite. The volume fraction of delta ferrite evolved in the interdendritic regions and the austenite phase retained in the matrix are very low compared to the huge volume of the martensite matrix. This may contribute to some of the residual stress in the micro-level between different crystallographic planes of body centered cubic delta ferrite, face centered cubic austenite, and body centered tetragonal martensite crystals. Indeed, precipitation of metallic carbides and sulphides along with the eutectic delta ferrite may have some contribution in the volumetric changes in those crystallographic planes. In addition, it is apparent that the HAZ in the substrate may also significantly contribute to producing tensile stresses due to its cyclic distortion in the subsequent heating and cooling during the laser cladding. Similar observations were made by Chen et al. [12] during their examination of P20 Tool Steel.

High hardness and high residual stresses generated in the laser cladding are detrimental for the cladded parts as they lead to surface cracking and fracture during their service life. Hence, the post cladding heat treatments (PCHT) were performed at 565°C for an hour for the both samples A and B to relieve some of the stresses and to achieve the moderate hardness levels required for some specific applications and machining of the components.

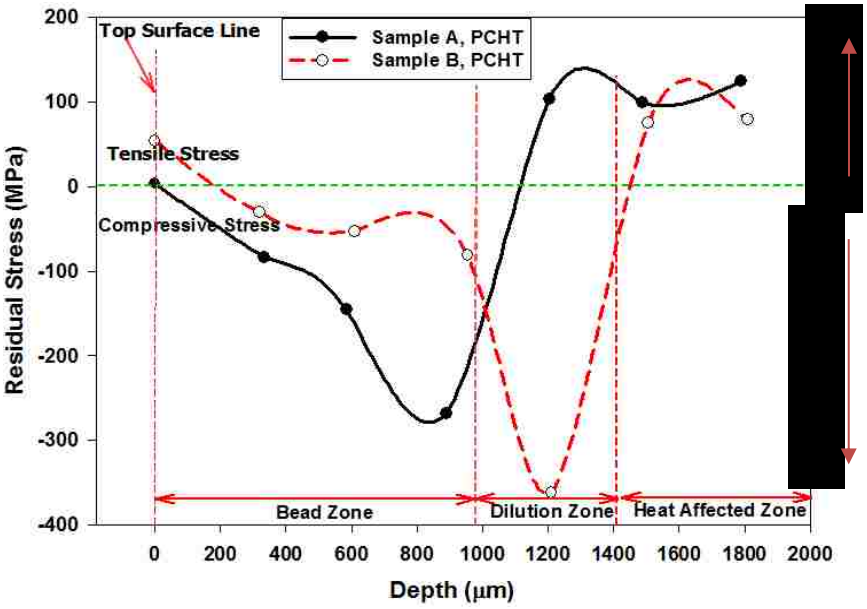

Figure 3. 6 Residual stress profile of (a) sample A (b) Sample B after post cladding heat treatment (PCHT) at 565°C for 1 hr.

It is found that the post cladding heat treatment reduced the compressive residual stress abruptly from 420 MPa to 268 MPa in sample A (Fig. 3.6). The tensile stress is almost completely relived from the surface of sample A and becomes more compressive throughout the sample, except some tensile modes are retained in the HAZ. A similar effect has been observed in sample B. The full bead zone, and dilution of sample B were almost relieved from the tensile stresses (486 MPa to 54 MPa) while a subsided compressive stress (1002 MPa to 363 MPa) is retained in the same area at a depth of 1200 micron from the surface. The tensile stresses in the HAZ for both samples were also reduced slightly when

compared to the tensile stresses observed at the top surface of the clad bead. As compressive stress is beneficial for the fatigue life of materials [22], the PCHT improved the fatigue life of the laser cladded parts through reducing and homogenizing sharp compressive stresses. The PCHT has almost compeltely removed the tensile stress from the top surface of the cladded parts in both samples (Fig. 3.6).

The effect of the PCHT on the residual stresses of both samples A and B has tremendously affected the microhardness profile of both samples. Figure 3.7 shows that microhardness had been decreased abruptly from 594 to 385 $HV_{0.2}$ throughout the bead zone of sample A after post cladding heat treatment. The hardness of the bead zone becomes more homogenous compared to the as cladded sample. Similarly, sample B shows a sharp decrease of hardness in the bead zone from 743 to 421 $HV_{0.2}$ after the same level of PCHT. The PCHT reduced the hardness around 35% and 43% in the bead zone of sample A and B, respectively. Also, the hardness had been reduced gradually in the dilution and HAZ of both samples, which improves the toughness of the samples [2].

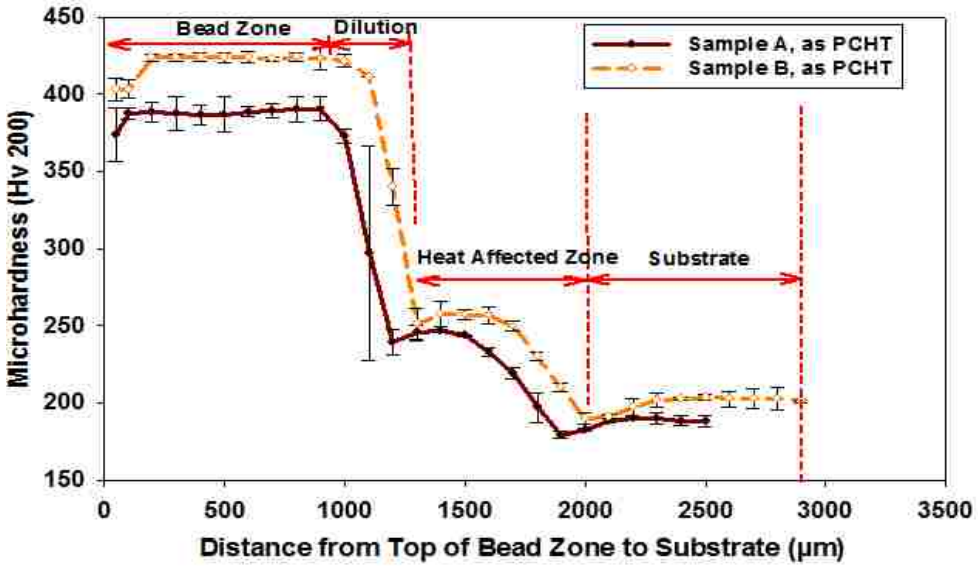

Figure 3. 7 Microhardness profile throughout the bead zone, dilution zone, heat effected zone, and substrate materials in the post cladding heat treatment (PCHT) for sample A and B.

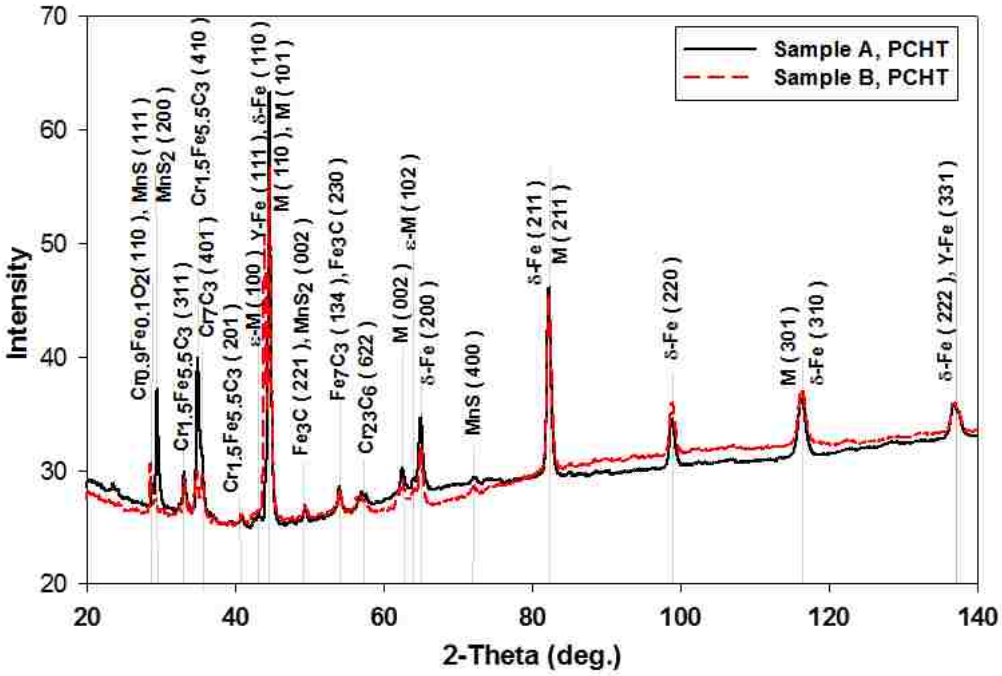

Figure 3. 8 XRD analysis of sample A and Sample B after post cladding heat treatment (PCHT).

The XRD Results of PCHT samples presented in Fig. 3.8 show the existence of delta ferrite and two forms of martensite. One form of martensite had a body centered tetragonal (bct) structure with a space group of I4/mmm (139), and the other one was a thermally stress induced hexagonal close packed (hcp) structured ε-martensite (space group P63/mmc, 194). It is significant to note that the retained austenite still existed after the heat treatment, which suggested higher temperature or longer time might have been required for complete phase transforamtion. Precipitation of more metallic carbides such as $Cr_{1.5}Fe_{5.5}C_3$, and Fe_3C, with additional metallic sulfides, were observed after the PCHT. All phases identified through XRD analysis are tabulated in Table 3.3 with their respective crystallographic planes, diffraction angles, and space group.

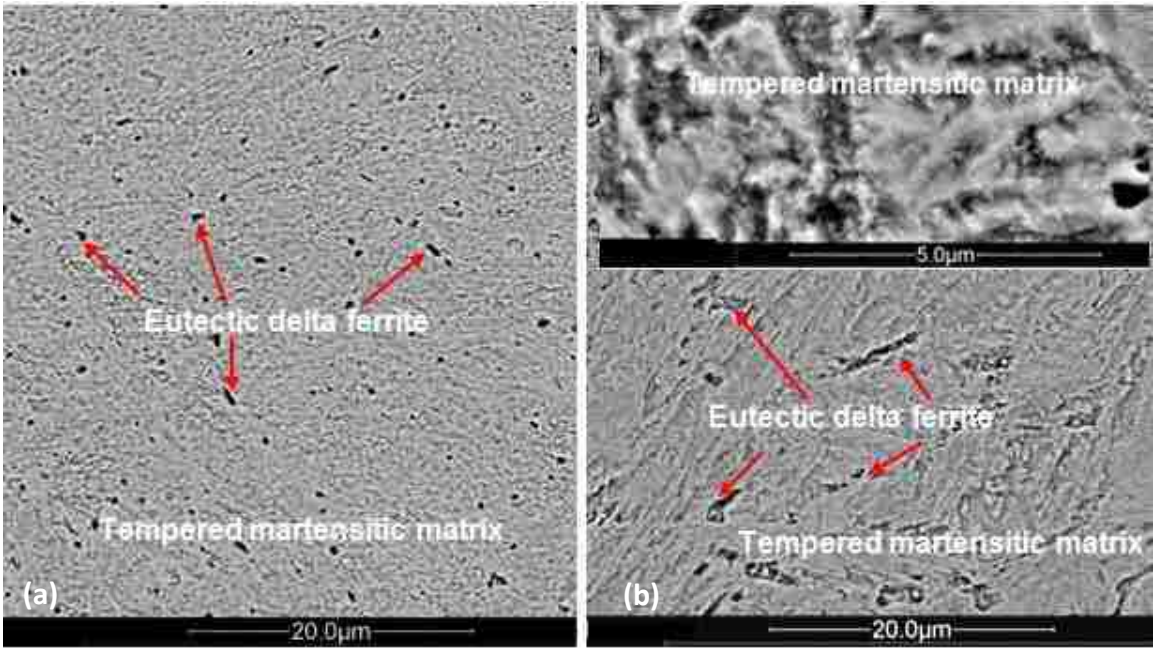

Figure 3. 9 SEM cross-sectional microstructure (BSE) of Bead zone after post cladding heat treatment (PCHT) (a) Sample A, (b) Sample B, Bead zone: skeletal form of second phase in the tempered martensitic matrix (etched with Ralph reagent).

It is important to note that the eutectic delta ferrites (second phases) were disappeared after the PCHT, as can be seen in Fig. 3.9a and 3.9b for both samples. Moreover, both images show the skeleton traces left behind on the tempered martensite matrix as the eutectic delta ferrites fadded in the microstructure. The microstructural analysis showed a finer morphology in sample A compared to that of sample B.

Conclusions

This detailed investigation of microstructures, residual stresses, and micro-hardness depth profile for laser cladded and post cladding heat-treated sample A and B have led to the following conclusions:

- The higher level of laser power and laser speed but lower laser energy resulted in a higher hardness (743 $HV_{0.2}$) and higher residual stress (486 MPa tensile stresses, 1002 MPa compressive stress) in sample B when compared to those of sample A.
- Non-equilibrium cooling rate in laser cladding process resulted in formation of non-equilibrium phases such as eutectic delta ferrite (δ_e-Fe), martensite, retained austenite, and metallic carbides like $Cr_{23}C_6$, Cr_7C_3, Fe_7C_3 and (Cr. Fe)C.
- The post cladding heat treatment (PCHT) showed a thermally stress induced hcp structured ε-martensite along with the bct martensite in the tempered bead zone. Precipitation of more metallic carbides such as $Cr_{1.5}Fe_{5.5}C_3$ and Fe_3C phases were found with additional metallic sulfides compared to the as cladded samples. Matrix morphology of Sample A became finer than Sample B with fine skeleton marks due to fading of the eutectic delta ferrite.
- After the post cladding heat treatment, 99% and 89% of the tensile stresses were removed from the top surface of the cladded samples A and B, respectively. Compressive stresses were also substantially reduced and homogenized throughout the bead zone in both samples. The PCHT significantly reduced the microhardness around 35% and 43% in the bead zone of sample A and B.

References

[1] M. K. Alam, J. Urbanic, S. M. Saqib, and A. Edrisy, "Effect of Process Parameters On The Microstructural Evolutions of Laser Cladded 420 Martensitic Stainless Steel," in *Materials Science and Technology Conference Proceedings (MS&T15),*

October 4-8,Columbus, OH, USA, 2015, pp. 35–54.

[2] S. H. Baghjari and S. A. A. Akbari Mousavi, “Effects of pulsed Nd:YAG laser welding parameters and subsequent post-weld heat treatment on microstructure and hardness of AISI 420 stainless steel,” *Mater. Des.*, 2013, vol. 43, pp. 1–9.

[3] J. Chen, S. H. Wang, and L. Xue, “On the development of microstructures and residual stresses during laser cladding and post-heat treatments,” *J. Mater. Sci.*, 2012, vol. 47, no. 2, pp. 779–792.

[4] Vilar, R. “Laser cladding,” *J. Laser Appl.*, 1999, vol. 11, no. 2, p. 64.

[5] J. Lippold and D. Kotecki, “Welding Metallurgy and Weldability of Stainless Steels,” *Wiley-Interscience*. John Wiley & Sons, New Jersey, 2005, pp 56-86.

[6] J. Chen, L. Xue, and S. Wang, “Microstructure Characterization of Laser-Consolidated AISI 420 Stainless Steel,” in *Materials Science and Technology (MS&T)* 2008, Pittsburgh, Pennsylvania, USA, pp. 1388–1396.

[7] M. Fenech, B. Mallia, M. Grech, and J. C. Betts, “Post-deposition heat treatment of co-deposited Cr3C2 and AISI 410 stainless steel using the coaxial laser deposition technique,” *J. Mater. Sci.*, 2013, vol. 48, no. 5, pp. 2224–2235

[8] A. Guo, W., Kar, “Microstructural analysis and performance evalution in laser cladding of stainless steel on the plain carbon steel,” in *Elevated Temperature Coatings: Science and Technology lll*, 1999, pp. 231–241.

[9] C. Köse and R. Kaçar, “The effect of preheat & post weld heat treatment on the laser weldability of AISI 420 martensitic stainless steel,” *Mater. Des.*, 2014, vol. 64, pp.

221–226.

[10] G. Telasang, J. Dutta Majumdar, N. Wasekar, G. Padmanabham, and I. Manna, “Microstructure and Mechanical Properties of Laser Clad and Post-cladding Tempered AISI H13 Tool Steel,” *Metall. Mater. Trans. A*, 2015, vol. 46, no. 5, pp. 2309–2321.

[11] J. Grum and M. Žnidaršič, “Microstructure, Microhardness, and Residual Stress Analysis of Laser Surface Cladding of Low-Carbon Steel,” *Mater. Manuf. Process.*, 2004, vol. 19, no. 2, pp. 243–258.

[12] J.-Y. Chen, K. Conlon, L. Xue, and R. Rogge, “Experimental study of residual stresses in laser clad AISI P20 tool steel on pre-hardened wrought P20 substrate,” *Mater. Sci. Eng. A*, 2010, vol. 527, no. 27–28, pp. 7265–7273.

[13] P. Farahmand and R. Kovacevic, “An experimental–numerical investigation of heat distribution and stress field in single- and multi-track laser cladding by a high-power direct diode laser,” *Opt. Laser Technol.*, 2014, vol. 63, pp. 154–168, Nov.

[14] J. Katsuyama, M. Udagawa, H. Nishikawa, and Kunio ONIZAWA, “Evaluation of Weld Residual Stress near the Cladding and J-weld in Reactor Pressure Vessel Head for the assessment of PWSCC Behavior,” *E-Journal Adv. Maint.*, 2010, vol. 2, pp. 50–64.

[15] K. Aggarwal, “Investigation of Laser Clad Bead Geometry to Process Parameter Settings for Effective Parameter Selection, Simulation, and Optimization -MASc Thesis,” University of Windsor, 2014.

[16] R. Steiner, *ASM Handbook Volume 1, Properties and Selection: Irons, Steels and High Performance Alloys*, 10th ed. ASM International, 1993.

[17] J. F. Grubb, "Martensitic Stainless Steels," in *Uhlig's Corrosion Handbook*, Edition., R. W. Revie, Ed. Hoboken, NJ, USA: John Wiley & Sons, Inc., 2000, pp. 667–676.

[18] E. Weidmann, "Struers Application Notes - Metallographic Preparation of Stainless Steel." Struers A/S, Copenhagen, 2005.

[19] P. V. Yibin Xu, Masayoshi Yamazaki, "National Institute for Materials Science (NIMS) AtomWork," *Inorganic Materials Database for Exploring the Nature of Material - Jpn. J. Appl. Phys*, 2011, in English [Online]. Available: http://crystdb.nims.go.jp/. [Accessed: 23-Dec-2015].

[20] ASTM Standard E915, "Standard Test Method for Verifying the Alignment of X-Ray Diffraction Instrumentation for Residual Stress Measurement," *ASTM B. Stand.*, vol. i, no. June 1996, pp. 1–4, 2010.

[21] S. A. David, S. S. Babu, and J. M. Vitek, "Welding : Solidification and Microstructure," *JOM, J. Miner. Met. Mater. Soc.*, 2003. no. June.

[22] Y. C. Lin and S. C. Chen, "Effect of residual stress on thermal fatigue in a type 420 martensitic stainless steel weldment," *J. Mater. Process. Technol.*, 2003, vol. 138, no. 1–3, pp. 22–27.

[23] M. M. A. Khan, L. Romoli, M. Fiaschi, F. Sarri, and G. Dini, "Experimental

investigation on laser beam welding of martensitic stainless steels in a constrained overlap joint configuration," *J. Mater. Process. Technol.*, 2010, vol. 210, no. 10, pp. 1340–1353.

[24] R. S. Huang, L. Kang, and X. Ma, "Microstructure and Phase Composition of a Low-Power YAG Laser-MAG Welded Stainless Steel Joint," *J. Mater. Eng. Perform.*, 2008, vol. 17, no. 6, pp. 928–935.

[25] I. Hemmati, V. Ocelík, and J. T. M. De Hosson, "The effect of cladding speed on phase constitution and properties of AISI 431 stainless steel laser deposited coatings," *Surf. Coatings Technol.*, 2011, vol. 205, no. 21–22, pp. 5235–5239.

[26] S. Liang, H. Zhang, M. Xia, R. Chen, E. Han, and Z. Fan, "Microstructure and mechanical properties of melt-conditioned high-pressure die-cast Mg-Al-Ca alloy," *Trans. Nonferrous Met. Soc. China*, 2010, vol. 20, no. 7, pp. 1205–1211.

[27] S. Da Sun, Q. Liu, M. Brandt, M. Janardhana, and G. Clark, "Microstructure and Mechanical Properties of Laser Cladding Repair of AISI 4340 Steel," in *28th International Congress of the Aeronautical Sciences (ICAS)*, 2012, Brisbane, Australia, no. i, pp. 1–9.

[28] M. M. A. Khan, L. Romoli, R. Ishak, M. Fiaschi, G. Dini, and M. De Sanctis, "Experimental investigation on seam geometry, microstructure evolution and microhardness profile of laser welded martensitic stainless steels," *Opt. Laser Technol.*, 2012, vol. 44, no. 5, pp. 1611–1619.

[29] H. J. Niu and I. T. H. Chang, "Microstructural evolution during laser cladding of

M2 high-speed steel," *Metall. Mater. Trans. A*, 2000, vol. 31, no. 10, pp. 2615–2625.

[30] E. Folkhard, *Welding Metallurgy of Stainless Steels*. New York: Springer- Verlag Wien, 1988.

[31] M. D. B. MATEŠA, I. SAMARDŽIĆ, "The Influence of Heat Treatment on Delta Ferrite.," *Metalurgija*, 2012, vol. 51, no. 2, pp. 229–232.

[32] P. Wang, S. P. Lu, N. M. Xiao, D. Z. Li, and Y. Y. Li, "Effect of delta ferrite on impact properties of low carbon 13Cr-4Ni martensitic stainless steel .," *Mater. Sci. Eng. A*, 2010, vol. 527, no. 13–14, pp. 3210–3216.

[33] N. Lewis, M. J. Cieslak, and W. F. Savage, "Microsegregation and eutectic ferrite-to-austenite transformation in primary austenite solidified CF-8M weld metals," *J. Mater. Sci.*, 1987, vol. 22, no. 8, pp. 2799–2810.

CHAPTER 4 Microstructural Analysis of the Laser-Cladded AISI 420 Martensitic Stainless Steel

Introduction

AISI 420 martensitic stainless steel (SS) has excellent mechanical properties such as high tensile strength and moderate corrosion resistance. Properties of this steel grade can be altered by post-heat treatment [1]. AISI 420 SS is used in many diverse industrial applications, such as pressure vessels, mixer blades, cutting tools, and medical components [2]. This stainless steel is considered to be one of the potential alloys for additive manufacturing of functional components using laser cladding process.

Laser cladding (LC), or direct energy deposition, is one of the Additive Manufacturing (AM) processes that utilizes laser power to melt coaxially fed metallic powders (or wire) to coat part of a substrate or make a functional component using a layer stacking strategy. LC is a complex metallurgical process that involves transient heat transfer and highly non-equilibrium solidification [3]. As the laser beam reaches the substrate, a significant amount of its energy is directly absorbed by the substrate and the powder particles, which then creates a melt pool on the substrate [4], [5]. Moreover, the surface tension gradient drives the fluid flow within the melt pool and penetrates into the substrate causing the energy transfer through a mass convection mechanism. During this process, the melted powder particles are swiftly mixed in the melt pool which combines three governing processes: (i) heat conduction, (ii) continuity, and (iii) momentum [4], [5]. All three processes happen within a fraction of time so that the temperature and high-velocity fields in the melts create a highly non-equilibrium state during the rapid

solidification. This can generate a very high cooling rate, up to 10^{3-5} ºC/s, due to (i) its controlled heat input, (ii) small and thin layer melt pool, and (iii) heat conduction to the bulk substrate [6]. Therefore, the microstructure generated in the laser-cladded coating is greatly influenced by the super-high cooling rate. Solid state phase transformation, metastable phases, or extended solid solutions are the characteristics of such rapid solidification [7]. Coatings with such microstructures generally cannot be achieved by the conventional process. Hence, the use of laser cladding with 420 SS has been increasing recently for both coating and surface engineering applications in the pipeline as well as in the tool and die industries due to its excellent resistance to wear, corrosion, and high-temperature oxidation properties.

Several studies [6], [8]–[11] reported microstructural characterizations for laser-cladded iron-based materials. Chen et al. [6] studied the laser consolidated AISI 420 stainless steel (420SS) and observed a fine dendritic microstructure in a directionally solidified nature with duplex austenite (A) and martensite (M) phases. They also reported 53.9 vol.% of retained austenite in their findings, which remained even after post-heat treatment at 1008 °C for 30 minutes, followed by tempering at 477 °C. In other studies, Alam et al. [12], Baghjari et al. [2], and Köse et al. [13] reported the presence of eutectic-delta ferrite as the second phase along with the martensite and traces of retained austenite in the laser cladding/welding of 420 SS.

Sun et al. [9] found martensite within the fine austenite dendrites due to rapid cooling rates in the laser deposited AISI 4340 clad layer. They reported that the microhardness of the clad was 30-40% higher than the base material, which was explained by the martensite formation. Hemmati et al. [10] investigated laser deposited AISI 431

martensitic SS coatings and speculated that the austenite dendrite boundaries worked as effective obstacles against the growth of martensite lathes and stopped the martensitic transformation in various locations.

Wu [11] examined the powder cladding of Fe, Cr, W, Ni, and C with a weight ratio of 10:5:1:1:1. It was found that the surface layer microstructure consisted of the primary phase as γ-austenite with interdendritic lamellar eutectic, $\gamma + (\gamma + M_7C_3)$, where γ-austenite was a non-equilibrium phase with an extended solid solution of alloying elements. TEM observation and X-ray diffraction also revealed a high density of dislocations, stacking faults, and twins in both the primary and the eutectic γ-austenite. However, no martensite was reported in the as-cladded microstructure.

In the authors' earlier studies [1], [12] substantial variations in the hardness and residual stress depth-profile of a single bead laser-cladded 420 SS was observed. To understand those results, the present study investigates the microstructures in the main three regions of the bead zone, dilution zone, and interface zone using electron microscopy techniques. The analytical investigation of microstructures presented in this work was not found in the previous studies to the best of the authors' knowledge. Identifying and understanding of the microstructural evolutions is a crucial step towards the future development of the LC processes and will provide a guideline for industrial applications.

Experimental Methodologies

The 420 SS laser cladding was performed using a 4 kW fiber connected diode laser coupled to an articulated robotic arm, as shown in Fig. 4.1a. A coaxial deposition head (Fig. 4.1b) was employed to clad powder material onto a 10 mm thick flat bar of

medium carbon steel substrate. The powder grain sizes were between 53-180 µm with a powder density of 4.37 g/cm^3. The chemical composition of the powder is shown in Table 4.1.

A 2.5 kW high power laser beam was focused on the substrate steel bar to generate a molten pool with the 420 SS metallic powders injected simultaneously at the rate of 20 g/min into the focal area of laser (using the process parameters shown in Table 4.2) with coaxially flowing argon gas as a shield to protect the molten pool from oxidation. A series of single beads were deposited by the robot movement onto the substrate.

A 2.5kW power laser at a speed of 10mm/s with a spot diameter of 4.3mm generates 17.22 J/mm^3 laser energy density. It is to be noted that the laser energy density was calculated using a formula of (laser power, watt)/(spot area, mm^2)(laser speed, mm/s) [14].

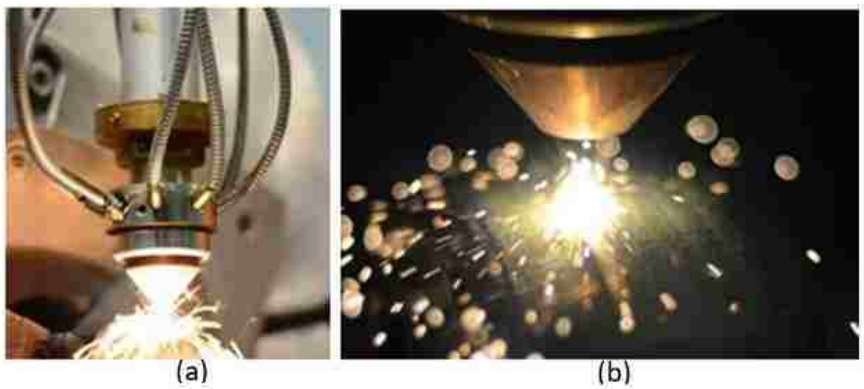

Figure 4. 1 Laser cladding process with (a) Robotic Arm, (b) Coaxial powder deposition head.

Table 4. 1 Chemical composition of AISI 420 stainless steel powder

Chemical Elements	**Percentage of composition (%)**
Carbon	0.23
Manganese	1.2
Chromium	12.6
Silicon	0.5

Iron	Balance

Table 4. 2 Process parameters

Process Parameters	**Data**
Laser power	2500 W
Laser speed	10 mm/s
Powder feed rate	20 g/min
Focal length of lens	400 mm
Contact tip to workpiece distance	21 mm
Laser spot diameter	4.3 mm
Laser energy	17.22 J/mm^3
Argon gas flow rate	23 CFH (cubic feet per hour)

For cross-sectional investigation of the microstructures, the samples were cut transversely by wire EDM and then mounted in epoxy powder using a Buehler hot mounting press. The metallography sample preparation was done using a series of grinding and polishing solutions as per Struers' application note (stainless steel) [15] for a cross-sectional view. Murakami reagent and Kalling reagent II were used as chemical etchants.

TEM thin-foil samples were prepared from three different zones of the laser-cladded 420 stainless steel sample, as shown in Fig. 4.2. The thin-foil samples were prepared using focused ion beam (FIB) milling in a dual beam Zeiss NVision 40 workstation equipped with a Schottky field emission gun (FEG) filament scanning electron microscope (SEM).

TEM imaging was done using the JEOL 2010F equipped with a large solid angle for high X-ray throughput and a Gatan Imaging Filter for energy-filtered imaging. The instrument was fitted with a field emission gun X-FEG Schottky emitter and a monochromator that lowered the energy spread of the electrons below 0.25 eV. FIB and TEM imaging was done at the Canadian Centre for Electron Microscopy at McMaster University.

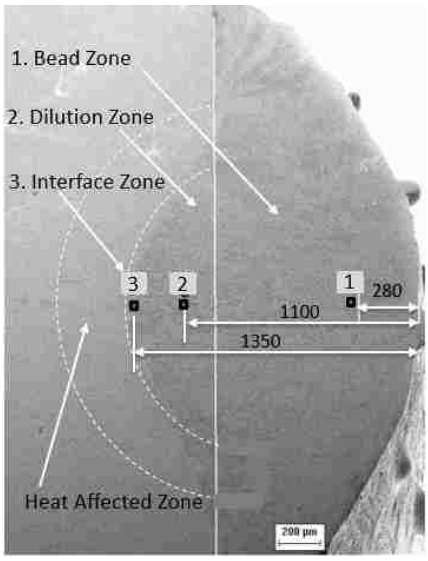

Figure 4. 2 Cross-sectional SEM image with the locations of TEM samples.

Results

Fig. 4.3a shows a cross-sectional OM image of the single bead laser-cladded 420 SS sample that revealed the bead zone, dilution zone, and interface zone, while Fig. 4.3b shows the enclosed area in Fig. 4.3a at a higher magnification. Bead zone is defined as the region above the horizontal line of the substrate, and the region below the horizontal line defined as the dilution zone (Fig. 4.3a). Generally, the dilution zone is an inter-diffusion zone between the cladding and the substrate materials. Though there is no distinct line between the bead zone and the dilution zone, the root of the bead that goes inside the substrate where the molten substrate and the liquid cladded materials diffuse together is considered as the dilution zone. The dilution zone has two parts: the upper part, which mingled with the bead zone, and the lower part that has a clear interface with the heat-affected zone of the substrate. For this reason, the study was extended to an interface zone. Apparently, the bead zone and the dilution zone look continuous and similar in the optical microscopy (OM) image (Fig. 4.3b). However, the TEM study revealed different

microstructural features, as discussed in the later sections.

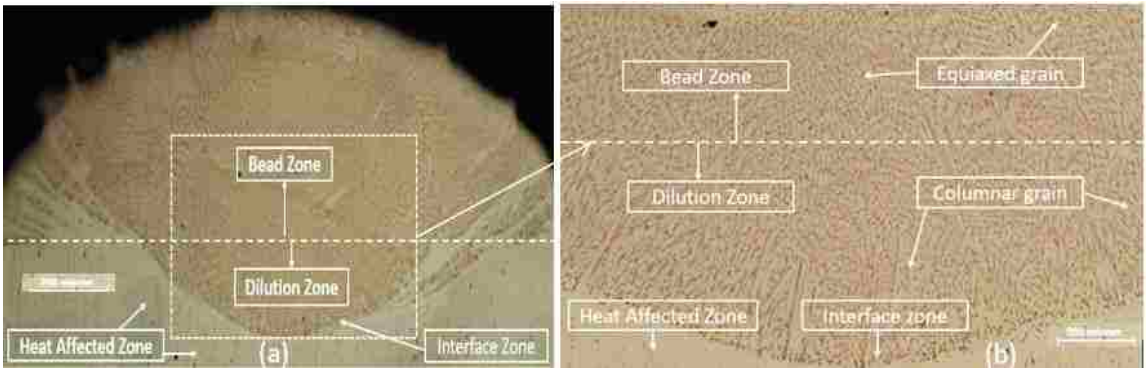

Figure 4. 3 (a) OM image shows a cross-sectional view of laser-cladded 420 stainless steel single bead sample, (b) higher magnification view from the enclosed areas in Fig. 4.3a shows the bead zone: mainly equiaxed grain, dilution zone: a combination of equiaxed and columnar grain, interface zone: mainly columnar grain; (Etchant: Murakami reagent).

Fig. 4.3b shows mainly equiaxed grains in the bead zone and a combination of both equiaxed and columnar grains in the dilution zone, while only columnar grains in the interface zone. Similar patterns were commonly observed in the non-equilibrium solidification of laser welding [14].

Fig. 4.4a is a secondary electron SEM image showing the ion milled cross-section of the bead zone. Fig. 4.4b shows a similar image from the cross-section of the interface zone between the dilution and HAZ, where the eutectic delta ferrite appeared as a second phase in the martensitic matrix. The volume percentage of delta ferrite in the bead zone was estimated at 6.06 % (vol.) using “Image Pro-plus” image analysis software. A similar amount of delta ferrite (6.23 vol.%) was observed in the dilution zone. This amount was in agreement with the calculated delta ferrite (up to 5%) from the Schaeffler and Balmforth diagram [12], [16] based on the respective chromium equivalent 13.1 and nickel equivalent 8.1 in the alloy.

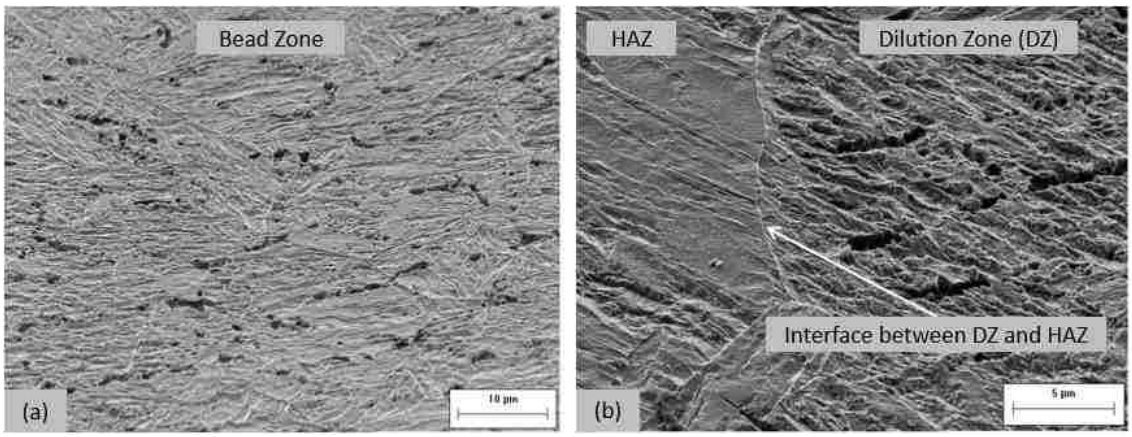

Figure 4. 4 Back-scattered SEM images showing the ion milled cross-sections of (a) bead zone, (b) interface zone between the dilution and heat affected zone (HAZ) (Etchant: Kallings' reagent).

Fig 4.5 shows back-scattered SEM images from the ion milled cross-section of the bead zone, dilution zone, and interface zone. Plate-like martensite with internal twins was revealed at different orientations in the bead zone (Fig. 4.5a). Lath-like martensite and twins were observed at the dilution zone (Fig 4.5b). Fig. 4.5c shows lath martensite as well in the interface zone. The lath martensite in the interface zones are larger than those observed in the dilution zones.

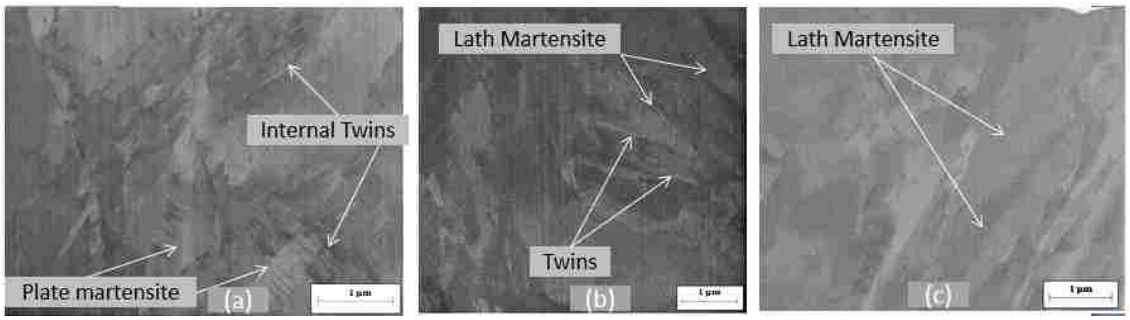

Figure 4. 5 Back-scattered SEM images showing the ion milled cross-section of (a) bead zone with internal twins in the plate-like martensite, (b) dilution zone with twins and lath-like martensite, and (c) interface zone with lath-like martensite.

The detailed TEM results for each zone are presented in the following sections.

4.3.1 Bead Zone

Fig. 4.6a is a bright field scanning transmission electron microscopy (STEM) image of the bead zone. This Fig. 6a shows plate-like martensite that seems to be a packet of martensite that consisted of thin plate and lenticular plate martensite. Other microstructural features such as a high density of dislocations, internal twins, and nano-carbide precipitates were also observed in this plate-like martensite. Different morphologies were identified by the following definitions, where the lenticular martensite is one kind of plate martensite having midrib structure. Martensite/Austenite (M/A) interface of lenticular martensite is smoothly curved compared to a planer M/A interface of thin plate martensite[17]. On the other hand, lath martensite was parallelly oriented with each other and have a planer interface. The martensite plates were not aligned with each other and oriented at a different angle. The enclosed areas (b, c, and d) in Fig. 4.6a were shown at higher magnification in Figs. 4.6b, 4.6c, and 4.6d identifying these features. The width of the thin plate martensite (Fig. 4.6b) was around 0.13 μm, while the lenticular martensite (Fig. 4.6c) was between 0.1 and 0.15 μm. The carbide precipitates in Fig. 4.6d were identified as $M_{23}C_6$, mainly $Cr_{23}C_6$ phase using XRD analysis with 10-20 nanometers in width and 30-50 nm in length. Fig. 4.6e reveals a region with a high density of dislocations. Fig. 4.6f represents a bright field TEM image of the bead zone with the respective SAED patterns on the insert. Plate martensite in the image was identified to be ά-martensite and formed on the zone axis of [111]. Internal twins were visible in the large martensite plate (Fig. 4.6f).

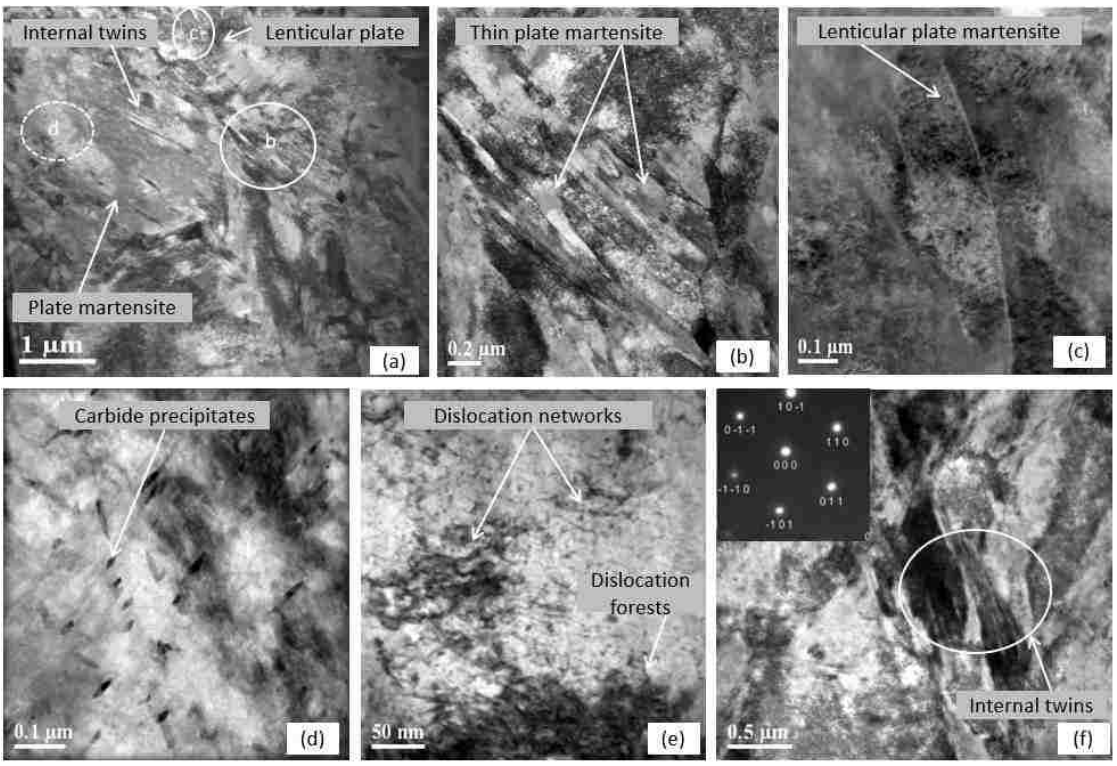

Figure 4. 6 Bright field STEM image reveals (a) plate-like martensite with internal twins. The encircled area (b, c, and d) in Fig. 6a was shown at higher magnification in Figs. 4.6b, 4.6c, and 4.6d. (b) thin plate martensite, (c) lenticular plate martensite, (d) carbide precipitates ($Cr_{23}C_6$), (e) dislocation networks, and dislocation forest, (f) SAED pattern with internal twins in the bead zone.

-

4.3.2 Dilution Zone

Fig. 4.7 represents TEM and STEM bright field and dark field images of the dilution zone. Fig. 4.7a shows a combination of plate and lath martensite morphologies formed on the zone axis of [120] in this zone. The respective SAED patterns confirmed that all martensite morphologies belonged to ά-martensite. Fig. 4.7b shows a STEM bright field image while Fig. 4.7c shows the same in a dark field image. Both images reveal lath martensite in the dilution zone. The width of lath martensite is 0.1-0.2 µm compared to the adjacent martensite plate of 0.4-0.6 µm.

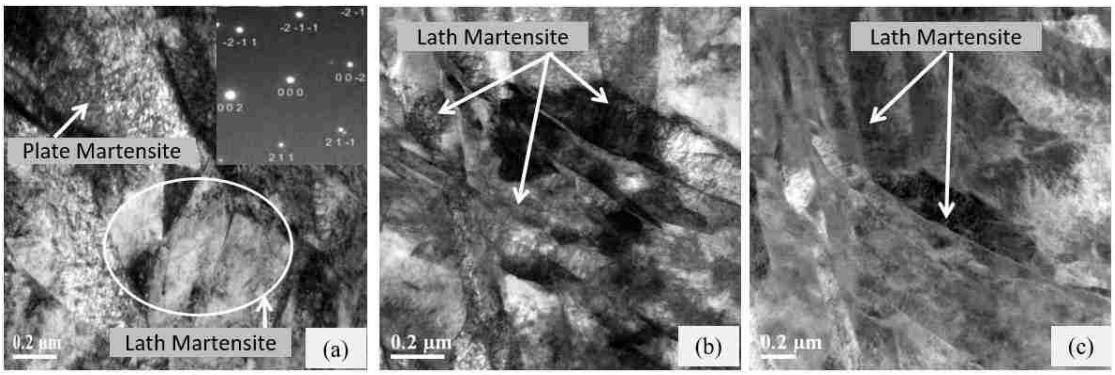

Figure 4. 7 (a) TEM bright field image of lath martensite with SAED pattern, (b) STEM bright field image, (c) STEM dark field image with lath martensite in the dilution zone.

Fig. 4.8 reveals more bright field STEM images of the dilution zone showing parallel twins (Figs. 4.8a-b), carbide precipitates (Fig. 4.8b), and another type of precipitates with tangled dislocation (Fig. 4.8c) in the dilution zone. Various sizes of twins were observed in this zone that varied in width and length. The large size twins were 75-128 nm in width and 2.1-2.9 µm in length, while the medium size twins were 33-44 nm in width and 500-600 nm in length. Small sizes of 20 nm width and 390 nm length of twins were also observed in this zone. These twins are known as the primary sources of martensitic transformation [18], [19].

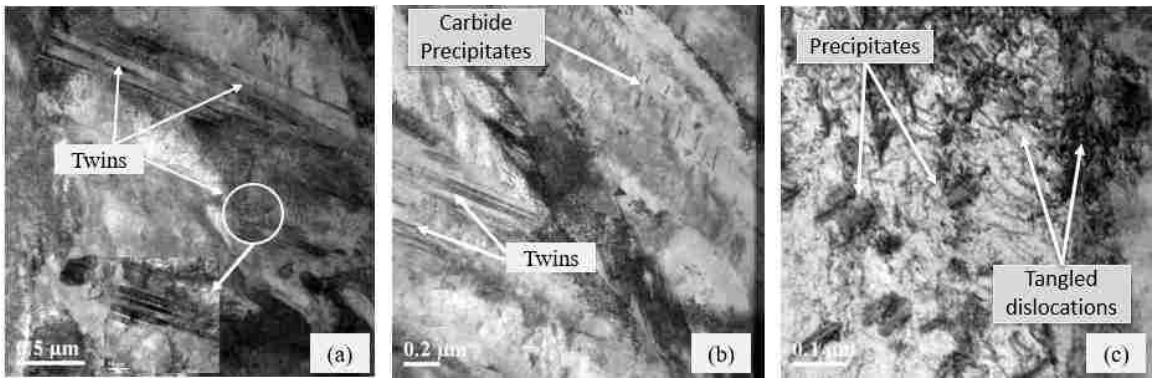

Figure 4. 8 (a) STEM bright field images of twins, (b) carbide precipitates, (c) typical precipitates with tangled dislocations in the dilution zone.

The carbide phases observed (Fig. 4.8b) in this zone were approximately 10-20 nanometers in width and 120-160 nm in length, which is slightly larger than those found in the bead zone. They were found embedded in the martensite plate. These are $M_{23}C_6$ types carbide mainly $Cr_{23}C_6$ phase as per X-ray diffraction results shown in Fig. 4.12 in the discussion section. Apart from the carbide phases, another nano-sized distinct precipitate approximately 25 nm in width and 90 nm in length (Fig. 4.8c) was observed in this zone that was mainly found within the tangled dislocations, where EDS analyses showed a higher percentage of carbon.

4.3.3 Interface Zone

Fig. 4.9a is a TEM bright field image that reveals lath martensite in the interface zone between the dilution and HAZ. The respective SAED pattern in Fig. 4.9a confirmed that these lath martensite morphologies were belonged to ά-martensite and formed on the zone axis of [111]. Fig. 4.9b shows STEM Bright field images of large lath martensite. The width of lath martensite found in the interface area was between 1 μm - 0.9 μm, which was bigger than the width found in the dilution zone (between 0.4 - 0.6 μm). In Fig. 4.9c, the TEM dark field image reveals a very thin film of retained austenite (identified as the illuminated phases in dark field images) in the interface zone. This parent phase was leftover during the sudden diffusionless military transformation with the synchronized movement of atoms to the product martensite. The retained austenite was identified in a similar way by Bhadeshia [20] on the martensitic transformation in AISI 4340 type steel.

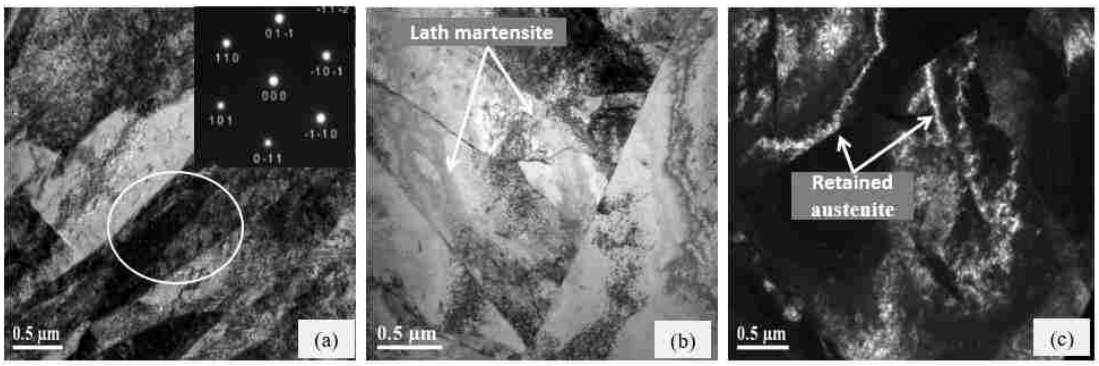

Figure 4. 9 (a) TEM bright field image of lath martensite morphology with respective SAED pattern; (b) STEM Bright field images of lath martensite; (c) TEM dark field image of retained austenite in the interface zone.

Discussions

The OM/SEM studies provided an overall mapping of the solidification pattern and microstructural evolutions in the three clad regions of bead zone, dilution zone, and the interface zone (between the dilution and the HAZ) for a single bead laser cladding of 420 SS. The overall solidification pattern varied from the planer to columnar and to the equiaxed grains, as shown in Fig. 4.3. The solidification parameters, e.g., temperature gradient (G), the solid/liquid interface growth rate (R), and the G/R ratio, can explain the grain morphology[21]. Fig. 4.10 shows the variation of G, R, and G/R ratio in the bead zone, dilution zone, and interface with the HAZ. These parameters were calculated from the authors' earlier study to correlate with the grain morphology observed in this study [22]. As shown in Fig. 4.10, the G decreased from a high value (6647 °C/cm) in the interface zone to a low value (5623 °C/cm) at the top of the bead zone, while the R value increased in those respective zones from 1.7 cm/s to 2.6 cm/s. The value of G/R ratio also decreased with the increasing value of R in those zones.

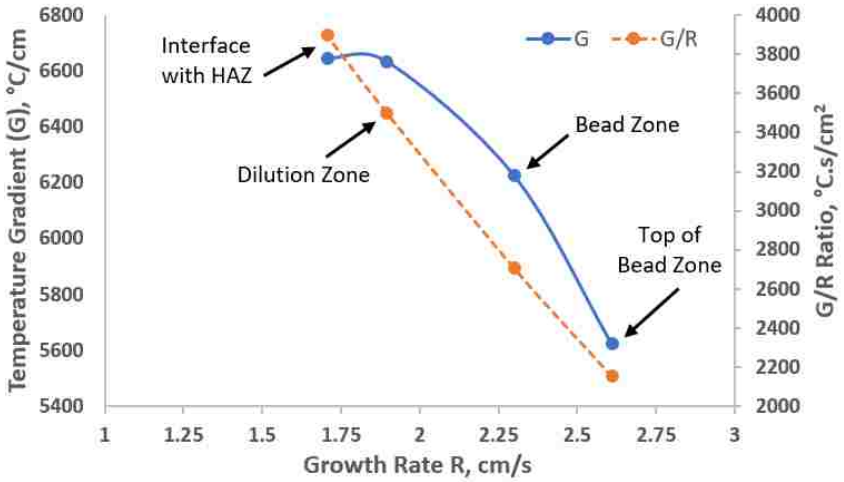

Figure 4. 10 Variation of the temperature gradient (G), solid/liquid interface growth rate (R), and G/R ratio in the bead zone, dilution zone, and interface with the HAZ (data are adopted from the authors' earlier work [22]).

An inversed relationship was revealed between the G and R as well as the G/R and R, which showed a significant effect on the grain morphologies. As can be seen in Figs. 4.3b and 4.10, comparatively a higher G value corresponding to a lower R in the interface zone resulted in mostly columnar grains, while a lower G value with a higher value of R in the bead zone leads to equiaxed grain. Similarly, the G/R ratio indicated a very strong linear relationship with the R and showed an important impact on the grain morphologies. As observed in Figs. 4.3 and 4.10, a higher value of G/R in the interface zone (3896 °C.s/cm^2) leads to mainly columnar grain while a lower value of G/R at the top of the bead zone (2154 °C.s/m^2) leads to equiaxed grain. Since the dilution zone was located in between the interface and bead zone with a G/R value of 3499 °C.s/cm^2, it consisted of both columnar and equiaxed grain. Zhang et al. [23] reported a similar trend indicating that G was higher in the interface zone near the substrate (bottom of the molten pool) and lower at the top of the bead zone. They also found an inverse relationship between the G and R as R was higher at the top of the bead zone and lower at the interface zone with a value close to zero.

Kou [21] studied the effect of G and R on the microstructure resulting from welding (Fig. 4.11). This investigation concluded that the grain structure changed from planer to columnar and to equiaxed or dendrites as the ratio of G/R decreased. It is important to note that the G/R ratio determines the solidification mode; however, the G.R product controls the scale of the solidified structure. If the G/R ratio reduces below a critical value as it happens in the laser cladding process, then a transition from columnar to equiaxed grain occurs [10], [24]. At the same time, the higher the G.R product, the higher the cooling rate, which results in a finer grain structure.

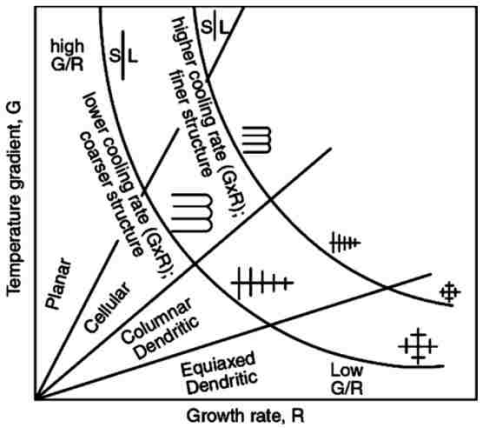

Figure 4.11 Effect of solidification parameters (e.g., G and R) on the grain structures (Reprinted with permission from reference [21]).

The XRD analysis as shown in Fig. 4.12 has confirmed the major metallurgical phases like martensite and delta ferrite, along with other minor phases in their respective crystallographic planes [1]. The presence of these nonequilibrium phases was a direct consequence of the rapid solid-state phase transformation from the primary delta ferrite to austenite upon rapid cooling of melt-pool below the temperature of 1100°C.

Upon rapid solidification, the austenite transformed to martensite when the temperature dropped below the martensite start temperature (M_s). The regular diffusive

solid-state transformations were suppressed due to the super high cooling rate and the high degree of undercooling observed in the laser cladding [16], [25]–[27]. The volume fraction of martensite increased rapidly upon the completion of martensitic transformation at martensite finish temperature (M_f). However, some delta ferrites (enriched in ferrite promoting element, e.g., Cr) that did not transform to austenite on further cooling were found as residuals along the grain boundary or sub-grain boundary at the end of solidification, as observed in Fig. 4.4.

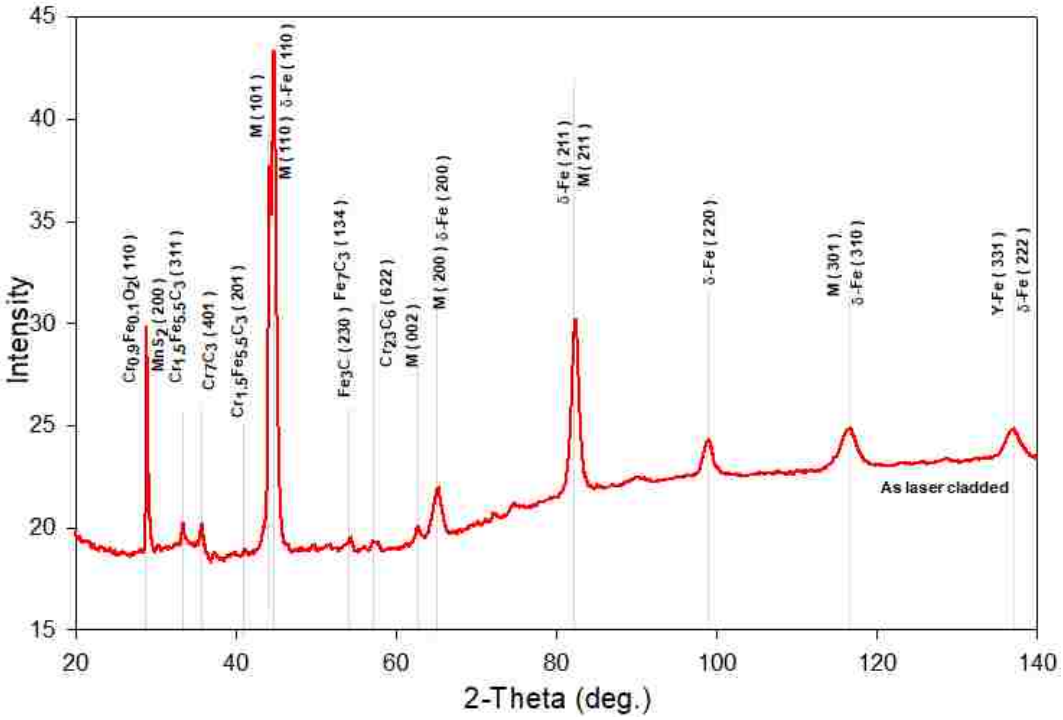

Figure 4. 12 X-Ray diffraction pattern of laser-cladded 420 stainless steel single bead sample (data are adopted from the authors' earlier work [1]).

The detailed TEM study and the SAED pattern shown in the results section (Figs. 4.6-4.9) revealed ά-martensite in all three zones. Generally, ά -martensite has a body-centered tetragonal (BCT) structure. Due to the relatively low carbon content and a low

percentage of interstitials, this type of martensite is introduced here as BCC rather than BCT [28]. Four types of morphology of ά-martensite substructure were revealed in this study, namely, plate martensite, thin plate martensite, lenticular martensite, and lath martensite throughout the bead zone, the dilution zone and in the interface zone between dilution and the HAZ.

The bead zone showed plate martensite packet composed of thin plate and lenticular martensite morphologies (Fig. 4.6). The dilution zone shows a combination of plate martensite lath martensite morphologies (Fig. 4.7), while the interface zone possessed only the lath morphology (Fig. 4.9). However, observing several martensite types indicated that a high cooling rate and undercooling had occurred in those three zones. In the authors' earlier study [22] of the simulation of laser cladding for the same alloy, an abrupt variation of temperature distribution with time was observed (Fig. 4.13a) that subsequently generated a high variation of cooling rates (Fig. 4.13b) in those zones. These rates will vary differently with different alloy and different process parameters.

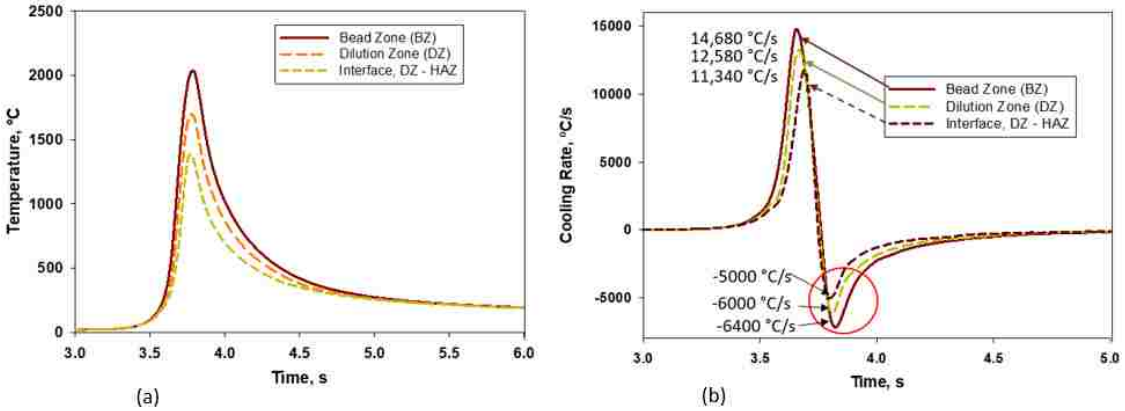

Figure 4. 13 (a) Variation of Temperature and (b) cooling rate with time in the bead zone, dilution zone, and interface zone between the dilution and heat affected zone (HAZ) (data are adopted from the authors' earlier work [22]).

The martensitic phase transformation was occurred at a high cooling rate of 14,680 ºC/s presented in Fig. 4.13b resulting in plate martensite in the bead zone for this type of steel. The dilution and interface zone showed a comparatively lower cooling rate of 12,580 ºC/s and 11,340 ºC/s, respectively resulting a combination of both plate and lath martensite in the dilution as well as large sized lath in the interface zone. These cooling rates were much higher than the conventional water quenching (150 ºC/s) of medium or high carbon steel [29]. However, a sharp drop in cooling rate to an extreme negative value, as shown in Fig. 4.13b indicated the occurrence of a high degree of supercooling during the solidification stage of laser cladding. This contributes to the formation of metastable and nonequilibrium phases, such as twins, high density of dislocation, and nano-sized carbide phases of $M_{23}C_6$ observed in microstructure (Figs. 4.6-4.9). The density of dislocations observed in the bead zone (Fig. 4.6e) was apparently higher than the dilution zone (Fig. 4.8c). The nano-sized carbide particles (mainly $Cr_{23}C_6$) observed in the bead and dilution zones (Figs. 4.6d and 4.8b) were free from interacting with dislocations and the size of the carbide particles increased in the dilution zone. Dislocation activities can be observed clearly in Fig 4.8c as well as precipitates highlighted in the figure. EDS analyses showed that this precipitate to be rich in (Fe.Cr)C. XRD analysis (Fig. 4.12) confirmed the existence of a $Cr_{1.5}\,Fe_{5.5}C_3$ phase. These nanoscale metastable precipitates were expected to be $Cr_{1.5}\,Fe_{5.5}C_3$ and might be formed during the martensitic transformation. Easterling and Swann [30] reported interactions between a similar kind of precipitates and dislocations. When the precipitate encircled with two parallel dislocations, the martensite discs was formed, which eventually transformed the precipitates into martensite and acted as a source of martensite nucleation. Several other investigations[31]–[39] have also

reported the nature of interactions between dislocations and precipitates through experiments, analytical modeling, and computer simulations. In all cases, those nanoscale precipitates were found with tangled dislocations, and the effect of those precipitates were correlated with the precipitation hardening leading to an increase of yield strength. Apart from the above discussions on precipitates, internal twins were largely observed in the plate martensite found in the bead zone (Fig. 4.6). Kelly and Nutting [40] observed internal structure of parallel twins, each about 0.1 μm thick within martensite plates. Gular et al. [41] had a similar observation about the internal twins and plate martensite. These internal twins were believed to be one of the main characteristics of plate martensite. Generally, plate martensite was found in the high carbon quenched steel [42]. It was unusual to see the plate martensite in this low carbon stainless steel. However, having a high cooling rate in the bead zone and the dilution zone resulted this martensitic transformation. Also, alloying elements might influence the formation of this plate martensite morphology [48]. In addition, various sizes parallel twins were observed in the dilution zone (Fig. 4.8). These parallel twins were the primary sources of martensite. Hence, a solid-state martensitic transformation had occurred in the laser cladding of 420 SS. This transformation is found to be related to the formation of twinning. Christian [18], [19]and Nishiyama [43], [44] also reported twinning as the initial stage of martensitic transformation. All the above-mentioned microstructural features have contributed significantly towards the high hardness reported in Fig. 4.14. The transformation from plate to lath martensite, increase in lath size, increase in carbide length, and decrease in area fraction of high dislocation density regions explained the decrease in hardness in the dilution zone.

Fig. 4.14 also shows that the bead zone has a very high tensile stress (486 MPa) at the top, which is almost equivalent to the yield strength of this alloy. This stress gradually decreases throughout most of the bead zone until it transforms to compressive stress (up to 275 MPa) in the bottom of the bead zone. This compressive stress sharply increased in the dilution zone from 280 MPa to 1002 MPa and showed an inflection point at the dilution zone interface, where it then transformed to tensile stress in the HAZ.

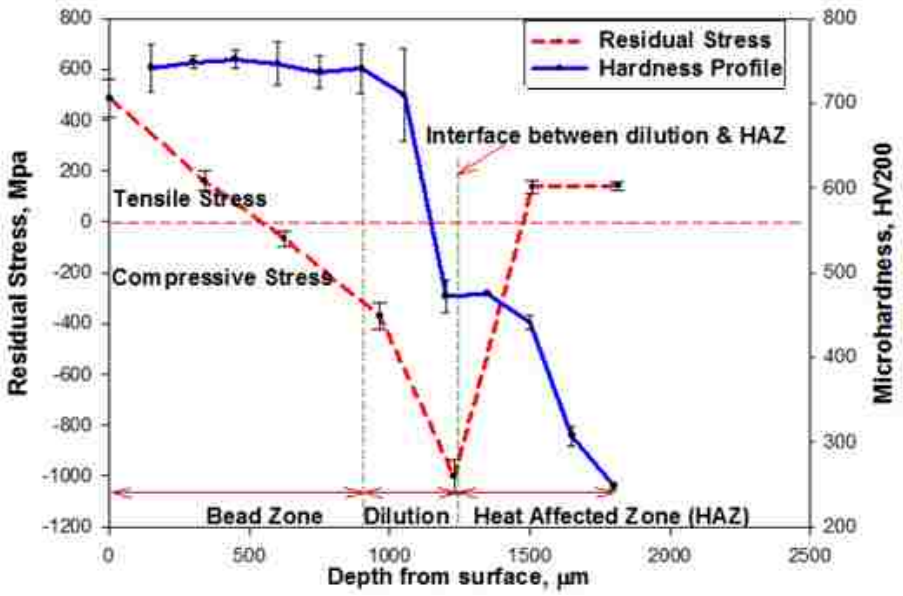

Figure 4. 14 Microhardness and residual stress profile in the bead zone and dilution zone (data are adopted from the authors' earlier work [1]).

The variation in the residual stress can be explained by martensitic transformation in those respective zones. The martensitic transformation first occurred in the bead zone due to the high rate of cooling, as was confirmed by the formation of plate-like martensite. Subsequently, phase transformation happened in the dilution and interface zone accompanied with an increase in volume. The volume expansion in the dilution and interface zone was constrained by the bead zone that had already transformed into rigid

plate-like martensite. Hence this restraint resulted in residual compressive stress in the dilution and interface zone while creating tensile stress in the bead zone. Thus, the anisotropic volume change during the martensitic transformation caused the residual stress in those three zones [45], [46]. Similar observations were reported by Oliveira et al. in Co-based laser clad layers [47].

Thus, the martensitic transformation with various morphologies provided crucial information about the development of residual stress throughout the bead and dilution zone as well as in the interface between the dilution and heat affected zone. However, the microhardness is also affected by the other factors such as nano carbide precipitations, dislocation density, and distribution of chemical composition.

Summary and Conclusion

The comprehensive microstructural analysis was performed on three distinct zones of bead zone, dilution zone, and interface zone for a laser-cladded AISI 420 SS single bead. The results are highlighted as follows:

1. The microstructural solidification pattern was varied from the columnar grains in the interface and dilution zone to the equiaxed grains in the bead zone as the value of G/R decreased with an increasing value of R in those respective regions.
2. Formation of plate-like martensite in 420SS was attributed to the high rate of cooling in the bead zone along with the effect of alloying elements (Cr).

3. The martensitic matrix showed various morphologies of ά-martensite, namely, plate martensite, thin plate martensite, and lenticular martensite in the bead zone; plate and lath martensite in the dilution zone, while large lath martensite in the interface zone.
4. Twinning may be considered as the primary sources of martensitic transformation due to substantial number of twins observed in the dilution zone.
5. The morphological differences of ά-martensite and presence of various metastable phases observed in each zone have significantly contributed to the variation of hardness.
6. Extremely high cooling rates caused the martensitic phase transformation during the laser cladding of 420 SS. The first martensitic transformation occurred in the bead zone with the formation of plate like martensite. Subsequently, the second phase transformation occurred in the dilution and interface zone with the formation of both plate and lath like martensite that created high compressive stress in these zones and high tensile stress in the bead zone.

References.

[1] M. K. Alam, A. Edrisy, J. Urbanic, and J. Pineault, "Microhardness and Stress Analysis of Laser - Cladded AISI 420 Martensitic Stainless Steel," *J. Mater. Eng. Perform.*, vol. 26, no. 3, pp. 1076–1084, 2017.

[2] S. H. Baghjari and S. A. A. Akbari Mousavi, "Effects of pulsed Nd:YAG laser welding parameters and subsequent post-weld heat treatment on microstructure and hardness of AISI 420 stainless steel," *Mater. Des.*, vol. 43, pp. 1–9, 2013.

[3] D. Lepski and F. Bruckner, "Laser cladding," in *The Theory of Laser Materials Processing*, Online., vol. 119, J. Dowden, Ed. Springer Netherlands, 2009, pp. 235–279.

[4] S. K. Mishra, “Laser Cladding and Alloying for Aerospace Applications,” in *Aerospace Materials Handbook*, S. Zhang and D. Zhao, Eds. CRC Press, Tailor & Francis Group, 2013.

[5] C. S. Toyserkani, E., Khajepour, A., *Laser Cladding*. New York: CRC Press, 2005.

[6] J. Chen, L. Xue, and S. Wang, “Microstructure Characterization of Laser-Consolidated AISI 420 Stainless Steel,” in *Materials Science and Technology (MS&T) 2008*, 2008, no. Lc, pp. 1388–1396.

[7] M. Zhong and W. Liu, “Laser surface cladding: the state of the art and challenges,” *Proc. Inst. Mech. Eng. Part C J. Mech. Eng. Sci.*, vol. 224, no. 5, pp. 1041–1060, Jan. 2010.

[8] S. Bhattacharya, G. P. Dinda, A. K. Dasgupta, and J. Mazumder, “Microstructural evolution of AISI 4340 steel during Direct Metal Deposition process,” *Mater. Sci. Eng. A*, vol. 528, no. 6, pp. 2309–2318, 2011.

[9] S. Da Sun, Q. Liu, M. Brandt, M. Janardhana, and G. Clark, “Microstructure and Mechanical Properties of Laser Cladding Repair of AISI 4340 Steel,” in *28th International Congress of the Aeronautical Sciences (ICAS)*, 2012, no. i, pp. 1–9.

[10] I. Hemmati, V. Ocelík, and J. T. M. De Hosson, “Microstructural characterization of AISI 431 martensitic stainless steel laser-deposited coatings,” *J. Mater. Sci.*, vol. 46, pp. 3405–3414, 2011.

[11] X. Wu, “Rapidly solidified nonequilibrium microstructure and phase transformation of laser-synthesized iron-based alloy coating,” *Surf. Coatings Technol.*, vol. 115, pp. 153–162, 1999.

[12] M. K. Alam, J. Urbanic, S. M. Saqib, and A. Edrisy, “Effect of Process Parameters On The Microstructural Evolutions of Laser Cladded 420 Martensitic Stainless Steel,” in *Materials Science and Technology Conference Proceedings (MS&T15), October 4-8*, 2015, pp. 35–54.

[13] C. Köse and R. Kaçar, “The effect of preheat & post weld heat treatment on the laser weldability of AISI 420 martensitic stainless steel,” *Mater. Des.*, vol. 64, pp. 221–226, 2014.

[14] M. M. A. Khan, L. Romoli, R. Ishak, M. Fiaschi, G. Dini, and M. De Sanctis, “Experimental investigation on seam geometry, microstructure evolution and microhardness profile of laser welded martensitic stainless steels,” *Opt. Laser Technol.*, vol. 44, no. 5, pp. 1611–1619, 2012.

[15] E. Weidmann, “Struers Application Notes - Metallographic Preparation of Stainless Steel,” Struers A/S, Copenhagen, 2005.

[16] J. Lippold and D. Kotecki, “Welding Metallurgy and Weldability of Stainless Steels,” *Wiley-Interscience*. John Wiley & Sons, New Jersey, pp. 56–86, 2005.

[17] A. Shibata, T. Murakami, S. Morito, T. Furuhara, and T. Maki, “The origin of midrib in lenticular martensite,” *Mater. Trans. Japan Inst. Met.*, vol. 49, no. 6, pp. 1242–

1248, 2008.

[18] J. W. Christian, “Twinning and Martensititc Transformation,” *J. Phys. Colloq.*, vol. 35, pp. C7-64, 1974.

[19] J. W. Christian, “Military Transformations: An introductory Survey,” in *Physical properties of martensite and bainite, {Special Report} 93*, The Iron and Steel Institute, 1965, pp. 1–25.

[20] H. K. D. H. Bhadeshia and D. V. Edmonds, “New Crystallographic and Morphological Observations on the Martensite Transformation in AISI 4340 Type Steel,” in *International Conference on Martensitic Transformation, Boston, USA*, 1979, p. IV-9-13.

[21] S. Kou, *Welding Metallurgy, Second Edition*, vol. 822, no. 1–3. 2003.

[22] N. Nazemi, J. Urbanic, and M. K. Alam, “Hardness and residual stress modeling of powder injection laser cladding of P420 coating on AISI 1018 substrate,” *Int. J. Adv. Manuf. Technol.*, vol. 93, no. 9–12, pp. 3485–3503, 2017.

[23] Z. Zhang, P. Farahmand, and R. Kovacevic, “Laser cladding of 420 stainless steel with molybdenum on mild steel A36 by a high power direct diode laser,” *Mater. Des.*, vol. 109, no. August, pp. 686–699, 2016.

[24] W. Kurz, C. Bezençon, and M. Gäumann, “Columnar to equiaxed transition in solidification processing,” *Sci. Technol. Adv. Mater.*, vol. 2, no. 1, pp. 185–191, 2001.

[25] M.McGuire, *Stainless Steels For Design Engineers*, First. Material Park, Ohio: ASM International, 2008.

[26] P. K. S. Erhard Klar, *Powder Metallurgy Stainless Steels: Processing, Microstructures, and Properties*. ASM International, 2007.

[27] L. Costa, R. Vilar, T. Reti, R. Colaco, A. M. Deus, and I. Felde, “Simulation of phase transformations in steel parts produced by laser powder deposition,” *Mater. Sci. Test. Informatics Ii*, vol. 473–474, pp. 315–320, 2005.

[28] R. Naraghi, “Martensitic Transformation in Austenitic Stainless Steels - MASc Thesis,” Royal Institute of Technology, SE-100 44 Stockholm, Sweden, 2009.

[29] H. J. French and Z. Klopsch, “Initial temperature and mass effects in quenching, Technologic Papers of the Bureau of Standards, US Government, V19, T-295,” 1922.

[30] K. E. Easterling and P. R. Swann, “The Mechanism of Nucleation of Martensite in Precipitates of Iron in a Copper Matrix,” in *Mechanism of Phase Transsformation*, 1968, pp. 152–155.

[31] D. J. Bacon, Y. N. Osetsky, and D. Rodney, “Chapter 88 Dislocation-Obstacle Interactions at the Atomic Level,” *Dislocations in Solids*, vol. 15, no. 09, pp. 1–90, 2009.

[32] A. Dutta, M. Bhattacharya, and P. Barat, “Statistics of dislocation pinning at localized obstacles,” *J. Appl. Phys.*, vol. 116, no. 14, 2014.

[33] A. Keyhani and R. Roumina, “Quantification of Dislocation-Precipitate Interactions,” pp. 1–20, 3033.

[34] W. Bin, L. Zhenyu, Z. Xiaoguang, W. Guodong, and R. D. K. Misra, “Precipitation behavior of nanoscale cementite in hypoeutectoid steels during ultra fast cooling (UFC) and their strengthening effects,” *Mater. Sci. Eng. A*, vol. 575, pp. 189–198, 2013.

[35] A. Ramar and R. Schäublin, “Analysis of hardening limits of oxide dispersion strengthened steel,” *J. Nucl. Mater.*, vol. 432, no. 1–3, pp. 323–333, 2013.

[36] J. Fu, G. Li, X. Mao, and K. Fang, “Nanoscale cementite precipitates and comprehensive strengthening mechanism of steel,” *Metall. Mater. Trans. A Phys. Metall. Mater. Sci.*, vol. 42, no. 12, pp. 3797–3812, 2011.

[37] B. A. Bilby, “On the interactions of dislocations and solute atoms,” *Proc. Phys. Soc. Sect. A*, vol. 63, no. 3, pp. 191–200, 1950.

[38] E. Clouet, S. Garruchet, H. Nguyen, and M. Perez, “Dislocation interaction with C in a-Fe: A comparison between atomic simulations and elasticity theory,” *Acta Mater.*, vol. 56, pp. 3450–3460, 2008.

[39] A. Lehtinen, L. Laurson, F. Granberg, K. Nordlund, and M. J. Alava, “Effects of precipitates and dislocation loops on the yield stress of irradiated iron,” *Sci. Rep.*, vol. 8, no. 1, pp. 1–12, 2018.

[40] P. M. Kelly and J. Nutting, “Strengthening Mechanism in Martensite,” in *Physical properties of martensite and bainite, {Special Report} 93*, The Iron and Steel Institute, 1965.

[41] E. Güler, T. Kirindi, and H. Aktas, “Comparison of thermally induced and deformation induced martensite in Fe-29% Ni-2% Mn alloy,” *J. Alloys Compd.*, vol. 440, no. 1–2, pp. 168–172, 2007.

[42] G. Krauss and A. R. Marder, “The morphology of martensite in iron alloys,” *Metall. Trans.*, vol. 2, no. 9, pp. 2343–2357, 1971.

[43] Z. Nishiyama, *Martensitic Transformations*. New York: Academic Press Inc., 1978.

[44] Z. Nisrayama and K. Shimizu, “Recent Study of the Martensite by Transmission Electron Microscopy in Japan,” *J. Electronmicrosc.*, vol. 12, no. 1, pp. 28–36, 1963.

[45] A. Weise and G. Fritsche, “Martensitic Transformation and Residual Stress Generation During Thermomechanical Treatment,” *Mater. Manuf. Process.*, vol. 12, no. 1, pp. 125–135, 1997.

[46] Z. Hu and J. Zhao, “Effects of martensitic transformation on residual stress of P91 welded joint,” *Mater. Res. Express*, vol. 5, no. 096528, 2018.

[47] U. de Oliveira, V. Ocelík, and J. T. M. De Hosson, “Residual stress analysis in Co-

based laser clad layers by laboratory X-rays and synchrotron diffraction techniques," *Surf. Coatings Technol.*, vol. 201, no. 3–4, pp. 533–542, 2006.

[48] M. Umemoto, E. Yoshitake and I. Tamura, "The Morphology of Martensite in Fe-C, Fe-NiC, Fe-Cr-C Alloys," *Journal of Materials Science*, vol. 18, pp. 2893-2904, 1983.

CHAPTER 5 Electron Backscatter Diffraction (EBSD) Analysis of Laser-Cladded AISI 420 Martensitic Stainless Steel

Introduction

The use of martensitic stainless-steel powder with the laser-cladding (LC) process has increased in surface treatment applications for the die and tool industry, as well as in the pipeline industry [1–5]. AISI 420 martensitic stainless steel (MSS) powder is widely used in the refurbishment of the worn surface of tools and dies, using the laser cladding process, due to the high hardness and moderate corrosion resistance of the coated surface [6]-[7]. LC is a novel process that uses a high-power laser beam to melt coaxially fed metallic powders (or wire) to coat part of a substrate or to make a functional component following a computer-controlled tool path and CAD file [8]. The LC process offers distinct advantages over the conventional cladding by welding, as it creates bead zone with high hardness, 100% diffusion bonding with a low dilution zone, and a minimal heat-affected zone (HAZ) in the substrate [9],[10]. However, LC is associated with rapid solidification with an extremely high cooling rate to the extent of 14,580 °C/s[11]. The high cooling rate promotes martensitic transformation in the solidified 420 MSS without introducing an additional post-processing technique. This solid-state transformation is involved with the volume changes of martensite and associated residual stress and strain that lead to coating distortion and failure.

Several researchers [6,12–20] studied the laser cladding of 420 MSS, AISI H13 tool steel, and Co-based alloys deposited onto steel substrates. Alam [6] et al. examined the residual stress and hardness profile of laser-cladded 420 MSS. They observed a high

level of tensile stresses in the bead zone and HAZ and a high level of compressive stress in the dilution zone. Chen et al. [18] investigated the development of process-induced residual stresses in the clad and their correlation with microstructural evolutions in the clad and heat-affected zone (HAZ) of laser-cladded and post cladding heat-treated AISI P20 tool steel on a pre-hardened wrought P20 base material. Zhang et al.[20] studied a heat transfer model, the effects of the laser-powder interaction, the temperature-dependent material properties, the temperature history, the temperature gradient, and solidification rate related to laser cladding of 420 MSS modified with 4% molybdenum on a mild steel A36 substrate. In a recent study with the laser-cladded 420 MSS, Alam et al. [11] observed that the columnar grains were epitaxially growing from the interface between the heat affected zone and dilution zone. In the same study [11], TEM analysis of the 420 MSS revealed the presence of plate martensite, lath martensite, and a combination of both with a high density of dislocations in those three regions. However, the microstructural behavior in terms of grain orientation and image quality of the crystal structure in the evolved phases of 420 MSS fabricated with laser cladding need to be further studied to understand the correlation between the residual stress/strain and distortion in the crystal lattice of the coated materials. To the best of the authors' knowledge, the grain misorientation and image quality of the grain substructure associated with the martensitic transformation were not yet studied in the earlier study.

The objective of this study is to characterize the microstructure of a single bead coating in the bead zone (BZ), the dilution zone (DZ), and an interface zone (IZ) between the dilution and the heat affected zone (HAZ) using the EBSD technique. Electron backscatter diffraction (EBSD) or orientation imaging microscopy (OIM) provides

information on the image quality, grain orientation, microstructure, and texture of polycrystalline materials [21]. These data sets allow the researchers to construct some important maps such as the inverse pole figure (IPF), the grain orientation spread (GOS), and the grain average image quality (IQ), etc. These maps are helpful to determine the grain orientation for the different phases, grain misorientations, dislocation densities, and strain or deformation in the crystal lattice structure [21]. To accomplish this objective, three approaches were considered in evaluating the grain orientation, grain misorientation, as well as the image quality of the martensitic sub-structure generated in the laser-cladded AISI 420 MSS. The first approach was to investigate the grain orientation using Inverse pole figure (IPF) mapping, while the second approach was to investigate the grain misorientation by measuring the GOS, as well as the third approach was to investigate the diffraction pattern by measuring the IQ metrics in those regions to evaluate associated residual strain or stress developed in those zones respectively.

Materials and Experimental Methodologies

AISI 420 MSS powder with grain sizes between 53-180 μm and a powder density of 4.37 g/cm^3 was used in a coaxial powder laser cladding process to clad the powder materials onto a 10 mm thick flat bar of medium carbon steel substrate. The laser cladding was performed using a 4 kW fiber connected diode laser coupled to an articulated robotic arm. The chemical composition of the powder is shown in Table 5.1.

A 2.5 kW high power laser beam was used to generate a molten pool on the AISI 1018 steel substrate with the 420 MSS metallic powders injected simultaneously at the rate of 20 g/min with coaxially flowing argon gas (as a carrier and shield to protect the molten pool from oxidation) along with other process parameters as shown in Table 5.2 and Fig.

5.1a. A series of single beads were deposited on the substrate by following the process parameters, as stated in Table 5.2. For this EBSD study, a sample was selected from those series of single beads block, as shown in Fig. 5.1b.

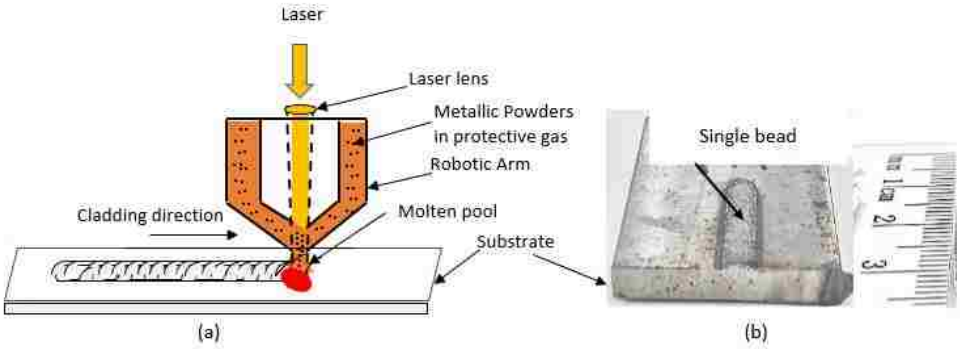

Figure 5. 1 (a) Schematic view of the laser cladding process; (b) Cross-sectional image of single bead laser-cladded sample with AISI 420 Martensitic Stainless Steel

Table 5. 1 Chemical composition of AISI 420 martensitic stainless-steel powder

Chemical Elements	**Percentage of composition (%)**
Carbon	0.23
Manganese	1.2
Chromium	12.6
Silicon	0.5
Iron	Balance

Table 5. 2 Parameters of the laser cladding process

Process Parameters	**Data**
Laser power	2500 W
Laser speed	10 mm/s
Powder feed rate	20 g/min
Focal length of lens	400 mm
Contact tip to workpiece distance	21 mm
Laser spot diameter	4.3 mm

The single bead sample was cut transversely by using a wire EDM. Then it was mounted in epoxy powder in a Buehler hot mounting press. The metallography sample preparation was done for EBSD characterization by using a series of grinding and polishing solutions as per Struers' application note for stainless steel [22].

The Electron Backscatter Diffraction (EBSD) analyses were performed in a field emission scanning electron microscope (FEG-SEM) (Nova Nano-SEM, FEI) that is equipped with Orientation Imaging Microscopy software by OIM 6.2 by EDAX. Three OIM scan areas (300x300 μm) were selected from the center of the BZ (center), DZ (center), and IZ between the DZ (interface) and HAZ. Those respective areas were scanned using a step size of 0.1 μm. Using the EBSD technique, Inverse pole figure (IPF), Grain Orientation Spread (GOS), and grain average Image Quality (IQ) were measured.

Results

Fig. 5.2 shows the cross-sectional view of an OM image (Fig. 5.2a) and an SEM image (Fig. 5.2b) of the single bead laser-cladded 420 SS sample with the bead zone, dilution zone, interface and the heat affected zone (HAZ) labeled on the image. The bead zone is the upper part, and the dilution zone is the lower part of the clad. The substrate base line is marked as a solid white line for a single bead track (Fig. 5.2) of a laser- cladded sample. The dilution zone has two parts: the upper part, which mingled with the bead zone, and the lower part that has a clear interface (marked as a dotted white curved line) with the heat-affected zone of the substrate [11]. For this reason, an interface zone (lower part of the dilution zone with HAZ) was also chosen to be examined. Heat affected zone (HAZ) is within the AISI 1018 steel substrate.

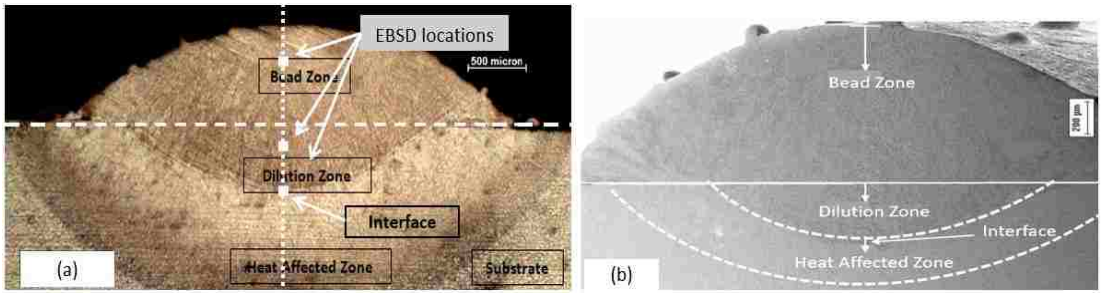

Figure 5. 2 Cross-sectional (a) OM image; (b) SEM image of a single bead AISI 420 Martensitic Stainless Steel: three zones are marked on the image.

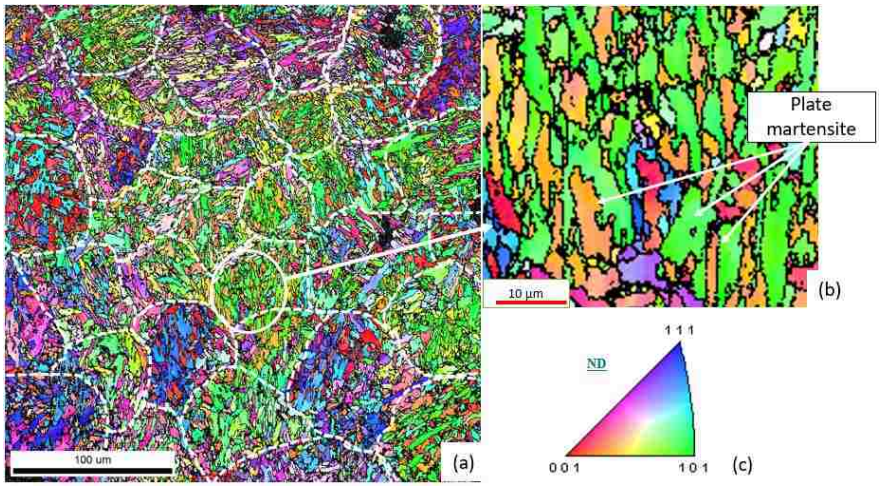

Figure 5. 3 (a) Electron Backscatter Diffraction (EBSD) Inverse Pole Figure (IPF) maps show martensite grain orientation in the cross-section of bead zone (BZ, center), (b) selected highlight from BZ; (c) stereographic triangle of IPF color map.

Figs. 5.3-5.5 show EBSD inverse pole figure (IPF) maps of three scans taken from the cross-section of the central bead zone (BZ, center), dilution zone (DZ, center), and interface zone (IZ) between the DZ (Interface) and HAZ respectively. The colors in Figs. 5.3-5.5 represent the crystallographic orientation normal to the observed planes in those zones, indicated in the stereographic triangle superimposed in those figures while the black lines show the boundaries between the sub-structures. These zones revealed the existence of various orientations and the hierarchical nature of martensitic structure (lath and plate) within the prior-austenitic grain boundary (PAGB, marked as white dotted lines), where

the packets of martensitic grains were oriented at a combination of different crystallographic planes such as {001}, {101}, {111), {112}, {102}, and {212}. The highlighted and selected portion of those maps shown with the respective zones (in Figs. 5.3-5.5 b) revealed the types of martensite substructures and their specific orientations with the color codes.

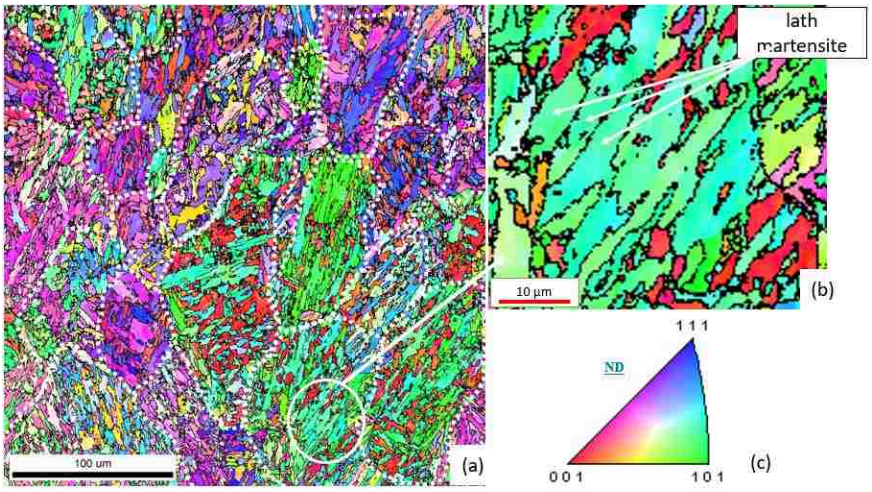

Figure 5. 4 (a) Electron Backscatter Diffraction (EBSD) Inverse Pole Figure (IPF) maps show martensite grain orientation in the cross-section of dilution zone (DZ, center); (b) selected highlight from DZ; (c) stereographic triangle of IPF color map.

Fig. 5.3 reveals equiaxed prior austenite grains (PAG) in the bead zone (BZ). The average PAG size in the BZ is ~62 microns, with an aspect ratio of 1.26. Fig. 5.4 shows a combination of both equiaxed and columnar type PAG grains in the center of dilution zone DZ (C), while Fig. 5.5 shows long columnar PAG in the dilution zone (DZ, interface) and planer grains in the interface zone (IZ). The average PAG size in DZ(C) and DZ(I) is ~51 and ~72, respectively, with the respective PAG aspect ratio of 2.03 and 2.91.

Fig. 5.6 shows the statistical analysis of the size distribution of martensite grains in the BZ, DZ (C), and DZ (I). It reveals that dilution zone (both in the center and interface)

has bigger sized martensitic grains (diameter up to 25 microns) compared to the bead zone with a higher percentage of area fraction of those grains.

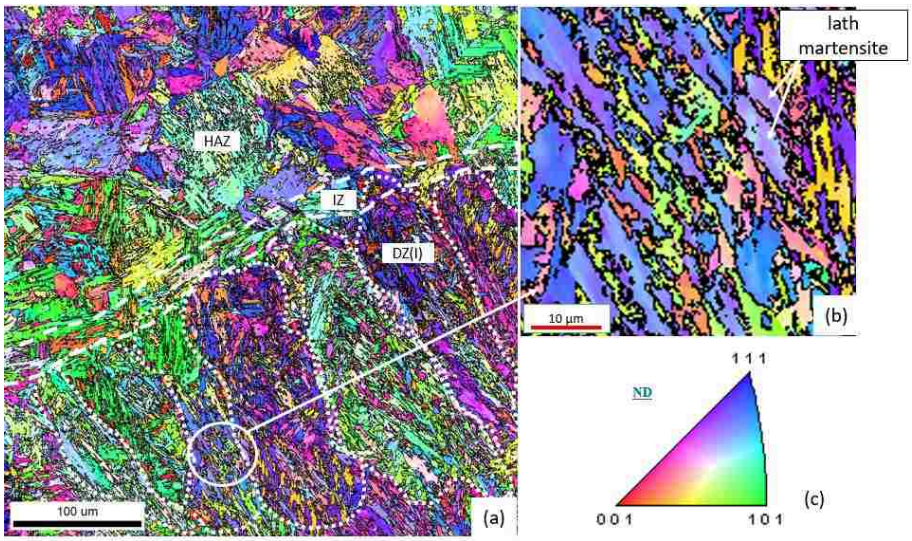

Figure 5. 5 (a) Electron Backscatter Diffraction (EBSD) Inverse Pole Figure (IPF) maps show martensite grain orientation in the cross-section of interface zone (IZ) between dilution zone (DZ, Interface) and heat affected zone (HAZ); (b) selected highlight from DZ(I); (c) stereographic triangle of IPF color map.

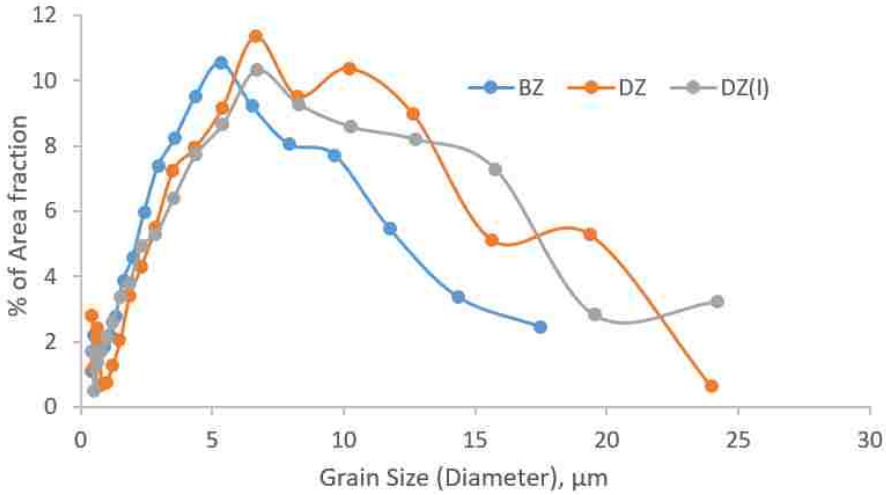

Figure 5. 6 Statistical analysis of grain size (martensite) distribution throughout the cross-section of bead zone (BZ, center), dilution zone (DZ, center), and Dilution zone (DZ, interface).

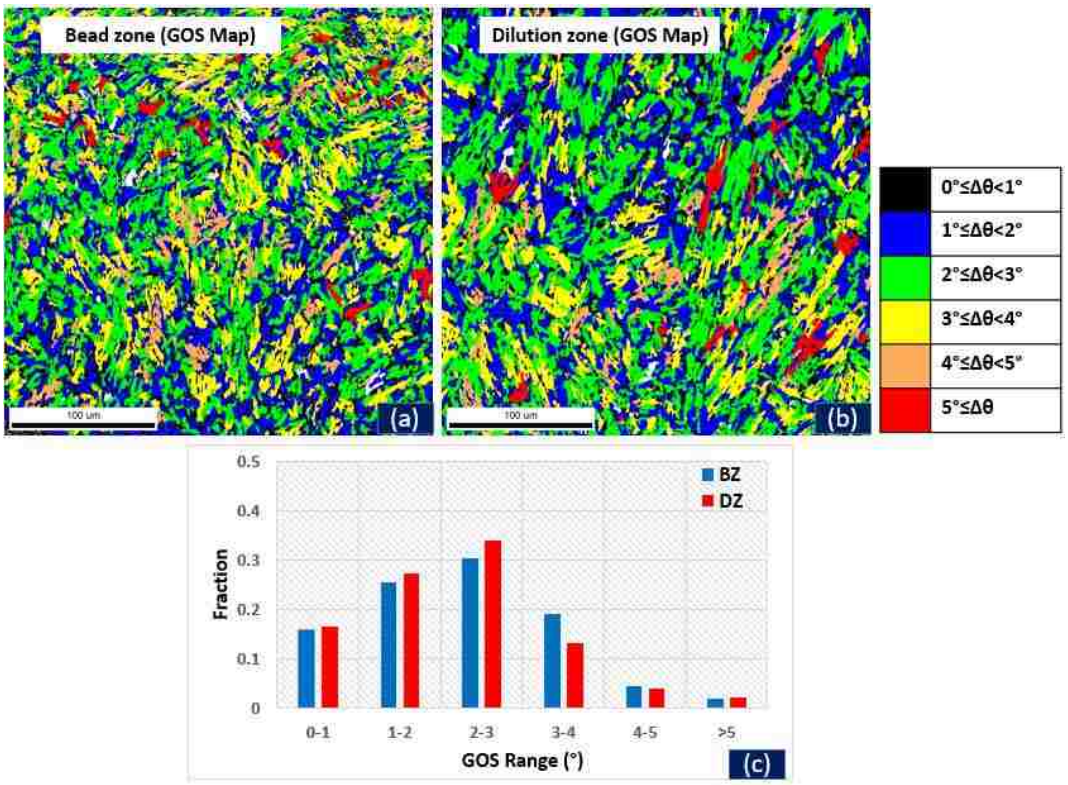

Figure 5. 7 Electron Backscatter Diffraction (EBSD) Grain Orientation Spread (GOS) maps show grain orientation in the cross-section of (a) bead zone and (b) dilution zone with color-coded grain misorientation at different GOS angle; (c) Bar chart shows fraction of grain in the Bead zone (BZ) and Dilution zone (DZ) against various GOS angle ranges.

Fig. 5.7 shows the Electron Backscatter Diffraction (EBSD) Grain Orientation Spread (GOS) maps in the cross-section of the bead zone (Fig. 5.7a) and the dilution zone (Fig. 5.7b) with color-coded grain misorientations at different GOS angle ranges. The GOS of a grain is defined as the mean value of misorientations between the average orientation of the grain and all pixels of the grain, while the GOS for a set of grains is the mean value of the GOS values of all grains [23]. Fig. 5.7c displays the quantification of grains against the various GOS angle ranges. It shows that a higher fraction of grains (26%) in the bead zone (BZ) have a high angle GOS (3°-5°) compared to the dilution zone (DZ), while the DZ shows a higher fraction of grains (78%) with a low angle GOS (0°-3°). However, the

differences for the very low (<1°) and very high angle (>5°) GOS in both zones were insignificant.

Fig. 5.8a shows an SEM image of a cross-section of the interface zone (IZ) between the Dilution Zone (DZ, Interface) and the Heat Affected Zone (HAZ). This Figure is provided here to show the distinction between these zones. Fig. 8b depicts the EBSD Grain Orientation Spread (GOS) maps for the cross-section of the Dilution zone (DZ, Interface), Interface Zone (IZ), and Heat Affected Zone (HAZ) with the color-coded grain misorientation at different GOS angle ranges. A statistical comparison was made for these three special areas (zones) in Fig. 5.8c. It reveals that a higher fraction of grains (65%) in the Dilution Zone (DZ, Interface) shows low angle GOS in contrast to a higher fraction of grains (59%) in the Heat Affected Zone (HAZ) that shows high angle GOS (3°-5°).

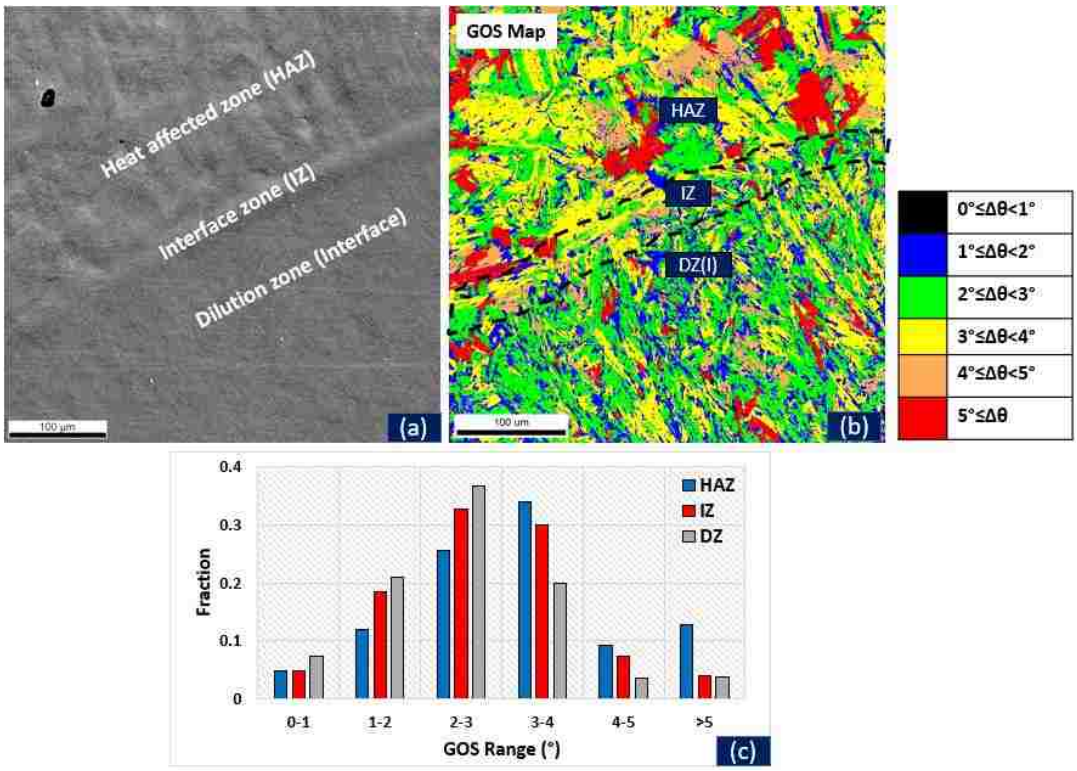

Figure 5. 8 (a) SEM images shows a cross-section of interface zone (IZ) between the Dilution zone (DZ, Interface) and Heat Affected Zone (HAZ); (b) Electron Backscatter

Diffraction (EBSD) Grain Orientation Spread (GOS) map shows color-coded grain misorientation with different GOS angle ranges in those respective zones; (c) Bar chart shows fraction of grains in the Dilution Zone (DZ, Interface), Interface Zone (IZ), and Heat Affected Zone (HAZ) against various GOS angle ranges.

Fig. 5.9 shows the grain average Image Quality (IQ) maps deduced from the Electron Backscatter Diffraction (EBSD) in the three OIM scans at the three selected areas, as defined earlier. It quantifies the quality of the corresponding diffraction pattern in the diffraction volume of the cross-section of BZ(C), DZ (C), DZ (I), IZ, and HAZ, respectively. It is reported [24–26] that the IQ value is affected by the induced residual stress or strain in the diffracting volume. As the strain increases, the image quality (IQ) decreases. The residual stress causes lattice distortion and thus, the EBSD's ability to index decreases since it is based on the ideal bcc crystal structure. The highly strained or stressed areas appear in a darker color (towards the blue color, low IQ value) compared to the less strained or stressed areas. The lighter the color contrast (towards the red color), the less the strain and stress, and the higher the IQ value. Although this color coding is arbitrary, this norm is well practiced in the earlier publications [25],[27]. Fig. 5.9a shows the top of the BZ(C) has a darker blue color with a low IQ value (note the labelled orientations in the figures). When moving from the top to the bottom of the BZ(C), the IQ value increases, and the grains become a lighter green color. The quantified IQ values are plotted against the depth (where the top is 0 μm, and the bottom is 300 μm) of the bead zone (Fig. 5.9d). Fig. 5.9b shows that the top of the DZ(C) has a lighter contrast diffraction pattern (mostly yellow and light green) and the bottom of the DZ(C) has a darker pattern (mostly green and yellow). The IQ values are plotted in Fig. 5.9e. It indicates that the top of DZ has a high IQ value compared to the bottom of this zone. When moving towards the bottom of the DZ, the IQ value increases. Fig. 5.8c shows IQ maps of the three interface regions,

namely DZ (I), IZ, and HAZ. The IQ values are plotted in Fig. 5.9f-g. When moving from the DZ(I) to the interface and interface to the HAZ, the IQ value increases. However, away from the interface to the rest of the substrate, the IQ value decreases.

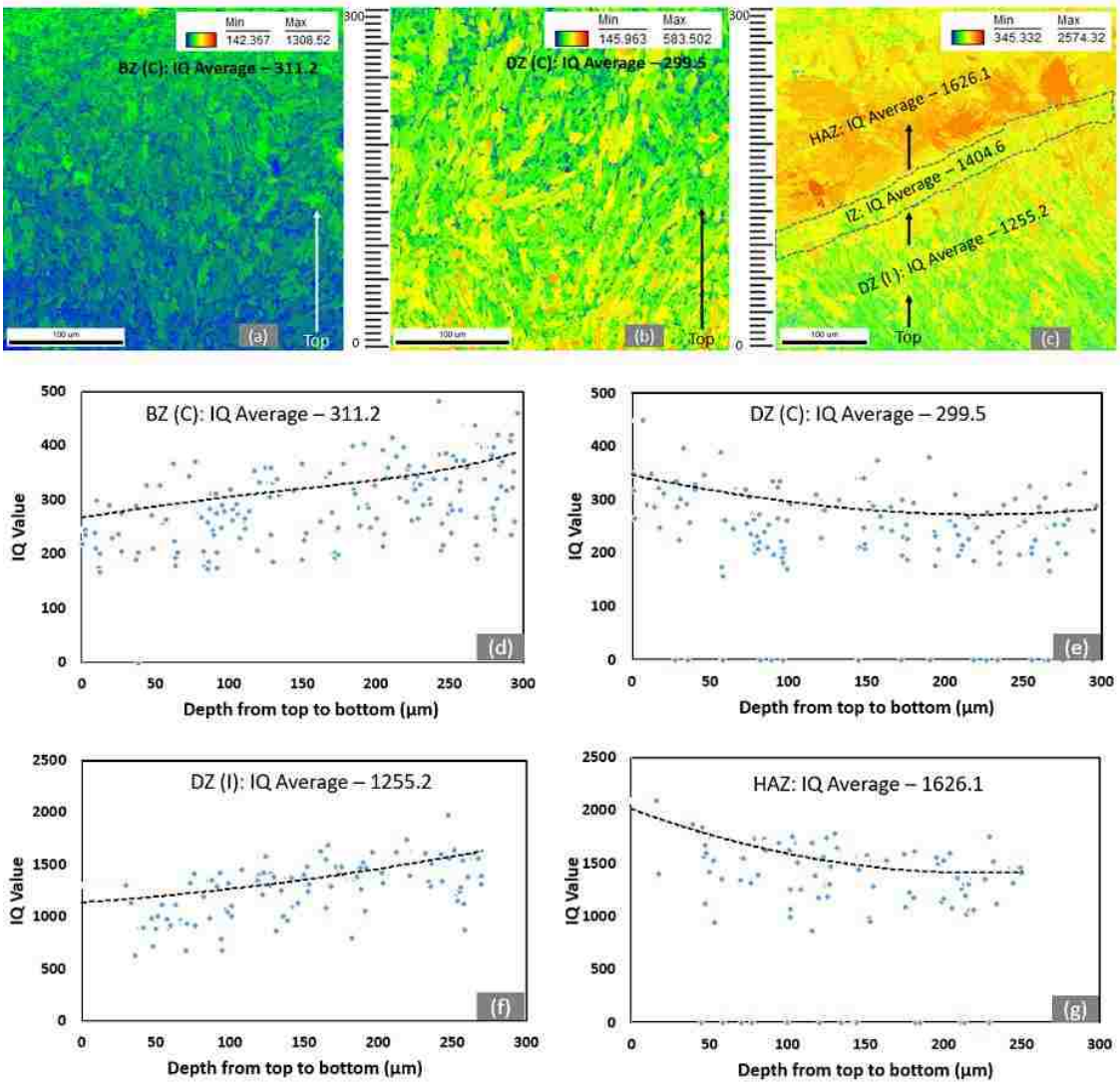

Figure 5. 9 Electron Backscatter Diffraction (EBSD) Grain Average Image Quality (IQ) maps (with color bar showing minimum and maximum IQ value) show the quality of diffraction pattern in the diffraction volume of the cross-section of (a) bead zone (BZ, Center); (b) dilution zone (DZ, Center); (c) combinedly interface zone (IZ) between the dilution zone (Interface) and heat affected zone (HAZ); (d) variation of IQ value in the BZ (Center); (e) variation of IQ value in the DZ (Center); (f) variation of IQ value in the DZ(Interface); (g) variation of IQ value in the HAZ.

Discussions

EBSD results revealed the existence of various orientations and the hierarchical nature of the martensitic structures (packets of lath and plate) in the bead zone, dilution zone, and interface with HAZ (as shown in Figs. 5.3-5.5) within the prior-austenitic grain boundary (PAGB, marked as white dotted lines). The packets of martensitic grains were oriented at a combination of different crystallographic planes such as {001}, {101}, {111), {112}, {102}, and {2,1,2}. However, EBSD results did not reveal any retained austenite in those zones. It was also difficult to find out the second phase (δ-ferrite), as revealed in our earlier study [6] due to the similarities (with a low tetragonality and low carbon contents) between the crystallographic structures of δ-ferrite (bcc) and ά-martensite (bct). It was impossible to distinguish these two phases from each other by using the OIM software with this traditional EBSD technique. Therefore, martensite has been indexed as the main phase in this martensitic stainless steel. The earlier study [11] confirmed that the martensitic transformation occurred (where martensite is dominating phase) at the various zone of the single bead laser cladding of this 420 MSS.

As can be seen in Fig. 5.5, at first, the planer grains were nucleated in the interface zone from where the solidification started, and then the columnar austenite grains were developed epitaxially from the interface. This kind of solidification behavior is observed usually in laser welding or cladding [28]. Then due to the effect of solidification parameters such as the temperature gradient (G), the solid/liquid interface growth rate (R), and the G/R ratio, the grain morphology varied from columnar to equiaxed (Fig. 5.3) and a combination of both (Fig. 5.4) in the bead zone and dilution zone respectively [11]. Later on, those austenite grains transformed to martensite as the temperature reached to below the

martensite start temperature (Ms) due to the extremely high and differential cooling rate observed in all those zones during laser cladding [11]. The aspect ratio of PAG in the DZ(I) is 2.91, which is higher than those of 2.03 and 1.26 observed in the DZ (C) and BZ (C), respectively. This aspect ratio provided crucial information on the shape of the PAG in all those zones. Also, the martensite substructure grain size distribution (Fig. 5.6) revealed that both dilution zones had bigger sized (diameter) grains compared to the grains in the bead zone which indicated that martensitic transformation occurred in those zones with differential cooling rates, which was observed in the authors' earlier study [11]. It is to be noted here that the HAZ is part of the AISI 1018 substrate, which has a different chemistry and was free from any melting or solidification. Different grain morphologies and orientations occurred here due to the severe heat effect associated with laser cladding of 420 MSS on this substrate.

The solid-state transformation that occurred in the laser-cladded part led to a differential volume change in those zones, which created strains and distortion in the crystal lattice structure. This volume change and distortion created the grain misorientation and the induced residual stress or strain. This grain misorientation was quantified by the grain orientation spread (GOS) using Electron Backscatter Diffraction (EBSD). The GOS parameter was used to measure the intragranular lattice distortion or deformation in the crystal structure [29]. A high angle GOS value indicates a high distortion in the grain. The GOS is the average value of the orientation spread in a grain, where the orientation spread is defined as the misorientation angle between all the points in a grain[30]. The GOS value provides information on the highly deformed regions within a grain.

As shown in Fig. 5.7c, the BZ has a higher fraction of grains (26%) with a high angle GOS (3°-5°) compared to the DZ, which indicates that most of the grains at the BZ were highly strained. A similar trend was observed in the HAZ (Fig. 5.8c), where a higher fraction of grains (59%) was at a high angle of GOS (3°-5°), indicating the availability of highly deformed grains in HAZ. On the other hand, a low angle GOS was observed in the DZ (C) and DZ (I) for a higher fraction (78% and 65% respectively) of grains, which indicated that low distortion was developed in the overall dilution zone. Importantly, 30%-33% fraction of grains showed both low and high angle GOS in the interface zone. This indicated that the interface is an inflection zone between the low and high angle GOS when compared to the DZ and HAZ.

On the other hand, residual stress and strain can be quantified by the grain average image quality (IQ), a parameter used in the EBSD technique that measures crystallographic imperfection of the diffraction volume[27,31]. The IQ is proportionally related to the sharpness of the Kikuchi Pattern, which is affected by the presence of crystalline defects such as dislocation, strain, and distortion [32]. A highly dislocated or elastically distorted lattice will have a weak and blurry Kikuchi Pattern and would be expected to have a low IQ [32]. As can be seen in Figs. 5.9a and 5.9d, the IQ value was very low at the beginning and increased to a higher value at the end of the bead zone. The range of the IQ value is within 142-485. This indicated that a high level of stress developed at the beginning of this zone and steadily decreased towards the end of the zone due to variations of the dislocation density and the grain sizes of the martensitic substructures. Subsequently, in the dilution zone (Fig. 5.8b), the IQ value gradually decreased from a higher value to a lower value in

the range of 145-450, which indicated an increase of RS from the beginning to the end of this zone.

Interestingly, the IQ value further increased from the end of the DZ (I) towards the interface zone (Fig. 5.9c) and then decreased when moved away from the interface to the rest of the HAZ (Figs. 5.9c and 5.9 f-g). It indicated that the RS value decreased from the end of DZ (I) towards the interface and then increased from the interface to the rest of the HAZ in the substrate. The above-mentioned variations of IQ value throughout those zones of a single bead cladding has similarities with the status of RS shown in Fig. 5.10 and supported by the earlier TEM study[11] that revealed a variation of martensitic phases and dislocation density in those zones.

Fig. 5.10 shows the residual stress (RS) contour mapping observed in the bead zone, dilution zone, and heat affected zone (HAZ). This map was created using the experimental and simulated data from the authors' earlier works [6,19]. [Along the centerline of the bead, the RS was measured using the experimental XRD technique. Then the RS value was simulated at 300μm apart from both sides of the centerline of the bead. The authors' earlier study [19] found a good fit between the experimental and simulated RS]. As shown in Fig. 5.10, the RS decreased throughout the bead zone and transformed from tensile to compressive stress at the end of the bead zone and then continued to increase towards the whole dilution zone. The RS then decreased towards the interface with HAZ. When moving away from the interface to the HAZ, the RS increased again and transformed to tensile stress. Regardless of the type of RS, a high RS was observed in the DZ. This trend for the RS was found to be very similar to the trend for the reverse IQ mapping in all those zones, as shown in Fig. 5.9.

Thus, the IQ maps provided crucial information about the crystal structure with an indication of the distribution of the residual stress and strain in the selected zones. Though the IQ is affected by the presence of other factors such as the dislocation density, microstructural phases, chemical composition, and solid-state martensitic phase transformation, the synergistic effect of those factors is directly related to the development of RS and IQ value. This qualitative and quantitative analysis revealed that the IQ value is inversely proportional to the RS and found to be significantly effective in evaluating the RS distribution in those three zones when compared to the experimental RS values measured by the XRD technique. A new method will be initiated to convert the IQ value into an RS value in a future study.

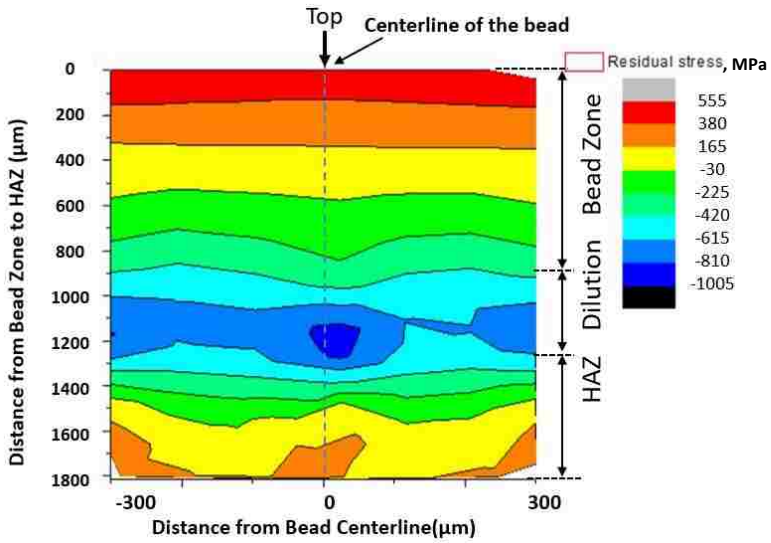

Figure 5. 10 Contour mapping of residual stress observed in the bead zone, dilution zone, and heat affected zone (HAZ). ‘‘positive (+) stress’’ indicates the tensile residual stress and the ‘‘negative stress’’ designated as compressive residual stress. (data are adopted from the authors' earlier work [6], [19]).

Summary and Conclusions

A comprehensive EBSD analysis was performed in the selected areas of bead zone, dilution zone, and interface zone for a laser-cladded AISI 420 MSS single bead. The results are highlighted as follows:

- The IPF map provided detailed information on the grain morphology and revealed planar to columnar and columnar to equiaxed grains in the interface, dilution, and bead zones. The IPF maps also revealed the PAG sizes and their aspect ratio, which confirm the grain shape and grain distribution in those zones.
- No retained austenite was found, and delta-ferrite could not be distinguished from the martensite phase due to the similarity in their crystal structures (bcc vs. bct).
- Variations in the size distribution of martensitic substructure in the various zones of the laser-cladded sample indicated occurrence of a differential cooling rate during martensitic transformation.
- The GOS approach revealed that most of the grains at the BZ and HAZ were highly strained, and 26-59% fraction of the grains was at a high angle of GOS (3°-5°), indicating highly deformed grains in both regions. This could be one of the reasons for the devolvement of tensile stress in those regions.
- The IQ value was found to be inversely proportional to the RS value found in the earlier study. This IQ approach is an effective and helpful tool to evaluate the RS distribution in those zones of laser-cladded AISI 420 MSS.

- This EBSD study revealed the microstructural evolutions occurred in the laser cladded 420 MSS from a crystallographic point of view and thus expected to create new information on the orientation of prior austenite grain sizes, their aspect ratio, grain misorientation, and the image quality of the diffraction pattern of the martensitic substructure observed in the three regions of a single bead cladding. These results are expected to be used as a foundation for the laser-based additive manufacturing application of 420 martensitic stainless steel.

References.

[1] I. Hemmati, V. Ocelík, J.T.M. De Hosson, The effect of cladding speed on phase constitution and properties of AISI 431 stainless steel laser deposited coatings, Surf. Coatings Technol. 205 (2011) 5235–5239. doi:10.1016/j.surfcoat.2011.05.035.

[2] C. Navas, A. Conde, B.J. Fernández, F. Zubiri, J. de Damborenea, Laser coatings to improve wear resistance of mould steel, Surf. Coatings Technol. 194 (2005) 136–142. doi:10.1016/j.surfcoat.2004.05.002.

[3] P. Wen, Z. Cai, Z. Feng, G. Wang, Microstructure and mechanical properties of hot wire laser clad layers for repairing precipitation hardening martensitic stainless steel, Opt. Laser Technol. 75 (2015) 207–213. doi:10.1016/j.optlastec.2015.07.014.

[4] T. DebRoy, H.L. Wei, J.S. Zuback, T. Mukherjee, J.W. Elmer, J.O. Milewski, A.M. Beese, A. Wilson-Heid, A. De, W. Zhang, Additive manufacturing of metallic components – Process, structure and properties, Prog. Mater. Sci. 92 (2018) 112–224. doi:10.1016/j.pmatsci.2017.10.001.

[5] I. Hemmati, V. Ocelík, J.T.M. De Hosson, Microstructural characterization of AISI 431 martensitic stainless steel laser-deposited coatings, J. Mater. Sci. 46 (2011) 3405–3414. doi:10.1007/s10853-010-5229-2.

[6] M.K. Alam, A. Edrisy, J. Urbanic, J. Pineault, Microhardness and Stress Analysis of Laser - Cladded AISI 420 Martensitic Stainless Steel, J. Mater. Eng. Perform. 26 (2017) 1076–1084. doi:10.1007/s11665-017-2541-x.

[7] B. Mahmoudi, M.J. Torkamany, A.R.S.R. Aghdam, J. Sabbaghzade, Laser surface hardening of AISI 420 stainless steel treated by pulsed Nd:YAG laser, Mater. Des. 31 (2010) 2553–2560. doi:10.1016/j.matdes.2009.11.034.

[8] C.S. Toyserkani, E., Khajepour, A., Laser Cladding, CRC Press, New York, 2005.

[9] M.K. Alam, J. Urbanic, S.M. Saqib, A. Edrisy, Effect of Process Parameters On The Microstructural Evolutions of Laser Cladded 420 Martensitic Stainless Steel, in: Mater. Sci. Technol. Conf. Proc. (MS&T15), Oct. 4-8, Columbus, Ohio, USA, 2015: pp. 35–54.

[10] B. Graf, S. Ammer, A. Gumenyuk, M. Rethmeier, Design of experiments for laser metal deposition in maintenance, repair and overhaul applications, Procedia CIRP. 11 (2013) 245–248. doi:10.1016/j.procir.2013.07.031.

[11] M.K. Alam, A. Edrisy, R.J. Urbanic, Microstructural Analysis of the Laser-Cladded AISI 420 Martensitic Stainless Steel, Metall. Mater. Trans. A. 50 (2019) 2495–2506. doi:https://doi.org/10.1007/s11661-019-05156-6.

[12] G. Telasang, J. Dutta Majumdar, N. Wasekar, G. Padmanabham, I. Manna, Microstructure and Mechanical Properties of Laser Clad and Post-cladding Tempered AISI H13 Tool Steel, Metall. Mater. Trans. A. 46 (2015) 2309–2321. doi:10.1007/s11661-015-2757-z.

[13] P.J. Maziasz, E.A. Payzant, M.E. Schlienger, K.M. McHugh, Residual stresses and microstructure of H13 steel formed by combining two different direct fabrication methods, Scr. Mater. 39 (1998) 1471–1476. doi:10.1016/S1359-6462(98)00349-2.

[14] R. Cottam, J. Wang, V. Luzin, Characterization of microstructure and residual stress in a 3D H13 tool steel component produced by additive manufacturing, J. Mater. Res. 29 (2014) 1978–1986. doi:10.1557/jmr.2014.190.

[15] P. Farahmand, R. Kovacevic, An experimental–numerical investigation of heat distribution and stress field in single- and multi-track laser cladding by a high-power direct diode laser, Opt. Laser Technol. 63 (2014) 154–168. doi:10.1016/j.optlastec.2014.04.016.

[16] J. Chen, S.H. Wang, L. Xue, On the development of microstructures and residual stresses during laser cladding and post-heat treatments, J. Mater. Sci. 47 (2012) 779–792. doi:10.1007/s10853-011-5854-4.

[17] U. de Oliveira, V. Ocelík, J.T.M. De Hosson, Residual stress analysis in Co-based laser clad layers by laboratory X-rays and synchrotron diffraction techniques, Surf. Coatings Technol. 201 (2006) 533–542. doi:10.1016/j.surfcoat.2005.12.011.

[18] J.-Y. Chen, K. Conlon, L. Xue, R. Rogge, Experimental study of residual stresses in laser clad AISI P20 tool steel on pre-hardened wrought P20 substrate, Mater. Sci. Eng. A. 527 (2010) 7265–7273. doi:10.1016/j.msea.2010.07.098.

[19] N. Nazemi, J. Urbanic, M.K. Alam, Hardness and residual stress modeling of

powder injection laser cladding of P420 coating on AISI 1018 substrate, Int. J. Adv. Manuf. Technol. 93 (2017) 3485–3503. doi:10.1007/s00170-017-0760-9.

[20] Z. Zhang, P. Farahmand, R. Kovacevic, Laser cladding of 420 stainless steel with molybdenum on mild steel A36 by a high power direct diode laser, Mater. Des. 109 (2016) 686–699. doi:10.1016/j.matdes.2016.07.114.

[21] T. Maitland, S. Sitzman, EBSD technique and materials characterization, Scanning Microsc. Nanotechnology. Tech. Appl. (2007) 41–76.

[22] E. Weidmann, Struers Application Notes - Metallographic Preparation of Stainless Steel, Struers A/S, Copenhagen, 2005. doi:01.05 / 62140005.

[23] A. Ayad, N. Allain-Bonasso, N. Rouag, F. Wagner, Grain Orientation Spread Values in IF Steels after Plastic Deformation and Recrystallization, Mater. Sci. Forum. 702–703 (2011) 269–272. doi:10.4028/www.scientific.net/MSF.702-703.269.

[24] S.T. Wardle, L.S. Lin, A.D. Cetel, B.L. Adams, Orientation imaging microscopy: Monitoring residual stress profiles in single crystals using and imaging quality parameter, IQ, in: G.W. Bailey, A.J. Garratt-Reed (Eds.), 52nd Annu. Meet. Microsc. Soc. Am. San Fr. CA, USA, 31 July–5 August, San Francisco Press: San Francisco, CA, USA, America, San Francisco, CA, 1994: p. 680–681.

[25] S.I. Wright, M.M. Nowell, D.P. Field, A review of strain analysis using electron backscatter diffraction, Microsc. Microanal. 17 (2011) 316–329. doi:10.1017/S1431927611000055.

[26] P. Ferro, F. Bonollo, F. Bassan, F. Berto, Strain evolution in cold-warm forged steel components studied by means of EBSD technique, Materials (Basel). 10 (2017). doi:10.3390/ma10121441.

[27] S.I. Wright, M.M. Nowell, EBSD Image Quality Mapping, Microsc. Microanal. 12 (2006) 72–84. doi:10.1017/S1431927602010346.

[28] S.A. David, S.S. Babu, J.M. Vitek, Welding : Solidification and Microstructure, JOM, J. Miner. Met. Mater. Soc. (2003).

[29] N. Allain-Bonasso, F. Wagner, S. Berbenni, D.P. Field, A study of the heterogeneity of plastic deformation in IF steel by EBSD, Mater. Sci. Eng. A. 548 (2012) 56–63. doi:10.1016/j.msea.2012.03.068.

[30] M.H. Alvi, S. Cheong, H. Weiland, A.D. Rollett, Microstructural evolution during recrystallization in hot rolled aluminum alloy 1050, in: 1st Intl. Symp. Metall. Model. Alum. Alloy. TMS, Pittsburgh, 2003: pp. 191–197. http://www.scopus.com/inward/record.url?eid=2-s2.0-2342511408&partnerID=40&md5=bff5cc2001ace486a024e9641f8e27a6.

[31] X. Tao, A. Eades, Alternatives to Image Quality (IQ) Mapping in EBSD, Microsc. Microanal. 8 (2002) 692–693.

[32] J. Wu, P.J. Wray, C.I. Garcia, M. Hua, A.J. Deardo, Image quality analysis: A new method of characterizing microstructures, ISIJ Int. 45 (2005) 254–262. doi:10.2355/isijinternational.45.254.

CHAPTER 6 Mechanical Behavior of Additive Manufactured AISI 420 Martensitic Stainless Steel

Introduction

Stainless steel (SS) alloys are widely used in the automotive, die and tools, aerospace, medical device, and pipeline industries because of their relatively low density, high strength, and excellent corrosion resistance. This group of steel can be ferritic, austenitic, martensitic or combination of all phases depending on the chemical composition and major alloying elements (e.g. Cr, Ni). Among all SS alloys, AISI 420 Martensitic stainless steel (MSS) properties can be altered by heat treatment [1]. It has a growing demand in the automotive, medical and aerospace industries due to its moderate corrosion resistance, high hardness, and good tensile properties [1]. In the pre-hardened and tempered condition, the alloy has a tensile strength in the range of 700 - 930 MPa depending on the process parameters [2]. This SS can be processed by conventional manufacturing processes such as casting, metal forming, powder metallurgy, welding, or recently developed additive manufacturing [3]. This steel alloy shows improved mechanical properties when fabricated by using a novel additive manufacturing (AM) technique called laser cladding (LC) or direct energy deposition (DED) [4–8]. However, due to repeated heat cycles during melting and solidification (side by side bead deposition and multiple layers), the LC or DED process resulted in anisotropy 3D components [9–14].

The DED process utilizes laser power to melt the coaxial metallic powders (or wire) to fabricate a near-net shape in a layer by layer manner directly from a 3D CAD model [15].

This process is an extension of the laser cladding process, which is also used to modify or improve the surface properties of industrially used components which give engineers the ability to tailor the mechanical properties of materials to suit a wide range of different applications [16]. This process is also known by many different names such as direct metal deposition (DMD) or laser powder deposition (LPD), laser engineered net shaping (LENS), direct laser deposition (DLD), and direct laser fabrication (DLF [17,18]. In this study, the term "laser cladding" will be used as the AM process.

Several studies reported the microstructure and mechanical behavior of iron-based alloys fabricated with laser cladding or similar laser-based additive manufacturing processes. Khodabakhshi et al. [3] reported the mechanical behavior of austenitic S316-L and martensitic S410-L stainless steel fabricated with powder-feed laser additive manufacturing (LAM). They compared their uniaxial tensile testing results with the commercial counterparts of those SS at different testing mode with different strain rates (0.001, 0.01, 0.1, and 1.0 $sec^{-1,}$ respectively). The LAM austenitic stainless steel showed lower yield strength (YS) and ultimate tensile strength (UTS) [YS (281-304) MPa, UTS (433-463) MPa] when compared to the commercial counter parts [YS 304-365 MPa, UTS (617-641) MPa] for all testing modes. Interestingly, they observed higher mechanical properties in the LAM martensitic SS [YS (375-391) MPa, UTS (537-672) MPa] compared to the commercial grade [YS (156-278) MPa, UTS (238-387) MPa]. Lower ductility was observed in the both LAM stainless steels when compared to the commercial grades.

Ravi et al. [4] investigated SC420 stainless steel processed with the Direct Laser Fabrication (DLF). They reported that the DLF process can create three-dimensional (3D) near net-shape metallic parts with varying thickness along the vertical direction with a

higher yield strength (1000 MPa) and tensile strength (1400 MPa) but with low elongation (5%). They did not observe any influence of deposition direction on the yield and tensile strength but with brittle fracture surface in both direction with very low ductility. They applied high isostatic pressure (HIP) at high temperature (1000 °C) that reduced residual stresses and improved the tensile properties. The microstructure was consisted of tempered martensite with carbide and ferrite phases at the grain boundary. Deev et al. [11] studied anisotropic mechanical properties of 316 SS deposited by laser melting. They found a strong dependence of the parameters related to the powder melting and the build direction on the mechanical properties.

Krakhmalev et al. [19] studied the microstructural evolutions in the AISI 420 martensitic stainless steel during selective laser melting, where they observed differences in microstructure and hardness in the few top layers in comparison to the rest of the sample. The last few deposited layers showed a hardness of 750HV as well as 21±12 vol.% austenite phase compared to the rest of the sample. The rest of the sample consisted of thermally decomposed martensite and abnormally high amounts of austenite (57±8 vol.%) with a hardness in the range of 500–550HV. It was indicated that the occurrence of thermal cycling during the additive manufacturing process resulted in partitioning and austenite reversion in the inner regions of the sample [19].

Kurzynowski et al. [20] reported the influences of laser power input, scanning speed, and building strategies on the microstructure, texture and tensile properties of 316 L stainless steel processed by selective laser melting (SLM). They reported that in the as-built condition, the microstructure was characterized by columnar grains of austenite with intercellular segregation of Mo, Cr and Si, and non-equilibrium eutectic ferrite.

Additionally, they found that the cellular substructures of austenite, a trace of ferrite, as well as the crystallographic texture, were strongly affected by the laser energy density and scanning strategy. Consequently, they observed a double increment in the yield strength with a much smaller improvement in the ultimate tensile strength in comparison to a similar alloy that has been fabricated conventionally.

Considering the growing demand and rapid commercialization of various AM technology, it is necessary to expand further research in characterizing the mechanical properties of martensitic stainless steel built with the laser cladding AM solutions at different direction and orientations. Moreover, there is not much reported data related to the AISI 420 MSS, although this material has uses in many domains using AM techniques. It is also important to compare those materials properties with the similar alloy processed with traditional manufacturing methods. This study investigates the mechanical properties of as-cladded AM AISI 420 samples and discussed the results in terms of microstructural development in the longitudinal (LD) and transverse (TD) directions. Then as a solution to navigate the directionality, post cladding heat-treatment was proposed, and the mechanical properties and the microstructure were compared with those from the AM sample. Furthermore, as an alternative solution, the test results of the other AM samples (built with cross-layered as well as at 30° angle to the horizontal base) were discussed.

Materials and Experimental Procedure

The chemical composition of the AISI 420 MSS powder that was used for building laser-cladded AM samples is shown in Table 6.1. The stainless-steel powder sizes were between 53-180 μm with the powder density of 4.37 g/cm^3. A commercial grade pre-

hardened AISI 420 MSS (as shown in Table 6.1) was also selected for comparison with the as-cladded AM sample. As per the manufacturer's note, this rolled steel was re-heated in the range of 982-1066 °C and soaked at the austenizing temperature before quenching in warm water and subsequently tempered at 149-427 °C for 1-2 hours with air cooling.

Table 6. 1 Chemical composition (%) of AISI 420 MSS powder and Commercial grade MSS.

Alloy	C	Mn	Si	Cr	P	Ni	S	Mo.	V	Co
420 MSS Powder	0.23	1.2	0.5	12.3	0.015	-	0.009	-	-	0.02
420 MSS Com. Gr.	0.26	1.1	0.11	12.26	0.023	0.17	0.108	0.03	0.04	-

As shown in Fig. 6.1, the laser-cladded AM 3D block samples (45x45x25 mm) of AISI 420 MSS were produced using the laser cladding process. This laser-based AM process was carried out with a 4 kW fiber diode laser coupled to an articulated robotic arm and employed a coaxial powder deposition head. A 2.5 kW high power laser beam was focused (using a 400 mm focal length) on the substrate steel plate in order to generate a molten pool with the 420-stainless steel metallic powders injected simultaneously at the rate of 20 g/min with coaxially flowing argon gas as a shield to protect the molten pool from oxidation. The LC process was performed when the substrate plate was positioned at both a horizontal orientation ($\alpha = 0°$) and an angular orientation ($\alpha = 30°$) while the deposition head was normal to the base.

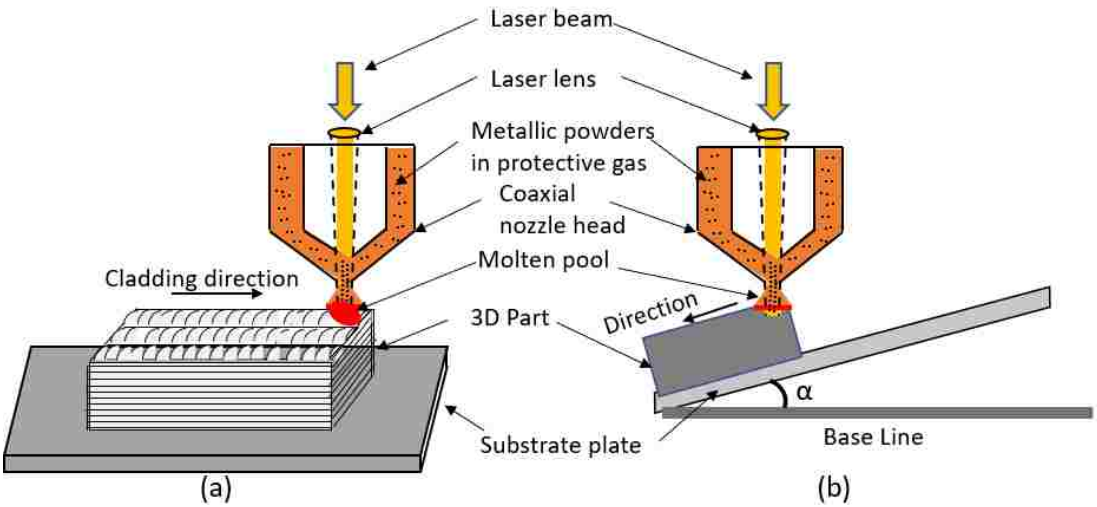

Figure 6. 1 Schematic view of powder deposition for the fabrication of the 3D parts using the laser cladding process, (a) base orientation, and (b) angular deposition, α = 30°.

A miniature type tensile test specimen (as shown in Fig. 6.2b) was designed to study the mechanical behavior. Two test specimens were cut from each 3D block samples (Fig. 6.2a, built at horizontal) in the longitudinal (bead deposition path) and the transverse direction of the deposition. Similar test specimens were also prepared from the commercial grade pre-hardened AISI 420 MSS in the longitudinal (rolling) to compare the test results with the additive manufactured (AM) sample. The tensile test was carried out under ambient conditions as per the control method defined by ASTM E-8 standard [22] on a constant strain rate of 0.007 mm/s using a universal testing machine with a capacity of 50kN (MTS-Criterion 43).

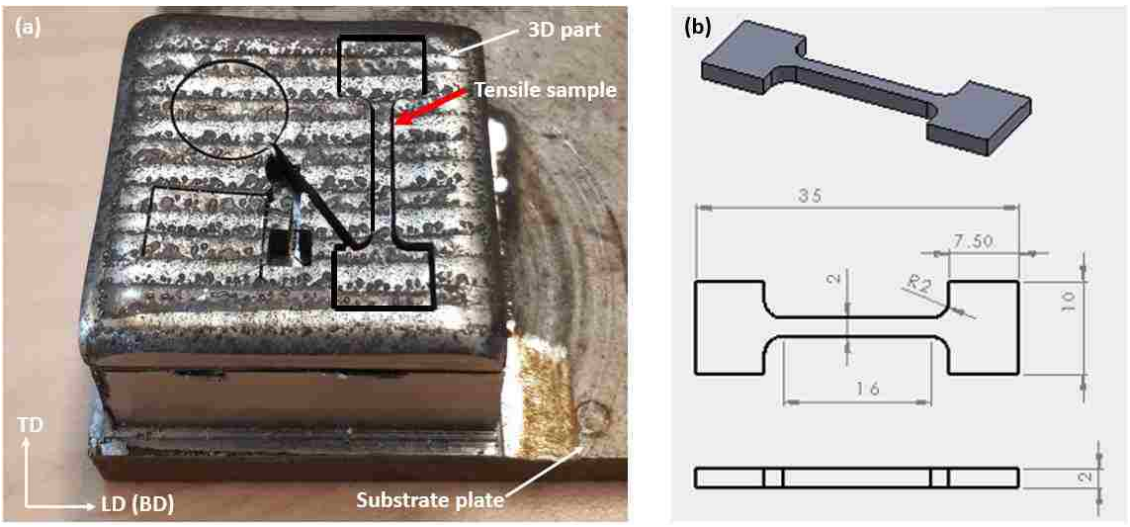

Figure 6. 2 (a) Laser-cladded AM sample, (b) Schematic view of the micro-tensile test specimen with dimensional specifications in mm.

Two samples from the transverse direction were selected for heat treatment. The samples were kept inside the furnace for an hour at (565±10)°C. The aim of this heat treatment was to compare the microstructure and tensile properties of the as-cladded transverse sample with the heat-treated sample from the same direction.

The metallographic samples were cut transversely (TD) and longitudinally along the build direction (BD) by wire EDM, as shown in Fig. 6.3. The respective samples were then mounted in hot epoxy powder using a Buehler mounting press. The grinding was done as per the Struers application note using 220 µm silicon carbide papers and 9 µm water-based diamond suspension [23]. The samples were then polished with 3 µm and 1 µm diamond suspension. The final polishing was done using 0.04 µm colloidal silica, followed by ultrasound cleaning with ethyl alcohol (95%). Furthermore, the samples were etched with Ralph's reagent by swabbing with surgical grade cotton to observe microstructural characteristics.

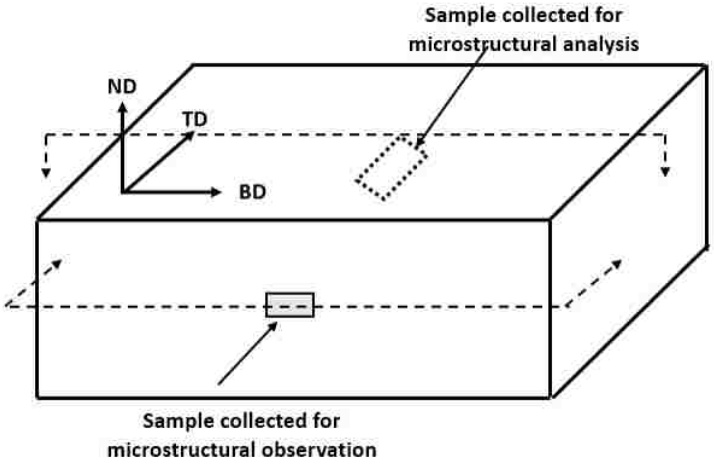

Figure 6. 3 Schematic location of the sample for microstructural and EBSD analysis; BD-laser cladding build direction, TD-Transverse Direction, ND- Normal Direction.

The electron microscopy observations were done with an FEI Quanta 200 FEG scanning electron microscope (SEM) equipped with energy dispersive X-ray spectroscopy (EDS). The Electron Backscatter Diffraction (EBSD) analyses were performed for AM samples in a field emission scanning electron microscope (FEG-SEM) (Nova Nano-SEM, FEI) that is equipped with Orientation Imaging Microscopy software (OIM 6.2) by EDAX.

Results and Discussion

6.3.1 Mechanical Properties: Longitudinal Direction

Fig. 6.4a shows the engineering stress-strain curve of the as-cladded AM sample and the pre-hardened commercial grade sample of AISI 420 MSS. These curves are from one test sample of each type. On an average, a higher ultimate tensile strength (1117 MPa) was achieved from the as-cladded and additively fabricated sample compared to the pre-hardened commercial grade rolled sample (1087 MPa) in the longitudinal direction. The yield strength (0.2%) of the as-cladded sample (493 MPa) was also higher than the

commercial grade sample (483 MPa). Moreover, the as-cladded samples show higher percentage of area reduction (34%) than the pre-hardened sample (28%).

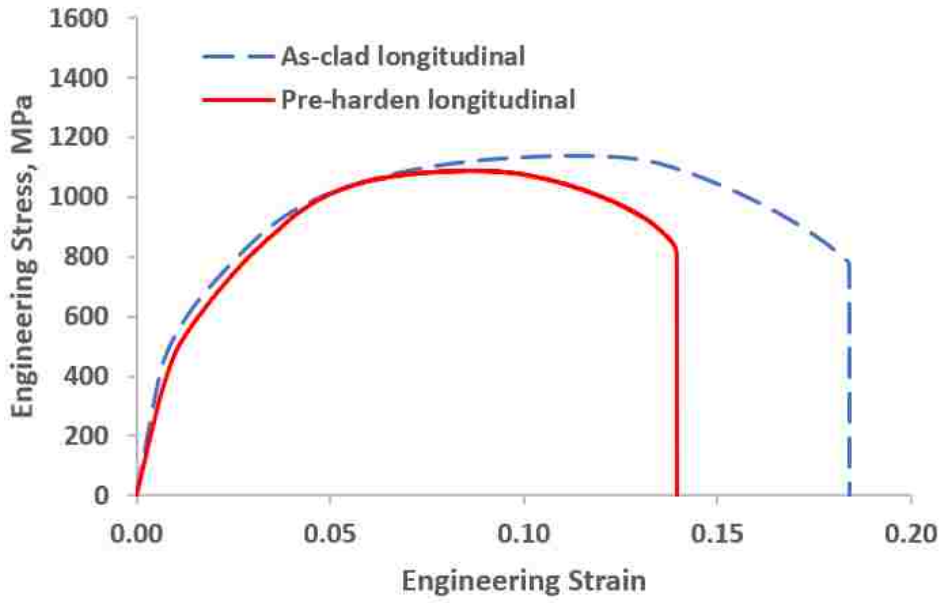

Figure 6. 4 Comparison of engineering stress and strain between the as-cladded (AC-L) and pre-hardened (PH-L) samples in the longitudinal direction.

The above results show that for the additively fabricated sample, the ductility has been increased by 21% compared to the pre-hardened rolled sample. To understand the reason behind this improved mechanical property, it is necessary to investigate the microstructural behavior of the additive manufactured (AM) sample and the pre-hardened rolled sample of AISI 420 MSS.

6.3.1.1 Microstructural Behavior: Longitudinal Sample

Fig. 6.5 shows SEM image of the cross-sectional microstructure of both pre-hardened commercial grade (Fig. 6.5a) and laser-cladded AM sample (Fig. 6.5b) of AISI 420 MSS. Fig. 6.5a shows chromium carbide ($Cr_{23}C_6$), retained austenite (γ-Fe), tempered martensite (α′- Fe) phases within the prior austenite grain boundary (PAGB). The grain

sizes of those phases are measured as retained austenite ~ 7.32 µm, carbide ~ 2.1 µm, and PAG ~ 78 µm. On the other hand, Fig. 6.5b shows delta ferrite (black), retained austenite (dull gray) in the martensitic matrix. X-ray diffraction confirmed the presence of those main phases in the laser-cladded 420 MSS [6]. However, the grain sizes of those phases are very fine in the AM sample (Fig. 6.5b) compared to the pre-hardened rolled sample, and it is hard to quantify them using a similar SEM technique. Hence, the EBSD technique is employed for the quantification of grain sizes in the as-cladded AM sample for both etched and non-etched samples. It is to be noted here that in the etched AM sample (Fig. 6.5b), the Ralph reagent attacked the delta-ferrite phase in a preferential manner compared to the martensite phases leaving a dark (corroded) delta ferrite phase and light grey retained austenite and dark grey martensite phase [24]. A similar observation was recorded in the authors' earlier study [6] and in the austenitic stainless steel by other researchers [25].

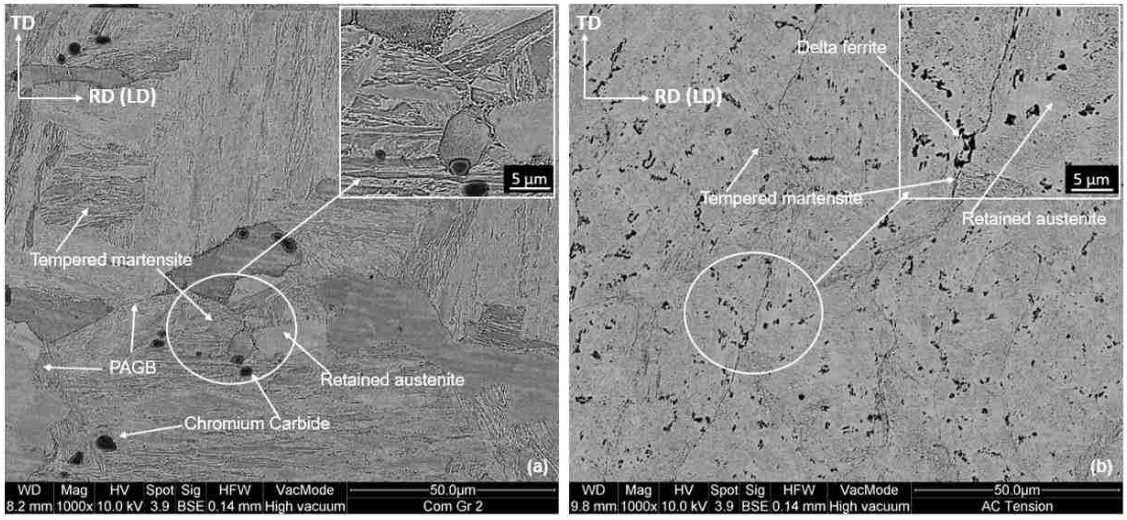

Figure 6. 5 SEM image of cross-sectional microstructure (a) Pre-hardened rolled sample, (b) as-cladded AM sample of AISI 420 MSS (etched with Ralph reagent); PAGB – Prior austenite grain boundary.

6.3.1.1.1 EBSD Analysis: Longitudinal Sample

The inverse pole figure (IPF) map shown in Fig. 6.6 reveals the microstructure of the cross-section (ND-BD) of the as-cladded AM sample. Four prior austenite grains were identified (PAG 1, 2, 3, and 4) in the map, as shown in Fig. 6.6a. The average grain size of the PAG was measured to ~28 µm. A unique color map shown in Fig. 6.6b indicates the presence of retained austenite grains (green color), which are surrounded by martensites and ferrites (red regions). It is important to note that it is extremely difficult to distinguish between the δ-ferrite (bcc) and α′-martensite (bct) using the traditional EBSD techniques due to the similarity between the crystalline structure of these two phases (with a low tetragonality and low carbon contents). The volume fraction of the retained austenite (green region) was calculated to be ~4.7%, while the volume fraction of the martensite and ferrite region (combinedly, red region) was ~95.3%. The average grain size of the retained austenite phase and the martensite and ferrite was measured to be ~0.51 µm and ~0.68 µm respectively.

An IPF EBSD map of the partitioned retained austenite grains is shown in Fig. 6.6c, which indicates that the RAG inside each of the PAG have the same color, which may suggest that they have the same crystal orientation. For example, the RAG inside the PAG of grain # 1, are all colored red, indicating a <001>//ND crystal orientation (following the IPF color key presented in Fig. 6.6). In order to confirm this result, the RAG inside PAG grain #1 were partitioned and plotted separately, as shown in Fig 6.7a. On the other hand, the orientation distribution functions (ODFs) were calculated from the measured Euler angles (Bunge notation) using a harmonic series expansion method with a Gaussian half-width of 5° and a series rank of 22, and the resulting textures were plotted on the $\varphi_2 = 45°$

section of the Euler space (Fig. 6.7b). It can be seen from the ODFs that the retained austenite (RA) textures has a cube crystal orientation {001}<100>. Thus, it confirms the crystal orientation of all the RAG (red color RA in PAG grain # 1), as found in IPF map of Fig. 6.6c.

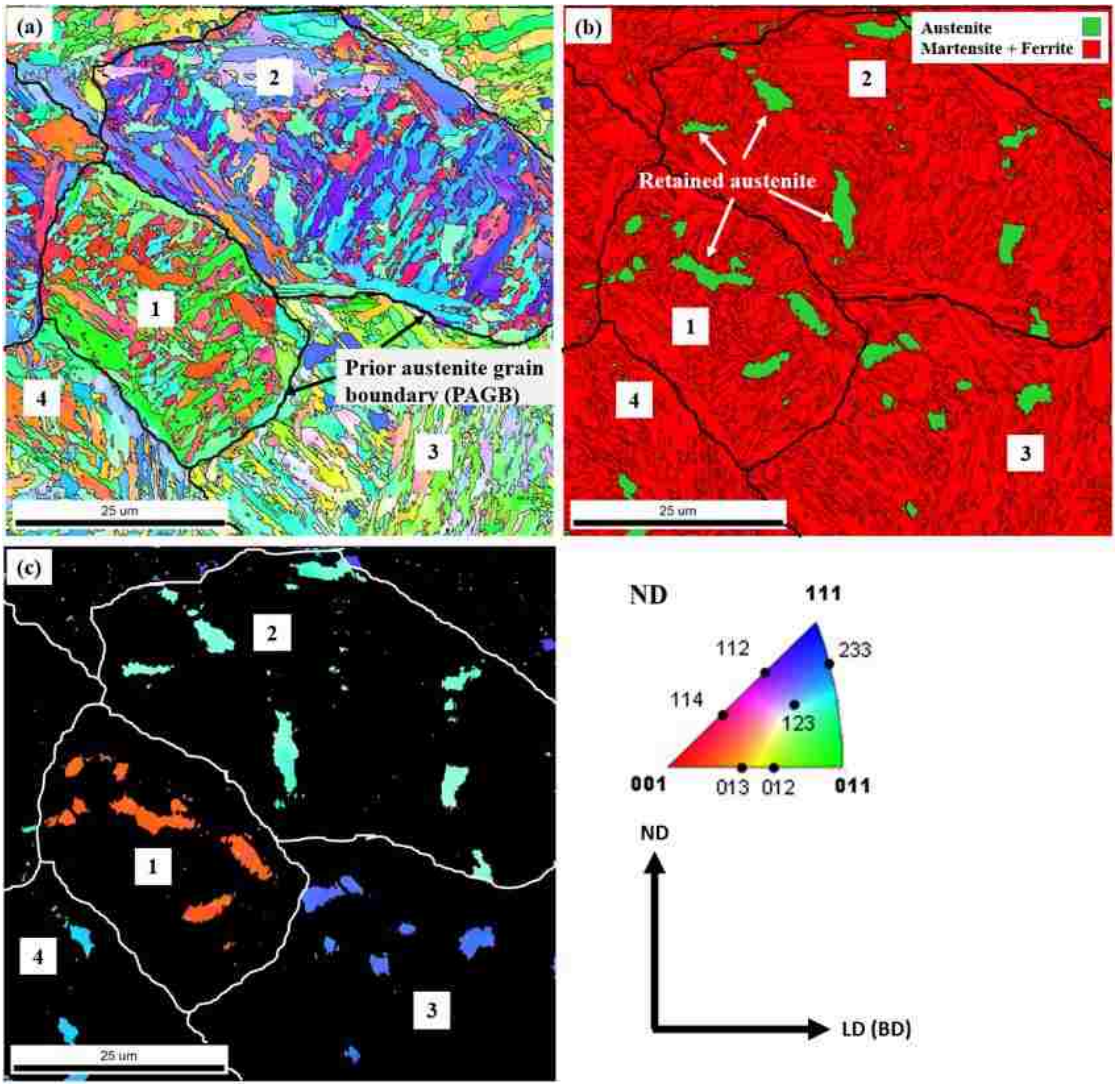

Figure 6. 6 Microstructure of the as-cladded AM AISI 420 MSS (BD-ND cross-section): (a) EBSD IPF map of the phases in the specimen, (b) a unique color map distinguishing the austenite grains (green) from the ferrite + martensite regions (red), and (c) EBSD IPF map of the RAG only after partitioning from the rest of the phases.

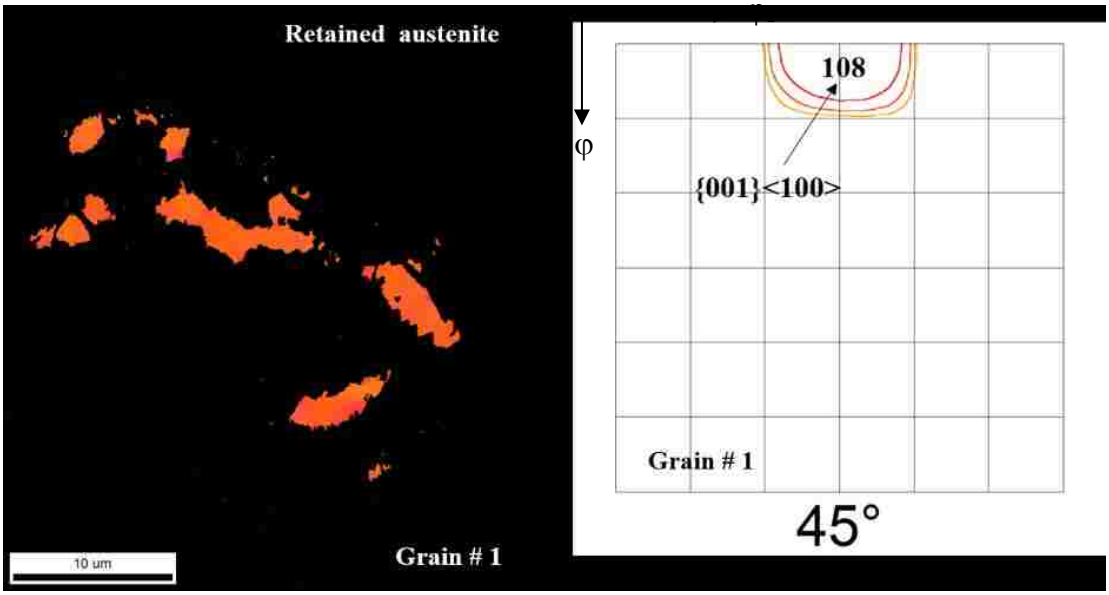

Figure 6. 7 The RAG inside the PAG # 1: (a) the IPF of the RAG only, and (b) the $\varphi_2 = 45°$ ODF section showing the crystal orientations of the retained austenite grains.

In order to measure the volume fraction of the martensite and ferrite phases separately, an EBSD scan was performed on an etched sample (Fig. 6.8). As indicated earlier, etching results in selective corroding of the delta ferrite phase, thus leaving behind the austenite and martensite phases which can distinguished from each other easily using EBSD. The regions that were not indexed in Fig. 6.8a and b correspond to the delta ferrite, which had an overall volume fraction of ~15.7%. This volume fraction of delta ferrite is extremely higher than the earlier finding in a single bead cladding [5]. It could be due to an excessive etching effect on the residual delta ferrite (black phase in Fig. 6.8 a-b). Thus, the over etched delta ferrite shows higher volume fraction. On the other hand, the martensite grains constituted ~74.5% of the scanned area, with an average grain size of ~ 1.02 µm. The retained austenite grains were partitioned from the rest of the phases (Fig. 6.8c) and had a volume fraction of ~9.8%, and an average grain size of ~1.04 µm. These results suggest that the phase distribution and grain size are anisotropic throughout the

thickness of the AM sample, which could be due to the different heating and cooling rates within the same sample during the manufacturing process.

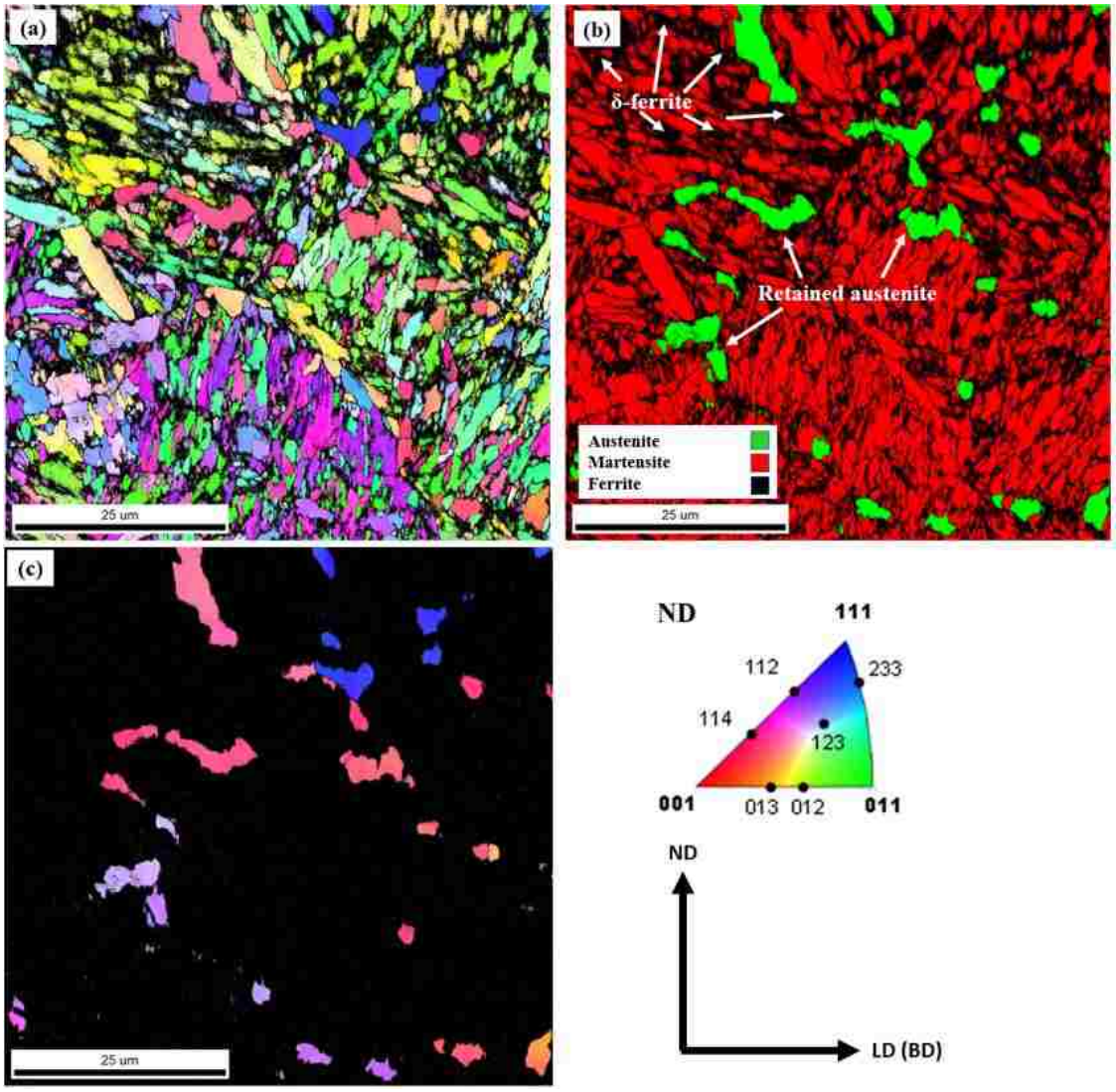

Figure 6. 8 Microstructure of the as-cladded AM AISI 420 MSS (BD-ND cross-section) after etching: (a) EBSD IPF map of the phases in the specimen, (b) a unique color map distinguishing the austenite grains (green) from the martensite grains (red) and ferrite grains (black), and (c) EBSD IPF map of the RAG only after partitioning from the rest of the phases.

Compared to the pre-hardened rolled sample, the average grain sizes of retained austenite and PAG are reduced substantially by 89% and 61%, respectively in the AM

sample. This is due to the high cooling rate (e.g., up to $1.5x10^4$ °C/s) observed in the laser cladding based AM sample [5].

6.3.2 Mechanical Properties: Transverse Direction

Mechanical testing for the transverse directions has different mechanical characteristics. Fig. 6.8 shows the engineering stress-strain curve of the as-cladded and heat-treated AM sample in the transverse direction (TD). A higher ultimate tensile strength (1774MPa) was revealed when the load was applied in the transverse direction of the as-cladded sample. Also, a linear strain hardening was observed in those AM samples. Though an average 13% total elongation was observed in this sample, there was no necking at a 2% area reduction. Hence a sudden failure of strength at the UTS was observed. The additive multi-layers grain boundary might work as obstacles in the transverse direction.

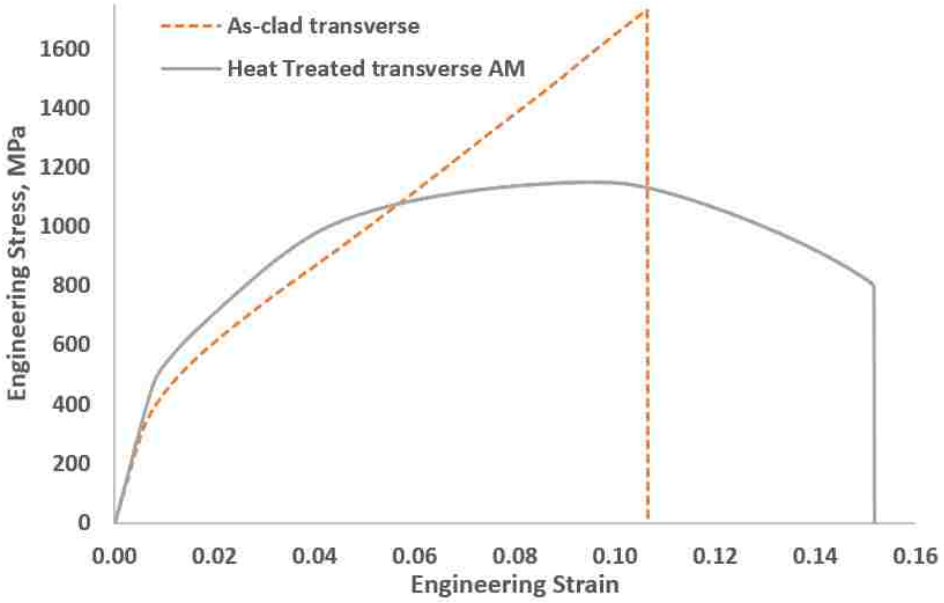

Figure 6. 9 Comparison of engineering stress and strain among the as-cladded (AC-T) and heat-treated (HT-T) AM samples in the transverse direction.

This transverse AM sample also shows lower yield strength (443 MPa) compared to the longitudinal one (493 MPa). Therefore, a stress-relief heat-treatment at 565°C for an

hour was proposed to get rid of this directionality and anisotropy of mechanical properties in the AM sample. This post-processing technique on the same transverse sample improved the ductility to 15 % and yield strength to 561 MPa. Consequently, this has led to a drop in the tensile strength, which was reduced to 1195 MPa (~33% decrease). However, these tensile properties are still higher than the as-cladded and pre-hardened sample in the longitudinal direction.

6.3.2.1 Cross-sectional Microstructure and Heat Treatment: Transverse Sample

Fig. 6.10 shows SEM images of a transverse cross-section of the as-cladded (Fig. 6.10a) and heat-treated (Fig. 6.10b) AM sample. Fig. 6.10a revealed that bead layers were crisscrossed through some inter-diffusion layers. The inter-diffusion layers were generated by the repeated heat cycling due from depositing the successive bead layers. These cumulative layers across the transverse direction caused differential strain during tensile loading resulting in sudden brittle failure at the observed ultimate tensile strength (UTS). As discussed, the alternate layers of successive beads and inter-diffusion zones (Fig. 6.10a) contributed towards the anisotropy in the mechanical properties of transverse AM samples. The inter-diffusion layers shown in Fig. 6.10a were not straight or parallel to each other as assumed; rather, they branched from one layer to the other due to the multi-layer solidification that occurred in this alloy. Previous studies confirmed that the temperature distribution and the size of the melt pool may increase from one layer to the next layer because of heat accumulation in the multilayer laser claddings [26], which might have contributed to the variation of those inter-diffusion layers. However, after heat treatment at 565°C for an hour, those layers of beads and inter-diffusion zones (Fig. 6.10b) had been diminished almost entirely for the transverse AM sample. Fig. 6.10c shows retained

austenite in the tempered martensitic matrix. This one-hour heat treatment drastically improved the yield strength (561 MPa) by ~ 27% compared to its as-cladded transverse sample. Although there was a 33% decease in the tensile strength (1195 MPa), it was associated with a dramatic increase of ~15% in ductility (in terms of total elongation), which made this heat-treated transverse sample more competitive than the as-cladded longitudinal one.

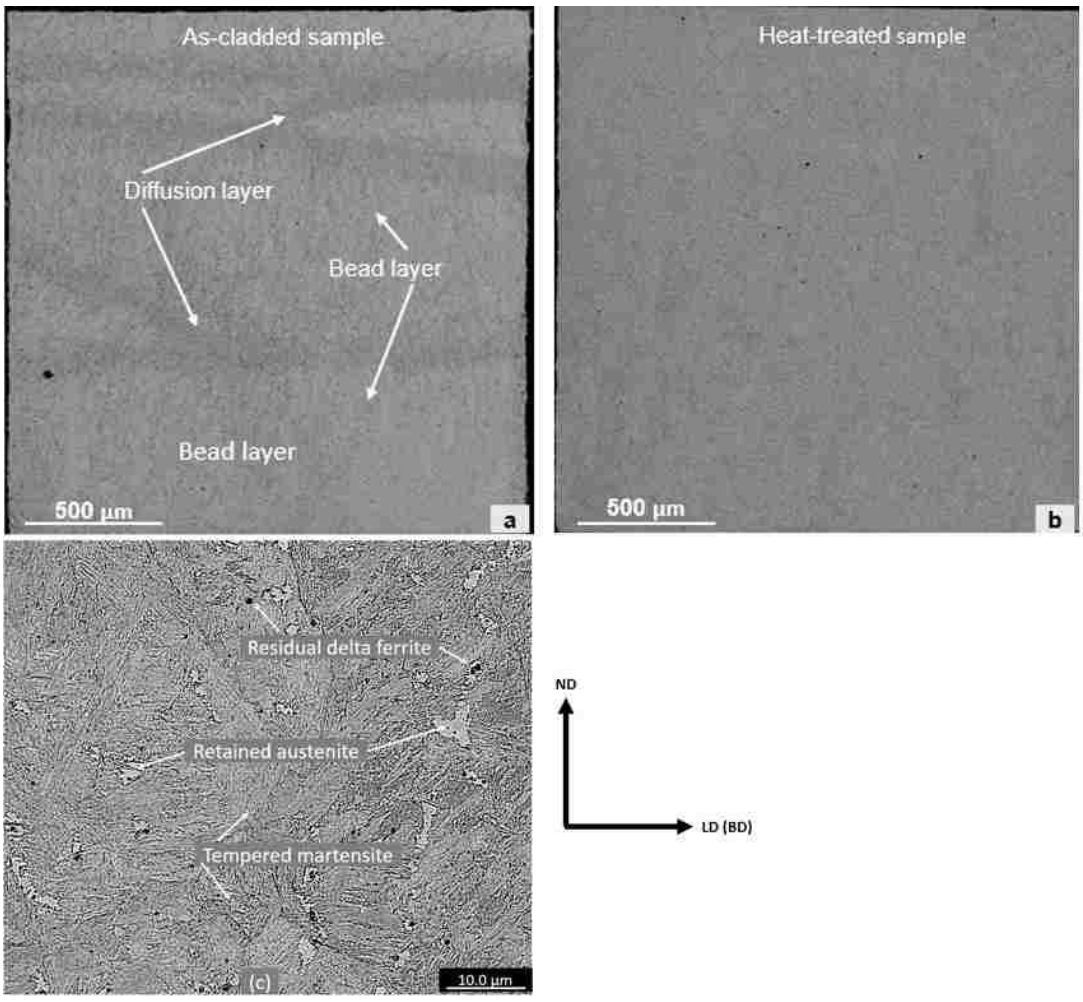

Figure 6. 10 Cross-sectional SEM image of (a) the as-cladded and (b) heat-treated sample (transverse direction); (c) magnified image of Fig. 6.10b.

6.3.3 Comparison of Mechanical Properties with Cross-Layered and Angular Deposited Sample

In addition to the stress-relief heat-treatment, this study was extended to explore alternative solutions to overcome the directionality and anisotropy observed in the above-mentioned AM samples. For further investigation, more AM samples were built using cross layered tool path with alternative layers in the longitudinal and transverse directions as well as using angular powder deposition technique (at 30°) against the horizontal base by employing a six-arm based robotic head. In the subsequent section of this paper, the results of mechanical behavior of those AM samples are presented and discussed.

Fig. 6.11. shows the engineering stress and strain curve of the as-cladded AM samples built by using cross layered (L+T) tool path and alternative powder deposition techniques at 30° in the longitudinal and transverse directions. It was revealed that these AM samples (cross-layered and 30° deposition) showed a high yield strength (of 521 and 495 MPa respectively) and a high UTS (of 1236 and 1297 MPa respectively) compared to the sample from the as-cladded AM in the longitudinal direction. Moreover, no sudden failure was observed at UTS of these samples when the load was applied in the transverse direction. Furthermore, AM samples built at 30° angular deposition showed 18% total elongation in the transverse direction. Average results of the main mechanical properties are summarized in the Table 6.2 from all tension tests mentioned earlier. The maximum values are bolded, and the minimum values are italicized.

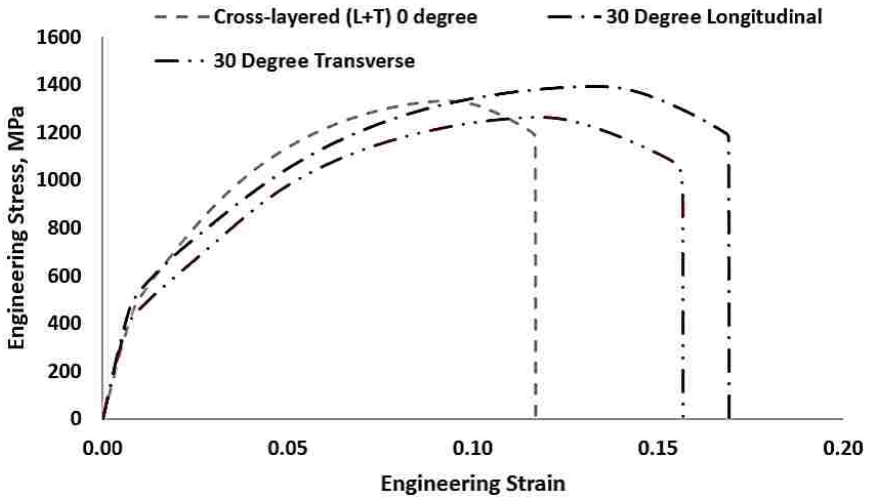

Figure 6. 11 Comparison of engineering stress and strain curve of the as-cladded AM samples built at cross layered (longitudinal+ transverse) and at 30° in the longitudinal as well as in the transverse directions.

Table 6. 2 Summary of tension tests for various sample orientations.

Sample orientation	0.2% Yield Strength (MPa)	Tensile Strength (MPa)	% of Area Reduction	% of Total Elongation
AC-L	493 ± *67*	1117 ± *32*	**34 ± *3***	**18± *0.9***
AC-T	*443 ± 18*	**1774 ± *58***	*2 ± 0.4*	*13± 3.8*
AC-HT-T	**561 ± *6***	1195 ± *66*	32 ± *0.3*	15± *0.6*
PH-L	*483 ± 67*	*1087 ± 3*	*28 ± 2*	*14± 0.6*
AC-(L+T)-0°	521 ± *14*	1236 ± *134*	21 ± *0.7*	*13± 1.7*
AC-30°L	495 ± *64*	1297 ± *43*	28 ± *2*	16± *0.7*
AC-30°T	470 ± *113*	1423 ± *44*	32 ± *0.6*	**18± *1.7***

As noted above, this laser-cladded AISI 420 MSS showed higher levels of mechanical properties when compared with a similar 420 commercial grade MSS (along the rolling direction in a pre-hardened condition). With the exceptions of sudden failure in the transverse direction, the laser-cladded AM samples showed ~16% increase in yield strength, ~ 63% increase in tensile strength, and ~29% increase in ductility in terms of total % elongation.

Moreover, it was revealed that as-cladded AM samples fabricated at 30° angular deposition showed better tensile strength compared to the other AM samples fabricated at the base horizontal orientation. Hence, it is important to analyze the microstructural evolution in these samples.

6.3.3.1 Microstructure Evolution in Angular Deposited Sample

The cyclic thermal processing of successive bead layers during this alternative additive manufacturing technique has an influence on the microstructure of the 420 MSS. Fig. 6.12a reveals two types of microstructures in the layered AM sample that differs substantially across the bead layers. Fig. 6.12b shows precipitation of mostly granular type chromium carbide ($Cr_{23}C_6$), in the ferritic matrix. No retained austenite or traces of martensite lath were observed even in the magnified image (Fig. 6.12b). It seems the initial microstructure (of delta ferrite, retained austenite and martensite) of this part were dissolved during the re-melting with the successive bead layer deposition when the temperature level remained at austenitic zone. Then the austenite transformed to ferrite with precipitation of carbide at a very slow cooling rate during the successive bead layer deposition at a temperature that is higher than the martensite start temperature. It indicated that this part of the layer has gone through a special thermal treatment when the chromium carbide transformed into a granular or globular form through a spheroidizing annealing process [1]. The sizes of these granular shaped chromium carbide varied between 250-500 nm, which was not observed in the other AM samples. On the other hand, Fig. 6.12c shows retained austenite in tempered martensite with little residual delta ferrite. It seems that this part of the layers went through a different thermal treatment during the successive building

of bead layers at a distant vicinity (compared to Fig. 6.12b), which is very similar to a tempering heat-treatment.

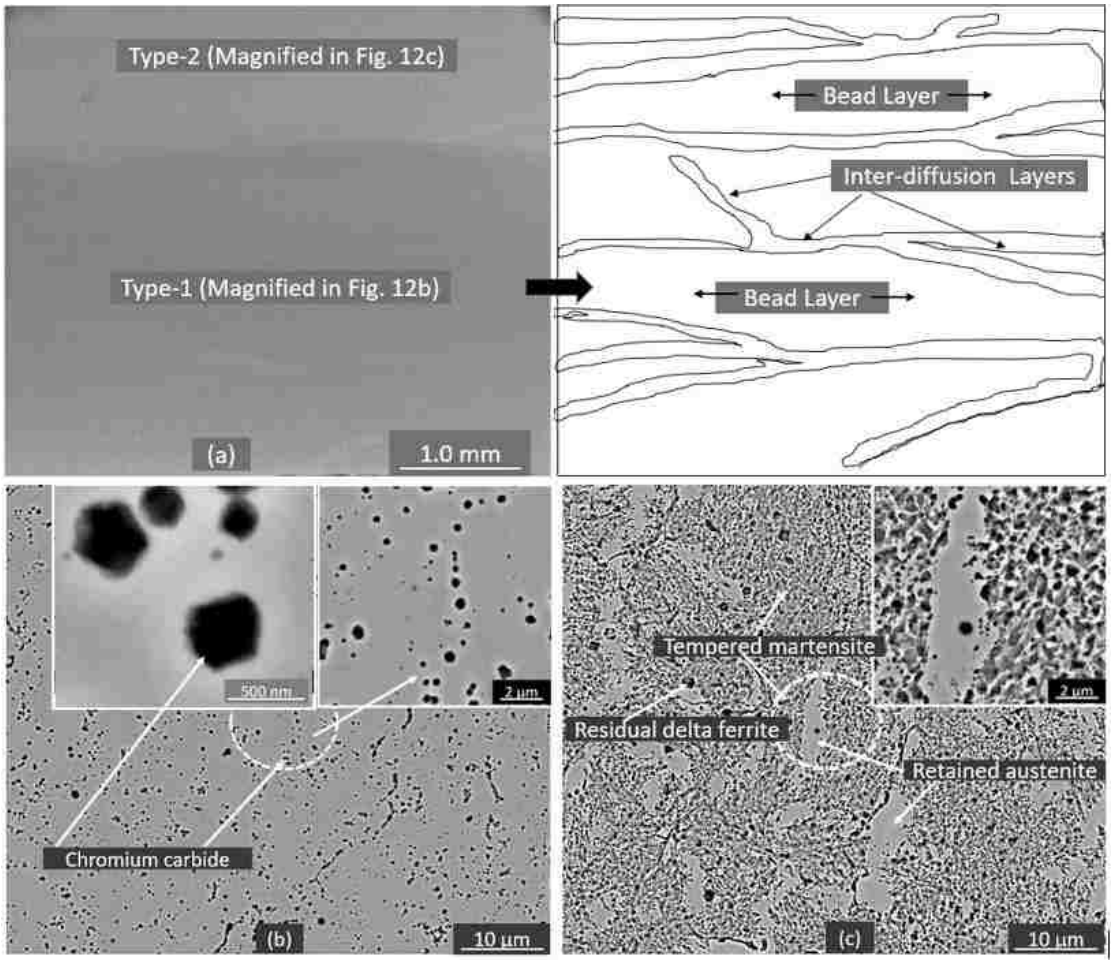

Figure 6. 12 (a) Cross-sectional SEM image of AM sample built at 30° angular deposition; (b) Magnified SEM image of type-1 microstructure in Fig. a; (c) Magnified SEM image of type-2 microstructure in Fig. 12a. (Etched with Ralph reagent).

Development of those dual sets of microstructures (ferritic matrix with precipitated carbide and tempered martensitic matrix with retained austenite) combinedly influenced the mechanical properties of angularly deposited AM samples in both the longitudinal and transverse directions. Additionally, this powder deposition technique was found to be very successful in combating the anisotropic problem in the transverse AM samples. Due to the development of unique microstructure shown in Fig. 6.12b and 6.12c, the tendency of

abrupt failure at UTS (in the transverse sample) was eliminated with higher ductility in those AM samples.

6.3.4 Fractography Analysis

The fracture surfaces of those tested samples were examined to reveal more information of the laser-cladded 420 stainless steel AM sample built at different orientations. Figs. 6.13a and 6.13b show fracture surfaces of the tensile specimen selected from the longitudinal and transverse direction (of AM samples), respectively. The ductile fracture was revealed in Fig. 6.13a with many small dimples where microvoids were initiated at the inclusions. The micro-voids nucleation sites were so numerous that the formation of micro-voids on the small inclusions retards the fracture until higher strains were reached, thus, increasing the elongation at fracture. Those voids gradually grew, and eventually, the ligaments between the microvoids were fractured. On the other hand, a brittle fracture was observed in Fig. 6.13b that is mostly intergranular with some dimples. In this intergranular fracture, the crack propagated through the prior austenite grain boundaries. It is most probably due to the segregation of residual delta ferrite in the grain boundaries that made it embrittled.

Fig. 6.13c shows the fracture surface of the heat-treated AM sample (selected from transverse direction). A transgranular ductile fracture was revealed with substantial plastic deformation. Many nano-sized microvoids were observed in the fracture surface, which coalescence into a crack that propagated rapidly into the necking area to make the ultimate fracture in the gauge length. It is assumed that the microvoids were nucleated from different inclusions at the inclusion-matrix interface. When the relatively hard inclusions did not deform at the same rate as the tempered martensitic matrix, microvoids were nucleated to

compensate the incompatibility. The overall fracture occurred when the microvoids had grown sufficiently to link up into a crack. This was reflected in its fracture surface, which was transformed from a coarse intergranular brittle fracture to a fully ductile fracture (Fig. 6.13c). This study strongly recommends a simple post-cladding heat treatment to minimize the directionality in the mechanical properties of as-cladded transverse sample.

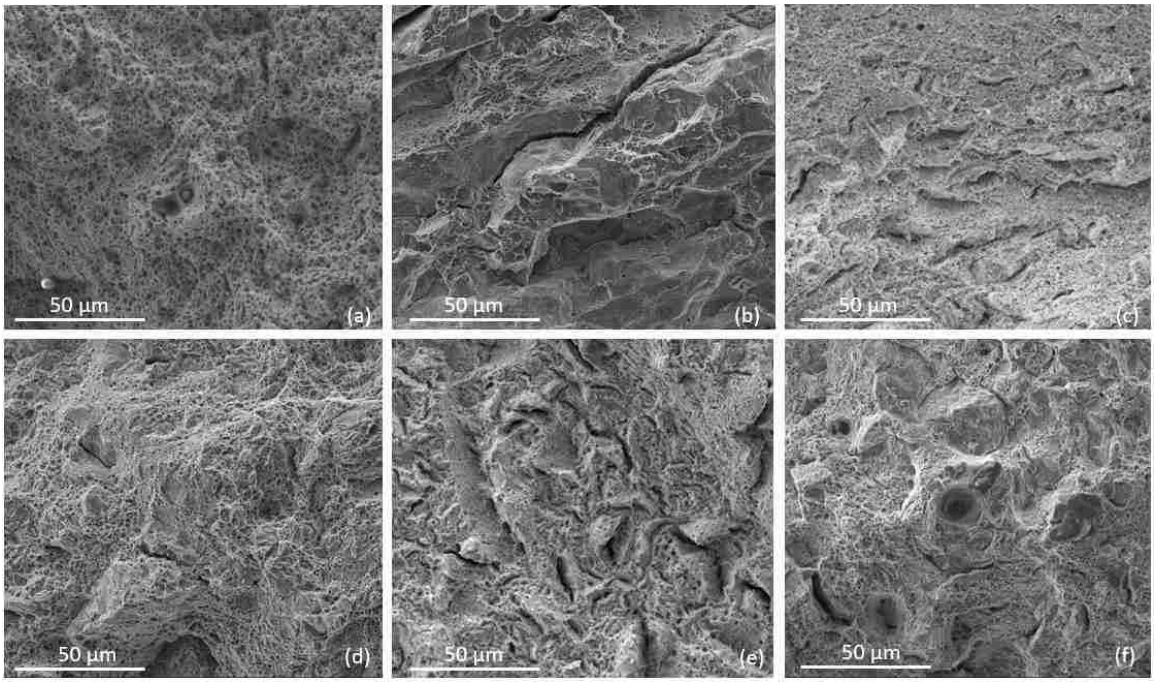

Figure 6. 13 Fracture surface of tensile specimen after tension testing, selected from (a) longitudinal as-cladded, (b) transverse as-cladded, (c) transverse heat-treated, (d) cross-layered (longitudinal + transverse) as-cladded, (e) As-cladded at 30° Longitudinal orientation, (f) As-cladded at 30° Transverse orientation of Laser-cladded AISI 420 Stainless steel.

Fig. 6.13d shows the fracture surface of the tensile specimen made with cross layered tool path (longitudinal and transverse) as-cladded condition while Figs. 6.13e and 6.13f represent the fracture surface of as-cladded tensile specimen made at 30° orientation in the respective longitudinal and transverse directions. A combination of transgranular (mostly) and intergranular (less) fracture was observed in cross-layered (L+T) sample.

Mostly transgranular ductile fracture was revealed in the longitudinal direction of AM sample built at 30° orientation. Conversely, a combination of intergranular and transgranular fracture, was observed with the same AM sample in the transverse direction.

The fracture surface shown in Fig. 6.13 indicated a significant difference for the samples built at different directions and orientations. A fully ductile fracture was observed in the as-cladded (longitudinal), and heat -treated samples showed high ductility (32% - 34%) in terms of percentage area reduction. On the other hand, a combination of intergranular and transgranular fracture surface observed in the cross-layered (L+T), and 30° angled sample showed medium ductility (20% - 28%), whereas, the coarse intergranular brittle fracture observed in the as-cladded transverse sample showed a very low ductility (2%) in terms of percentage area reduction.

Summary and Conclusions

In this study, the mechanical behavior of AISI 420 martensitic stainless steel (MSS) was characterized using tension testing of additive manufactured (AM) samples built at different orientations and directions of laser cladding. The microstructure of those AM samples was characterized using SEM and EBSD techniques, and the tension test results were correlated and compared against the commercial grade pre-hardened AISI 420 MSS. The results are summarized and concluded in the below points:

1. Laser-cladded samples from the transverse direction showed higher ultimate tensile strength (1774 MPa) compared to the longitudinal (build) direction of laser cladding (1117 MPa) and the rolling direction (longitudinal) of pre-hardened sample (1087 MPa) from commercial grade. However, the transverse sample

showed lower yield strength (443 MPa) compared to the longitudinal one (493 MPa).

2. Heat-treatment of transverse sample at 565 °C for an hour improved 27% of its yield strength (561 MPa) along with an increment of 15% ductility (in terms of total elongation) but with a sacrifice of its 32% tensile strength (to 1195 MPa). Heat treatment also changed the fractography nature from brittle to ductile fracture. Tensile properties of a heat-treated sample of transverse direction showed similar results observed in the longitudinal direction. This indicated that heat treatment can change the anisotropic nature of laser-cladded sample, which is very important for designing functional components.
3. EBSD analyses quantified the metallurgical phases in terms of volume fractions and grain sizes and revealed that the RAG has a similar crystal orientation within each PAGB. The EBSD scans have also shown the variations in the volume fraction and grain sizes of the different phases through the AM sample, indicating that the martensitic transformation occurred at different cooling rates within the same sample.
4. Laser-cladded samples built with cross-layered (mixed orientation, transverse + longitudinal) and built at 30° angular deposition in the longitudinal direction showed higher yield strength (521 and 495 MPa respectively) and progressively higher tensile strength (1236 and 1297 MPa respectively) compared to the regular horizontal base orientation (1117 MPa).
5. For design purpose, load bearing capacity should be considered in the longitudinal (building) direction of the laser-cladded AISI 420 MSS. Moreover, a simple post-

cladding heat treatment for an hour at 565 °C is strongly recommended to minimize the anisotropy in the mechanical properties of as-cladded transverse sample. Also, a building technique with 30° angle to the base (using table-table rotary stack to orient the specimen while deposition head is normal to the base) was found to improve the ultimate tensile strength as well as to improve and partially eliminate the directionality issue. This could be an important information for the designers with respect to "design for AM strategies".

6. These results are expected to be used for the laser-based additive manufacturing application of AISI 420 martensitic stainless steel in designing functional components. However, one prime limitation of these laser-based AM sample is found to be its low yield strength compared to the high tensile strength. The ratio of the yield strength vs. tensile strength needs to be improved to use this AM alloy in the potential automotive application. A bigger sample size needs to be designed as per ASTM standard to compare the test results from these miniature type test specimens in the future study.

References

[1] A.N. Isfahany, H. Saghafian, G. Borhani, The effect of heat treatment on mechanical properties and corrosion behavior of AISI420 martensitic stainless steel, J. Alloys Compd. 509 (2011) 3931–3936. doi:10.1016/j.jallcom.2010.12.174.

[2] J. Brnic, G. Turkalj, M. Canadija, D. Lanc, S. Krscanski, Martensitic stainless steel AISI 420 - Mechanical properties, creep and fracture toughness, Mech. Time-Dependent Mater. 15 (2011) 341–352. doi:10.1007/s11043-011-9137-x.

[3] F. Khodabakhshi, M.H. Farshidianfar, A.P. Gerlich, M. Nosko, V. Trembo, A. Khajepour, Materials Science & Engineering A Microstructure, strain-rate sensitivity, work hardening, and fracture behavior of laser additive manufactured

austenitic and martensitic stainless steel structures, 756 (2019) 545–561. doi:10.1016/j.msea.2019.04.065.

[4] G.A. Ravi, X.J. Hao, N. Wain, X. Wu, M.M. Attallah, Direct laser fabrication of three dimensional components using SC420 stainless steel, Mater. Des. 47 (2013) 731–736. doi:10.1016/j.matdes.2012.12.062.

[5] M.K. Alam, A. Edrisy, R.J. Urbanic, Microstructural Analysis of the Laser-Cladded AISI 420 Martensitic Stainless Steel, Metall. Mater. Trans. A. 50 (2019) 2495–2506. doi:https://doi.org/10.1007/s11661-019-05156-6.

[6] M.K. Alam, A. Edrisy, J. Urbanic, J. Pineault, Microhardness and Stress Analysis of Laser - Cladded AISI 420 Martensitic Stainless Steel, J. Mater. Eng. Perform. 26 (2017) 1076–1084. doi:10.1007/s11665-017-2541-x.

[7] M.K. Alam, J. Urbanic, S.M. Saqib, A. Edrisy, Effect of Process Parameters On The Microstructural Evolutions of Laser Cladded 420 Martensitic Stainless Steel, in: Mater. Sci. Technol. Conf. Proc. (MS&T15), Oct. 4-8, Columbus, Ohio, USA, 2015: pp. 35–54.

[8] M.K. Alam, R.J. Urbanic, N. Nazemi, A. Edrisy, Predictive modeling and the effect of process parameters on the hardness and bead characteristics for laser-cladded stainless steel, Int. J. Adv. Manuf. Technol. (2017). doi:10.1007/s00170-017-0898-5.

[9] Y. Kok, X.P. Tan, P. Wang, M.L.S. Nai, N.H. Loh, E. Liu, S.B. Tor, Anisotropy and heterogeneity of microstructure and mechanical properties in metal additive manufacturing: A critical review, Mater. Des. 139 (2018) 565–586. doi:10.1016/j.matdes.2017.11.021.

[10] A.A. Popovich, V.S. Sufiiarov, E. V. Borisov, I.A. Polozov, D. V. Masaylo, A. V. Grigoriev, Anisotropy of mechanical properties of products manufactured using selective laser melting of powdered materials, Russ. J. Non-Ferrous Met. 58 (2017) 389–395. doi:10.3103/S1067821217040149.

[11] A.A. Deev, P.A. Kuznetcov, S.N. Petrov, Anisotropy of mechanical properties and its correlation with the structure of the stainless steel 316L produced by the SLM method, Phys. Procedia. 83 (2016) 789–796. doi:10.1016/j.phpro.2016.08.081.

[12] L. Ji, J. Lu, C. Liu, C. Jing, H. Fan, S. Ma, Microstructure and mechanical properties of 304L steel fabricated by arc additive manufacturing, MATEC Web Conf. 128 (2017) 03006. doi:10.1051/matecconf/201712803006.

[13] W.E. Luecke, J.A. Slotwinski, Mechanical Properties of Austenitic Stainless Steel Made by Additive Manufacturing, J. Res. Natl. Inst. Stand. Technol. 119 (2014) 398. doi:10.6028/jres.119.015.

[14] T. Niendorf, S. Leuders, A. Riemer, H.A. Richard, T. Tröster, D. Schwarze, Highly anisotropic steel processed by selective laser melting, Metall. Mater. Trans. B

Process Metall. Mater. Process. Sci. 44 (2013) 794–796. doi:10.1007/s11663-013-9875-z.

[15] R.M. Mahamood, E.T. Akinlabi, Laser Additive Manufacturing, 3D Print. (n.d.) 154–171. doi:10.4018/978-1-5225-1677-4.ch008.

[16] E. Toyserkani, A. Khajepour, S. Corbin, Laser Cladding, CRC Press, New York, 2005.

[17] K. V. Wong, A. Hernandez, A Review of Additive Manufacturing, ISRN Mech. Eng. 2012 (2012) 1–10. doi:10.5402/2012/208760.

[18] D.D. Gu, W. Meiners, K. Wissenbach, R. Poprawe, Laser additive manufacturing of metallic components: materials, processes and mechanisms, Int. Mater. Rev. 57 (2012) 133–164. doi:10.1179/1743280411Y.0000000014.

[19] P. Krakhmalev, I. Yadroitsava, G. Fredriksson, I. Yadroitsev, In situ heat treatment in selective laser melted martensitic AISI 420 stainless steels, Mater. Des. 87 (2015) 380–385. doi:10.1016/j.matdes.2015.08.045.

[20] T. Kurzynowski, K. Gruber, W. Stopyra, B. Kuźnicka, E. Chlebus, Correlation between process parameters, microstructure and properties of 316 L stainless steel processed by selective laser melting, Mater. Sci. Eng. A. 718 (2018) 64–73. doi:10.1016/j.msea.2018.01.103.

[21] G. Telasang, J. Dutta Majumdar, N. Wasekar, G. Padmanabham, I. Manna, Microstructure and Mechanical Properties of Laser Clad and Post-cladding Tempered AISI H13 Tool Steel, Metall. Mater. Trans. A. 46 (2015) 2309–2321. doi:10.1007/s11661-015-2757-z.

[22] ASTM Int., Standard Test Methods for Tension Testing of Metallic Materials 1, Astm. (2009) 1–27. doi:10.1520/E0008.

[23] E. Weidmann, A. Guesnier, B. Taylor, Metallographic preparation of stainless steel, 2005. doi:01.05 / 62140005.

[24] K.B. Small, D. A. Englehart, Etching specialty alloys, Adv. Mater. Process. (2008) 32–37.

[25] Z. Wang, T.A. Palmer, A.M. Beese, Acta Materialia Effect of processing parameters on microstructure and tensile properties of austenitic stainless steel 304L made by directed energy deposition additive manufacturing, Acta Mater. 110 (2016) 226–235. doi:10.1016/j.actamat.2016.03.019.

[26] I. Hemmati, V. Ocelík, J.T.M. De Hosson, Microstructural characterization of AISI 431 martensitic stainless steel laser-deposited coatings, J. Mater. Sci. 46 (2011) 3405–3414. doi:10.1007/s10853-010-5229-2.

CHAPTER 7 Summary, Conclusions and Future Directions

The potential use of laser-based additive manufacturing process in creating functional 3D components as well as in the treatment of surface repair or refurbishment is being established as a sustainable industrial process. In this study, the laser cladding process was utilized to clad single bead samples as well as to build 3D additive manufactured (AM) samples in layers using AISI 420 MSS powder in a coaxial powder deposition method. This AM process has many process parameters such as the laser power (LP), powder feed rate (FR), laser speed (LS), contact tip to workpiece distance (CTD), and focal length (FL) that were associated with localized melting and non-equilibrium solidification in a cyclic manner. At present, there is a lack of scientific knowledge in characterizing the laser-cladded AISI 420 MSS. In this study, statistical modelling, X-Ray diffraction, SEM, TEM, and EBSD techniques, as well as hardness and tensile testing, were utilized to analyze the microstructural evolution and the mechanical behavior of laser-cladded single bead samples to the additive manufactured 3D samples built with AISI 420 MSS powder. The results have been either published or submitted to the peer-reviewed journal, as discussed in the Chapter 2-6. The summary and conclusions of all those chapters are briefly highlighted in the below sections, and some unresolved issues are proposed here as a future study.

Summary and Conclusions

7.1.1 Effect of Process Parameters

Multiple regression analysis revealed a statistically significant effect of process parameters on the single bead geometry and the bead microhardness. The FR and LS are found to be the most significant process parameters on the bead geometry characteristics

and the bead microhardness, respectively. Consequently, the interaction of the FR and LS has the most significant effect on the bead aspect ratios and bead microhardness, while the interaction of the FR and LP has the most significant effect on the bead wetting angle. The interaction of the LP and LS had the most insignificant effect on the predicted bead microhardness though this factor is still significant for the bead aspect ratio. Therefore, a very intriguing and complex relationship is observed within the process parameters and their interactions on the predicted bead geometry and bead microhardness. This analysis illustrates the difficulty in generating optimal solutions.

On the other hand, the CTD has the highest quadratic effect on the bead microhardness, followed by the LS. The FR has the highest quadratic effect on the bead geometry despite having the least effect on the bead microhardness. The FL has the least quadratic effect on all the responses except on the bead microhardness. The quadratic effects of those process parameters add significant curvature to the contour plots as well as identify a minimum, maximum, or a saddle point and ridge (rising ridge or a falling ridge) systems on the response surfaces of their respective 2D contour plots and 3D surface plots. Therefore, simplified and linearized models cannot effectively predict solutions unless the range of process settings is narrow. However, it is expected that the required bead geometry is achievable by automating the process parameter settings (in the CAD/CAM software) and varying them (specially, the LP, LS, and FR) with respect to the bead layer thickness during the laser-cladding AM process.

7.1.2 Metallography, Microhardness, and Residual Stress

The primary metallographic work and cross-sectional investigation of single bead as-cladded AISI 420 martensitic stainless steel revealed three distinct regions such as bead zone, dilution zone, and a heat affected zone with varying microhardness and residual stress profile. The higher-level hardness (743 $HV_{0.2}$) and residual stress (486 MPa tensile stresses, 1002 MPa compressive stress) were observed in the sample built with higher levels of laser power and laser speed compared to those of samples built with lower levels of power and speed. However, the post cladding heat treatment (PCHT) reduced 89% - 99% of the tensile stresses and homogenized the compressive stresses with substantial reduction throughout the bead zone of those cladded samples. Also, the PCHT has significantly reduced microhardness (by 35% - 43%) in the bead zone of those samples. It is expected that a simple post-cladding heat treatment (at 565 °C for an hour) is very important to minimize the residual stress and high hardness to make the part and coating machinable as required for the industrial application.

7.1.3 Microstructural Evolution

The primary microstructural analysis with optical and scanning electron microscopy (SEM) revealed non-equilibrium phases such as eutectic delta ferrite (δ_e-Fe), martensite, and retained austenite. X-ray diffraction confirmed those phases along with revealing metallic carbides like $Cr_{23}C_6$, Cr_7C_3, Fe_7C_3, and (Cr. Fe)C. The advanced comprehensive microstructural analysis with transmission electron microscopy (TEM) revealed various morphologies of ά-martensite, namely, plate martensite, thin plate martensite, and lenticular martensite in the bead zone; plate and lath martensite in the dilution zone; and large lath martensite in the interface zone. It was concluded that the

morphological differences of ά-martensite and presence of various metastable phases observed in each zone have significantly contributed to the variation of hardness and residual stress (RS). Also, an extremely high and differential cooling rate indicted that the first martensitic transformation occurred in the bead zone with the formation of plate-like martensite. Subsequently, the second phase transformation occurred in the dilution and interface zone with the formation of both plate and lath-like martensite, which created high compressive stress in these zones and high tensile stresses in the bead zone.

The EBSD parameters GOS (grain orientation spread) revealed that most of the grains at the BZ and HAZ were highly strained, and 26-59% fraction of the grains was at a high angle of GOS (3°-5°) indicating highly deformed grains in both regions. This could be one of the reasons for the devolvement of tensile stress in those regions. The other EBSD parameters IQ (Image Quality) maps indicated to be inversely proportional with the RS value. This IQ approach could be a very helpful tool to evaluate the RS distribution in those zones of single bead laser-cladded AISI 420 MSS. The EBSD analysis did not find any presence of retained austenite and was unable to distinguish the delta-ferrite from the martensite phase due to the similarity in their crystal structures (bcc vs. bct). Also, the EBSD analysis revealed variations in the size distribution of martensitic substructure in those zones that indicated occurrence of a differential cooling rate during martensitic transformation. Thus, TEM and EBSD analysis revealed the causes of residual stress and hardness variations in those zones of a single bead cladding.

7.1.4 Mechanical Behavior of Additive Manufactured (AM) Sample

The additive manufactured (AM) samples of AISI 420 martensitic stainless steel (MSS) built at different orientations and directions showed higher mechanical properties

compared to the pre-hardened commercial grade AISI 420 MSS. The AM samples showed higher UTS (1774 - 1117 MPa) compared to the commercial grade pre-hardened sample (1087 MPa). But the transverse AM sample showed lower ductility (2% in area reduction) compared to the pre-hardened (28%) as well as the AM sample (34%) in the longitudinal direction. However, heat-treatment of the transverse sample at 565 °C for an hour improved its yield strength up to 27% along with an increment of 47% in ductility (percentage of area reduction).

On the other hand, the AM samples built at 30° angle (to the regular horizontal base) showed higher mechanical properties (YS 495 MPa, UTS 1297 MPa) compared to the pre-hardened as well as other AM samples. The tendency of abrupt failure at UTS (in the transverse sample) was eliminated in these AM samples. While it is impossible to avoid applying load in the transverse direction of additive parts, for design purposes, the load bearing capacity should be considered in the longitudinal direction. For that reason, a simple post-cladding heat treatment (at 565 °C for an hour) is strongly recommended to minimize the anisotropy in the mechanical properties of as-cladded transverse sample. Moreover, shifting powder deposition mode from plain horizontal to the 30° angular base will also help to combat directionality and anisotropic properties in the AM samples. These results provide functional information, which can be used for AISI 420 martensitic stainless-steel components to be fabricated utilizing laser-based additive manufacturing approaches. However, one prime limitation of these laser-based AM samples is found to be their low yield strength compared to the high tensile strength. The ratio of the yield strength vs. tensile strength needs to be improved to use this AM alloy in any potential automotive application.

Recommendation for Future Directions

1. A detailed future study needs to be carried out with a new design of experiment (DOE) considering the variable laser energy (power/speed) input and using same materials' substrate of AISI 420 MSS powder. To maintain the repeatability as well as to verify the current test results, a bigger test specimen needs to be designed as per ASTM standard for comparison with the results from the current miniature type test specimens. For the future study, 3D additive samples need to be fabricated using different parts building technique, such as horizontal (0°) and angular powder deposition (20°, 30°, and 40°) with various wall thicknesses (2-5 mm) and sizes (200mm x 50mm) with keeping an option of various types of heat sink (e.g., holes, fins etc.) between the wall thickness of the 3D parts.
2. Development of residual stress in the AM parts is a challenge for using the parts as fabricated. A complete simulation-based study on the RS development in AM parts will be an important future contribution in the AM field to reduce the experimental cost of RS measurement.
3. To overcome the residual stress and anisotropic properties, a detailed future study needs to be carried out to extend the heat-treatment procedures at different temperatures and times for various samples built at different directions and orientations. The results from the future study can be compared with the test results from the current as-cladded AM samples.
4. Analyzing the thermal behavior in terms of heat accumulation, heat dissipation, and the overall heat transfer phenomenon of the additive layers is very important to understand the non-equilibrium solidification, as well as the anisotropic

properties in the additive, manufactured samples (built at horizonal bases and 20-40° angle to the base). However, these areas were beyond the scope of this current study. A future study is required to address the heat transfer issues in the AM samples using computational fluid dynamics (CFD) simulations and Finite element analysis (FEA).

5. An advanced EBSD and TEM study need to be carried out on the inter-diffusion zone and bead zone of layer-based AM sample to identify the delta-ferrite and differentiating this bcc phase from the martensite (bct) phase in the as-cladded AM samples. Special attention is required during the metallography of TEM sample preparation in order to locate the delta ferrite. The effect of delta ferrite on the mechanical properties also needs to be addressed in the future study.

Appendices - Copyright Letter from the Publishers and Co-authors

Appendix A – Copyright Letter for the Chapter 2

SPRINGER NATURE LICENSE
TERMS AND CONDITIONS

Jul 27, 2019

This Agreement between University of Windsor -- MOHAMMAD ALAM ("You") and Springer Nature ("Springer Nature") consists of your license details and the terms and conditions provided by Springer Nature and Copyright Clearance Center.

License Number	4556600809044
License date	Mar 26, 2019
Licensed Content Publisher	Springer Nature
Licensed Content Publication	The International Journal of Advanced Manufacturing Technology
Licensed Content Title	Predictive modeling and the effect of process parameters on the hardness and bead characteristics for laser-cladded stainless steel
Licensed Content Author	Mohammad K. Alam, Ruth Jill Urbanic, Navid Nazemi et al
Licensed Content Date	Jan 1, 2017
Licensed Content Volume	94
Licensed Content Issue	1
Type of Use	Thesis/Dissertation
Requestor type	academic/university or research institute
Format	print and electronic
Portion	full article/chapter
Will you be translating?	no
Circulation/distribution	<501
Author of this Springer Nature content	yes
Title	Microstructural Analysis of the Laser-Cladded AISI 420 Martensitic Stainless Steel
Institution name	University of Windsor
Expected presentation date	May 2019
Requestor Location	University of Windsor 401 Sunset Ave Windsor, ON N9C4E3 Canada Attn: University of Windsor
Total	0.00 USD

Terms and Conditions

Springer Nature Terms and Conditions for RightsLink Permissions

Springer Nature Customer Service Centre GmbH (the Licensor) hereby grants you a non-exclusive, world-wide licence to reproduce the material and for the purpose and requirements specified in the attached copy of your order form, and for no other use, subject to the conditions below:

1. The Licensor warrants that it has, to the best of its knowledge, the rights to license reuse of this material. However, you should ensure that the material you are requesting is original to the Licensor and does not carry the copyright of another entity (as credited in the published version).

   If the credit line on any part of the material you have requested indicates that it was reprinted or adapted with permission from another source, then you should also seek permission from that source to reuse the material.

2. Where **print only** permission has been granted for a fee, separate permission must be obtained for any additional electronic re-use.

3. Permission granted **free of charge** for material in print is also usually granted for any electronic version of that work, provided that the material is incidental to your work as a whole and that the electronic version is essentially equivalent to, or substitutes for, the print version.

4. A licence for 'post on a website' is valid for 12 months from the licence date. This licence does not cover use of full text articles on websites.

5. Where **'reuse in a dissertation/thesis'** has been selected the following terms apply: Print rights of the final author's accepted manuscript (for clarity, NOT the published version) for up to 100 copies, electronic rights for use only on a personal website or institutional repository as defined by the Sherpa guideline (www.sherpa.ac.uk/romeo/).

6. Permission granted for books and journals is granted for the lifetime of the first edition and does not apply to second and subsequent editions (except where the first edition permission was granted free of charge or for signatories to the STM Permissions Guidelines http://www.stm-assoc.org/copyright-legal-affairs/permissions/permissions-guidelines/), and does not apply for editions in other languages unless additional translation rights have been granted separately in the licence.

7. Rights for additional components such as custom editions and derivatives require additional permission and may be subject to an additional fee. Please apply to Journalpermissions@springernature.com/bookpermissions@springernature.com for these rights.

8. The Licensor's permission must be acknowledged next to the licensed material in print. In electronic form, this acknowledgement must be visible at the same time as the figures/tables/illustrations or abstract, and must be hyperlinked to the journal/book's homepage. Our required acknowledgement format is in the Appendix below.

9. Use of the material for incidental promotional use, minor editing privileges (this does not include cropping, adapting, omitting material or any other changes that affect the meaning, intention or moral rights of the author) and copies for the disabled are permitted under this licence.

10. Minor adaptations of single figures (changes of format, colour and style) do not require the Licensor's approval. However, the adaptation should be credited as shown in Appendix below.

Appendix — Acknowledgements:

For Journal Content:
Reprinted by permission from [**the Licensor**]: [**Journal Publisher** (e.g. Nature/Springer/Palgrave)] [**JOURNAL NAME**] [**REFERENCE CITATION** (Article name, Author(s) Name), [**COPYRIGHT**] (year of publication)

For **Advance Online Publication papers:**
Reprinted by permission from [**the Licensor**]: [**Journal Publisher** (e.g. Nature/Springer/Palgrave)] [**JOURNAL NAME**] [**REFERENCE CITATION** (Article name, Author(s) Name), [**COPYRIGHT**] (year of publication), advance online publication, day month year (doi: 10.1038/sj.[JOURNAL ACRONYM].)

For Adaptations/Translations:
Adapted/Translated by permission from [**the Licensor**]: [**Journal Publisher** (e.g. Nature/Springer/Palgrave)] [**JOURNAL NAME**] [**REFERENCE CITATION** (Article name, Author(s) Name), [**COPYRIGHT**] (year of publication)

Note: For any republication from the British Journal of Cancer, the following credit line style applies:

Reprinted/adapted/translated by permission from [**the Licensor**]: on behalf of Cancer Research UK: : [**Journal Publisher** (e.g. Nature/Springer/Palgrave)] [**JOURNAL NAME**] [**REFERENCE CITATION** (Article name, Author(s) Name), [**COPYRIGHT**] (year of publication)

For **Advance Online Publication** papers:
Reprinted by permission from The [**the Licensor**]: on behalf of Cancer Research UK: [**Journal Publisher** (e.g. Nature/Springer/Palgrave)] [**JOURNAL NAME**] [**REFERENCE CITATION** (Article name, Author(s) Name), [**COPYRIGHT**] (year of publication), advance online publication, day month year (doi: 10.1038/sj.[JOURNAL ACRONYM])

For Book content:
Reprinted/adapted by permission from [**the Licensor**]: [**Book Publisher** (e.g. Palgrave Macmillan, Springer etc) [**Book Title**] by [**Book author**(s)] [**COPYRIGHT**] (year of publication)

Other Conditions:

Version 1.1

Appendix B – Copyright Letter for the Chapter 3

SPRINGER NATURE LICENSE
TERMS AND CONDITIONS

Jul 27, 2019

This Agreement between University of Windsor -- MOHAMMAD ALAM ("You") and Springer Nature ("Springer Nature") consists of your license details and the terms and conditions provided by Springer Nature and Copyright Clearance Center.

The publisher has provided special terms related to this request that can be found at the end of the Publisher's Terms and Conditions.

License Number	4557391006747
License date	Mar 27, 2019
Licensed Content Publisher	Springer Nature
Licensed Content Publication	Journal of Materials Engineering and Performance
Licensed Content Title	Microhardness and Stress Analysis of Laser-Cladded AISI 420 Martensitic Stainless Steel
Licensed Content Author	Mohammad K. Alam, Afsaneh Edrisy, Jill Urbanic et al
Licensed Content Date	Jan 1, 2017
Licensed Content Volume	26
Licensed Content Issue	3
Type of Use	Thesis/Dissertation
Requestor type	academic/university or research institute
Format	print and electronic
Portion	full article/chapter
Will you be translating?	no
Circulation/distribution	>50,000
Author of this Springer	yes
Title	Microhardness and Stress Analysis of Laser-Cladded AISI 420 Martensitic Stainless Steel
Institution name	University of Windsor
Expected presentation date	May 2019
Requestor Location	University of Windsor 401 Sunset Ave Windsor, ON N9C4E3 Canada Attn: University of Windsor
Billing Type	Invoice
Billing Address	University of Windsor 401 Sunset Ave

Windsor, ON N9C4E3
Canada
Attn: University of Windsor

Total 0.00 USD

Terms and Conditions

Springer Nature Terms and Conditions for RightsLink Permissions

Springer Nature Customer Service Centre GmbH (the Licensor) hereby grants you a non-exclusive, world-wide licence to reproduce the material and for the purpose and requirements specified in the attached copy of your order form, and for no other use, subject to the conditions below:

1. The Licensor warrants that it has, to the best of its knowledge, the rights to license reuse of this material. However, you should ensure that the material you are requesting is original to the Licensor and does not carry the copyright of another entity (as credited in the published version).

   If the credit line on any part of the material you have requested indicates that it was reprinted or adapted with permission from another source, then you should also seek permission from that source to reuse the material.

2. Where **print only** permission has been granted for a fee, separate permission must be obtained for any additional electronic re-use.

3. Permission granted **free of charge** for material in print is also usually granted for any electronic version of that work, provided that the material is incidental to your work as a whole and that the electronic version is essentially equivalent to, or substitutes for, the print version.

4. A licence for 'post on a website' is valid for 12 months from the licence date. This licence does not cover use of full text articles on websites.

5. Where **'reuse in a dissertation/thesis'** has been selected the following terms apply: Print rights of the final author's accepted manuscript (for clarity, NOT the published version) for up to 100 copies, electronic rights for use only on a personal website or institutional repository as defined by the Sherpa guideline (www.sherpa.ac.uk/romeo/).

6. Permission granted for books and journals is granted for the lifetime of the first edition and does not apply to second and subsequent editions (except where the first edition permission was granted free of charge or for signatories to the STM Permissions Guidelines http://www.stm-assoc.org/copyright-legal-affairs/permissions/permissions-guidelines/), and does not apply for editions in other languages unless additional translation rights have been granted separately in the licence.

7. Rights for additional components such as custom editions and derivatives require additional permission and may be subject to an additional fee. Please apply to Journalpermissions@springernature.com/bookpermissions@springernature.com for these rights.

8. The Licensor's permission must be acknowledged next to the licensed material in print. In electronic form, this acknowledgement must be visible at the same time as the figures/tables/illustrations or abstract, and must be hyperlinked to the journal/book's homepage. Our required acknowledgement format is in the Appendix below.

9. Use of the material for incidental promotional use, minor editing privileges (this does not include cropping, adapting, omitting material or any other changes that affect the meaning, intention or moral rights of the author) and copies for the disabled are permitted under this licence.

10. Minor adaptations of single figures (changes of format, colour and style) do not require the Licensor's approval. However, the adaptation should be credited as shown in Appendix below.

Appendix — Acknowledgements:

For Journal Content:
Reprinted by permission from [**the Licensor**]: [**Journal Publisher** (e.g. Nature/Springer/Palgrave)] [**JOURNAL NAME**] [**REFERENCE CITATION** (Article name, Author(s) Name), [**COPYRIGHT**] (year of publication)

For **Advance Online Publication papers:**
Reprinted by permission from [**the Licensor**]: [**Journal Publisher** (e.g. Nature/Springer/Palgrave)] [**JOURNAL NAME**] [**REFERENCE CITATION** (Article name, Author(s) Name), [**COPYRIGHT**] (year of publication), advance online publication, day month year (doi: 10.1038/sj.[JOURNAL ACRONYM].)

For Adaptations/Translations:
Adapted/Translated by permission from [**the Licensor**]: [**Journal Publisher** (e.g. Nature/Springer/Palgrave)] [**JOURNAL NAME**] [**REFERENCE CITATION** (Article name, Author(s) Name), [**COPYRIGHT**] (year of publication)

Note: For any republication from the British Journal of Cancer, the following credit line style applies:

Reprinted/adapted/translated by permission from [**the Licensor**]: on behalf of Cancer Research UK: : [**Journal Publisher** (e.g. Nature/Springer/Palgrave)] [**JOURNAL NAME**] [**REFERENCE CITATION** (Article name, Author(s) Name), [**COPYRIGHT**] (year of publication)

For **Advance Online Publication** papers:
Reprinted by permission from The [**the Licensor**]: on behalf of Cancer Research UK: [**Journal Publisher** (e.g. Nature/Springer/Palgrave)] [**JOURNAL NAME**] [**REFERENCE CITATION** (Article name, Author(s) Name), [**COPYRIGHT**] (year of publication), advance online publication, day month year (doi: 10.1038/sj.[JOURNAL ACRONYM])

For Book content:
Reprinted/adapted by permission from [**the Licensor**]: [**Book Publisher** (e.g. Palgrave Macmillan, Springer etc) [**Book Title**] by [**Book author**(s)] [**COPYRIGHT**] (year of publication)

Other Conditions: requestor will advise the society in writing and in advance of the exercise of any of the foregoing rights ASM International (ASM) Mr. Stanley C. Theobald, Managing Director, 9639 Kinsman Road Materials Park, OH 44073-002, USA; e-mail: stan.theobald@asminternational.org

Version 1.1

Appendix C – Copyright Letter for the Chapter 4

SPRINGER NATURE LICENSE
TERMS AND CONDITIONS

Jul 27, 2019

This Agreement between University of Windsor -- MOHAMMAD ALAM ("You") and Springer Nature ("Springer Nature") consists of your license details and the terms and conditions provided by Springer Nature and Copyright Clearance Center.

License Number	4556600406541
License date	Mar 26, 2019
Licensed Content Publisher	Springer Nature
Licensed Content Publication	Metallurgical and Materials Transactions A
Licensed Content Title	Microstructural Analysis of the Laser-Cladded AISI 420 Martensitic Stainless Steel
Licensed Content Author	Mohammad K. Alam, Afsaneh Edrisy, Jill Urbanic
Licensed Content Date	Jan 1, 2019
Type of Use	Thesis/Dissertation
Requestor type	academic/university or research institute
Format	print and electronic
Portion	full article/chapter
Will you be translating?	no
Circulation/distribution	<501
Author of this Springer Nature content	yes
Title	Microstructural Analysis of the Laser-Cladded AISI 420 Martensitic Stainless Steel
Institution name	University of Windsor
Expected presentation date	May 2019
Requestor Location	University of Windsor 401 Sunset Ave Windsor, ON N9C4E3 Canada Attn: University of Windsor
Total	0.00 USD

Terms and Conditions

Springer Nature Terms and Conditions for RightsLink Permissions

Springer Nature Customer Service Centre GmbH (the Licensor) hereby grants you a non-exclusive, world-wide licence to reproduce the material and for the purpose and requirements specified in the attached copy of your order form, and for no other use, subject to the conditions below:

1. The Licensor warrants that it has, to the best of its knowledge, the rights to license reuse of this material. However, you should ensure that the material you are requesting is original to the Licensor and does not carry the copyright of another entity (as credited in the published version).

   If the credit line on any part of the material you have requested indicates that it was reprinted or adapted with permission from another source, then you should also seek permission from that source to reuse the material.

2. Where **print only** permission has been granted for a fee, separate permission must be obtained for any additional electronic re-use.

3. Permission granted **free of charge** for material in print is also usually granted for any electronic version of that work, provided that the material is incidental to your work as a whole and that the electronic version is essentially equivalent to, or substitutes for, the print version.

4. A licence for 'post on a website' is valid for 12 months from the licence date. This licence does not cover use of full text articles on websites.

5. Where **'reuse in a dissertation/thesis'** has been selected the following terms apply: Print rights of the final author's accepted manuscript (for clarity, NOT the published version) for up to 100 copies, electronic rights for use only on a personal website or institutional repository as defined by the Sherpa guideline (www.sherpa.ac.uk/romeo/).

6. Permission granted for books and journals is granted for the lifetime of the first edition and does not apply to second and subsequent editions (except where the first edition permission was granted free of charge or for signatories to the STM Permissions Guidelines http://www.stm-assoc.org/copyright-legal-affairs/permissions/permissions-guidelines/), and does not apply for editions in other languages unless additional translation rights have been granted separately in the licence.

7. Rights for additional components such as custom editions and derivatives require additional permission and may be subject to an additional fee. Please apply to Journalpermissions@springernature.com/bookpermissions@springernature.com for these rights.

8. The Licensor's permission must be acknowledged next to the licensed material in print. In electronic form, this acknowledgement must be visible at the same time as the figures/tables/illustrations or abstract, and must be hyperlinked to the journal/book's homepage. Our required acknowledgement format is in the Appendix below.

9. Use of the material for incidental promotional use, minor editing privileges (this does not include cropping, adapting, omitting material or any other changes that affect the meaning, intention or moral rights of the author) and copies for the disabled are permitted under this licence.

10. Minor adaptations of single figures (changes of format, colour and style) do not require the Licensor's approval. However, the adaptation should be credited as shown in Appendix below.

Appendix — Acknowledgements:

For Journal Content:
Reprinted by permission from [**the Licensor**]: [**Journal Publisher** (e.g. Nature/Springer/Palgrave)] [**JOURNAL NAME**] [**REFERENCE CITATION** (Article name, Author(s) Name), [**COPYRIGHT**] (year of publication)

For **Advance Online Publication papers:**
Reprinted by permission from [**the Licensor**]: [**Journal Publisher** (e.g. Nature/Springer/Palgrave)] [**JOURNAL NAME**] [**REFERENCE CITATION** (Article name, Author(s) Name), [**COPYRIGHT**] (year of publication), advance online publication, day month year (doi: 10.1038/sj.[JOURNAL ACRONYM].)

For Adaptations/Translations:
Adapted/Translated by permission from [**the Licensor**]: [**Journal Publisher** (e.g. Nature/Springer/Palgrave)] [**JOURNAL NAME**] [**REFERENCE CITATION** (Article name, Author(s) Name), [**COPYRIGHT**] (year of publication)

Note: For any republication from the British Journal of Cancer, the following credit line style applies:

Reprinted/adapted/translated by permission from [**the Licensor**]: on behalf of Cancer Research UK: : [**Journal Publisher** (e.g. Nature/Springer/Palgrave)] [**JOURNAL NAME**] [**REFERENCE CITATION** (Article name, Author(s) Name), [**COPYRIGHT**] (year of publication)

For **Advance Online Publication** papers:
Reprinted by permission from The [**the Licensor**]: on behalf of Cancer Research UK: [**Journal Publisher** (e.g. Nature/Springer/Palgrave)] [**JOURNAL NAME**] [**REFERENCE CITATION** (Article name, Author(s) Name), [**COPYRIGHT**] (year of publication), advance online publication, day month year (doi: 10.1038/sj.[JOURNAL ACRONYM])

For Book content:
Reprinted/adapted by permission from [**the Licensor**]: [**Book Publisher** (e.g. Palgrave Macmillan, Springer etc) [**Book Title**] by [**Book author**(s)] [**COPYRIGHT**] (year of publication)

Other Conditions:

Version 1.1

Appendix D – Permission Letter from the Co-authors

University of Windsor

Mohammad Alam <alam117@uwindsor.ca>

Request for permission
5 messages

Mohammad Alam <alam117@uwindsor.ca> Sun, Aug 4, 2019 at 8:59 AM
To: Navid Nazemi <navid.nazemi@camufacturing.com>, Navid Nazemi <nazemi@uwindsor.ca>

Dear Navid,
I hope you are doing well.
Please note that I am submitting my Ph.D. dissertation soon. I am including one manuscript, "Predictive Modeling and the Relative Effect of Process Parameters on the Bead Geometry and Microhardness for a Single Bead Laser Cladding of AISI 420 Stainless Steel", where you were a co-author with me.

Could you please give me your permission to use the above titled manuscript in my thesis?

With kind regards,

Mohammad K. Alam
Ph.D Candidate

Mechanical, Automotive and Materials Engineering Department
University of Windsor
401 Sunset Avenue
Windsor, ON N9B 3P4
Canada

Navid Nazemi <nazemi@uwindsor.ca> Sun, Aug 4, 2019 at 9:54 AM
To: Mohammad Alam <alam117@uwindsor.ca>
Cc: Navid Nazemi <navid.nazemi@camufacturing.com>

Hi Mohammad,

I hope you are doing well as well. Congradulations to finishing your PhD.
Of course you have the permission to use this article in your dissertation. I am honored having a chance working with you on this article.

I wish you success in all your future endeavors.

Best regards,
Navid

Navid Nazemi, Ph.D., P.Eng.
Structural Engineer, Buildings + Places
D 905.747.7855
navid.nazemi@aecom.com

AECOM
105 Commerce Valley Drive West, Markham, Ontario L3T 7W3
T 905-886-7022 F 905-886-9494
www.aecom.com

Mohammad Alam <alam117@uwindsor.ca> Sun, Aug 4, 2019 at 10:20 AM
To: Navid Nazemi <nazemi@uwindsor.ca>

Thank you so much Navid for your prompt reply and permission.
Yes indeed, it was a good opportunity to work with you.
Wishing you all the best at your endeavor.

With kind regards,

Mohammad K. Alam
Ph.D Candidate

Mechanical, Automotive and Materials Engineering Department
University of Windsor
401 Sunset Avenue
Windsor, ON N9B 3P4
Canada

University of Windsor

Mohammad Alam <alam117@uwindsor.ca>

Permission letter

3 messages

Mohammad Alam <alam117@uwindsor.ca> Sat, Aug 3, 2019 at 9:00 PM
To: Mehdi Mehdi <mehdi6@uwindsor.ca>

Dear Mehdi,
Thank you very much for your time and efforts in collaborating with me for two manuscripts. I appreciate your contribution to EBSD works in both manuscripts.
I need official permission from you as I am including those two manuscripts in my dissertation.

Could you please confirm that you are allowing me to use those manuscripts in my thesis?

With kind regards,

Mohammad K. Alam
Ph.D Candidate

Mechanical, Automotive and Materials Engineering Department
University of Windsor
401 Sunset Avenue
Windsor, ON N9B 3P4
Canada

Mehdi Mehdi <mehdi6@uwindsor.ca> Mon, Aug 5, 2019 at 1:37 AM
To: Mohammad Alam <alam117@uwindsor.ca>

Hello Mohammad,

I do confirm that you are allowed to use these results in your dissertation.

Regards,
MM
[Quoted text hidden]

Mohammad Alam <alam117@uwindsor.ca> Mon, Aug 5, 2019 at 8:17 AM
To: Mehdi Mehdi <mehdi6@uwindsor.ca>

Dear Mehdi,
Thank you very much for your confirmation.
It was indeed a good opportunity to work with you on the EBSD analysis.

Bets regards,

Mohammad K. Alam
Ph.D Candidate
Research Assistant
Mechanical, Automotive and Materials Engineering Department
University of Windsor
401 Sunset Avenue
Windsor, ON N9B 3P4
Canada

University of Windsor

Mohammad Alam <alam117@uwindsor.ca>

First Publication with James

6 messages

Mohammad Alam <alam117@uwindsor.ca> Thu, Feb 16, 2017 at 2:39 PM
To: James laptop <xrdlab@protoxrd.com>

Hello James,
I am very pleased to inform you that our residual stress analysis article has been published in the Journal of Materials Engineering and Performance. Here is the link:
http://link.springer.com/article/10.1007/s11665-017-2541-x
The article is attached for your review.

Best regards,

Mohammad K. Alam
Ph.D Student
Mechanical, Automotive and Materials Engineering Department
University of Windsor
401 Sunset Avenue
Windsor, ON N9B 3P4
Canada

Mohammad Alam <alam117@uwindsor.ca> Mon, Aug 5, 2019 at 8:53 AM
To: James Pineault <xrdlab@protoxrd.com>

Hello James,
Good morning. It has been a long time that I worked with you to publish a paper on the residual stress. I will be submitting my PhD dissertation soon where this manuscript is included. I need permission from you to include this paper in my thesis. Could you please confirm that you are allowing me to use this manuscript in my thesis?

Thanks for your time and consideration.

Best regards,

Mohammad K. Alam
Ph.D Candidate

Mechanical, Automotive and Materials Engineering Department
University of Windsor
401 Sunset Avenue
Windsor, ON N9B 3P4
Canada

James Pineault <xrdlab@protoxrd.com> Mon, Aug 5, 2019 at 9:04 AM
To: Mohammad Alam <alam117@uwindsor.ca>

Hi Mohammad,

Sure, please feel free to include any of the work in your thesis.

[Quoted text hidden]

Mohammad Alam <alam117@uwindsor.ca> Mon, Aug 5, 2019 at 9:13 AM
To: James Pineault <xrdlab@protoxrd.com>

Thank you very much James. It was indeed a great opportunity to work you with.
Best regards,

Mohammad K. Alam
Ph.D Candidate

Mechanical, Automotive and Materials Engineering Department
University of Windsor
401 Sunset Avenue
Windsor, ON N9B 3P4
Canada

Vita Auctoris

Mohammad Khurshed-ul Alam
MASc, Materials Engineering, University of Windsor
Email: alam117@uwindsor.ca
Publications:
https://scholar.google.com/citations?user=3h6IHKUAAAAJ&hl=en
https://www.researchgate.net/profile/Mohammad_Alam33/publications

Refereed contributions (Peer-reviewed Journal and Conference proceedings):

1. **M.K. Alam**, A. Edrisy, J. Urbanic, J. Pineault, Microhardness and Stress Analysis of Laser - Cladded AISI 420 Martensitic Stainless Steel, J. Mater. Eng. Perform. 26 (2017) 1076–1084. doi:10.1007/s11665-017-2541-x. **(Published)**

2. **M.K. Alam**, R.J. Urbanic, N. Nazemi, A. Edrisy, Predictive modeling and the effect of process parameters on the hardness and bead characteristics for laser-cladded stainless steel, Int. J. Adv. Manuf. Technol. (2017). doi:10.1007/s00170-017-0898-5. **(Published)**

3. **M.K. Alam**, N. Nazemi, R.J. Urbanic, S.M. Saqib, A. Edrisy, Investigating Process Parameters and Microhardness Predictive Modeling Approaches for Single Bead 420 Stainless Steel Laser Cladding. SAE Technical Papers, **(2017**) doi:10.4271/2017-01-0283. **(Published)**

4. N. Nazemi, **M.K. Alam**, R.J. Urbanic, S.M. Saqib, A. Edrisy, A Hardness Study on Laser Cladded Surfaces for a Selected Bead Overlap Conditions, SAE Technical Papers. **(2017)** doi:10.4271/2017-01-0285. **(Published)**

5. N. Nazemi, R.J. Urbanic, **M.K. Alam,** Hardness and residual stress modeling of powder injection laser cladding of P420 coating on AISI 1018 substrate. Int. J. Adv. Manuf. Tech. (**2017**) DOI 10.1007/s00170-017-0760-9 (**Published**)

6. **M.K. Alam**, J. Urbanic, S.M. Saqib, A. Edrisy, Effect of Process Parameters On The Microstructural Evolutions of Laser Cladded 420 Martensitic Stainless Steel, in: Mater. Sci. Technol. Conf. Proc. (MS&T15), Oct. 4-8, Columbus, Ohio, USA, (2015): pp. 35–54, (**Published**, Conference proceedings).

7. **M.K. Alam**, A. Edrisy, R.J. Urbanic, Microstructural Analysis of the Laser-Cladded AISI 420 Martensitic Stainless Steel, Metall. Mater. Trans. A. 50 (2019) 2495–2506. doi:https://doi.org/10.1007/s11661-019-05156-6. **(published).**

8. **M.K. Alam**, M. Mehdi, R.J. Urbanic, A. Edrisy, Electron Backscatter Diffraction (EBSD) Analysis of Laser-Cladded 420 Stainless steel, J. of Materials Characterization, **(2019)** MATERIALSCHAR_2019_1647 (Under review).

9. **M.K. Alam**, M. Mehdi, R.J. Urbanic, A. Edrisy, Mechanical Behavior of Additive Manufactured AISI 420 Martensitic Stainless Steel, Journal of Materials Science and Engineering A**, (2019)** MSEA-D-19-04444 (Under review).

Conference Presentation:

1**.** A. Edrisy, **M.K. Alam**, R.J. Urbanic, (**2018**) Laser Cladding of AIS 420 Martensitic Stainless Steel. XXVII International Materials Research Congress, Cancun, Mexico.

2. **M.K. Alam,** A. Edrisy, R.J. Urbanic, **(2017**) Characterization of Laser-Cladded 420 Martensitic Stainless Steel. 29th Canadian Material Science Conference CMSC17, Ottawa, Canada.

3. **M.K. Alam**, N. Nazemi, R.J. Urbanic, S.M. Saqib, A. Edrisy, **(2017**) Microhardness Predictive Modeling Approaches for Single Bead 420 Stainless Steel Laser Cladding. WCX17: SAE World Congress Experience, Detroit, MI, USA

4. N. Nazemi, **M.K. Alam**, R.J. Urbanic, S.M. Saqib, A. Edrisy, **(2017)** A Hardness Study on Laser Cladded Surfaces for a Selected Bead Overlap Conditions, WCX17: SAE World Congress Experience, Detroit, MI, USA

5. **M.K. Alam**, R.J. Urbanic, A. Edrisy, S.M. Saqib, (2015) Effect of Process Parameters on the Microstructural Evolutions of Laser Cladded 420 Martensitic Stainless Steel. International Conference on Material Science and Technology, MS&T15, Ohio, USA.